Doctoral School in Environmental Engineering

Modelling water budget at a basin scale using JGrass-NewAge system

WULETAWU ABERA WORKU
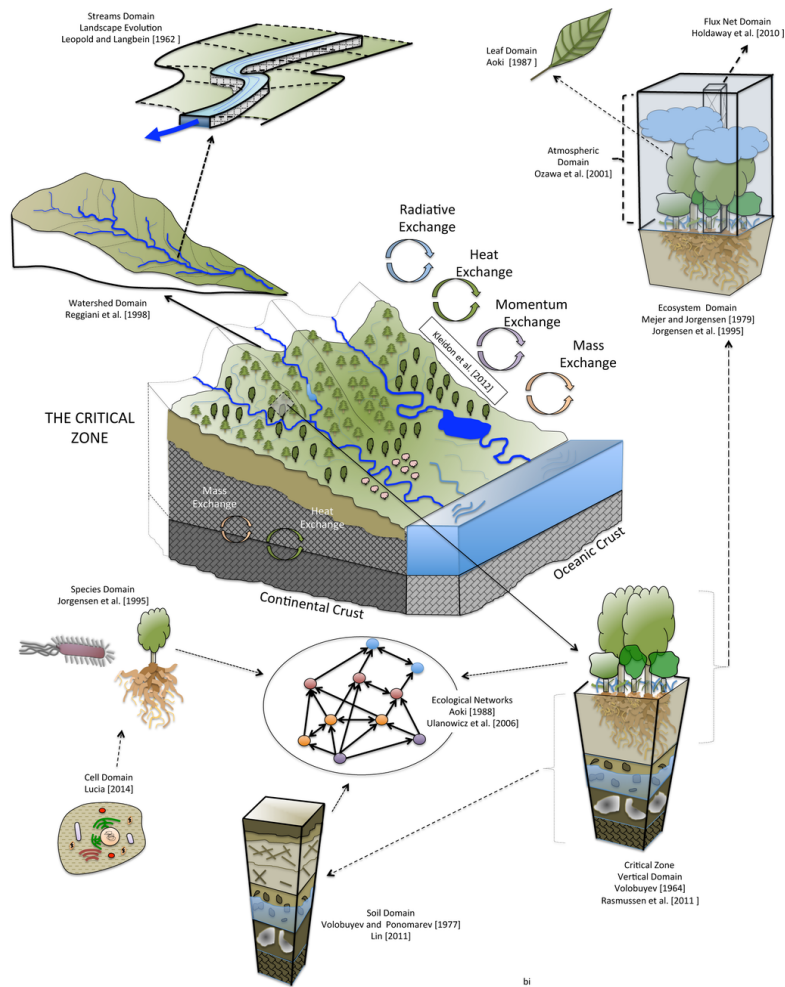
UNIVERSITY OF TRENTO - Italy

Department of Civil, Environmental and Mechanical Engineering

APRIL 2016

Doctoral thesis in Environmental Engineering, 27th cycle
Department of Civil, Environmental and Mechanical Engineering, University of Trento
Academic year 2015/2016

Supervisor: Professor Riccardo Rigon

Date of the defense: 28/04/2016

Signature from head of PhD committee:
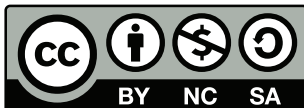
The figure on the cover page is taken from "Quijano, J., Lin, H. Entropy in the Critical Zone: A Comprehensive Review. Entropy 2014, 16, 3482-3536."

ACKNOWLEDGEMENTS AND DEDICATION

Here I am at the end of my PhD journey. To pass the ups and downs of life in general and the PhD journey in particular, there has been many people helping me directly and indirectly. Before and above all, GOD is always my mainstay.

First and foremost I would like to thank my supervisor, Professor Riccardo Rigon, for all his ideas, discussions, support, criticism, and thorough review of my works. His technical skills to solve problems at hand and long term envision and outlook for the subject of hydrology is exceptional. I also would like to thank him for demanding better research results; for challenging my decisions; and for providing me funds to cover part of my PhD studies and attend conferences, seminars and summer schools. These supports, both the financial and intellectual, contributes to my academic growth as a hydrologist. Prof, thank you for all!

I am indebted to Professor Marco Borga of Padova University for his support by providing me data, having comments and discussion on my works. He was also my MSc thesis supervisor, and the first person to introduce me to the subject of hydrology. My colleague and friend Dr. Giuseppe Formetta helped me a lot with the source codes and practicalities of JGrass-NewAge model system. The success of this PhD work is also comes from his immense support in the codes and informatics point of view. Thanks Giuseppe!. I am sincerely thankful to my research group members, Marialaura Bancheri and Francesco Serafin.

I would like to extend my heartfelt gratitude to Dr. Luca Brocca (Research Institute for Geo-Hydrological Protection, National Research Council, Italy) for his support for providing me data, for the discussion we have and the corrections he made on my work. I am thankful to my PhD examination committee, Prof. Erik Mosselman (Delft University of Technology, Delft, Netherlands), Prof. Mario Schirmer (Centre for Hydrogeology, University of Neuchatel, Switzerland), and Prof. Marco Toffolon (University of Trento, Italy) for their comments and discussions.

I am grateful to National Meteorological Agency (NMA) of Ethiopia, Ministry of Water Resources (MOWR) of Ethiopia, and University of Reading for providing me meteorological, discharge and TAMSAT satellite rainfall data for Upper Blue Nile basin respectively. I would like to extend my gratitude to all academic and administrative staffs of the Department of Civil, Environmental, and Mechanical Engineering of Trento university. The Department of Geography and Environmental studies of Mekelle University is always kind to me, and thankful for granting me a study leave.

I would like to thank my father, Abera Worku, and my mother, Taytu Mohamed,

i

SUMMARY

Water resources availability and its variability is one of the most pressing global problems. Hydrological models are useful to understand the water balance of a basin, providing information for water resource forecast, assessment, and management. The effectiveness of the models in estimating the freshwater space-time availability and variability, however, depends on concurrent and explicitly modeling of all water budget components instead of a single component estimation and optimization. The whole water budget modelling at basin scale requires a combined solution from hydrological and spatial information tools, in-situ and remote sensing data. The present dissertation describes an effort to improve estimation of each water budget component, and water budget closure at various spatial and temporal scales, by combining JGrass-NewAge model system, GIS spatial toolbox, in-situ and remote sensing data.

JGrass-NewAge is a system which deploys modern informatics to facilitate models maintainability and reproducible research. It integrates advanced GIS features and the Object Modelling System version 3 infrastructures, which allow for a component-based modelling experience. This means that JGrass-NewAGE is not actually a model, but a set of elements (the components) that can be combined just before runtime to produce various modelling solutions. Topics like calibration of processes, the interpolation forcing and the assessment of forecasting errors can therefore be faced with consistent and solid approaches. In this context also the use of some remote sensing resources can be inserted appropriately and with new techniques. For all the analysis, two significantly different basins, in terms of size and hydrological processes, are considered as case studies. These are Posina river basin in northeast Italy (small size basin) and Upper Blue Nile basin (large size basin) are used as case study.

The uDig Spatial Toolbox (uST) GIS infrastructure that is used for generating the hydromorphological parameters is described in the second chapter. A large number of tools are included in uST for terrain analysis, river network delineation, and basin topology characterization. In addition, the geomorphological settings necessary to run JGrass-NewAGE are shown.

The third chapter studies the effect of spatial discretization and the hillslope size on basin responses. The possible epistemic uncertainty exerted by the use of subbasin spatial discretization of topographic information in the semi-distributed hydrological modelling has been studied. The use of different spatial representation in hydrological modelling context has been also studied by comparing JGrass-NewAGE with a model configuration called PeakFlow. The latter is an implementation of the geomorphological

unit hydrograph based on the width function. The experiment indicates that the Peak-Flow model, with a more accurate spatial representation, reproduce the storm events slightly better than the JGrass-NewAGE model.

In the fourth chapter, the thesis set-up JGrass-Newage modelling solution for the estimation of hydrological modelling inputs (rainfall, snow, temperature data) and estimates them, as well as with their errors. Regards to the meteorological forcings (mainly temperature and precipitation), in Posina river basin where there are relatively dense meteorological stations, the effects of different interpolation schemes were evaluated. Since the hydrological processes from rainfall is different from snowfall, a new method of separating rainfall and snowfall was introduced using MODIS imagery data.

In the fifth chapter, JGrass-NewAGE was used to estimate the whole set of water balance components. For evapotranspiration (ET) estimation, the Priestley-Taylor component of JGrass-NewAGE is used. In order to calibrate its parameter a new method based on the water budget was implemented. This method uses two different hypothesis on available data (budget stationarity "Budyko hypothesis", and local proportionality of actual evapotranspiration to soil moisture availability). Finally the spatial and temporal dynamics of water budget closure of Posina river basin is presented.

The sixth chapter concerns about the inputs data, particularly precipitation, for water balance modeling in a region where ground-based gauge data are scarce. Five high-resolution satellite rainfall estimation (SRE) products were compared and analysed using the available rain gauge. The basin rainfall is investigated systematically, and it was found that, at some locations, the difference in mean annual rainfall estimates between these SREs very high. In addition to the identification of the best performing products, the chapter shows that a simple empirical cumulative distribution (ecdf) mapping bias correction method can provide a means to improve the rainfall estimation of all SREs, and the highest improvement is obtained for CMORPH.

In the seventh chapter, using the capability of JGrass-NewAGE components and different remote sensing data, the spatio-temporal water budget of Upper Blue Nile basin is simulated. The water budget components (rainfall, discharge evapotranspiration, and storage) were analyzed for about 16 years at daily time step using the modeling solution and remote sensing data set. For the verification of the approaches followed, wide ranges of remote sensing data (MODIS ET product MOD16, GRACE, and EUMETSAT CM SAF cloud fractional cover) are used.

TABLE OF CONTENTS

INTRODUCTION

1.1 Introduction

Water is essential for survival of life on earth, and is also the major determining factor for society economic growth, health, quality of life. Nevertheless, globally, it is under unprecedented pressure. The demands for freshwater resource are increasing due to growing requirement for agriculture, industry and increasing population growth. However, its availability is hampered by many recent problem such as climate and land use change, water pollution and economic growth. Besides, the competition in water use by different economic sectors (i.e. for drinking, agriculture, hydropower, domestic, industry) and ecosystems escalates the water scarcity (Jury and Vaux, 2005). Water shortage is not the only problem, but also the variability of the hydrological cycle affects the society. Countries with high hydroclimatic variability would require huge investment on infrastructures and strong water institutions. The latter case is true particularly in developing countries where majority of the society depends on agriculture.

To cope up with freshwater problems, Hall et al. (2014) identified three important elements: (1) institutions, legal systems and organizations that can effectively govern and plan the water resources (Pahl-Wostl, 2007); (2) infrastructures that can be used for water storage (dam, water transfer, and levees), desalination technology, and other flood reduction structures (Gleick, 2003); and (3) water resource information that is essential for operating institutions and infrastructure. In fact, countries level of economic growth can be described (Hall et al., 2014) (figure1.1) based on the interlink between institutional

capacity and the nature of hydrological variability,.
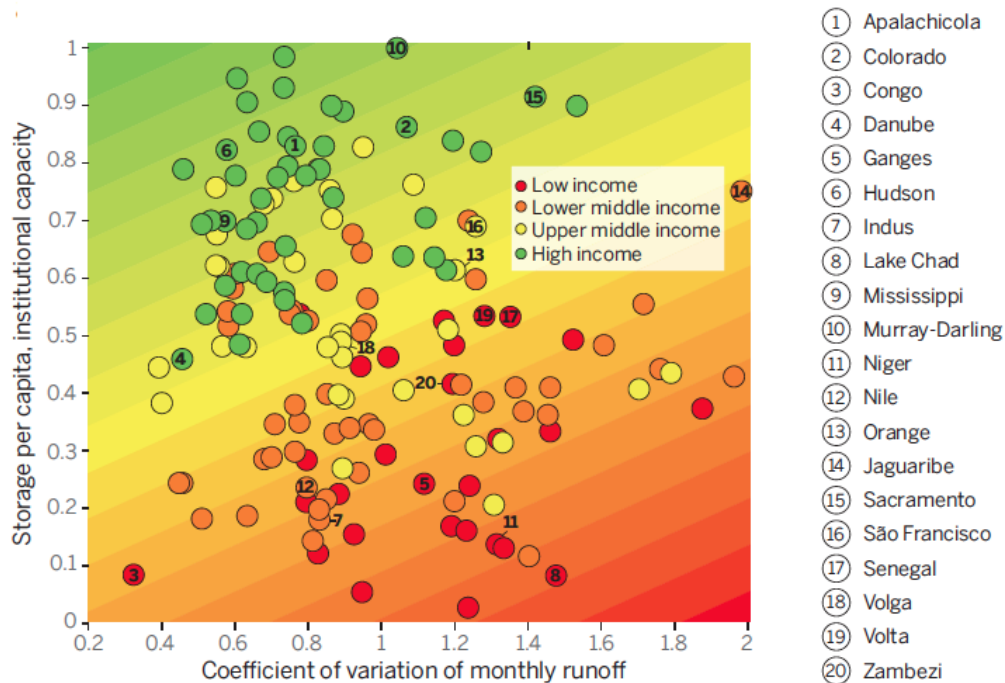
Figure 1.1: The interlink between hydrological variability; investment in infrastructure and institutional capacity; and the economic growth (Hall et al., 2014)

On the contrary to the fact that it is a key for water resource management and governance, information on spatial and temporal domain of hydrological cycle is usually scarce (Buytaert et al., 2014; Hannah et al., 2011). Instead, effective managment requires scientifically rigorous evidence of each water budget component.

Since the first formulations of rational method in 1850 (Mulvany, 1850), many hydrological models has been developed to understand and/or provide information (data and knowledge) on different water cycle components. Historical evolution and thorough review of many hydrological models and their applications can be refereed in Todini (2007); Davison and van der Kamp (2008); Praskievicz and Chang (2009); Moradkhani and Sorooshian (2008). Traditionally, most hydrological modeling has been rather limited to the understanding (or estimation) of a particular process (flux) at a particular point. For instance, in the last decades, rainfall-runoff modeling has been the main modeling exercise, in which case, most commonly the objective has been the estimation of peak discharges, or discharge hydrograph, at basin outlet, without a clear understanding of the internal processes. In the recent years, however, tremendous effort has been advancing the representations and estimations of physical processes and fluxes using fully

distributed, physically based models. Due to their data demanding and computationally expensive nature their application were rather limited to small and experimental basin.

Semi-distributed models are in the middle of simple rainfall-runoff lumped modeling and fully distributed physically based models. This group of models are better in combining the advantage of a less computational demand, and the ability to explicit represent the major hydrological fluxes that are of interest for water resources management. Notwithstanding the availability of myriads of hydrological models, basin water budget components such as evapotranspiration and water storage are rarely characterized and analyzed even if the estimation of all the components at various temporal and spatial scale is the modern day societal demand. For this reason, for instance, the EU Water Framework Directive endorsed and promoted models that cover entire fresh water cycle (Højberg et al., 2013).

1.2 Challenges in basin water resources modelling

In regards to the societal needs and the hydrological scientific community future goals, Wood et al. (2011) identified six major challenges that we re-interpreted here below from our experience.

The **quantification of spatially and temporally continuous water fluxes and total water availability at various scales** is the main (grand) challenge of modelling. All the water fluxes (precipitation, evapotranspiration, discharge) and the total water storage of a basin are equally important factors determining the water availability. The challenge comes from the data sets, tools, and approaches used to estimate the water budget and its closures (Wood et al., 2012). In addition to the procedures and methods, its purpose i.e. the provision of reasonable accurate hydrological information for operational purposes such as agriculture and water resources infrastructure (irrigation, hydropower dams etc), is real challenge of hydrological science.

In practice, tackling this grand challenge and improve the representations of water resources have many problems. Effective use of different data sources; modeling frameworks and modeling solutions; and spatial data analysis and visualization tools have to be combined. Specifically, the challenges of water budget modelling can be outlined as follows:

Challenge 1: The use of efficient and innovative GIS tools to generate hydrogeomrphological parameters that can be used in hydrological modelling. Hydrological models are based on highly spatially variable information, and the use of efficient GIS tools is

necessary. While there has been many GIS tools available, the challenge is to find one that is suited and based on strong dedicated functionalities that can be used to drive hydrological models (Sui and Maggio, 1999).

Challenge 2: The second challenge is how to better estimate and predict precipitation and the other important auxiliary meteorological data required by hydrological applications. Capturing the space-time heterogeneity of precipitation (and other auxiliary meteorological forcings) for accurate water resource modelling, has always been at the center of hydrological research, and still is a very important open problem (Nicótina et al., 2008). The efforts to improve this challenge goes in two directions. The first one is efficient use of available data, when they exist, by using sophisticated tools for spatial information generations. The other challenge (**Challenge 3**) is the separation of precipitation into snowfall and rainfall.

Challenge 4: The modeling and optimization in hydrological literature has been highly tailored to discharge forecasting. The estimation of the whole water budget at various scale with reasonable performances for each of the hydrological cycle components is a problem of different complexity.

Challenge 5 is the efficient utilization of satellite data in regions where data are scarce. In spite of its recent advancement, satellite data has many problems and that need to be addressed properly before use. Comparison between the available satellite data sets and ground measurements needs to be applied using different error and bias reduction strategies.

Thus, (**Challenge 6**) is the optimal combination of different remote sensing data, not only rainfall data, ground based measurements, statistical techniques and hydrological models to estimate and forecast water resources at any location of the basin.

The contribution of this research is to address all the above-mentioned challenges of basin hydrological modelling, estimate the water budget at various spatial and temporal scales, and thereby provide a methodological framework to advance the hydrological forecasting.

1.3 Objectives of this study

In order to achieve the above goals, the specific objectives addressed are to:

- Describe the GIS tools and algorithms that are useful to provide topographic data for hydrological modeling inputs;

- Examine the effects of topographic descretization on basin hydrological response;

- Obtain improved accuracy of water budget inputs and other meteorological forcing estimates from in situ observation;

- Obtain an improve precipitation estimates from remote sensing products in areas where in situ observations are scarce;

- Improve methods to estimate discharge and evapotranspiration fluxes.

- Set-up standardized working framework for water budget closure for basins of various sizes (from ten to hundreds thousand square kilomtres) by combining different components of the JGrass-NewAge system and remote sensing data;

- Estimate water budget closure of Posina river basin and Upper Blue Nile river basin at high temporal and spatial scale.

1.4 Organization of the thesis

The thesis is organized based on the logical flows of challenges raised in section 1.2. Chapter two is about a specialized set of GIS tools that are useful to generate spatial the hydro-geomorphological parameters that are subsequently used in the hydrological modeling. In this chapter the capability of JGrasstools are discussed.The third chapter is an extension of the first chapter, and is more specialized to the geomorphological characterization of semi-distributed model in general and JGrass-NewAGE in particular. The chapter aims to examine the effects of topographic discretization on hydrological modeling. The fourth chapter is about how to approach (challenge 2 and 3) basin water budget estimation problems, i.e. estimation of spatio-temporal water budget modeling inputs (rainfall, snow, temperature data), as well as their errors. The fifth chapter is extension of the fourth chapter (challenge 4), and aims to solve the water budget at small scale using the input data modeled in chapter four.

Chapter six uses a different approaches for estimating the precipitation in area where in-situ observations are scarce (challenge 5). In this chapter different satellite rainfall products have been compared and the performances of a bias correction method is evaluated. In chapter seven, is shown an effort to model a large-scale basin using JGrass-NewAGE capability and remote sensing data sets (challenge 6). The general conclusion, chapter eight, is presented to draw the overall summary of the thesis and try to establish the significance of the work.

Each of the chapters is designed to stand alone, as they go from introduction to the methods followed, and then to the results and conclusion of the chapter. So, readers are free to select and read a particular chapter of interest.

THE uDIG SPATIAL TOOLBOX FOR HYDRO-GEOMORPHIC ANALYSIS [*]

This chapter focuses on the use and functionality of uDig GIS Spatial Toolbox. Obviously, GIS underpins the development of distributed hydrological models. It supports hydrological modeling in preprocessing input data, facilitate (or support) modelling and analysis and postprocessing the output data. The Spatial Toolbox of uDig GIS is a specialized toolset for topographical analysis, geomorphometry and hydrology. The chapter describe the advantages of uDig GIS Spatial toolbox over the other several commercial GIS software packages, and explain the algorithms of some of hydrogeomorphological parameters that can be used in distributed hydrological models.

2.1 Introduction

Since efforts in the late 1980s (Bras et al., 1988.; Band, 1986, 1993; Moore et al., 1991) much progress has been made in extending terrain modelling and implementing the mathematical findings of geomorphometry (Evans et al., 2003, e.g.) into usable tools (e.g. Wilson and Gallant, 2000; Pike, 2002; Rigon R and A, 2006) . Furthermore, the availability of Digital Elevation Models (DEMs) has promoted the automatic derivation of river basin features by researchers and practitioners in hydrology and geomorphology.

---

[*]This chapter is based on "Abera, W., Antonello, A., Franceschi, S., Formetta, G., Rigon, R., 2014. The uDig Spatial Toolbox for hydro-geomorphic analysis, in: Clarke and Nield (eds.) geomorphological techniques (online edition) Edition. British Society for Geomorphology, London, UK."

Given that the tools available were sometimes prohibitively expensive, some researchers provided their tools as a free product (e.g. Lindsay, 2005; Wood, 2009), but, with few exceptions (e.g. Garbrecht and Martz, 1997; Mitasova and Neteler, 2004), and the suite Sextante (http://www.sextantegis.com/docs.html), they provided just the executable of their code, and did not disclose the source code. Since then, with the objective to offer open source alternatives for terrain analysis, various software has been developed. LandSerf is an open source tool designed to provide high quality geomorphological visualization and analysis (Wood, 2009), which includes specific tools for fractal analyses of landscape surfaces. Whitebox Geospatial Analysis Tools, formerly known as TAS, was developed with the objective of providing free and improved visualizations and spatial analyses in GIS (Lindsay, 2005). TauDEM (Terrain Analysis Using Digital Elevation Models) derives from decades of theoretical and applicative work in hydrologic DEM analysis and watershed delineation by Tarboton (e.g. Tarboton, 1997). GRASS GIS is for many purposes similar to the uDig tools presented in this chapter (e.g. Jasiewicz and Metz, 2011). GeoNet derives from recent research by Passalacqua and coworkers on filtering landscape geometries with wavelet tools (e.g. Lashermes and Foufoula-Georgiou, 2007), and on channel initiation (Passalacqua et al., 2010b,a). The uDig (User-friendly Desktop Internet GIS) Spatial toolbox merges the visualization and spatial analysis capabilities commonly found in raster GIS packages with an extensive list of sub-programs specifically designed for research in hydrology and geomorphology. In comparison to many of the other toolkits mentioned, the Spatial Toolbox is a real GIS toolkit (like the one in GRASS) with the advantages of being able to access geographical databases, transform and treat several common geographical data formats, handle and conjointly use vectorial and raster data, and generate the most common data formats in output. Additionally, while most users will find the sole availability of executable code satisfactory, only the full availability of source code internals provides researchers with complete control over the final results of their analyses. For this reasons, the uDig Spatial Toolbox was designed to provide a userfriendly, open source, well-documented, new generation, GIS for specific applications in hydrology and geomorphology, but also effective for more generic environmental applications. For historical reasons, the tools in the uDig Spatial Toolbox are also called JGrasstools. They are organized into four toolboxes: Raster processing (RP); Vector processing (VP); HortonMachine (HM); and Others. Most of the geomorphometry analysis tools are in the HortonMachine toolbox. This chapter will concentrate on those functionalities which are useful to geomorphological analyses contained in the HortonMachine toolbox, but will also touch on those command options

that can produce vectorial features of geomorphological entities, without going into a detailed description. The Raster processing toolbox has basic tools for raster corrections and operations (that work through the Map Calculator in ArcGIS), whereas the Horton-Machine has functionality that ranges from standard analysis of DEMs (such as slope, aspect, curvature) to more specific hydro-geomorphological modeling solutions, which are explained under each category. Raster processing and HortonMachine have some tools which output vectorial features, the Vector Processing toolbox provides many tools for vectorial hydro-geomorphological analysis. Table 2.1 presents the general functionalities of the four toolboxes.

Table 2.1: The list of uDig spatial toolboxes and summary of their general functionalities

Toolbox	Functionalities
Raster processing	Raster data correction and calculations
Vector processing	Wide range of Vector data analyses such as vectorizer, buffer zone, line and polygon topological analyses etc.
HortonMachine	From simple digital raster terrain analyses to more advanced hydro-geomorphological analyses
Others	Design of water supply and sewer systems for urban environments, and other tools

In the next sections, some selected raster processing and HortonMachine tools are described in detail. In showcasing the virtues of the uDig Spatial Toolbox, the Posina River Basin has been selected as a case study to illustrate the application of some tools. The Posina River Basin is located in the north-western part of the Pre-Alps of Vicenza, between the Astico Valley and Monte Pasubio. The surface area of the basin at Stancari is 116 km^2. Geomorphologically, the basin shape is roughly circular and enclosed by a series of mountains with elevations reaching 2000 m and above (Borga et al., 2000). The location and associated DEM of the Posina River Basin are shown in figure 2.1.

2.2   Raster Processing

The Raster Processing toolbox contains a set of tools for the preparation of topographic data for hydro-geomorphological applications. Figure 2.2 shows the typical appearance of the uDig Spatial Toolbox. When the Spatial Toolbox is open, for any tool, there are three tabs that serve to input and the output variables. The third tab contains the help associated with the selected the tool, with a short explanation of what the tool does.
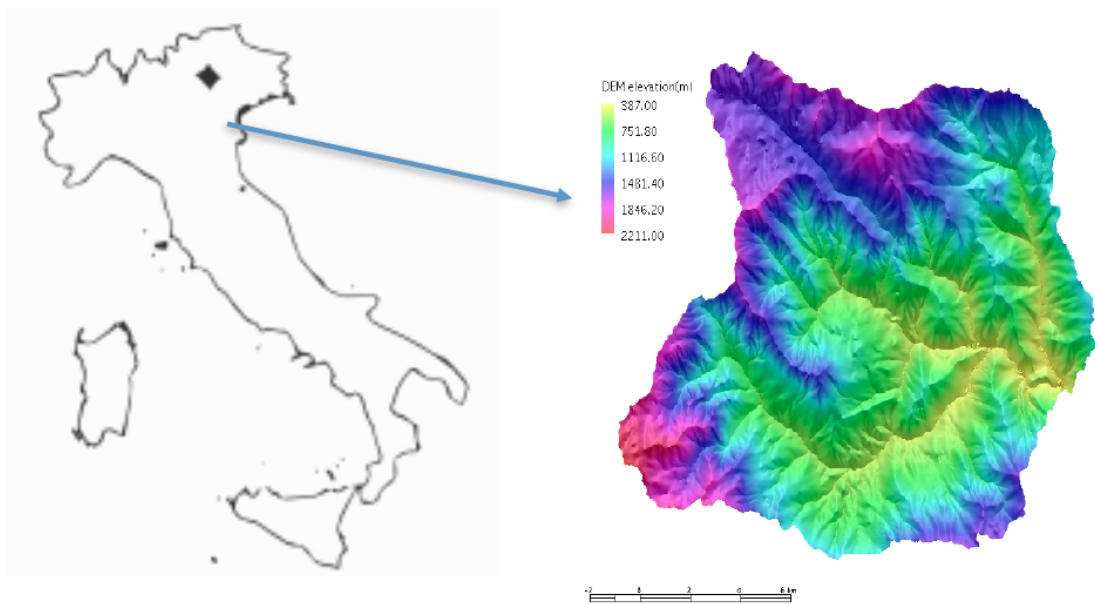
Figure 2.1: The location and the DEM of Posina river basin, the case study
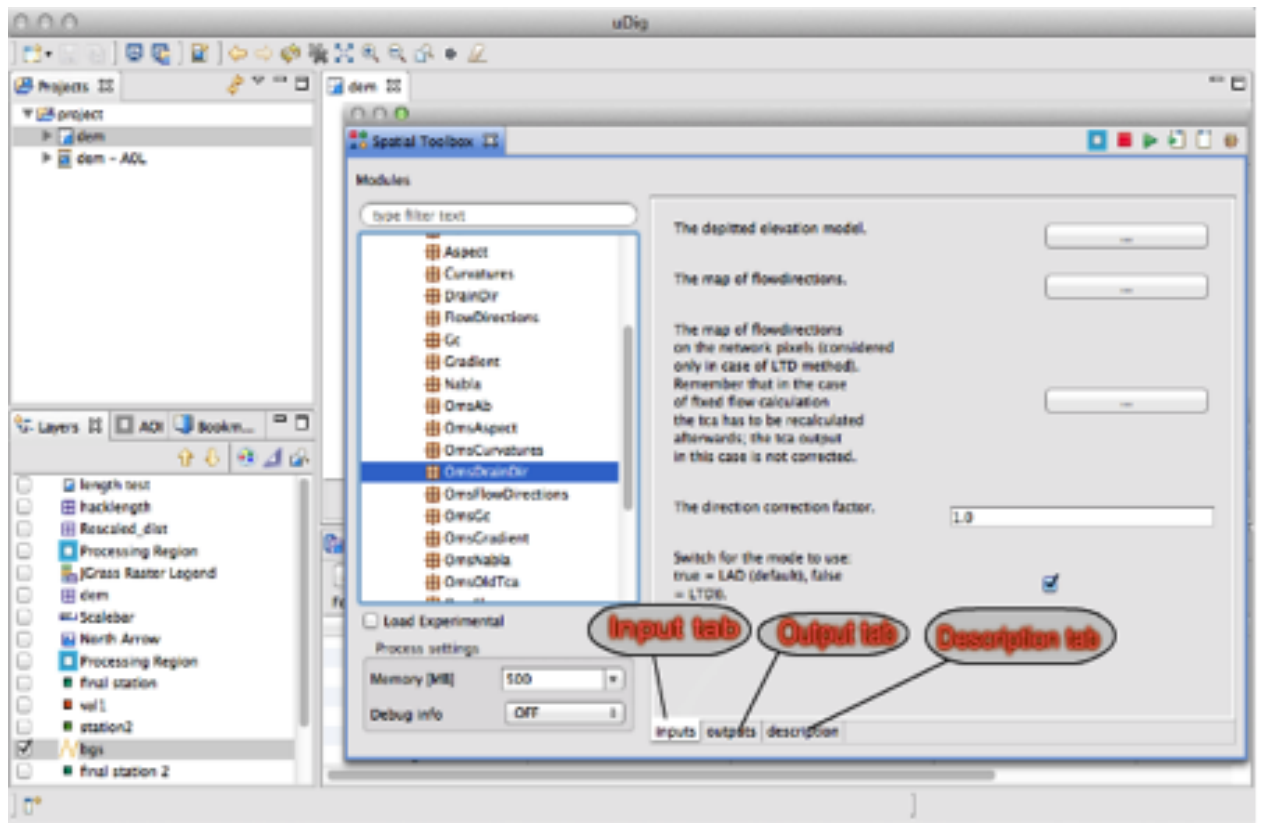
Figure 2.2: uDig GIS interface with spatial toolbox overlay and the three tabs: inputs, outputs and descriptions tabs at the bottom of the toolbox.

Raster processing toolbox contains tools for the quick manipulation of raster maps (the relevant tools are listed in table 2.2).

There are about 30 tools under the RP toolbox that can be implemented. However, there is not the scope to explain all of them here, therefore a little more detail will be provided about a selection of the more interesting tools within the RP toolbox. Among the list of tools presented in table 2.2, a very useful one for advanced raster map manipulation is the raster calculator (MapCalc), which allows complex calculations involving numerical and logical functions. With Mapcalc one can perform the most common mathematical operation on a map, modify maps values, combine maps, multiply, divide one map by another map (i.e. the values contained in one map for the corresponding values of another map), select part of a map, and so on. Ranglookup, Rastercorrector, and Rasterconverter provide summary statistics of raster maps. The Rangelookup tool is particularly important as it identifies the raster data included between user-defined range values. RasterSummary tool is useful as it provides basic summary statistics (such as the minimum, maximum, mean, standard deviation, histogram, and the NaN value) of the raster map.

Table 2.2: Some of the tools available in the Raster Processing toolbox of uDig.

Raster Processing Tools	Functionalities
BobTheBuilder	Builds human artifacts (such as dams) on a raster map
CutOut Raster	masking and cutout with some threshold
KernelDensity	Estimates the kernel density
MapCalc	Performs map algebra on raster map
Mosaic ImageMosaicCreator	Patches rasters and creates mosaics of shapefiles for images
PointRasterizer and LineRasterizer	Rasterizes vectorial point and line features respectively
CannyEdgedetector	Performs edge detection operations
Profile	Creates profiles over raster maps
RangeLookUp	Reclassifies and assigns values of maps for a given ranges of raster values
RasterConverter	Converts rasters from one format to another
RasterCorrector	Corrects some raster values
RasterDiff	Calculates the difference between two rasters
RasterReprojector	Re-projects maps
RasterResolutionResampler	Resamples the raster map coverage
RasterSummary	Calculates the summary statistics of a raster map
RasterVectorIntersector	Analyzes raster maps within a polygon vector (intersection)

A group of tools for rasterizing vector data includes BobTheBuilder, PointVector-

izer and LineVectorizer. BobTheBuilder rasterizes human artifacts, such as dams and buildings, which could be useful to include in the raster maps. PointVectorizer and LineVectorizer rasterize point and line features, such as measurement stations and river channels respectively.

Finally, SurfaceInterpolator is useful for interpolating landscape data (such as elevation and temperature) from point measurement to the whole study area. Two surface interpolation algorithms are incorporated in this tool: the Thin Plate Spline (TPS) Interpolator and the Inverse Weight Distance (IWD) Interpolator (e.g. Goovaerts, 2000). These methods can be applied to create Digital Terrain Models (DTM) from a set of GPS points or digitized maps, as well as models of other continuous environmental variables, for instance, surface temperature.

2.3 HortonMachine Functionality in Geomorphometry

The HortonMachine toolbox is organized into seven broad categories of commands: DEM manipulation; Geomorphology indices; Network related analysis; Hydrogeomorphology model tools; Basin related tools; Hillslope related attribute tools; and spatial statistics tools. Each of these will now be outlined in turn, and tables 2.3 and 2.3 present the selection of tools useful for hydrogeomorphological applications.

2.3.1 DEM manipulation toolbox

The DEM manipulation tools contain subprograms used for preparing DEMs for analysis. These subprograms include routines to remove flats, spikes, and depressions from DEMs (pitfiller), to extract streams (ExtractNetwork), to extract subbasins (ExtractBasin, SplitSubbasins), and to find the basin outlets (Wateroutlet). Depression filling is perhaps the most widely implemented algorithm for depression removal and is found in all the terrain analysis tools (e.g. TauDEM - Tarboton (1997); Rivix - Peckham (2008); TAS - Lindsay (2005); GRASS - Jasiewicz and Metz (2011)). JGrasstools uses the algorithm presented by Tarboton et al. (1991).

Table 2.3: Some of the tools for DEM manipulations, geomorphology, hydrogeomorphology and statistics available in the HortonMachine toolbox.

HortonMachine Tools	Functionalities
1. DEM Manipulations	(e.g. Moore et al., 1991; Palacios-Velez and Cuevas-Renaud, 1986; Rigon R, 2006)
ExtractBasin	Extracts a basin by using the flow direction map
Markoutlets	Marks the outlets of a basin on the drainage direction map
Pitfiller	Fills the depression points of the DEM
SplitSubbasins	Labels the sub-basins of a basin using stream ordering
Wateroutlet	Extracts the watershed for a defined outlet
2. Geomorphology tools	(e.g. Orlandini et al., 2003; Tarboton, 1997; Mitasova and Neteler, 2004; Moore et al., 1991; Garbrecht and Martz, 1997).
Aspect, slope, Gradient, curvature	Calculate aspect, slope, gradient and curvature type of the map respectively
FlowDirections, DrainDir, LeastCostFlowDirections	Calculate the D8 method drainage direction, drainage directions minimizing the deviation from the real flow, and least cost method drainage directions respectively
Tca, Gc	Calculate contributing areas and topographic classes, respectively
3. Hydro-geomorphology	
Hillshade	Calculates the shadows of the DEM
Skyview	Calculates the skyview factor of the DEM
Insolation	Estimates the amount of shortwave radiation on a surface for a given of time
4. Statistics	
Cb	Calculates the histogram and the statistical moments of a set of data from a map with respect to another map
SumDownStream	Calculates the sum values of a map from upstream to downstream following the flowdirections
Jami	An interpolation method
Variogram	Calculates the experimental semivariogram
Kriging	Implements the ordinary kriging interpolation algorithm

2.3.2 Geomorphology toolbox

The Geomorphology toolbox contains tools for calculation of slopes, curvatures, drainage directions and contributing areas, among many others. One of the simplest geomorphological attributes maps is the aspect map, a map that shows which side a slope is directed, this can be calculated using the Aspect tool from the DEM (figure 2.3).

Terrain attributes are based on local neighbourhoods and reflect a simple application of the differential geometry of curves on surfaces (Peckham and Gyozo, 2007). Algorithms involving upslope or downslope calculations (i.e. those within the basic topographic attributes and network related measures tools) rely on the steepest descent (or D8) flow-routing algorithm (O'Callaghan and Mark, 1984) because of the need for unique, non-diverging flowpaths. Two other algorithms involving analysis of neighbourhoods are implemented in uDig because using the pure D8 method for the drainage direction estimation causes deviation from the real flow direction identified by the gradients. The first algorithm implemented according to Orlandini et al. (2003) is the D8-LAD (least angular deviation), which minimizes the total angular deviation. The second algorithm, D8-LTD (least transversal deviation), minimizes the total deviation length of the flow going downstream. uDig (through the uDig Spatial toolbox) is currently the only GIS that contains these algorithms.

A third algorithm available is the multiple flow directions algorithm, first implemented by Fairfield and Leymarie (1991). This is used mainly for comparison, since this effect is barely found in nature (e.g Orlandini et al., 2012), and D8-LAD and D8-LTD recover very precisely the real drainage directions. Gradient calculation (Gradient, Slope) is another standard tool present in all modern toolboxes.

The classification of topographic sites into three different classes of curvature is another important tool (Tc, Gc). Longitudinal (or profile), normal and planar curvatures for each pixel are helpful to estimate the deviation of the gradient vector. Profile curvature measures the topographic curvature (i.e. the gradient deviation) along a flow line following the steepest descent path, and planform curvature measures the curvature of contour lines on topographic maps. Detailed description of different landform curvatures is found, for instance, in Tarolli et al. (2012). In combination with some other general tools, provided by the uDig Spatial Toolbox, these tools can provide the information shown in figure 2.4 (see also complementary material at http://abouthydrology.blogspot.it/2014/05/theudig- spatial-toolbox-paper.html). Figure 2.4 shows the elevation, slope and curvatures along the main stream of the Posina. Two knickpoints are particularly evident in the elevation plot, which reflect changes of gra-
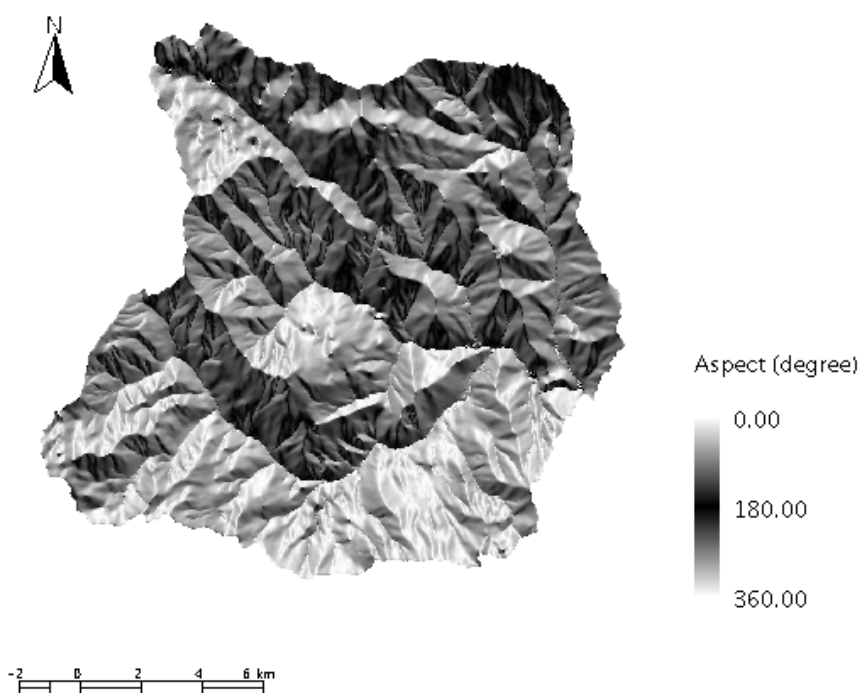
Figure 2.3: Aspect map of the Posina river basin, with enhanced visualization using the style editor tools in uDig GIS.

Table 2.4: Some of the tools available in the Network sub toolbox and their general functionalities.

HortonMachine Network tools	Functionalities
ExtractNetwork	Extracts the raster network from DEM (Orlandini et al., 2012; Montgomery and Dietrich, 1988, 1989)
HackLength	Calculates the distance of each pixel to the divides going upstream and along the flow directions (Rigon R, 2006)
NetDiff	Calculates the difference between the value of a quantity in two network points with different numbering
Netnumbering	Assigns identification (id) numbers to the network links
NetworkAttributesBuilder	Extracts the network as a shapefile and adds networks attributes to it some (Rodriguez-Iturbe and Rinaldo, 1997; Rigon et al., 1996)
DistanceToOutlet	Calculates the planar projection of the distance of each pixel to the outlet (D'Odorico and Rigon, 2003)
NetShape2Flow	Transforms the network shapefile to a flow raster map

15

dient and curvature. The curvatures, in turn, are both positive starting after the first knickpoint, as expected, and identifying the presence of convergent-convex sites typical of a valley, and of channel geomorphology.

2.3.3 Network toolbox

The main tasks available in the Network toolbox in uDig are related to watershed extraction, various basin morphometric analyses, stream network extraction and analysis. These are presented in table 2.4. The stream network extraction tool uses three alternative approaches: total contributing area threshold; slope-area threshold; and curvature based. The first, and most common, method of extracting a channel is by setting some threshold on the total contributing area (Tca), representing the total area of upslope cells. Cells with a total contributing area greater than a given threshold area are considered to be flow channel, since Tca is considered a surrogate of discharge (O'Callaghan and Mark, 1984).

In addition to the contributing-area threshold method, a slope-area threshold method based on work by Montgomery and Dietrich (1992) and a curvature based stream delineation method (Tarboton and Ames, 2001) have been implemented in the stream network extraction tool. Furthermore, stream network analysis includes utilities to order channel streams (using Hack and Horton- Strahler ordering schemes, e.g. Rodriguez-Iturbe and Rinaldo (1997)). From this ordering, it is possible to derive statistics associated to the network, to estimate Shreve's magnitude, and to measure link-average slopes and lengths and from them estimate, for instance, Horton laws (e.g. number and length of channels per Horton order, bifurcation ratio, and length ratio; see Rodriguez-Iturbe and Rinaldo (1997)).

The HackStream tool provides the channel ordering based on Hack's stream enumeration (Rigon et al., 1996). In Hack's ordering, the main channel of the network is assigned the order 1, the channels that flow into it are assigned the order of 2, and the branches that flow into channels of order 2 are assigned the order of 3, and so on.

The most common and popular method of channel classification is according to the Horton-Strahler ordering scheme (Horton, 1945; Strahler, 1957), which is implemented in the NetworkAttributesBuilder tool: the network is divided into links that connect either two tributary junctions (internal links) or a tributary junction and a channel source point (external links: Rigon et al. (1996)). This ordering system assigns order 1 to the source; and when two or more streams of the same order, n, meet they form a stream of order, n+1. When two streams of different orders, n and m with n > m, meet
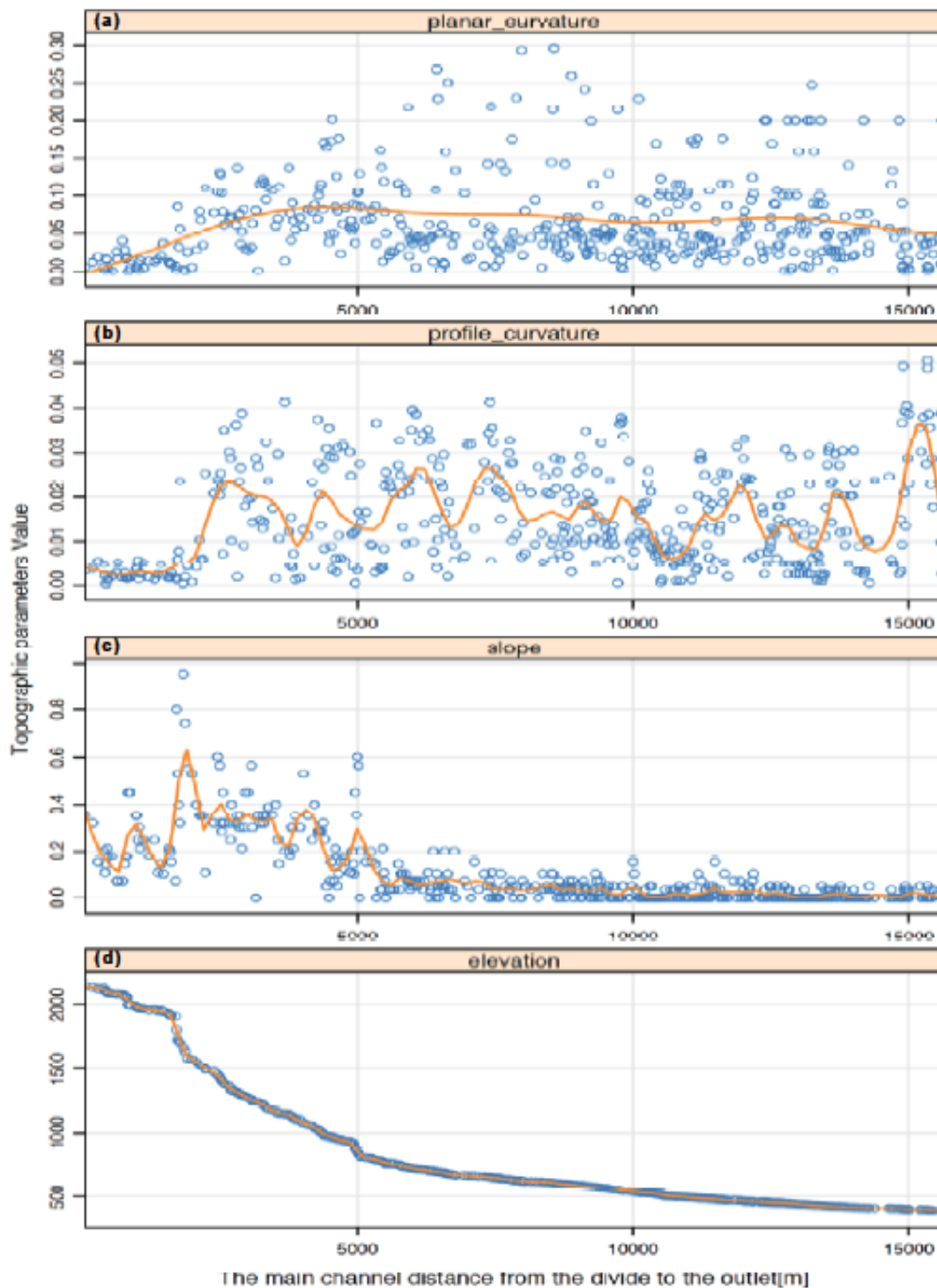
Figure 2.4: The topographic parameters: (a) planar curvature, (b) profile curvature, (c) slope and, (d) elevation, in the main stream of case study basin of Posina.

the order of the channel they form remains with the order of the greater of the two, n. The NetworkAttributesBuilder produces not only the raster enumeration, but also the vectorial features of the stream ordering.

Another method for labeling channel links and associated hillslope is the so-called Pfafstetter coding method (e.g. Verdin and Verdin (1999)). It provides the topographical connectivity between channels and hillslopes. The technical description of the Pfafstetter numbering schemes (PNS) as implemented in the Pfaf tool is given by Formetta et al. (2014b). The generalization of this coding system, implemented in the uDig Spatial Toolbox, can also take account of the presence of dams and irrigation channels. The Pfaf tool produces a shapefile (i.e. a vectorial feature) that contains, besides the enumeration itself (as shown in figure 2.5), the associated properties, such as the starting and ending point of a link, the elevation drop and other properties.

Figure 2.5: The pfafstetter enumeration scheme for the Posina river basin, as implemented in uDig GIS spatial toolbox for channel networks and hillslopes.

2.3.4   Hillslope toolbox

The Hillslope toolbox contents are presented in table 2.5. They include tools for the classification of hillslope points into categories derived from information about curvatures,

tools for evaluating distances of hillslope points to streams, and tools for calculating statistics of any quantity in a hillslope. In addition to the estimation of pixels curvature, based on the longitudinal (profile) and transversal curvatures mentioned before, the topographic class (Tc) tool subdivides the sites of a basin in different topographic classes. The program has two outputs: the more detailed nine topographic classes (Parsons, 2002) and an aggregated topographic classification with three fundamental classes. Figure 6 is a visual comparison of an example of detailed nine and aggregated three topographic class maps of Posina river basin.

Planar curvature represents the degree of divergence or convergence perpendicular to the flow direction, and profile curvature shows convexity or concavity along the flow direction. By combining these two main curvatures, the topographic class (Tc) tool identifies 9 classes, which are three planar type sites (parallel-planar, divergent-planar convergent-planar sites), three convex type sites (parallel-convex, divergent-convex and convergent-convex sites), and three concave type sites (divergent-concave, parallel concave and convergent-concave sites). These attributes can be summarized into three fundamentals classes (concave, convex and planar sites). The graphical depiction of the curvature classification of hillslopes is shown in figure 2.7.

Table 2.5: The list of tools in Hillslope and Basin sub toolbox and their general functionalities.

HortonMachine Tools	Functionalities
Hillslope toolbox	(e.g. Parsons, 1988; Rodriguez-Iturbe and Rinaldo, 1997)
H2CA	Estimates some attributes of hillslopes associated to a common channel network.
H2cd	Calculates hillslope distance from river network
Tc	Subdivides hillslopes into topographic classes
Basin toolbox	(e.g. Rigon et al., 2011; D'Odorico and Rigon, 2003)
BasinShape	Creates sub-basin shape file following the netnumbering tool
RescaledDistance	Calculates the rescaled distance of each pixel from the outlet
TopIndex	Calculates the topographic index of each sites

In general terms, divergent-convex landforms are associated with the dominance of hillslope processes, while convergentconcave landforms are associated with valley-dominated erosion (e.g. Tarolli and Dalla Fontana, 2009). Mapping these divergent and convergent sites is essential for the geomorphological and hydrological analyses of a basin, the local divergence and convergence roughly identifying convex zones as hillslope
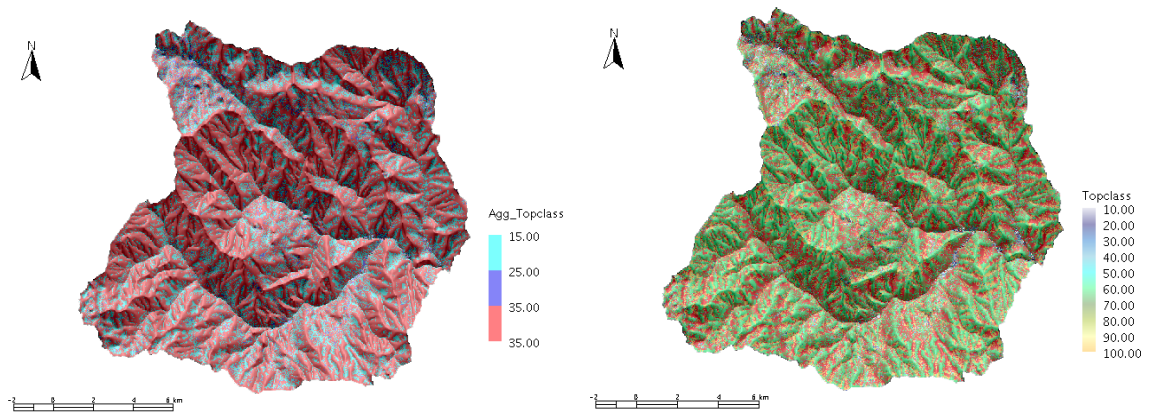
Figure 2.6: Hillslope topographic classes map of the Posina river basin. The first map (left) shows the nine hillslope classes based on topographic curvature (planar-planar sites (10), convex-planar sites (20), concave-planar sites (30), planar-convex sites (40), convex-convex sites (50), concaveconvex sites (60), planar-concave sites (70), convex-concave sites (80), and concave-concave sites (90)). The second map (right) shows the three principal topographic classes (concave sites (15), planar sites (25), and convex sites (35)) of the basin.

Figure 2.7: The subdivision of the hillslope sites according to their curvature (after Parsons (1988).

zones, the concave zones as valleys, which are subject to different processes (as also enlighten by figure 2.4).

Other tools from this toolbox were used, for instance, to produce the calculations in D'Odorico and Rigon (2003) to evaluate the distance of any point in a hillslope to a channel. The hillslope to channel distance (H2cd) calculates the distance of each point on the hillslope to the channel network following the steepest descent (see figure 2.8).

H2CA calculates the distance a drop of water released (or rained) in any point in a hillslope takes to arrive into a channel. H2CA plus H2Cd is the total length from any point in a basin to the basin outlet. It is useful to separate these tools so as to associate to each of them a different residence time, as was done by Rinaldo et al. (1995).
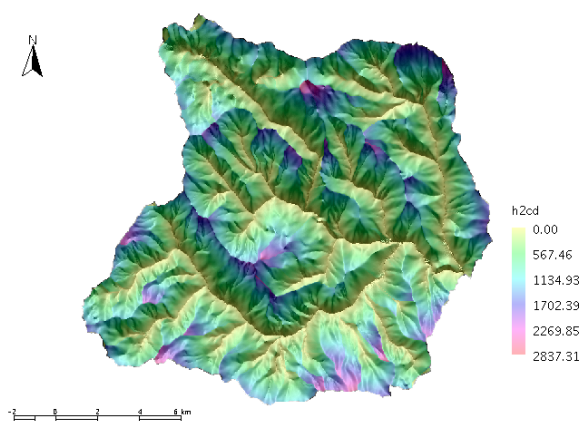
Figure 2.8: The map of the distance of each hillslope pixel to the channel (h2cd) in the Posina basin.

Figure 2.8 shows the distribution of distances from any point in a hillslope to channel versus the distance of the hillslope to the outlet. The figure was obtained after a little manipulation of the data (produced by the tool) made with R (http://www.r-project.org, please see the complimentary material). It clearly shows that the mean hillslope lengths of the Posina catchment are increasing downstream. The command Drainage Density (which equals the total network length per contributing area) can be used to obtain the homonymic quantity. Historically the two quantities, H2CA and drainage density were thought to be inversely proportional (e.g. Rodriguez-Iturbe and Rinaldo, 1997), and the second was often used to infer the first because easier to estimate from maps.
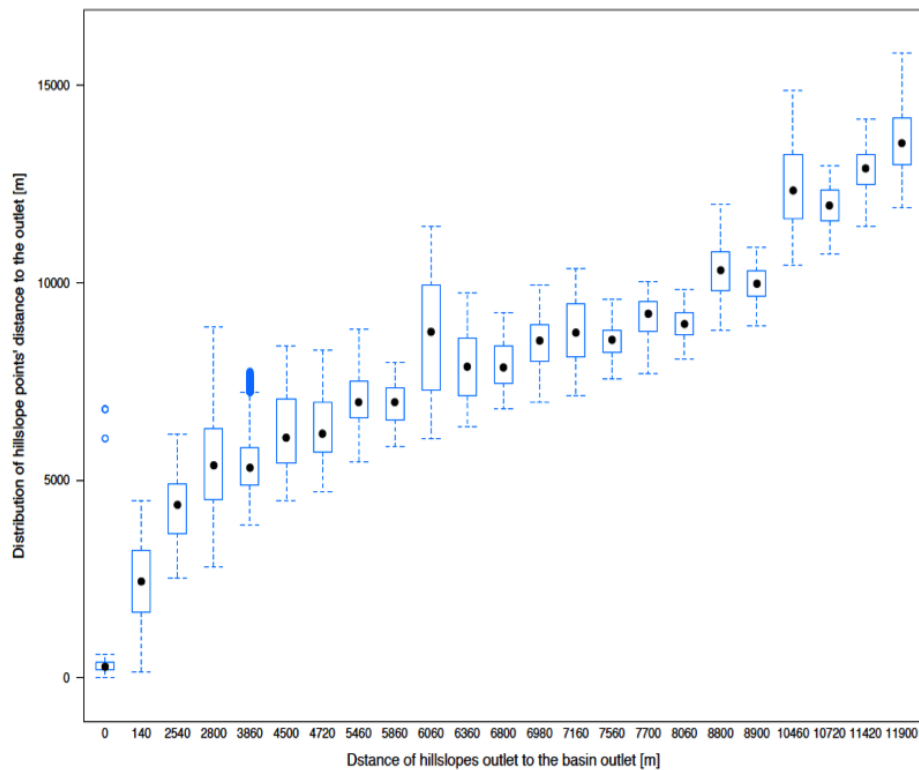
Figure 2.9: The distribution of hillslope pixel distance to the outlet versus the mean hillslope distance.

2.3.5 Basin toolbox

The Basin toolbox in the HortonMachine toolbox contains models to estimate basin wide characteristics (shown in table 2.5). They include, among others, methods to evaluate the width function (e.g. D'Odorico and Rigon, 2003; Rigon et al., 2011) and the rescaled width function (RescaledDistance; Rinaldo et al. (1995)), and topographic index (TopIndex) which is commonly used to quantify topographic control on hydrological processes which accumulate soil moisture (Beven and Kirkby, 1979). This has been criticised as a model for deriving maps of soil (see Barling et al. (1994); Lanni et al. (2012)), however, the topographic index still remains a useful visualization of the process of saturation, which can serve as a first approximation to understand which points saturate first (e.g. Crave and Gascuel-Odoux, 1997; Hjerdt et al., 2004). The rescaled distance is the distance of each pixel from the outlet measured along the drainage directions, weighted by the ratio of the water velocity in channels and on the hillslope. If the ratio of velocities is taken equal to one, the normal planar projection of the distances to outlet for any point in a basin is obtained.

The topographic index classifies the basin based on its ability to generate surface flow, according to Beven and Kirkby (1979). As is known, sites with a higher topographic index tend to become saturated before sites with a lower topographic index. The map showing the topographic index and the rescaled distances for each pixel of the study basin is shown in figure 2.10. BasinShape is a tool which creates feature collections of subbasins extracted by the netnumbering tool. It is useful for extracting important information form each sub-basin, such as area, perimeter, max elevation, minimum elevation, mean elevation etc.
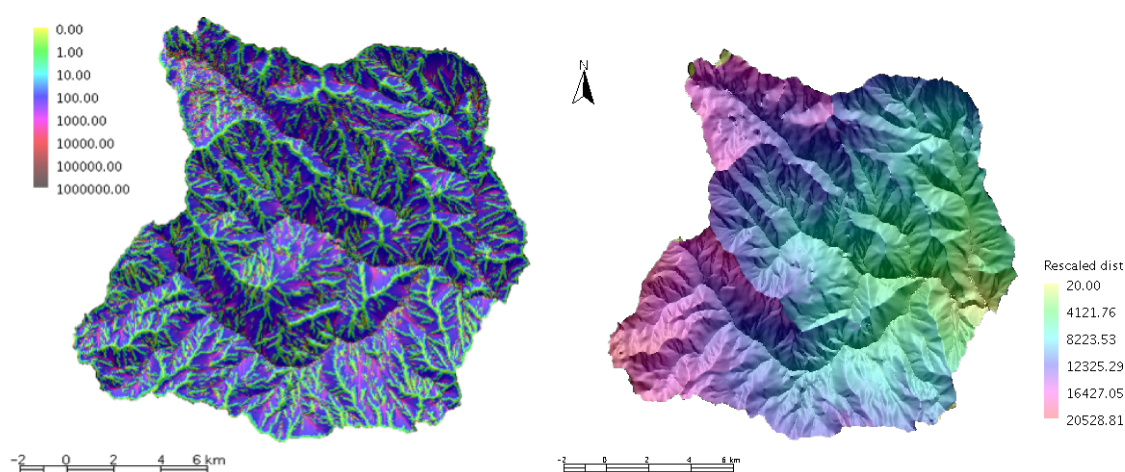
Figure 2.10: The map of the topographic index (left) and the rescaled distance (right) for the Posina river basin.

2.3.6 Statistics toolbox

In addition to the terrain analysis functionalities described above, the spatial toolbox also incorporates statistical tools (presented in table 2.4). Among these, there are tools for both deterministic and geostatistic interpolation algorithms. These include Just Another Meteo Interpolator (JAMI) and kriging interpolation tools. JAMI is a robust approach of interpolating different meteorological data presented in Formetta (2013). The geostatistical technique implemented in the statistical toolbox is kriging. At the moment, the ordinary kriging algorithm (Goovaerts, 1997, 2000) is the one implemented in the toolbox. If input data are provided as time series, the kriging runs over all the time steps, estimating a different semivariogram model, and the parameters used for kriging interpolation, for each time step.

23
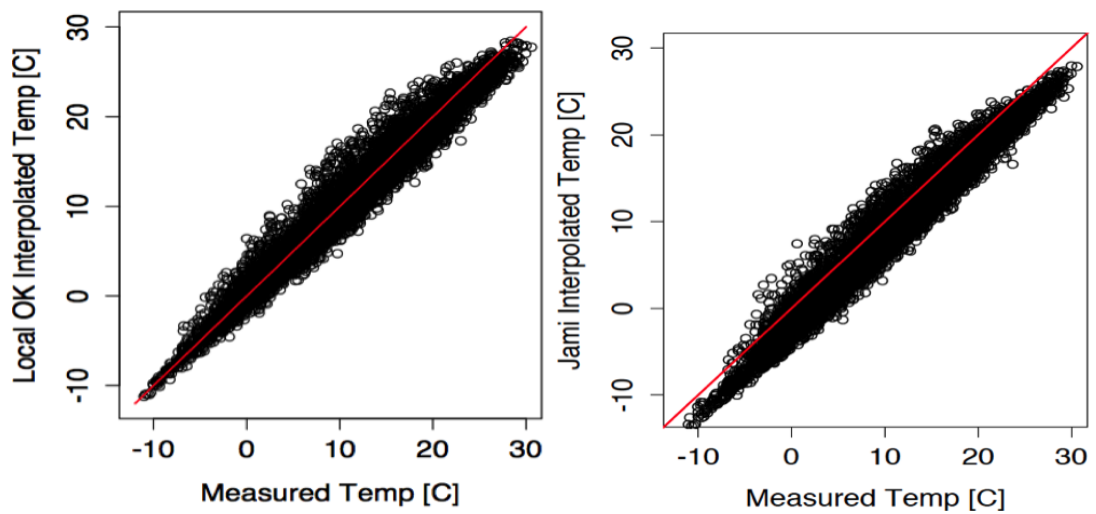
Figure 2.11: Scatter plot of measured and ordinary kriging interpolated (left: with R^2 = 0.78) and JAMI interpolated (right: with R^2 = 0.74) hourly temperature for one year (1995), in one of the measurement station in Posina river basin.
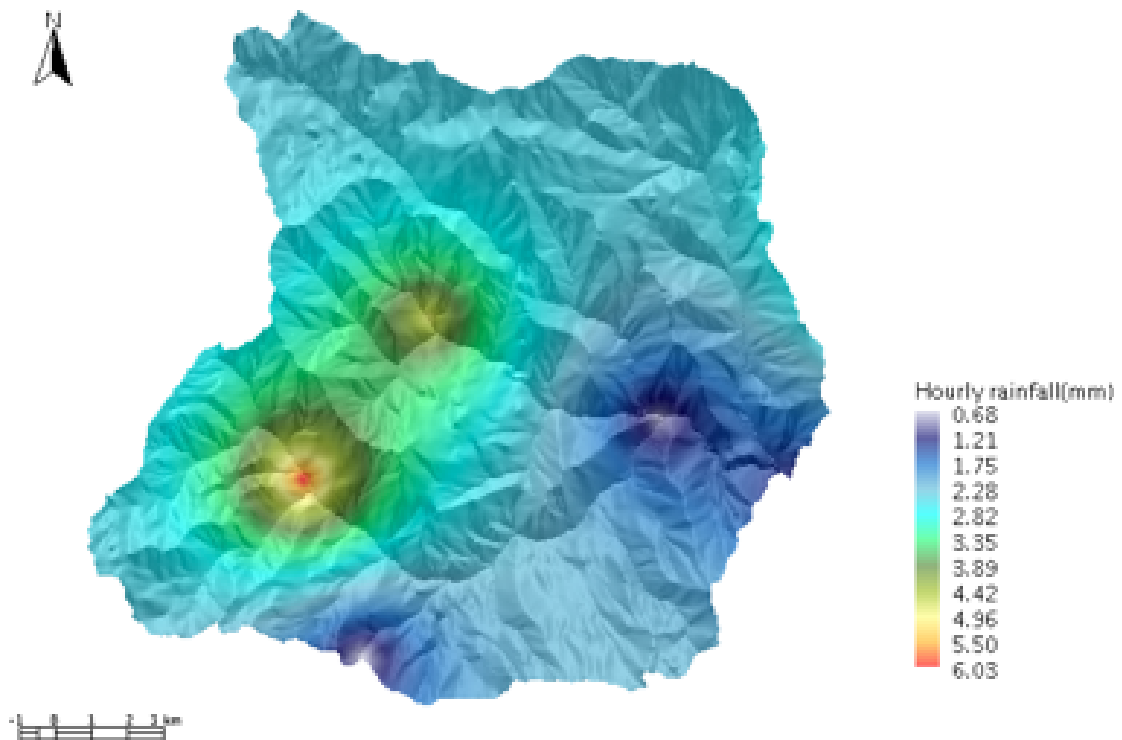
Figure 2.12: The grid-based rainfall interpolation using Ordinary kriging for the Posina basin

The kriging tool provides both point (nonregular grid) and regular raster grid outputs. Figure 2.11 and 2.12 are examples of grid and point interpolations obtained using exponential semivariogram model fitting. Figure 2.11 is a scatter plot comparing measured and interpolated hourly meteorological data (temperature).

2.4 Further characteristics of the Spatial Toolbox

The geomorphological tools described in the previous sections are made even more effective by the general characteristics that the Spatial Toolbox inherits from uDig, which are summarize briefly below.

2.4.1 Visualization

The graphical user interface (GUI) of the Spatial Toolbox allows multiple images to be displayed simultaneously with transparency effects, facilitating the visual inspection of multiple terrain attributes. Displayed images can also be combined with shaded-relief images to enhance visualization of terrain. In these composite-relief models, variations in colour correspond to the displayed attribute and tonal variations correspond to hill shading. Vector data may be overlaid onto raster images to enhance data visualization and interpretation. Spatial Toolbox is distributed with a standard set of colour palettes, which have been set as the default. Nonetheless, users can eventually create custom palettes for specific purposes using the Palette manager.

2.4.2 Importing and exporting data

DEMs are the main input data to Spatial toolbox, but the program can utilize many other types of spatial data, including satellite imagery. Raster import / export functions include read and write ArcView raster formats, GRASS images, Surfer grids, Autodesk .dwg and device independent bitmaps. The program can also read all the supported raster data included in the GDAL (http://www.gdal.org) library and the Shuttle Radar Topography Mission (SRTM) data (http://www.ppp.org). JGrasstools in Spatial toolbox reads and writes shapefiles, GRASS ASCII and native (supported since the GRASS 5.0) vector file formats, and delimited XYZ vector point files. Graphical output (i.e. displayed images with vector overlays) can be saved as MS-Windows bitmap (.wbmb), jpg, jpeg, and Portable Network Graphics files (.png), which can be read by most graphical packages and several wordprocessing programs.

2.5 Concluding remarks

The uDig Spatial toolbox is a powerful, research-grade environmental modeling environment. The main tools have been described in this chapter, however many more tools are available, particularly an advanced Hydrological model called JGrass- NewAGE modelling system (Formetta, 2013; Formetta et al., 2014c, 2013b, 2014d), complete sub-models for estimating rainfall-runoff, radiation, evapotranspiration, snow water equivalent, landslide models like SHALSTAB (Montgomery and Dietrich, 1994), and CIS-LAM (Lanni et al., 2012), peak flow modelling (Rigon et al., 2011). Tools in JGrasstools are ideal for both research and student instruction due to ease of use and free availability. Therefore, we believe, the uDig Spatial toolbox is suited to be used in research and education in physical geography, hydrology, geomorphology, climatology, environmental science and watershed modelling.

THE EFFECT OF SPATIAL DISCRETIZATION ON HYDROLOGICAL RESPONSE, IN THE CASE OF SEMI-DISTRIBUTED HYDROLOGICAL MODEL *

This chapter focuses on how geomorphological descretization affects basin hydrological response. The studies elsewhere on spatial descretization and hydrological modelling performance does not provided conclusive results. Hence, here, the emphasis is to analyze how different level of spatially explicit representation of geomorphological information on topographically based hydrological response (particularly rescaled distance and width function, as used in many applications as minimalist model of basin hydrologic response). While many topographic descriptor detailed in chapter 2 can be used to assess the effect of geomorphology on basin response, rescaled distance and width function are used in this study. The study results clearly shows the possible epistemic uncertainty introduced when geomorphological information is lost due to subbasin descritization, as used in most semi-distributed models. The analysis is supported by two model simulation experiment, PeakFlow model which uses detail topographic information, and JGrass-NewAGE model which uses semi-distributed (aggregated) topographic information. While impacts of different level of spatial representation on basin hydrological response using the analysis of width function is clearly expressed, it is unsuitable to infer this from hydrological models which involves calibration procedure.

---

*This chapter is based on "Abera, W., Formetta, G., Rigon, R., The effect of spatial discretization in Semi-distributed hydrological modelling, in preparation for Journal of Hydrological Processes"

3.1 Introduction

Due to limiting factors of fully distributed hydrological modelling such as high computational demands, unrealistic process representation domain(i.e. grid cells), the lack of data (Garbrecht and Martz, 2000), sometimes semi-distributed modelling approach is preferred for water resource assessment and water simulation studies. The DEM grid cell ignores the large scale spatial correlations structures of geomorphic features, while subbasin approach respect large and meaningful geomorphic structures (Bogaart and Troch, 2006). Based on the above limitation of grid scale partition and the advantage of some level of aggregation, basin discretization into different homogeneous units is the base for most distributed and semi-distributed hydrological models. For instance, KINEROS (Smith et al., 1995) is based on partitions of the basin into topographical variables in which channel link and hillslope are extracted and characterized by slope, length and other geometry. In the case of TOPMODEL, basin topographic variables for hydrological modelling is represented by the the so-called topographic index, λ. The WEPP (Flanagan and Nearing, 1995), AGNPS, PRMS (Leavesley et al., 1983) assumes detail delineation of subbasins into hillslopes using contributing area. SWAT (Neitsch et al., 2002) uses subbasin discretization and further divide the sub-basins to the homogeneous units called HRUs, based on the combination of topographic elements(slope), landuse, and soil maps. Zhang et al. (2013) summarized the effect of basin partitioning for semi-distributed modelling purpose in three ways: the effects on the aggregation patterns of other meterological forcing inputs; the effects on the topographic values (slope, shape, aspect, etc) caused by the change in the subbasin shape and size; and the effects on the river channel connectivity and subbasin size. All these affects the models result.

In the last decade, different researchers investigated the effect of spatial discretization on basin rainfall-runoff modelling using different level of basin partitioning (K Ajami et al., 2004; Muleta et al., 2007; Kumar and Merwade, 2009; Ghosh and Hellweger, 2011; Tripathi et al., 2006; Jha et al., 2004; Kuo et al., 1999; Chen and Mackay, 2004; Dehotin and Braud, 2008; Githuia and Thayalakumaranb, 2011; Berni et al., 2008). Recently, Lobligeois et al. (2014) conducted an extensive analysis on different level of spatial descretisation on 3620 events in 181 catchments of France. However, their result did not show clear trend on the performances of hydrological modeling with different spatial characterizations, and the results are inconclusive. This could be due to the effect of calibration process. In other words, the interaction of many forcing inputs error (such

as rainfall, evapotranspiration), lack of methods to treat all into hydrological forecast, and complex interaction within the model structure can offset the errors. Therefore, the structural errors of the spatial descretisation comes from all the input representation in the modelling. As a result, the error due to partitioning of each inputs (meteorological average, and topological average) should be treated separately and integrated in the modelling uncertainty. Thus, we believe there is a need to clarify the impacts of geomorphological discretisation.

The idea persuaded here is to use the topographic information itself to analyse the errors induced by the use of different level of geomorphological based hydrological modelling. Following the theoretical formulation by Rodríguez-Iturbe and Valdés (1979), basin geomorphological structure as a base for hydrological response modelling has been an active research of hydrology in the last two decades (Rodríguez-Iturbe et al., 1982; Rinaldo et al., 1991; Snell and Sivapalan, 1994; Gupta et al., 1980; Gupta and Mesa, 1988; Marani et al., 2001). In literature, the geomorphological implication of hydrological responses is followed two approaches (Cudennec, 2007).

The first one is based on the flow distance distribution of each grids in the DEM to the outlet which is introduced by Kirkby (1976). This concept is formalized in the theory of width function. Width function is an important quantifier of a basin geomorphology and hydrology description (Di Lazzaro, 2009; Troutman and Karlinger, 1984; Veitzer and Gupta, 2001; Moussa, 2008; Marani et al., 1994; Wang and Wang, 2002) and it is the area of the basin with flow distance to the basin outlet. The hydrological distance has two components (D'Odorico and Rigon, 2003), the one from each pixel to the channel network and from the channel network to the outlet.

The second approach is based on the use of hydrological responses modelling following the original framework of GIUHs (Rodríguez-Iturbe and Mejía, 1974). The formulations of the geomorphological parameters for hydrological response is developed in the theory of GIUH by the pioneering work of Rodríguez-Iturbe and Valdés (1979), and latter by many researches (Rodríguez-Iturbe and Valdés, 1979; Rodríguez-Iturbe et al., 1982; Rinaldo et al., 1991; Snell and Sivapalan, 1994; Gupta et al., 1980; Gupta and Mesa, 1988; Marani et al., 2001). It is revealed that hydrological responses of a basin is not only based on signature of geomorphological structure of the channel network but also on the hillslope length characterization (Botter and Rinaldo, 2003; Rinaldo et al., 1991, 1995; D'Odorico and Rigon, 2003; Marani et al., 2001). The work of D'Odorico and Rigon (2003) provided framework to analyse how hillslope and channels travel time affect in the generation of hydrological responses. Hence, the interpretation of geomorphological

signature of water travel time to basin outlet is perceived well. The idea of GIUH is that the holding time of non-interacting and identical rainfall injected to the basin at the outlet is equal to probability density function (pdf) of the the holding time (Gupta et al., 1980).

Two approaches are followed to quantify the effects of the subbasin partitioning for hydrological response modelling purposes. In the first approach, the rescaled distance and width function, as used in fully-distributed and semi-distributed model, are calculated for both gird by grid partition and subbasin (or hillslope) partition.

In the case of fully-distributed hydological models, the grid by grid partition assumed to maintained all the possible geomorphometric properties; whereas in the case of using some level of subbasin partition as representative units, for instance, the distance of each units (and each pixels inside) is represented by the average value. For analyzing this effect, the basin width function is computed for full DEM, and later after geomorphological discretization into subbsasin, the width function is recomputed for the same basin. This changes all geomorphometries and geomorphological properties that can be used as input in hydrological model. In addition, comparison of channel network extraction methods were carried out in quantitative terms by computing the rescaled distance of grid by grid and HRU partition. Hence, the difference between the fully (pixel by pixel) and semi-distributed (hillslope, or subbasin, or HRU) width function can be argued as the main and immediate impacts of geomorphological subbasin discretization (see section 3.2). In the second approach, in order to further investigate, two hydrological models that are based on the two topographic representations (use of topographic information in the model structure) are used. For this, PeakFlow model (section 3.3.1) and JGrass-NewAge model (section 3.3.2) which uses width function instantaneous unit hydrograph (WFIUH) and topographic information averaged at HRU units, respectively, are selected. The description and practicality of the two hydrological models are provided in section 3.3.

The purpose of this study is, therefore, to understand the effects of basin geomorphological partitioning on hydrological responses modelling. In this research we attempt to single out and investigate the effect of geomorphological spatial partitioning on hydrological response. Specifically, we have three objectives: i. evaluate the effects of HRUs descretization based on basin width function, by comparing fully-distributed and semi-distributed topographic information; ii. investigate the effects of three types of channel-hillslope extraction methods using rescaled width function; and iii. compare the fully-distributed (GIUH) based and semi-distributed (aggregated at HRU) based hydrological models.

The next sections describes the methods and concepts on the use of rescaled width function and the two hydrological models used to investigate the effects of basin partitioning on basin hydrological responses.

3.2 The rescaled width function approach

The relationship between basin morphology and hydrologic response with the objective of describing the hydrological response of a basin has been a well established research interest (Rinaldo et al., 1991; Rodríguez-Iturbe and Valdés, 1979; D'Odorico and Rigon, 2003). The spatial distribution of the flowpath of the points in a basin to the outlet is one of the most important approaches to study hydrological response. The probability density function of travel times, f (t), from any point in the basin to the outlet is geomorphologic width function, W(x) (Gupta et al., 1980; Kirkby, 1976; D'Odorico and Rigon, 2003), and analytically characterized in many researches (Rinaldo et al., 1991; D'Odorico and Rigon, 2003; Moussa, 2008). Due to the important contribution of hillslope to the total resident time, the proper representation of total travel time requires the estimation of the distances of each pixels in the hillslope and in channel to the outlet (D'Odorico and Rigon, 2003).

This approach is based on the idea that each pixel in the basin is connected to the outlet through the flowpath distance. The flow distance is the distance for a drop of water to flow from a particular pixel to the channel and then though the channel to the outlet. Recognizing the processes in the hillslopes which ignored in the original width function (Rodríguez-Iturbe and Valdés, 1979), in this study, the flow distance of each hillslope and channel grid to the outlet is considered. The analytical approach to formulate the distances is based on D'Odorico and Rigon (2003), where the distance is rescaled to the different processes in the channel and hillslopes. The rescaled distance $x^{'}$ of a point to the outlet is then calculated by equation (3.1):

$$x^{'} = x_c + r x_h \qquad (3.1)$$

where $r = u_c/u_h$, x_c is the channel distance, and x_h is the hillslope distance. u_c and u_h are channel and hillslope velocity respectively. Assuming constant velocity at hillslope and channel, the ratio of the velocity, u_c/u_h is the only parameters to estimate the distance of each pixel to the outlet, while the two distance can be extracted from the basin DEM analysis (D'Odorico and Rigon, 2003). To characterize the effects of subbasin

discretization at a basin scale, the geometric analysis of rescaled distance is calculated.
Di Lazzaro (2009) and Di Piazza et al. (2011) used the spatial statistical moments of
geomorphological width function framework to characterize the hydrological response
of a basin. In this case, we used the following statistical moments of the rescaled width
function:

- The first order moments of the width function , $\langle x \rangle$,

- The second order moments, $Var(x)$,

- The coefficient of variance, $CV(x)$,

- The maximum flow distance, L

Usually, the basin partition for hydrological modelling is based on some random
channel forming threshold area (A_T). Then the statistical moments can be estimated by
varying threshold area and extraction procedures (methods). For instance, D'Odorico
and Rigon (2003) formulated the first order moments of the rescaled width function of
grid by grid $\langle x_g' \rangle$ as:

$$(3.2) \qquad\qquad\qquad \langle x' \rangle_g = \langle x_c \rangle + r \langle x_h \rangle$$

Essentially the basin scale mean flow distance is the mean of basin channel flow distance
plus the mean of the hillslope distance weighted by the velocity ratio. Similarly, for
subbasin partitioning approach (such as hillslope, or HRU) the rescaled width function
cab be derived from averaged value at HRU and the channel distances, and it can be
proximate as:

$$(3.3) \qquad\qquad\qquad \langle x' \rangle_s = \langle x_c \rangle + r \langle \widehat{x_h} \rangle$$

subtracting the subbasin mean distance from the grid mean (the mean lag between
the two descretization rescaled distance) can be estimated using:

$$(3.4) \qquad\qquad\qquad \langle x' \rangle_g - \langle x' \rangle_s = r(\langle x_h \rangle - \langle \widehat{x_h} \rangle)$$

where $\langle x_c \rangle$ and $\langle x_h \rangle$ are the basin average channel and hillslope length respectively,
and $\widehat{x_h}$ is derived from the statistical average of all the HRUs (or any form of subbasin
partition) mean hillslope distance of the basin.
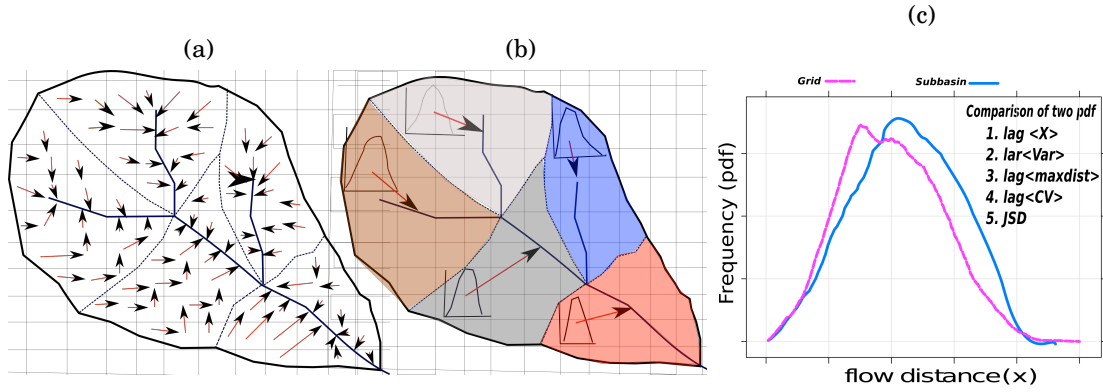
Figure 3.1: The sketch on the comparison of full distributed grid-by-grid DEM flowpath (a), subbasin partition flowpath (b), and plots of derived pdf of the two width functions (c).

The variance of the rescaled distance (Di Lazzaro et al., 2015) can be estimated using equation (3.5):

$$(3.5) \qquad var(x^{'}) = var(x_c) + var(rx_h) + 2cov(x_c, rx_h)$$

Similar formulation on basin scale width function statistical moments can be found in Di Lazzaro et al. (2015). The lag in the variance of the rescaled flow distance due to the use of subbasin descritization in the case of semi-dsitributed modelling can be given by equation (3.6):

$$(3.6) \qquad Var(x^{'}_g - x^{'}_s) = var(rx_h) + var(\widehat{rx_h}) - 2cov(rx_h, \widehat{rx_h})$$

Other statistics used are the coefficient of variance, CV, and the longest distances,L. Since CV is dimensionless, it can be compared across basin and can be used to estimate the lag due to the use of subbasin descretization. Similarly, by normalizing the error in $Var(.)$ and L to the total basin scale, these four rescaled flow distance statistical moments can be used to characterize the errors of aggregating the DEM topographic information into subbasin when used in semi-distributed models.

Hence, we define the width function variance ratio (WFVR) and width function longest length ratio (WFLR) as:

$$(3.7) \qquad WFVR = \frac{Var(x^{'}_s)}{Var(x^{'}_g)}$$

$$(3.8) \qquad WFLR = \frac{L(x_g') - L(x_s')}{L(x_g')}$$

Where the $WFVR$ and $WFLR$ are the width function variance ratio and maximum length ratio between the subbasin partition and grid partition. Both ratio ranges from 0 to 1, where 1 indicates there is no difference between grid and HRU partitioning moments at basin scale, and decreases when the effects of HRU descretization increases. These indices are useful to combine different basins to investigate the effect of descritization on basin hydrological response, and draw some generalization (power law) regards to the errors induced by basin partitioning.

Alternatively, both the rescaled distance and width function can be non-dimensional by normalized to the longest distance and total area of the basin (equation 3.9).

$$(3.9) \qquad x^* = \frac{x}{L} \quad and \quad w^* = \frac{w(x)}{A}$$

where x^*, w^*, A are the normalized rescaled distance, normalized width function, and the total area of the basin respectively. And the normalized rescaled width function is given by:

$$(3.10) \qquad \int_0^1 w^*(x^*) dx^* = 1$$

The use of normalized width function is intended to estimate the flow distance distribution which affects by the position of the channels and the shape of hillslopes. The analytical simplification of the width function for both the fully distributed and semi-distributed topographic rescaled width function can be shown in the sketch of figure 3.2.

Since the two distribution is expressed in pdf, then, the final comparison is analysed based on well established information-theoretic framework. This is useful to quantify the general information disorder (or loss) due to the use of subbasin (hillsope, HRU) descretization. There are some measure of information and discrimination (distance). In addition to statistical moments, the most popular desimilarity (similarity) index between two pdf (ρ_1, ρ_2) is Jensen-shannon divergince (JSD) is computed to compare two width function (Sánchez-Moreno et al., 2012; Lin, 1991):

$$JSD(\rho_1, \rho_2) = KLD\left[\rho_1, \frac{\rho_1 + \rho_2}{2}\right] + KLD\left[\rho_2, \frac{\rho_1 + \rho_2}{2}\right]$$

where

$$KLD(\rho_1, \rho_2) = \sum \rho_1 \log \frac{\rho_1}{\rho_2} \tag{3.11}$$

where KLD is Kullback-Leibler divergence or relative entropy (KLD is short) (Kullback and Leibler, 1951). JSD ranges between 0 and 1, with 0 being the most similar pdf and no information loss between the width function, and 1 being the most divergence and no mutual information between the two width function.

3.3 Hydrological models

The analysis of rescaled distance and width function for a basin hydrological response provide incomplete insight to the subject, because of hydrological response of a basin involves the geomorphological and dispersion parameters. To illustrate the issue more practically, the use of two hydrological models addressing the two spatial representation in the modelling structure (the one uses fully DEM information and another uses subbasin information) is required to complete the analysis. In this section, we aims to briefly describe two hydrological models used to elucidate the effects of geomorphological partitioning. Accordingly, PeakFlow model (five parameters; Rigon et al. 2011) which uses full topographic (DEM) information and rainfall-runoff component of JGrass-NewAge system (five parameters; Formetta et al. 2014c) depending on subbasin averaged geomorphological information are used for comparison.The comparison of the width function and the models are based on r, R^2, and KGE goodness-of-fit statistics (Appendix B).

3.3.1 The PeakFLow Model

PeakFlow is a hydrological model based on the geomorphological and hydrodynamic characteristics of a basin (Rigon et al., 2011). In PeakFlow model, the basin-scale travel time distribution $f(t)$, is expressed using the DEM topographic width function of study area (Rigon et al., 2011):

$$f(t) = \int_0^L W^{'}(x^{'}) f(t/x) dx \tag{3.12}$$

where $W^{'}(x^{'})$ is the concept of rescaled-width function as explained in the previous sections (rescaled by the velocity in the channel (u_c) and hillslope (u_h) for the drainage paths of channel network (x_c) and hillslopes(x_h). The $f(t/x)$ is the probability distribution

of travel times for the rain falling at a distance x (measured along the flow path)
from the outlet. Considering the hydrodynamic dispersion effects and diffusive-wave
approximation of the de Saint-Venant equations, the probability distribution of travel
times provided as solution of the Kolmogorov's backward equation (Mesa and Mifflin,
1986; Rigon et al., 2011; D'Odorico and Rigon, 2003):

$$(3.13) \qquad f(t|x) = \frac{1}{\sqrt{4\pi D t^3}} exp[-\frac{(x-ut)^2}{4Dt}]$$

Where D is the coefficient of hydrodynamic dispersion. Hence, Eq. (3.13) in Eq. (3.12)
gives width function based geomorphologic unit hydrograph (WFIUH). The hydrograph
is estimated according to PeakFlow is, thus, by:

$$(3.14) \qquad f(t) = \frac{1}{\sqrt{4\pi D t^3}} \int_0^L x' W'(x') e^{-(x'-u_c t)^{2/4Dt}} dx'$$

The model uses the full topographic information available from the DEM. Detail
derivation of each equation can be refereed at (Rigon et al., 2011).

3.3.2   JGrass-NewAGE Model

JGrass-NewAge model characterizes the topography by partitioning into homogeneous
units, HRUs, in which each HRU units are connected through the channel links (Formetta
et al., 2011, 2014c). The runoff production averaged at each HRU units using Hymod
model (Vrugt et al., 2002; Boyle et al., 2001; Formetta et al., 2011), then follows routing
procedures from the starting point of the link to the outlet of the HRU using non linear
variant of the Saint Venant equation integrated to each links (Bras, 1985). The runoff
production and propagation processes of JGrass-NewAGE model can be referred from
(Formetta et al., 2011, 2014c). The starting point of the link, the end point, the length
and slope of the links are the basin topographic inputs used in the model. Depends on the
aims, JGrass-NewAge model could be more or less distributed. Here, we are interested
to compare the effects of spatial descritization from the hydrological modelling point of
view. So we keep it less distributed and provide similar inputs with the PeakFLow model.
Hence, the rainfall, and evapotranspiration is the same for all the HRU units, and keep
the geomorphological information variability at HRU level, in contrast to the PeakFlow
model where the full grid DEM is used.

uDig GIS spatial toolbox (Formetta et al., 2014c), described in chapter 2, is used to pre-
pare the the digital watershed model setting for the hydrological model. Three alternative
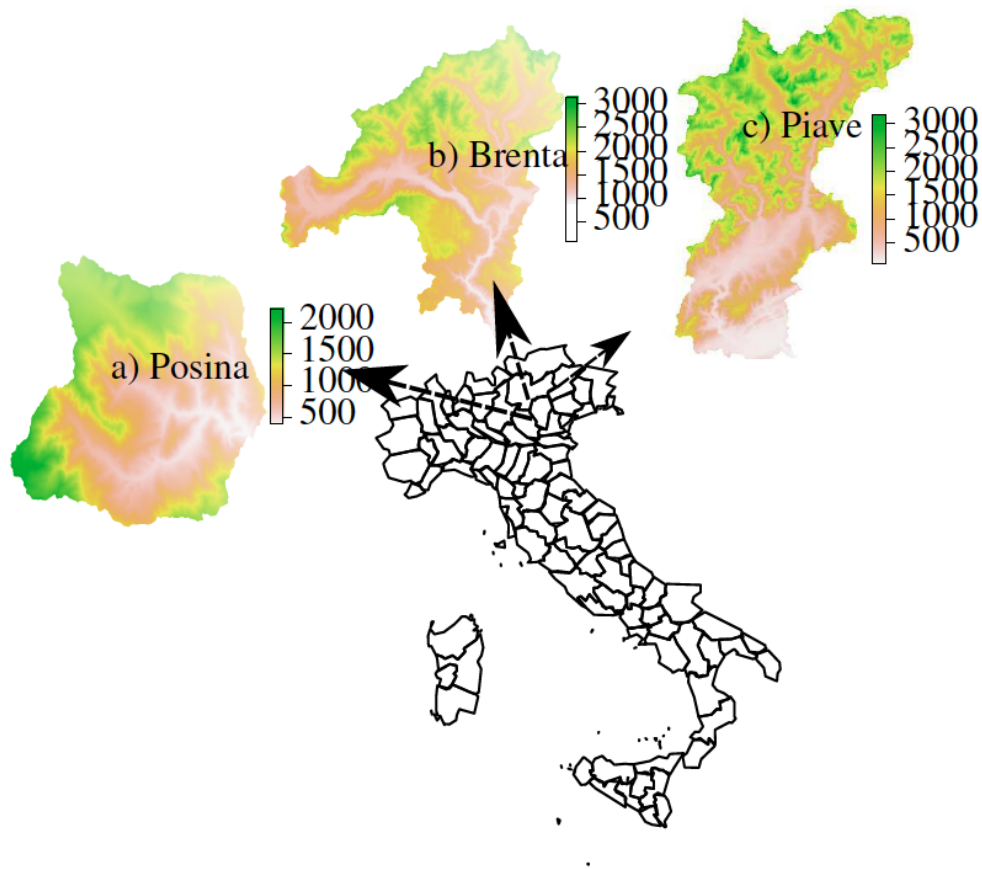
Figure 3.2: The location of three basins in Italy used in this study

methods of channel extraction are implemented in uDig GIS spatial toolbox (Formetta et al., 2014c). These are threshold value on the contributing areas, threshold value on both slope and total contributing area, and threshold value for the concave sites. Those different channel-hillslope extraction methods produce different HRU shape and geometry, and affect the HRU based width function pdf. Even for a given method, the selection of threshold area to extract channel networks affects the hillslope size, other model input averaging and eventually the model outputs. Since it determine the input and output of the model, the selection of threshold area should be carefully chosen (Zhang et al., 2013). For this, we systematically increased(decreased) the threshold area for channel extraction to decreased (increased) the hillslope area being extracted to search for appropriate hillslope size suitable for rainfall-runoff modelling.

3.4   Study basins and model application

The analyses described in this study is based on the application of rescaled width function
and hydrological models of hydrological response to the three basins: Posina river basin
(enclosed at Stancari), Brenta river basin (closed at Bassano del Grappa) and the Piave
river basin (closed at Montecastello). The width function analysis is based on all the three
basins. They are located in Northern mountainous part of Italy. Figure 3.2 indicates the
distribution of the three basins. Posina river basin is located in the North Eastern part
of pri-alpine mountainous parts of Veneto region. It is situated between the Adige and
Brenta valleys, has elevation range of about 1800 meters.

The Brenta river has total area of about 1640 km^2 and the main river course length
is about 72km when closed at Bassano del Grappa (Nicótina et al., 2008). The rainfall
patterns of the area are quite heterogeneous, with the heaviest rainfalls occurring mainly
in the eastern part of the basin. Piave river basin also situated in North-Eastern part
of the Italian peninsula. The area of the basin is about 3460 km^2. The elevation ranges
from 700 to 3160 m.a.s.l, and the mean annual precipitation is about 1500 mm and the
annual temperature is about $10^o c$. It is characterised by an artificial system of water
resources built between 1920 and 1960 (Nicótina et al., 2008). The rescaled distance and
width function is calculated for all the three basins in both the topographic partitioning
approaches. The differences between the two approaches is estimated using the statistical
moments of the width functions at the basin scale.

For the rainfall-runoff simulations, due to the availability of data, Posina river basin
is used. The rainfall data collected from 11 station in an around the basin is used to
estimate the mean value using kriging interpolation.

3.5   Results and discussions

3.5.1   The effects of HRU on basin hydrological response

The set of upscaling (use of different HRU size) experiments is conducted to investigate
the effects of spatial partitioning on hydrological response of the basin. Thus, starting
from the use of DEM, the three basins are partitioned progressively coarse grained i.e
using increasing threshold area (A_T). The A_T used ranges from 0.001% to 2% of the
basin. For instance, the experiment of width function on both grid and HRU on different
threshold area in Posina basin is shown at figure 3.3. It shows how the geomorphological
parameters change. Similarly, the comparison of normalized rescaled width function of
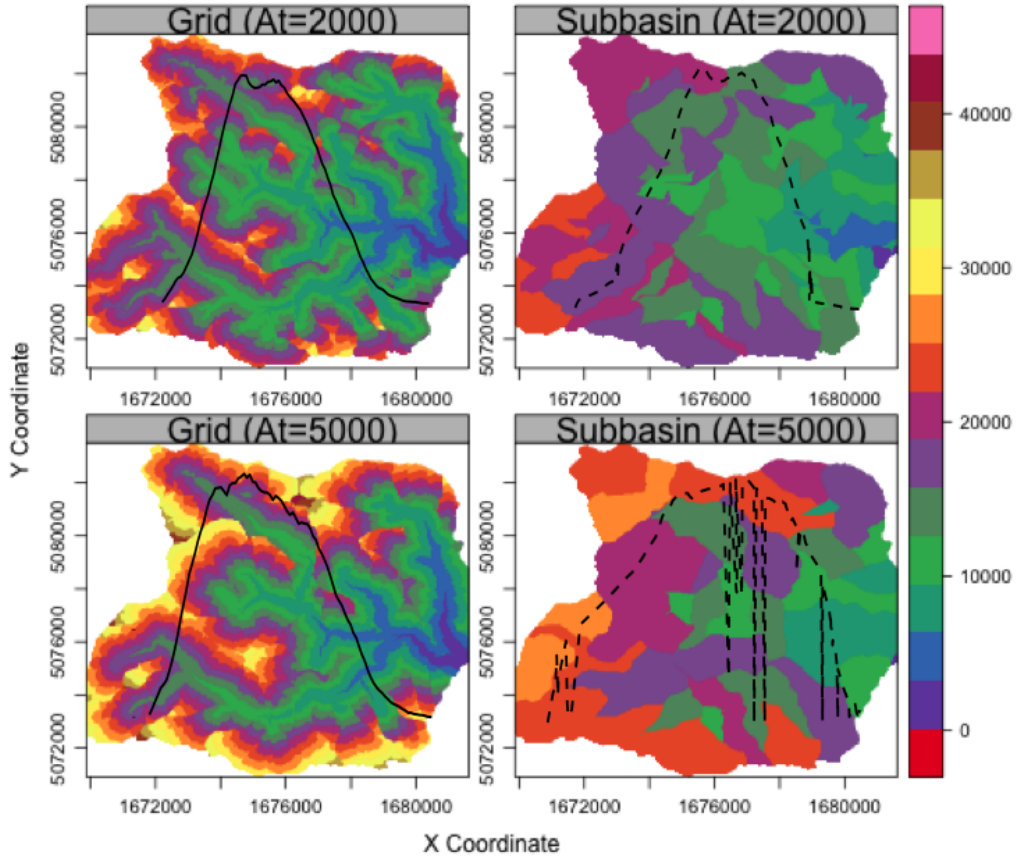
Figure 3.3: Examples of how A_T affects the basin rescaled width function in both grid (fully-distributed, first column) and HRU (semi-distributed model, second column) topographic partitioning in Posina basin.

grid by grid and HRU decretization for Brenta shows clear difference (figure 3.4). It shows that the highest error is at longer flow distances. As expected, the increase in A_T increases the errors of the width function between the two partitioning. The effect can be seen both on the rising and recession limb of the width function plots. Increasing the HRU sizes, by increasing the A_T, the HRU width function shifts to the right with gradual change in its shape. The comparison at Posina shows that rescaled distances averaged at HRU units is shorter and more narrower than the pixel based width functions. It is noted that the shortest and longest rescaled distance of the subbasin is larger and shorter than the shortest and longest rescaled distance of grid width function respectively (not shown).

As indicated in equation (3.1), the possible effects of threshold area and HRU size on the width function is influenced by the kinematic ratio, r. Hence, we assume three
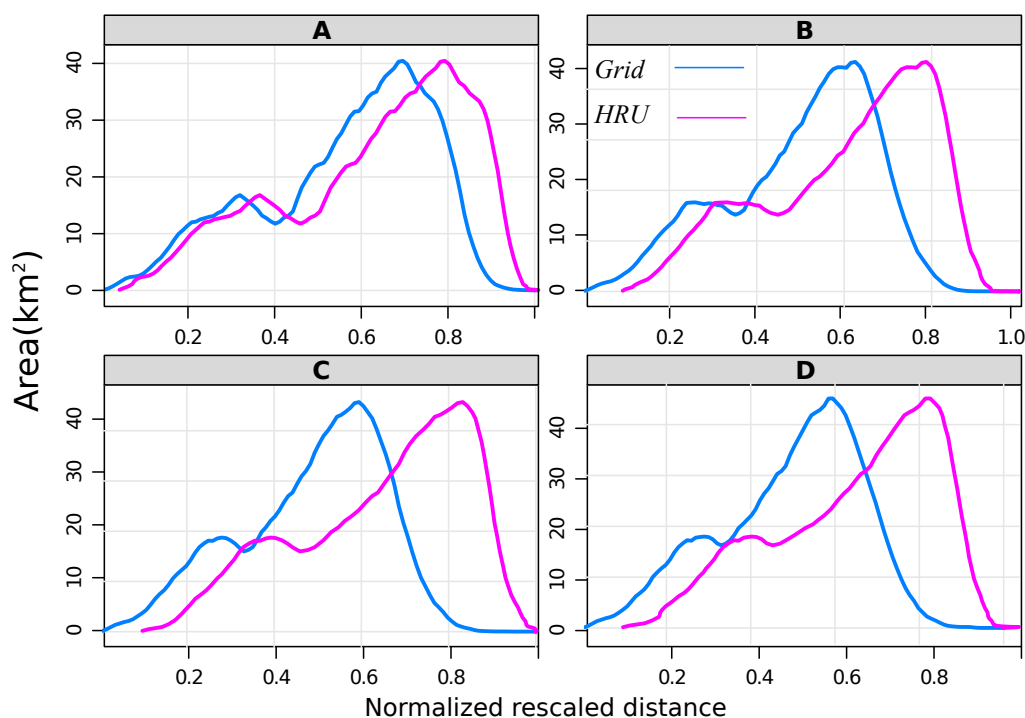
Figure 3.4: The comparison of grid and HRUs based normalized rescaled width function for different normalized threshold area A_T/A: 0.03% (a), 0.1% (b), 0.5% (c) and 1% (d) for Brenta basin, for a given $r = 10$.

r values ($r = 5$, $r = 10$, $r = 20$) to evaluate the effects on different partition, hence rescaled width function. It strongly affects the rescaled width function and the errors (lags) between the two descretization schemes (figure 3.5). To reduce the discontinuity in the HRU rescaled distances, figure 3.5 is shown in cumulative distribution (cdf) of the rescaled distances.

As shown in figure 3.5 the effects of A_T is not only on the HRU width function, it also affect the grid width function by influencing the proportion of hillslope and channel distance. Hence, the second experiment is to investigate the effect of A_T on the dynamic errors between the two partitioning. Figure 3.6 is the moments of rescaled distance for both grid and HRU discretization.

The effect of A_T (HRU size) on hydrological response of the basin (using width function as surrogate) can be hypothesize by deriving the errors (lags) of the HRU width function in reference to the DEM grid by grid width function. Accordingly, we did experiments of the rescaled width function for different HRU size level and r value, and the error between the two approach can be shown in figure 3.6. The gray area is the lags or errors in width function statistical moments between two width function. For
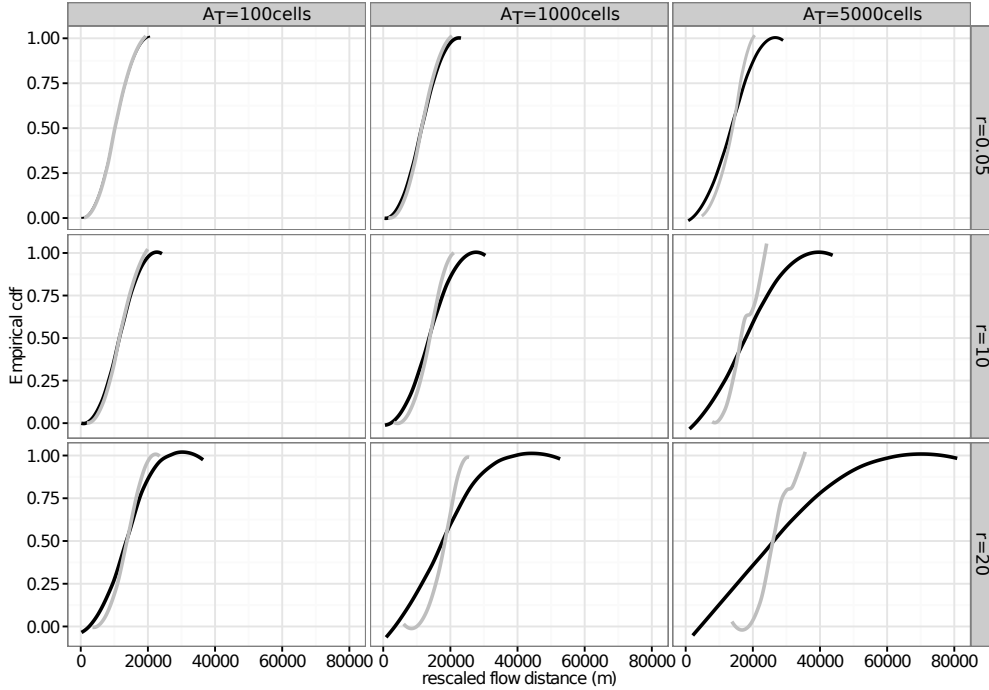
Figure 3.5: The cumulative distribution (cdf) of the grid (black) and HRU (gray) rescaled width function of Posina basin for some selected threshold area values($A_T = 100, 1000, 5000$ grid cells). The three rows are representing the effects of three different values of the rescaled width function parameter, r.

small threshold area, the errors between the two width function is relatively small, and it increases with increases in A_T.

The spatial moments of the width function analysed for A_T. The $\langle x \rangle$ of grid and HRU descretisation for a basin is the same, hence, the errors in $\langle x \rangle$ is almost zero. The other three moments ($Var(x^{'})$, CV, and L) for all the basins for both spatial descrtization is analysed and shown at figure 3.6. $Var(x^{'})$ increases when A_T increases for both approach but with different rates. Therefore, the errors in the $Var(x^{'})$ increases with A_T, and also get larger for high r value of the rescaled distance function.

To compare between different basins, and generalize the effect of HRU descretisation on topographic width function, we normalized the rescaled width function. The errors in the spatial moments of the two discretization can be plotted in scaling power law to characterize the general effects of subbasin on the topological hydrological response of a basin. The power law fitting could provide the scale invariance of the errors due to the use of different partitioning size. We have established the simple empirical equation on the bases of observed linear relationship of those errors and lags of statistical moments
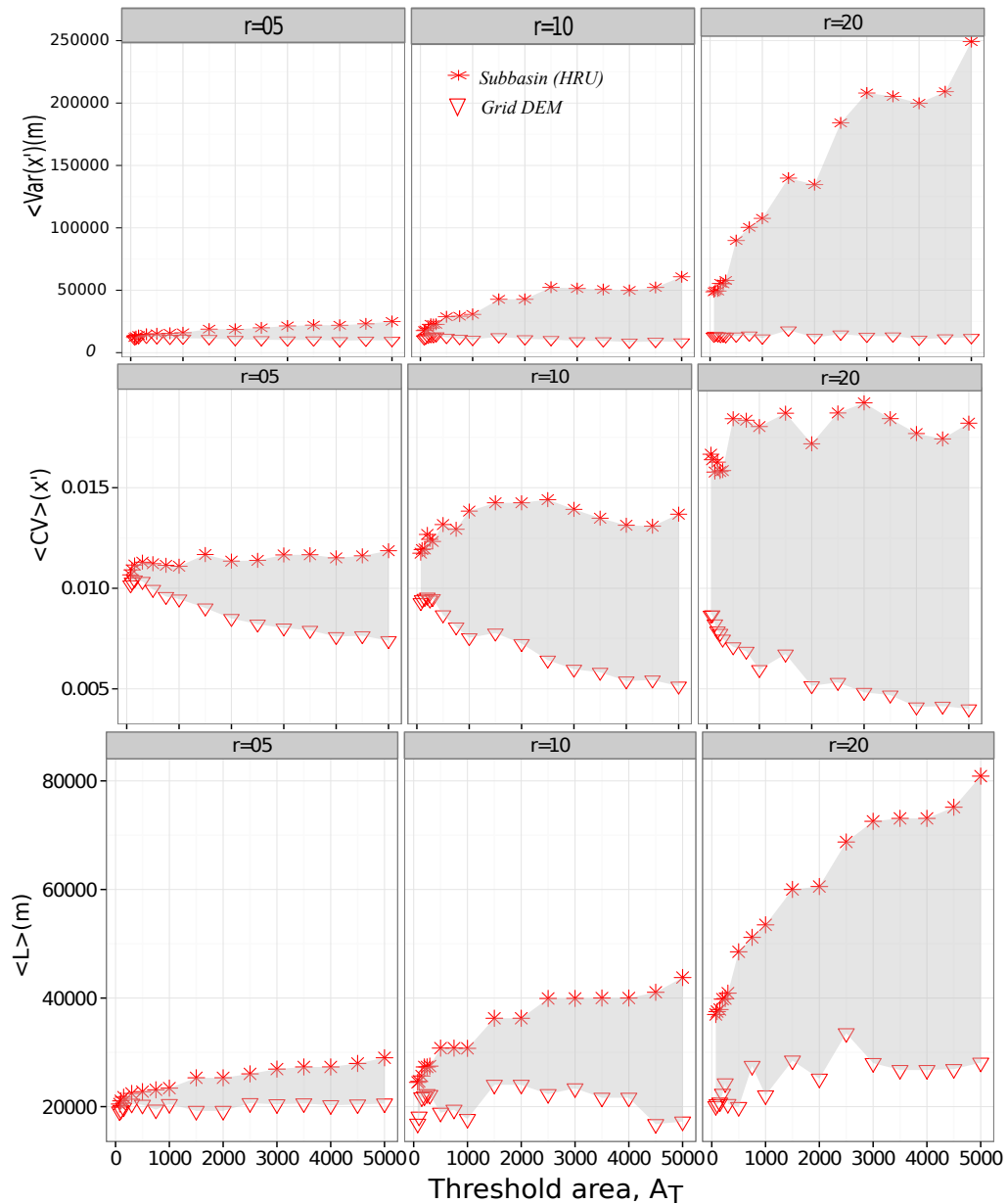
Figure 3.6: Moments of rescaled distance of the basin as function of channel threshold
area: (a) variance of rescaled distance; (b) coefficient of variation of rescaled distance; (d)
maximum of the geomorphological distance of the basin (width function), L. The mean
difference in the resident time is very small, and not easy to recognize to differentiate
the impacts of subbasin, because the raw mean of the mean is the same as the mean
(subbasin mean). However, the use of normalized width function can clearly show the
effects of subbasin discretization at a basin, because it shows the pdf of the flow distance,
and where the flow is more distribute and less distributed.

(WFVR, WFCVR, and lag(WFL)) with normalized threshold area, A_t/A in log-log plots.

$$(3.15) \qquad\qquad \xi = \lambda [\frac{A_T}{A}]^{-\alpha}$$

where ξ is the error parameters (WFVR, WFCVR, and lag (WFL)), λ and α is the two empirical parameters of the power law. Figure 3.7 is shows the errors in spatial statistics due to the use of HRU descrtisation as function of normalized threshold area A_t/A and rescaled distance r. The WFVR decreases with normalized threshold area A_T/A and rescaled distance r (figure 3.7).

Combining all the basins, WFVR is highly explained by the normalized A_T (HRU area) with $R^2 = 0.84$ and the other remaining factors (0.16) could be related to the shape, topographic distribution and DEM resolution of the basins. Rinaldo et al. (1995) indicates that the shape of the basin is one of the controlling factor of the width function. To identify how those factors affecting the power law, we separated the relation to each basin and the R^2 increases to 0.93 and above. For instance, for Posina basin (circular basin) the scaling law of the lags of the spatial moments is shown at figure 3.8. Similar analysis of the scaling law formulation for each basin and the results are presented in table 3.1.

In addition to the analysis on statistical moments error, the width function of both topographic partitioning is analysed using the goodness-of-fitness (GOF) indices. This is essentially mean that changing A_T, the width function of both grid and HRU partitioning changes and the GOF indices changes too. Looking to the trends of the GOF indices between the grid and HRU provides insight on the effects of the assumption of HRU on geomorphological hydrological responses of a basin. This results are shown at figure 3.9. The KGE value indicates that up to the normalized threshold area of 0.1% of the basin we can maintain the model structure simulation (width function) with KGE value of 0.97, while it drops fast with increasing normalized threshold area, and gets to 0.45 KGE value with 1%. It is important to note that the pattern in KGE and R^2 is the same for all the basin with various size and shape. This can be an important suggestion to the semi-distributed hydrological models which depend on topographic information. To maintain the high process based flow estimation with high GOF requires the considerably high topographic information in the model structure (normal threshold area less than 1%). This information is important for GIUH based hydrological models which claims to be useful in ungauged basins, for providing the epistemic uncertainty of the HRU based operations in hydrological modelling.
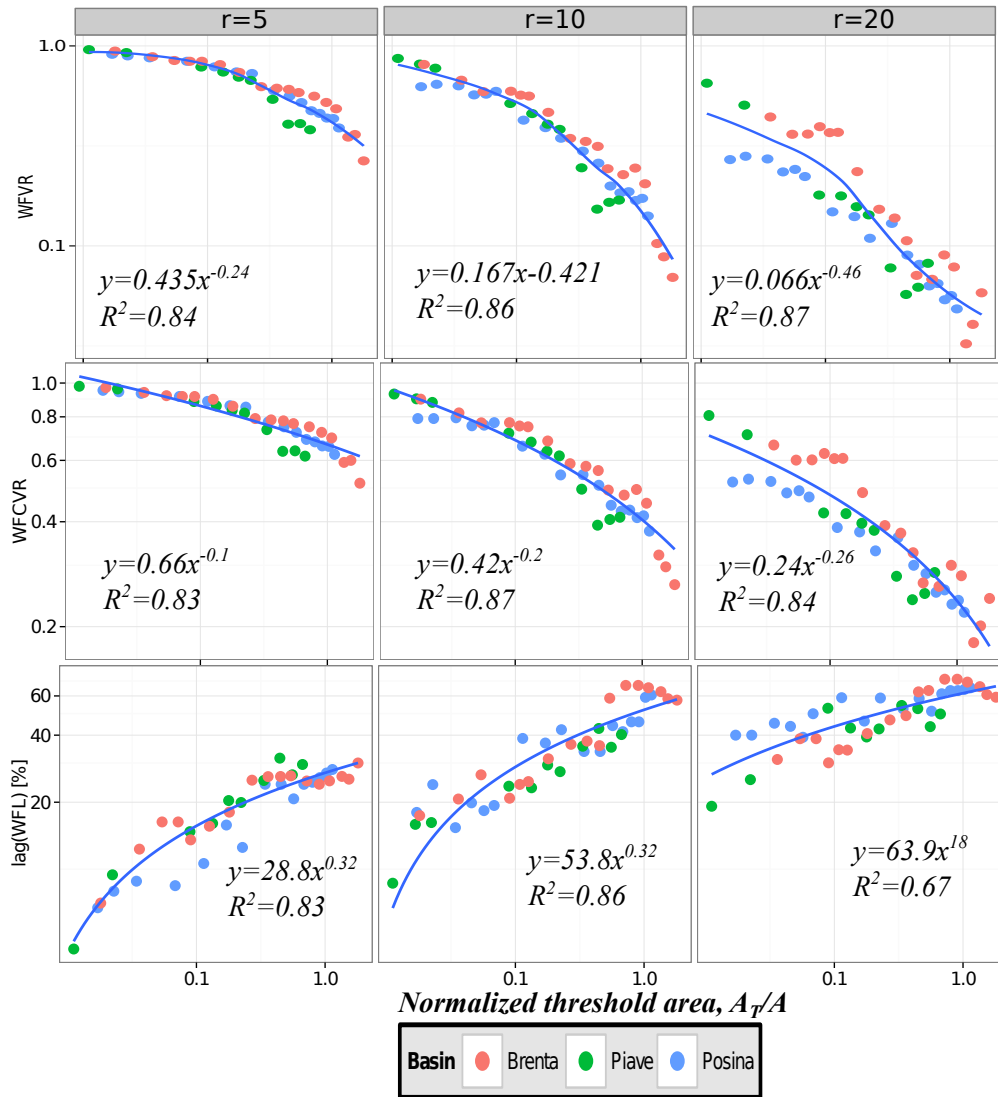
Figure 3.7: The log-log relationships between the width function error ($WFVR$, $WFCVR$, $lag(WFL)$), and normalized threshold area $\frac{A_T}{A}$ for the three study basins combined. Different dot color is representing different basins.

Lastly, as in the previous experiment, we use the grid by grid DEM and HRU based width function by systematically increasing the A_T, to estimate the divergence index value (JSD) between the two distributions. The JSD index indicates that the information loss in semi-distributed model due to the use of HRU topographic information is very small up to 0.03% of normalized threshold area, and after 0.1% it increases quickly and monotonically for all the three basins. For instance, with the normalized A_T of 1%, we lost 10% of the full grid by grid based width function information. In the case of semi-distributed hydrological models, based on the KGE and JSD values, the normalized
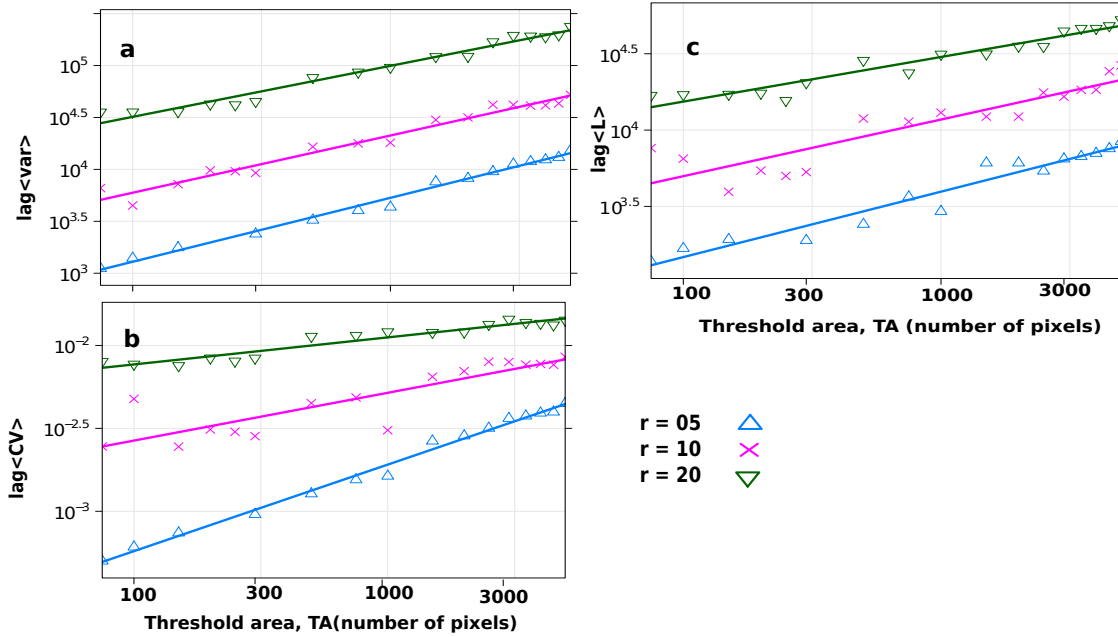
Figure 3.8: Example of the scaling function of normalized threshold area (%) and the lags of the spatial moments of the two descretization in Posina river basin. Refer to table 3.1 for the regression fitting parameters.

Table 3.1: The power law fitting of the spatial moment lag (error) of HRU and grid descretization rescaled width function. The r is the ratio of the velocity in the channel to hillslope used to define rescaled flow distance. The lags are the errors of the spatial moments (variance, CV, and the maximum distance L in the width function) between the HRU and grid based width function

Basin	r	lag(Var)			lag(CV)			lag(L)		
		λ	α	R^2	λ	α	R^2	λ	α	R^2
	r=5	75.8	0.61	0.99	0.00005	0.52	0.99	204.5	0.42	0.95
Posina	r=10	471.2	0.55	0.96	0.0007	0.29	0.75	903	0.37	0.82
	r=20	3339	0.49	0.97	0.0036	0.29	0.91	3997	0.29	0.93
	r=5	7080	0.85	0.99	0.00003	0.74	0.99	1146	0.53	0.96
Piave	r=10	3746	0.78	0.99	0.0002	0.58	0.98	3220	0.48	0.95
	r=20	164931	0.74	0.98	0.0012	0.38	0.93	8416	0.45	0.92
	r=5	26	0.65	0.98	0.00003	0.52	0.98	1131	0.30	0.90
Brenta	r=10	49.5	0.73	0.97	0.00002	0.47	0.96	407	0.52	0.94
	r=20	118	0.79	0.96	0.0001	0.34	0.93	676	0.54	0.94

A_T of 0.1% is recommended to maintain high GOF values and very low information loss in the rescaled width function of the basin ($KGE = 0.95$, $JSD = 0.03$).

In addition to the HRU sizes and A_T, the geometry and shapes of the HRUs affects
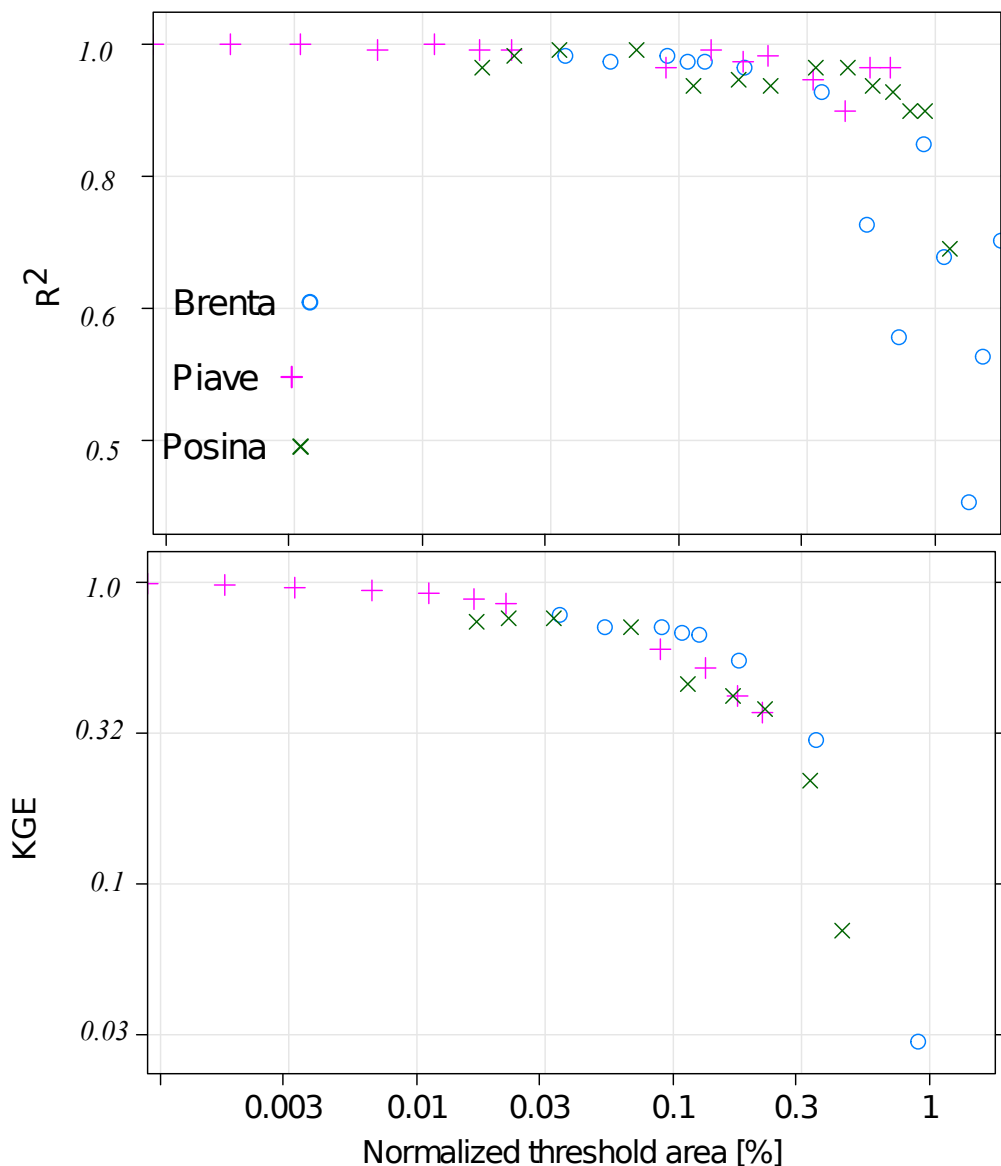
Figure 3.9: The R^2 and KGE value between the grid by grid and subbasin based width function.

the rescaled width function (Rinaldo et al., 1995), and here we further investigated how the shape of each HRU determine the width function and the geomorphological structure in the response modelling. The three alternatives of HRU discretization methods implemented in JGrass spatial Toolbox (Formetta et al., 2014c) is investigated using the mean routing distances versus the HRU centroids. In some semi-distributed hydrological models, for instance SWAT and JGrass-NewAge, the physico-statistical values at HRU centroids are used for further simplification to represent average process of
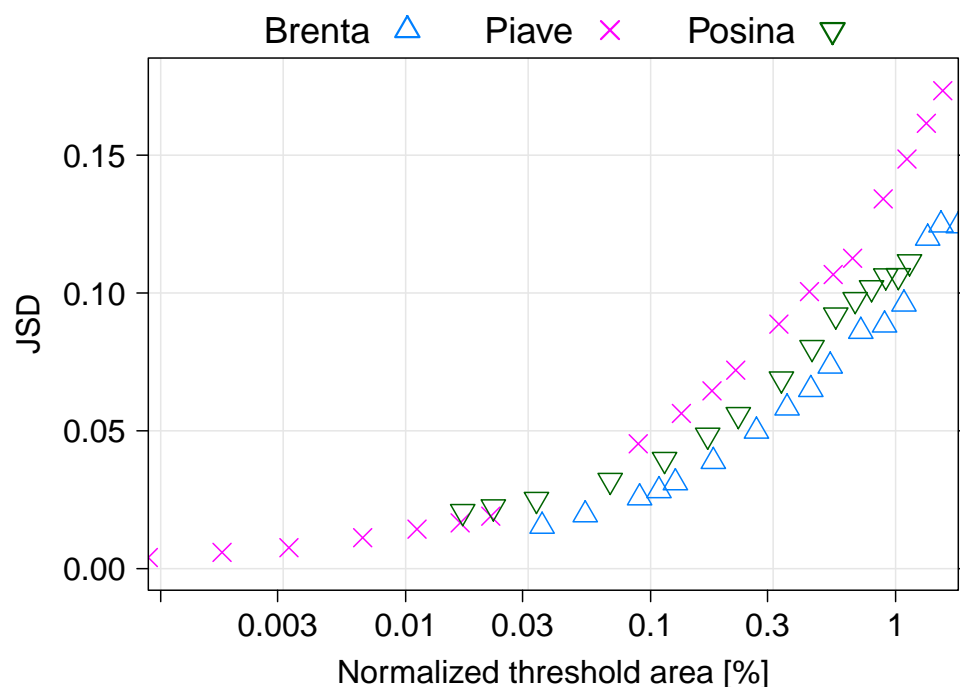
Figure 3.10: Jenson-shannon divergence of width function between the grid by grid and HRU for $r = 10$ in all the three basins.
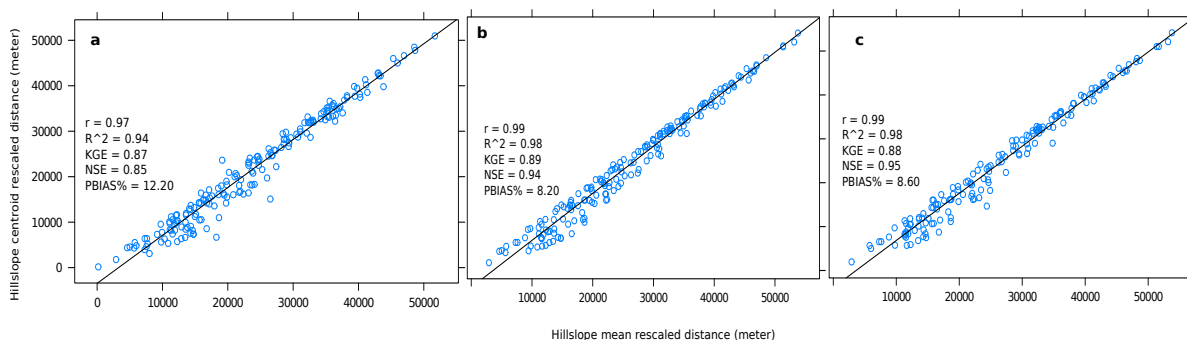
Figure 3.11: Scatter plots of hydrological rescaled distances at the outlet for Posina basin of the HRU centroids with mean HRUs extracted according to three methods: a) constant threshold area, b) threshold area-slope, c) threshold area methods at convergent sites

47

Table 3.2: Optimal paramater values of both models based on particle swarm calibration procedure.

JGrass-NewAge		PeakFlow	
Parameters	values	Parameters	values
C_{max}	349.07	r_1	19.65
B_{exp}	3.2	r_2	117.65
α	0.127	C	0.76
Rs	0.032	D	5099
Rq	0.218	A_{Sat}	0.85

that particular HRU. Using this scheme, keeping the same number of HRU extracted, We compared the rescaled flow distances of the HRU mean flow distance with HRU centroids. The scaterplot is shown at figure 3.11. It shows that the constant threshold area method has less GOF values ($NSE = 0.85, R^2 = 0.84$) in comparison to the other two methods (slope-area method with $NSE = 0.94, R^2 = 0.98$, and slope-area method at convergent site method with $NSE = 0.95, R^2 = 0.98$). Given the geomorphological and geometrical construction of the HRUs in the three methods, the centroid values of HRUs in the threshold-slope area and threshold area at convergent site are more closer to HRU mean flow distances. Hence, it is recommended that in preparing the geomorphological information for hydrological modelling, the two latter methods are preferred in capturing the statistical mean of the rescaled flow distances of the HRUs.

3.5.2 Models calibration and validation experiments

The hydrological modelling exercise in this section aims to investigate the role of topographic information discretezition on the basin response modelling. Keeping the same meteorological forcing for both rainfall-runoff models, the effects of topographic information representation on the model performance investigated. We calibrated model parameters at some selected events, and validated for the rest of the events. The models are calibrated on series of single event and then selects the best performing model parameter set for optimum. Some of the selected events used for the analysis are reported in table 3.3, and the corresponding simulations are also shown at figure 3.12. Automatic particle swarm (Eberhart and Shi, 2001) procedure is used to calibrate the model parameters. The optimized model parameters for both NewAge and PeakFlow model are presented at figure 5.2.

Three GOF parameters are used to compare the two models (brief description on the

Table 3.3: Some selected storm events used for validation, and the model performances values. The hydrogrphs of the simulation is shown at figure 3.12

	PeakFlow			JGrass-NewAge		
Event	NSE	KGE	R^2	NSE	KGE	R^2
16-Oct-1996	0.31	0.51	0.70	0.67	0.56	0.93
18-Dec-1997	0.64	0.66	0.85	0.67	0.56	0.88
06-Oct-1998	0.66	0.81	0.75	0.75	0.70	0.89
21-Oct-1999	0.17	0.55	0.86	0.14	0.44	0.82
07-Nov-1999	0.74	0.87	0.76	0.82	0.66	0.91
02-Nov-2000	0.82	0.83	0.82	0.66	0.62	0.85
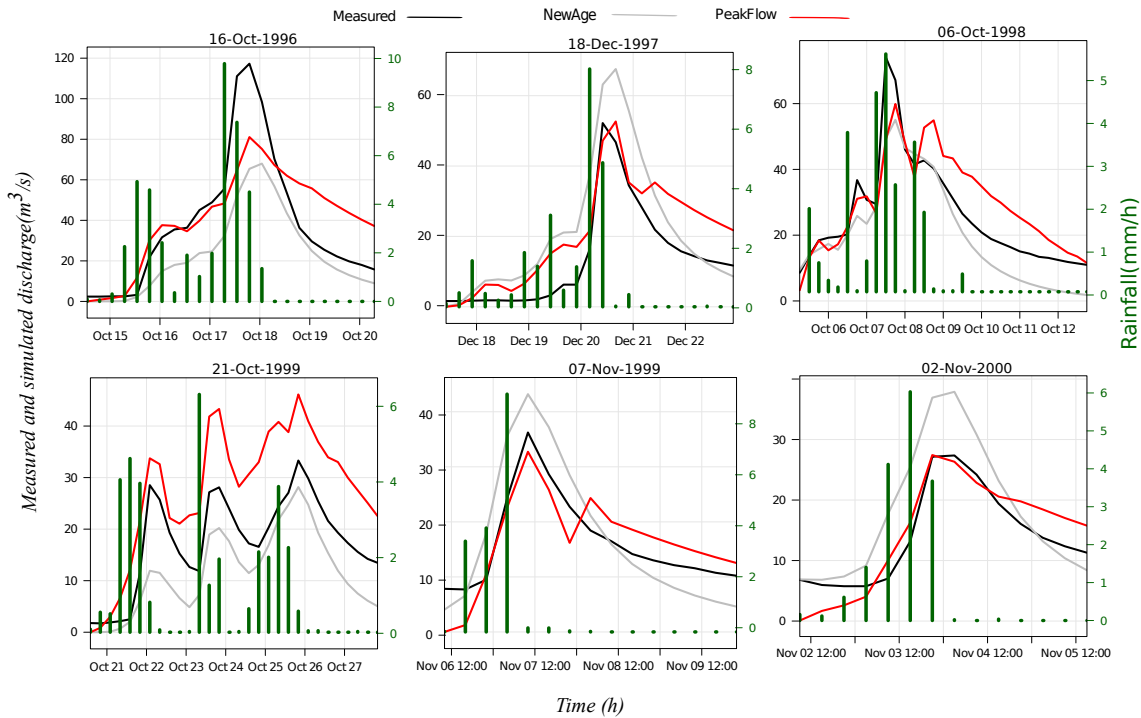
Figure 3.12: Hourly simulation of JGrass-NewAge and PeakFlow model for six selected events. The model performance of the two models of these events are shown at table 3.3. The bar in each plot is the rainfall of the events.

49

GOF indices are provided at appendix B). A sample of performances of the two models are reported at table 3.3. Generally, the performance of the models are mixed: poor to good. Inter-model comparison shows that JGrass-NewAge is better in some events (like 16-Oct-1996, and 12-Oct-2000) and PeakFlow model perform better in others (like event 02-Nov-2000). However, looking at the simulation hydrographs at figure 3.12, the model with the full topographic information based width function (peakFlow) were able to simulate the peak of the events better than JGrass-NewAge. However, the errors of the peakFlow model is mainly at the recession part of the hydrograph which always overestimate, and reduce the model performances (figure 3.12). In general, JGrass-NewAge captures the patterns of the hydrographs, and hence the R^2 is higher than the peakFlow model.

The simulation comparison indicates that the topographic representation into the models affects the model performances. As a premise, The PeakFlow model that uses the full topographic information (grid based width function) does not always perform better than the NewAge semi-distributed hydrological model.

3.6 Conclusions

In the present chapter, we analysed the effects of spatial descretization in basin response modelling using two approaches: 1) using grid and HRU based rescaled distance and its width function (WF), and 2) using two WFIUH based hydrological model which uses different level of topographic information i.e. one with full topographic information (peak-Flow), and the second one with semi-distributed information (HRU, JGrass-NewAge).

Since HRU in semi-distributed model is the representative units for all the processes, the errors due to averaging all inputs are complex and interlinked. Hence, we need to investigate each source of errors and uncertainty in our modelling predictions. Therefore, the use of flow distance of the basin to the outlet could be the first errors attached in the semi-distributed modelling efforts.

We found out that there is clear relationship between the HRU size (channel delineation threshold area) and the rescaled width function errors. The smaller the HRU size is used, as expected, the width function difference between the grid and the HRU is small, and vice-versa. Hence, for any threshold area consideration, there is a certain errors introduced to the modelling, and this can be incorporated in the predicted fluxes. We forward two remarks at this point: $\leq 0.3\%$ of the basin as minimum threshold area to maintaining high topographic information, which keeps the sources of error from

topographic partitioning is small; and otherwise, the topographic information error due to reduced topographic information need to be known and communicated in GIUH based hydrological predictions.

To finish the theoretical analysis on the effects of basin partition using the width function, the effects of discharge prediction at the outlet of the basin using two hydrological model (full topographic information and the other semi-distributed topographic information) using some events in Posina river basin is studied. Automatic calibration is done to fix the parameters for both models.

In general, it can be seen that the two models have small differences in performances with good capability of capturing the pattern (or variance of the simulation) in JGrass-NewAge and capability of simulating the peak of the hydrograph in PeakFlow. This study also confirm that, a premise that model with detail topographic information better estimate the peak event is not always valid.

Estimating water budgets at the basin scale with JGrass-NewAge: water inputs, their variability and uncertainty[*]

This chapter describe the efforts to generate accurate spatial information of meteorological forcing from in situ observations. For a series of tasks required in basin water budget modelling i.e. proper catchment partition, estimation of spatial field time series meteorological forcing data, and separation of rainfall and snowfall, this study provides sophisticated and consistent methods, and thereby set-up JGrass-NewAge model system in Posina river basin. The use of MODIS imagery data in rainfall/snowfall separation is effectively employed. Estimating forcing data (the input component) with appropriate tools and methods, as pursued in this study, helps for reasonable basin scale water budget closure.

4.1 Introduction

Estimating the terrestrial water balance at different scales is certainly an important task of modern hydrology (e.g. Eagleson, 1994). It can be obtained by integrating the

---

[*]This chapter is based on "Wuletawu Abera, Giuseppe Formetta, Marco Borga, and Riccardo Rigon. Estimating water budgets at the basin scale with JGrass-NewAge; part I: water inputs, their variability and uncertainty, Submitted to HESS"

water budget equation over an appropriate control volume, k:

$$(4.1) \qquad \frac{\partial S_k(t)}{\partial t} = J_k(t) + \sum_i Q_{ki}(t) - ET_k(t) - Q_k(t)$$

for an appropriate set of elementary control volumes connected together. In Eq.(5.1), S [L^3] represents the total water storage of the basin, J [L^3 T^{-1}], ET [L^3 T^{-1}], and Q [L^3 T^{-1}] are precipitation, evapotranspiration, and runoff (surface and groundwater) respectively. The Q_is represent input fluxes, of the same nature of Q, coming from adjacent control volumes.
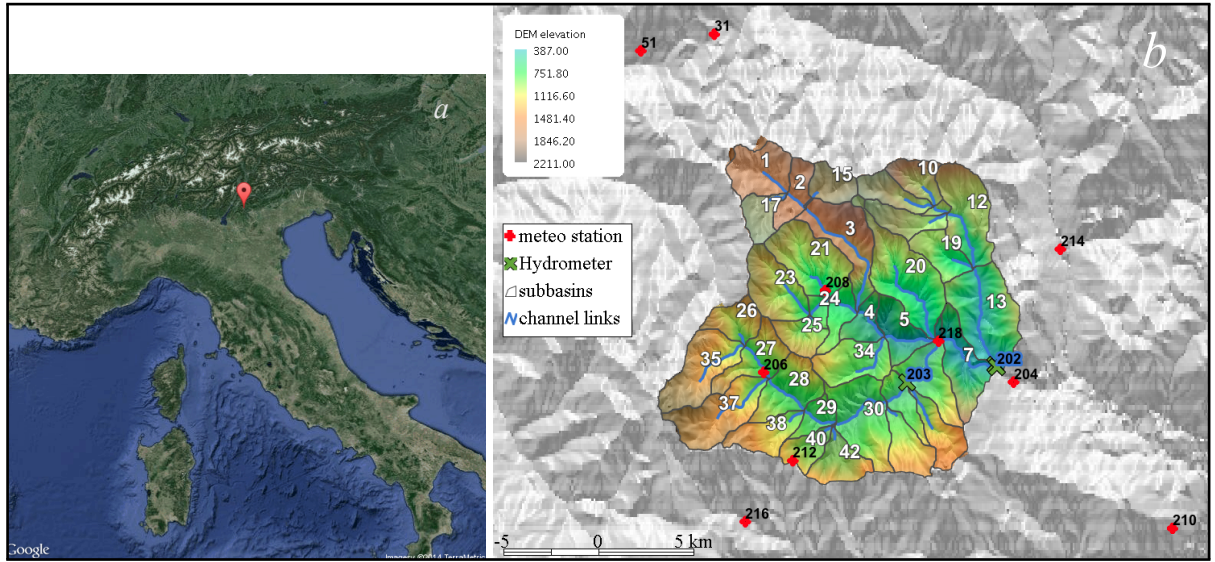
Figure 4.1: The location of the Posina basin in the Northeast of Italy (a) and DEM elavation, location of rain gauges and hydrometer stations, subbasin-channel link partitions used for this modelling (b).

It is clear that Eq.(5.1) is governed by two types of terms, which can be easily identified as "inputs" and "outputs". The outputs are certainly evapotranspiration, ET, and discharges, Q, including the Q_is, because they come from the assembly of control volumes. The inputs are $J(t)$, but this term has to be split into rainfall and snowfall. Moreover, other inputs are ancillary to the estimation of outputs, in particular temperature, T and radiation R_n. Another input of the equation is the definition of the domain of integration and its"granularity", i.e. its partition into elements for which a singe value of the state variables is produced.

In this chapter we discuss the estimation of all of these input quantities, with the scope to obtain a methodology that is generally applicable, following and expanding

the concepts developed in the case of cryospheric processes by Garen and Marks (2005). There are several objectives:

- Implement, assess and improve procedures for estimating spatial time series of the necessary meteorological inputs required for spatially distributed modelling;

- Introduce a new, simplified, method for performing the separation of rainfall from snowfall;

- Produce an estimation of errors involved in the above procedure, and eventually study their impact on estimating the outputs;

- Exploit the JGrass-NewAGE (see below) system capabilities to automatize procedures for producing spatial time series of meteorological data.

4.1.1 Literary review

Solving the water budget spatially requires a proper treatment of topographic data, hydrological parameters (i.e. time-constant but possibly space varying characteristics) and the creation of a time series of hydrological inputs fields.

Nowadays, topographic data means digital data. This discipline has a recent tradition, which started in the late eighties of the last century (e.g., Band, 1986; Tarboton, 1989; Moore, 1992), based on the use of Digital Elevation Models. It has been reviewed in Wilson and Gallant (2000), Peckham and Gyozo (2007) and, very recently, in Passalacqua et al. (2015), where new data retrieval techniques are also analyzed. Regarding the this chapter, the tools adopted are those described in Abera et al. (2014) and Formetta et al. (2014a) where further references can be found.

The model parameters, which are model‚Äôs dependent, are treated in chapter 4 and, therefore, the topic is not discussed here too.

We briefly discuss here the problem of spatial interpolation of meteorological data, especially of rainfall and temperature. Historically various methods have been used: Thiessen polygons (e.g., Thiessen, 1911; WMO, 1994), Inverse distance methods (IDW) (Ly et al., 2013), interpolation with splines (e.g., Hutchinson, 1995; Mitášová and Mitáš, 1993), Kriging (e.g., Matheron, 1981; Goovaerts, 1997) or other types of interpolation (e.g., Robeson, 1992; Li and Heap, 2011, and references therein). When data density is high, most methods produce similar results (Burrough and McDonnell, 2011) and some other methods are, indeed, equivalent (e.g., Borga and Vizzaccaro, 1997). In practice, the choice of method by scientists depends on the availability of the appropriate tools

to perform the analysis. However, the choice of Kriging recently gained momentum, especially because it can use auxiliary variables to help the interpolation. For instance, the influence of other terrain-related parameters such as relief, slope and aspect was investigated by Attorre et al. (2007). They found that universal kriging with external drift performed as well as the best method for most of the climatic variables analyzed. Last, but not least, Kriging implements some standard procedures to assess error of estimates that are less obvious to obtain with other methods.

Besides, e.g. (Goovaerts, 2000; Lloyd, 2005; Basistha et al., 2008; Ly et al., 2011), Kriging is seen to give better rainfall interpolation performances than other methods. Notable early contributions on this topic came by Creutin and Obled (1982); Tabios and Salas (1985); Phillips et al. (1992). Garen and Marks (2005); Tobin et al. (2011) give detailed reviews of the procedures to follow.

In principle spatial information for rainfall can also be derived from satellite (Ward et al., 2011; Tian et al., 2007; Kidd and Levizzani, 2011; del Jesus et al., 2015; Gebremichael and Hossain, 2010). Also, information from radar can be used for this scope, as in Borga (2002), Berne et al. (2004), Schuurmans et al. (2007), Velasco-Forero et al. (2009) and Schiemann et al. (2011), to cite a few.

However, since there is a dense network of stations around the basin that will be used as an example for this study, we restrict our use to ground-based data.

Concerning the temperature fields, it is a well known fact that elevation is the first order variable explaining temperature gradients (e.g. Lookingbill and Urban, 2003; Blandford et al., 2008; Dobrowski et al., 2009)(a decrease of about $0.6^oC/100$ m is generally accepted as a mean estimate, (e.g. Jabot et al., 2012)).

Therefore Kriging techniques accounting for the temperature lapse rate also seem appropriate for temperature interpolation (e.g. Dodson and Marks, 1997). An early paper using external drift charging to predict air temperature and precipitation was published by Hudson and Wackernagel (1994) and, not surprisingly,Carrera-Hernández and Gaskin (2007) found that the use of elevation as a secondary variable improves temperature prediction.

Although elevation is the main variation factor for air temperature, it is influenced by other factors. Both local and regional effects exist (Courault and Monestiez, 1999). Seguin et al. (1982) observed a temperature difference in close settings of 2 and 4^oC caused by the wet and dry areas, respectively. Proximity to the sea, topography, and the general atmospheric circulation patterns (CPs; **?**) also influence spatial variations of air temperature. All these factors are not easy to integrate using interpolation methods, and

will not be used in the present chapter.

One issue about which many papers dealing with precipitation in mountain areas are reticent is the separation between rainfall and snowfall.

This partition can be accomplished by using an appropriate, limited-area, meteorological model, like WRF (Dudhia et al., 2005; Caldwell et al., 2009) or ARPS (Xue et al., 2000, 2001), whose resolution can be pushed to one kilometre and below, so as to have appropriate spatial information usable in hydrological modelling. However, the ability of these models to forecast in a reliable, quantitative, form is still questionable. Other physical approaches to snowfall-rainfall separation are based on utilising the psychometric energy balance, e.g. Steinacker (1983) and Harder and Pomeroy (2013); Harder and Pomeroy (2014) and Ye et al. (2013) represent informative treatments and reviews of the topic.

Most hydrological models use variations of the phase separation method proposed by the U.S. Corps of Engineers (Army, 1956; Rohrer, 1989). Basically, this method introduces a threshold temperature, above which precipitation is liquid, and below which it is snow. The transition between phases can be smoothed in various ways.

In 1974, Auer Jr studied 1,000 surface weather observations to identify surface air conditions associated with snow and rain. He concluded that when the air temperature is 2.28^oC , the probability of rain and snow are 50% each, and that 95% probability for snow occurs at 1.18^oC and for rain at 5.68^oC. However, Ye et al. (2013), reports that these temperature thresholds can vary greatly from one place to another, as confirmed also by Kienzle (2008) studies in Canada.

For our modelling we followed the idea of Kitanidis and Bras (1980), as implemented by Kavetski et al. (2006), which assume an S-shaped separation curve. The smoother contains parameters that could be estimated if some snow data were available. In fact, MODIS remote sensing platforms offer products that can be used for this scope, as will be explained in section 3.3.

4.1.2 Chapter organization

The chapter is organized as follows: first descriptions of study area and experimental setup are given(section 7.2); then the methodologies (section 7.3) on control volume discretization (subsection 4.3.1), the input, $J(t)$, estimation at each control volume, and varieties of kriging interpolation methods are discussed (subsection 4.3.2). For the water balance in high resolution models, snowfall needs to be approached differently than rainfall, therefore, snowfall estimation procedures are discussed in subsection 4.3.3.

The results of the performances of the methods, the precipitation estimates at each
control volume, and the conclusions of the study are presented in section 5.4 and 5.5
respectively.

4.2 Study area, data set, and experiment setup

The NewAge system is applied to the Posina river basin. It is a small catchment (116
km^2), located in the the Alpine foothills of Veneto Region in Italy. The basin outlet is at
Stancari (figure 4.1a). Its climate is characterised as wet, with an annual precipitation
of 1645 millimeters and annual runoff of 1000 millimeters (Norbiato et al., 2008).

The basin area is covered by a DEM with a resolution of 20 x 20 metres. In the Posina
area, there are 12 meteorological stations and three discharge gauges. Generally, the
number and type of stations can be considered good for general hydrological applications.
However, all the stations lack other meteorological forcings such as solar radiation, wind
speed, relative humidity, and snow depth (or snow water equivalent). The coordinates
and elevations of the hydro-meteorological stations are reported in table 4.1. The mete-
orological stations provide hourly rainfall and temperature data, and the hydrometer
stations provide the hourly discharge data. The digital elevation map of the Posina river
basin and the distribution of weather measurement stations and hydrometers are shown
in figure 4.1b.

Precipitation and temperature data used for the study cover the period 1994 to 2012
(inclusive). Discharge data are available for all three gauge stations for the same period.
However, due to the lack of observed snow information in the basin, remote sensing data,
particularly MODIS data (Hall et al., 2006), were used for assessing the snow cover. Four
years of daily MODIS snow products (2002/2003, 2003/2004, 2004/2005, 2005/2006 of
winter seasons) are used to calibrate and validate the snow separation component. The
first three seasons are used for snow separation model parameters, while the last one
is used to evaluate the procedures. For the availability of all these data (including the
DEM) and its reproducibility (appendix F).

4.3 Methodology of inputs analysis

The following subsections provides the methods for each input term of the water balance
equation (5.1), which also correspond to the workflow in making the NewAGE systemc
operational.

Table 4.1: List of the meteorological stations and hydrometers used for meteorological (rainfall and temperature) spatial interpolation and rainfall-runoff model calibration and validation analysis in the Posina river basin. The last three stations are maked with a (*) to indicate that these are discharge guaging stations. The areas of the basin and subbasins draining to each hydrometer are given in brackets.

ID.	City	Z	X	Y
51	Folgaria UPO	1168	1668428	5086815
63	Lavarone UPO	1171	1674754	5089860
204	Brustol Velo d'Astico	328	1682121	5074661
206	Contr? Doppio Posina	725	1672938	5075022
208	Molini Laghi	597	1675208	5078024
210	Monte Summano	619	1687964	5069297
212	Passo Xomo Posina	1056	1674012	5071777
214	Pedescala	308	1683840	5079537
216	Valli del Pasubio	600	1672265	5069542
218	Castana Arsiero	430	1679369	5076164
201*	Rio Freddo at Valoje ($22.24 km^2$)	390	1681507	5075248
202*	Posina at Stancari ($116.2 km^2$)	388	1681524	5075140
203*	Posina at Bazzoni ($38.82 km^2$)	453	1678208	5074606

Differently from other approaches (e.g. Garen and Marks (2005)), we are concerned that even the "spatialisation" of inputs requires modeling and the determination of some parameters. These, when necessary, are explicited and characterised with the use of the calibration components, particularly the particle swarm algorithm (Kennedy et al., 1995; Formetta et al., 2014c), included in the NewAGE system.

4.3.1 Watershed partition

Pertinent to our approach is the use of a coarse degree of spatial information, at the level of the hydrologic response units (HRUs). These HRUs groups a set of hydrologically similar points close each other, that are treated as a single unit, on the basis of mathematical, physical or computational arguments. In other words, even if a information can be calculated at pixels level, for instance for exploiting the accurate knowledge of topography, this information is subsequently coarse grained for getting single values for any HRU. The rationale of this choice is to capture the 'meaningful' spatial heterogeneity in the input data and processes, similar to that adopted in other models (Lagacherie et al., 2010; Ascough et al., 2012).
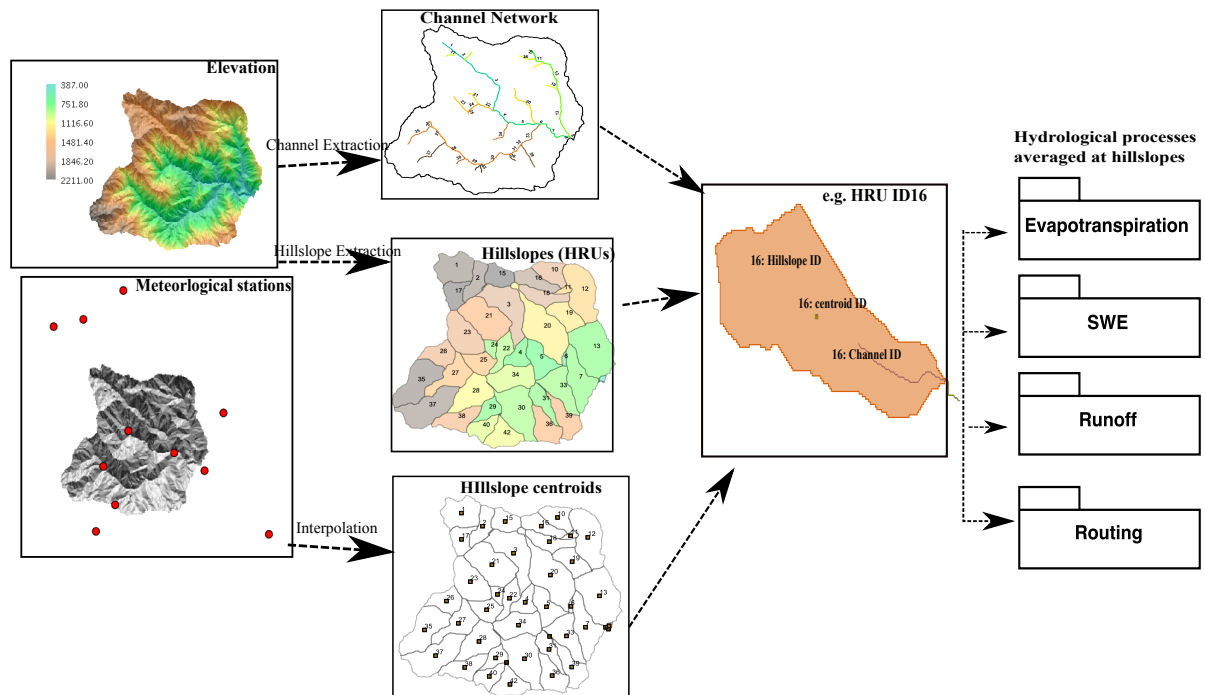
Figure 4.2: The workflow of model set-up for NewAge-JGrass hydrological model system

More specifically, in NewAGE the basin is partitioned into hillslopes and channel
links. This partition (Formetta et al., 2011; Abera et al., 2014) is carried out according
the procedure presented in Formetta et al. (2014c). Each hillslope and link is numbered
according to the Pfafstetter scheme (Formetta et al., 2014a), which defines an identifier
for each link and hillslope, and an order to transverse them.

Eventually, this approach allows the resolution of Eq. (5.1) for any of these units
independently, from the most uphill one to the outlet. However, depending on the process,
the value of each term in the equation can depend on some sub-HRU analysis. The overall
model-setup activities required for different components of the NewAge simulation are
summarised in figure 4.2. The OMS components implemented for the delineation of the
HRUs and the extraction of topographic attributes were described in detail in Abera et al.
(2014). In this chapter, the term hillslope, HRU, and subbasin are used alternatively
for the same basin partitioning concept. A total of 42 HRUs is chosen for the basin (as
depicted in Figure 4.1b). To illustrate the variability of hydrological quantities among
HRUs, a sample of HRUs (four HRUs: Id 1, 4, 13, and 37) are systematically selected to
represent different elevation (elevation ranges from 656 m to 1616 m) and position in
the basin. Hence, further analysis and results at the subbasin scales are shown at those
HRU throughout the chapter.

4.3.2 Meteorological Forcing Interpolation

The NewAge spatial interpolation (NewAge-SI) component takes care of spatial meteorological data at a specific point or in a grid format. It can elaborate data indifferently at hourly, daily, and monthly time steps. Here, NewAge-SI is used to interpolate meteorological variables from meteorological stations to points of interest (centroids of each HRU, or in any cell in the case of a specific grid format over the basin)

According to kriging theory, meteorological forcing measurements (rainfall and temperature), $z_{u\alpha}$, are considered as a particular realization of a random variable ($Z_{u\alpha}$) (Goovaerts, 1997; Isaaks and Srivastava, 1989). Detailed explanations and discussions on these variants of kriging can be found, for instance, in (Germann and Joss, 2001; Haberlandt, 2007; Hwang et al., 2012; Ly et al., 2013, 2011; Ruelland et al., 2008; Ashraf et al., 1997; Buytaert et al., 2006), and are not described in depth here. Before any kriging interpolation is done, an empirical semivariogram model is estimated (Cressie and Cassie, 1993), from:

$$(4.2) \qquad \gamma(h) = \frac{1}{2N(h)} \sum_{\alpha=1}^{N(h)} (Z_u - Z_{u+h})^2$$

where $N(h)$ denotes the set of pairs of observations $N(h)$ at location u and vector h distance apart. This empirical semivariogram may need to be fitted with the theoretical semivariogram to estimate semivariogram model parameters (nugget, sill and range), which are kriging model inputs. Four semivariogram models (exponential, spherical, gaussian, and linear) have been selected and implemented in the NewAge-SI, following (Prudhomme and Reed, 1999) arguments. Their analytical formulation is presented in appendix A. As methods for geostatistical interpolation, ordinary kriging (OK) and its local version, local ordinary kriging (LOK), were chosen (Goovaerts, 1997) for their simplicity. Because many researches have found that incorporating elevation data into the kriging interpolation improves the performances (Lloyd, 2005; Buytaert et al., 2006; Garen et al., 1994) of their models, we also considered detrended kriging (DK) and a local deternded kriging (LDK) (Phillips et al., 1992). This means that a linear, time-varying relationship between elevation and rainfall data is assumed and the fitting line is subtracted from observations. This linear model is regressed automatically by the component at each time step. The kriging is then left to calculate the residuals of the interpolation (e.g. Garen and Marks (2005)).

In order to assess the error of prediction of the estimated data, NewAge-SI offers the possibility of automatically perfoming cross-validation (leaving-one-out or Jackknife-

method; Isaaks et al., 1989), based on removing one data point at a time and performing
the interpolation for the location of the removed point using the remaining meteo-stations.
Finally, for this chapter, kriging is used to generate time series of meterological forcings
for the centroid of each HRU. These forcings, for the purposes of this study, are kept
constant over the whole HRU area.
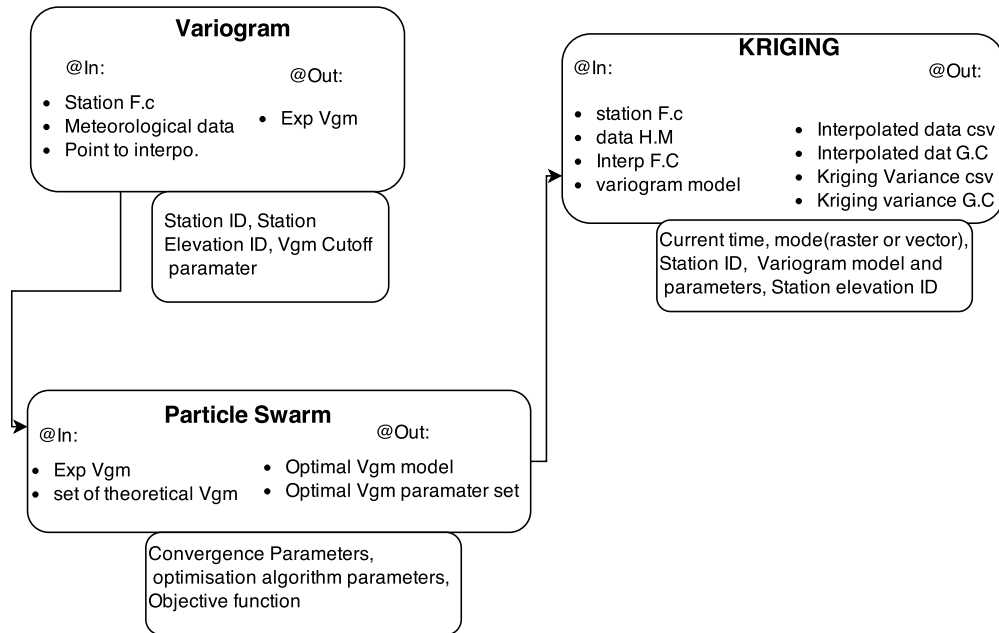
Figure 4.3: The Spatial interpolation component of the NewAge system (SI-NewAge).
The figure shows how different components are connected together, here the variogram
(semivariogram) component solves for the spatial structure of measured data in the
form of an experimental variogram. The particle swarm optimization algorithm uses
the experimental variogram to identify the best theoretical semivariogram and optimal
parameter sets for each time step. Lastly, Kriging uses the best semivariogram model
and optimal model parameters to estimate the meteorological data at the interpolation
point or as a raster for a given basin.

In order to understand the effects of the theoretical semivariogram model on kriging
and to compare the different kriging methods performances, we applied the following pro-
cedures. Firstly, we select a single kriging type (for instance OK) and fit the experimental
semivariogram with a single theoretical semivariogram (for instance, exponential) and
estimate the best semivariogram parameters. Secondly, we perform a cross-validation for
each station, computing estimated time-series forcing values for each (removed) station.
Thirdly, measured and estimated time-series forcing values are compared with GOF
indices (appendix **??**). Lastly, the GOF indices values calculated from 18 years of hourly

forcings (rainfall and temperature) data for each station are statistically averaged for all 12 stations. This procedure is obtained with the OMS-components configuration shown in Figure 4.3. Each of these steps is repeated for all four krigings for any of the four semivariogram models available (for a total of sixteen combinations analyzed). In addition, we developed an iterative procedure that selects a couple of best fitting semivariogram and best semivariogram parameters, time-step by time-step.

For the sake of brevity, the analysis based on automatic selection of the optimal semivariogram model and the best semivariogram model parameters for each time-step was done only for OK.

4.3.3 Snowfall modelling

The aggregated precipitation, J, for each HRU has to be separated into rainfall J_R and snowfall J_S. This is one of the critical tasks for any snowpack simulation, and strongly affects the result of any modelling, even if performed with more sophisticated tools, like SNOWPACK (Lehning et al., 1999) or GEOtop 2.0 (Endrizzi et al., 2014). One possibility is to use a micro-meteorological model, in which the separation comes about automatically, as in WRF (Skamarock et al., 2008). However, the standard procedure in hydrological models is to use simple mathematical expressions based on temperature (e.g. Garen and Marks (2005)). In our case, separation is based on a threshold temperature, T_S. When the HRU temperature is less than T_S, the precipitation, J, tends to be snow, J_S, otherwise it is rain, J_R. Temperature, in turn is modelled as explained in section 4.3.2 above. In NewAge, a smoothing of the threshold is applied as in (Kavetski et al., 2006; Formetta et al., 2014d):

$$(4.3) \qquad \begin{cases} J_R = \alpha_r * \left[\frac{J}{\pi} . \arctan\left(\frac{T-T_s}{m_1}\right) + \frac{J}{2} \right] \\ J_s = \alpha_s * [J - J_R] \end{cases}$$

Where $J[\text{mm t}^{-1}]$ is measured precipitation, $J_R[\text{mm t}^{-1}]$ is the rainfall, $J_S[\text{mm t}^{-1}]$ is the snowfall, $T_s\ [^oC]$ is the threshold temperature, and $m_1[-]$ is a parameter controlling the degree of smoothing. α_r, α_s and $m_1[-]$ are dimensionless coefficients to be calibrated. The calibration of these parameters is very problematic due to a lack of snow data, which in the Posina basin are completely absent. In similar cases, snow parameters (including modelling of metamorphism and runoff) are usually calibrated using discharge measurements, e.g. Li et al. (2012); He et al. (2014). However, here we have decided to calibrate snow on snow data and, therefore, we used MODIS snow

imagery data (MOD10A1 and MYD10A1), which is available globally. The procedures used are described in detail in appendix D. Both the fractional snow cover (FSc) and albedo information were used. The first establishes, pixel by pixel, the fraction of snow cover, the second is used for detecting when snow falls on old snow, which causes an increase in albedo.

At the moment, a manual optimization procedure is used to determine Eq.(4.3) parameters. The objective function used are the so called Accuracy index, AI, and Spearman rank correlation coefficient, ρ_{rank}. The Accuracy index, AI, is given by:

$$(4.4) \qquad AI = \frac{N_a + N_d}{N_a + N_b + N_c + N_d} \cdot 100$$

Where the terms N_i ($i \in \{a, b, c, d\}$) are the number of pixel combinations identified by using the confusion matrix given in table 6.2. The optimization procedures, as outlined in figure 4.4, maximize true positives and true negatives, while minimizing false positives and false negatives, therefore increasing the overall accuracy. This procedure optimizes Eq.(4.3) to estimate snowfall only at locations where MODIS (MOD10A1 and MYD10A1) shows snow data.

Table 4.2: Confusion matrix based on the four possibile results of the snowfall J_s simulation in comparison with the MODIS snow products. The four possibilities are: true positive (a); false positive (b); false negative (c); and true Negative(d).

	MODIS:Yes	MODIS:NO
SWE:Yes	a	b
SWE:NO	c	d

The binary data derived from the FSc does not show snowfall on snowfall. Hence, to include the new snowfall events on pixels already covered with snow, we used the FSc values (i.e new HRU area is covered by snow) and snow albedo. When associated to a precipitation, increase in snow albedo can be interpreted as a new snowfall. Hence, snow accumulation equation (Eq.4.3) is optimized against the FSC and the snow albedo using the Spearman rank correlation coefficient. The Spearman rank correlation (Kottegoda and Rosso, 1997) is used because it provides a means to quantify the monotonic relationship between two variables with no frequency distribution assumption (nonparametric). First, the values of the two variables (in this case snow albdo or FSc and J_s) are ranked, and then the correlation is computed based on the difference in the rankings as follows:

$$(4.5) \qquad \rho_{rank} = 1 - \frac{6.\sum_{k=1}^{n} D_k^2}{n(n^2 - 1)}$$

where D is the difference between the rank of the MODIS data (FSC or snow albedo) and snowfall, J_s, data at the Kth pair, and n is the number of observations. The higher the value of ρ_{rank}, the higher the correlation between J_s and snow albedo. Those parameters producing the highest ρ_{rank} are used to model the hourly time steps of snowfall for each HRU.

The derivation of snow separation parameters for each HRU is possible, however, as is pertinent to the overall analysis of other components of the study, single, global and optimized values of Eq.(4.3) parameters are derived.
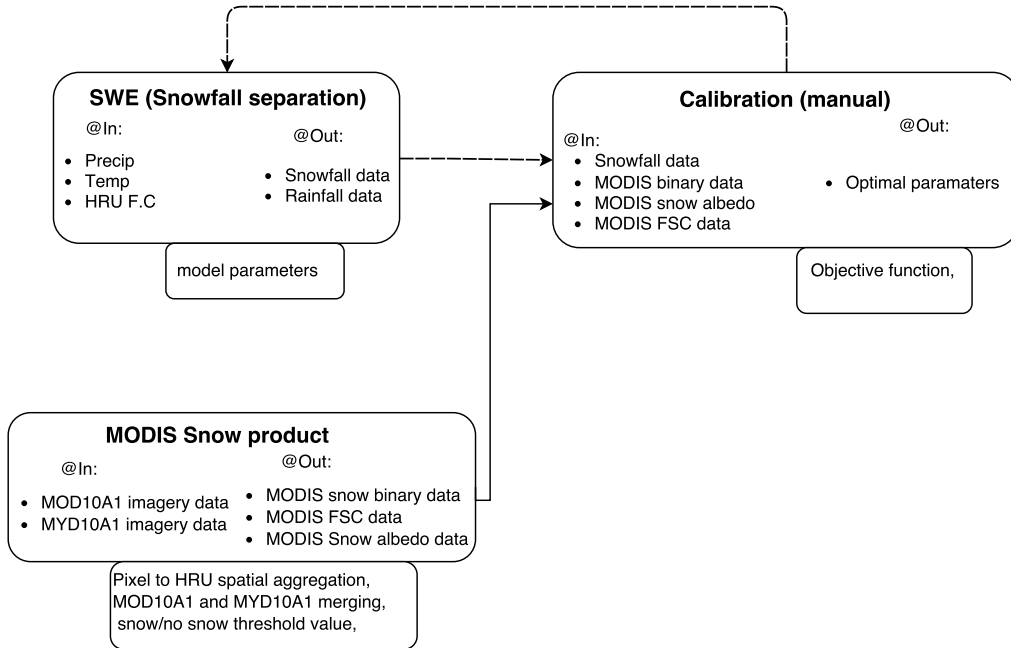
Figure 4.4: The Snow separation component, outlining how the MODIS snow products are used to calibrate the spatial snow accumulation (Eq. 4.3). The dashed line shows the iterative (calibration) process to optimize the equation. Due to the time step differences between MODIS and the separation model output, the manual calibration is preferred in this case.

4.3.4   Net Radiation

Net radiation is necessary for evapotranspiration estimation and for snow modelling. It derives from the local difference between downwelling radiation and upwelling radiation,
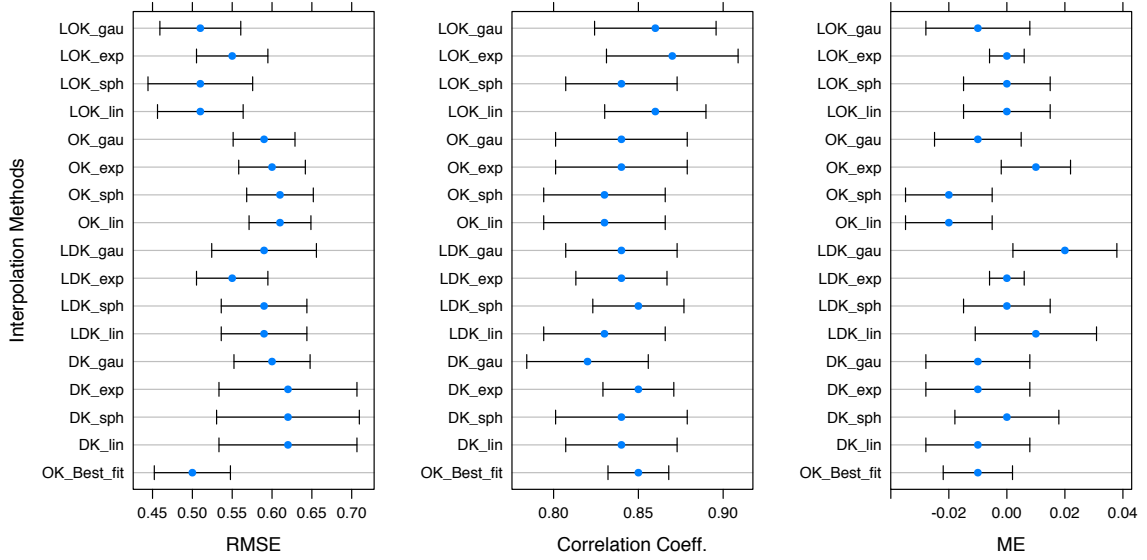
Figure 4.5: The mean performance value in terms of RMSE, correlation coefficient and mean error (from left to right respectively) of all the rainfall interpolation methods considered for this study. The dot in the middle is the mean value, while the length of the line represents the 95% confidence interval with respect to the mean.

and is usually subdivided into shortwave radiation and longwave radiation. Therefore, radiation budgets can be expressed, for any point in the landscape, as:

$$R_n = (1 - \alpha) R_s \downarrow + L \downarrow - L \uparrow \tag{4.6}$$

where R_n [J L^{-2} T^{-1}] is the net radiation, α [dimensionless] is the albedo, $R_s \downarrow$ [J L^{-2} T^{-1}] is the downwelling shortwave radiation, $L \downarrow$ [J L^{-2} T^{-1}] is the downwellling longwave radiation and $L \uparrow$ [J L^{-2} T^{-1}] is the upwelling longwave radiation. For details on R_n estimation, which includes geometric and topographic corrections, and various attenuation factors, please refer to Formetta et al. (2013b). With regards to longwave radiation, this can be estimated by:

$$L \downarrow = \epsilon_{all-sky} \cdot \sigma \cdot T_a^4 \tag{4.7}$$

$$L \uparrow = \epsilon_s \cdot \sigma \cdot T_s^4 \tag{4.8}$$

where $\sigma = 5.670 \cdot 10^{-8}$ is the Stefan-Boltzmann constant, T_a [K] is the near-surface air temperature, $\epsilon_{all-sky}$ [-] is the effective atmospheric emissivity, ϵ_s [-] is the soil emissivity

and T_s is the surface soil temperature. According to **?**, the Idso **??** model can be fruitfully used to estimate Eq.(4.7). It consists in adopting the following form for ϵ_{clear}:

(4.9) $$\epsilon_{clear} = 0.7 + 5.95 \cdot 10^{-4} \cdot e \cdot exp(1500/T_a)$$

where T_a [K] is the air temperature. The paper **?** also provides appropriate site-specific values of Eq.(4.8) parameters, and corrections for the presence of clouds. All of these estimators are implemented as OMS3 components and can be easily invoked inside any NewAGE modelling solution. They are assumed here as acquired and not discussed further.

4.3.5   Other meteorological fields

Other meterological data such as humidity, wind speed, and dew point, which are taken as essential data by Garen and Marks (2005), are not estimated here. However, they could be easily processed and spatially interpolated to the appropriate control volume if available. Their presence or absence greatly affects the modelling methods that can be used for estimating both snow pack evolution and evapotranspiration. For instance, depending on the availability of data, the choice of evapotranspiration tool can switch from the Priestley and Taylor Formula (Priestley and Taylor, 1972) to the Penman-Monteith equation (Penman, 1948; Monteith et al., 1965) or to other models. The snow modelling can also take on different formulations, such as the temperature-index model, which only requires precipitation and temperature data, or the energy-index models, which require more meteorological data inputs, such as shortwave radiation, humidity, and wind speed (Förster et al., 2014; Formetta et al., 2014d)

4.4   Results and discussions

4.4.1   Rainfall estimation, model performances and uncertainty

The overall performance of all the rainfall interpolation algorithms illustrated previously are depicted in figure 4.5. Both RMSE and correlation coefficient results indicate that the LDK and LOK outperform the other two groups of krigings. The LDK and LOK analyses are based only on the nearest five stations for each station. Both LDK and LOK show lower RMSE and higher correlation coefficients following cross-validation analyses (figure 4.5a). The idea that DK improves performance is not clearly visible in

this experiment. This may be due to the small number of stations from which to draw a
trend or to a more complex variability of rainfall at this scale and location. The mean
error value results (figure 4.5c) are not clear and were found to be inconsistent with
reports from the previous two performance indicators. Though the mean error value is
small, it was noticed that the mean error difference is between the kriging methods, not
between the semivariogram fitting within a single model.

It was found (in figure 4.5) that the automatic selection of the best semivariogram
model at each time step provides the lowest RMSE value, high correlation coefficients,
and short confidence interval for both RMSE and correlation coefficients. Though the
differences between all the kriging methods are relatively small, analysis of the variance
(one-tail ANOVA gives $\rho = 0.018$) test shows that the mean difference between methods
is significant.
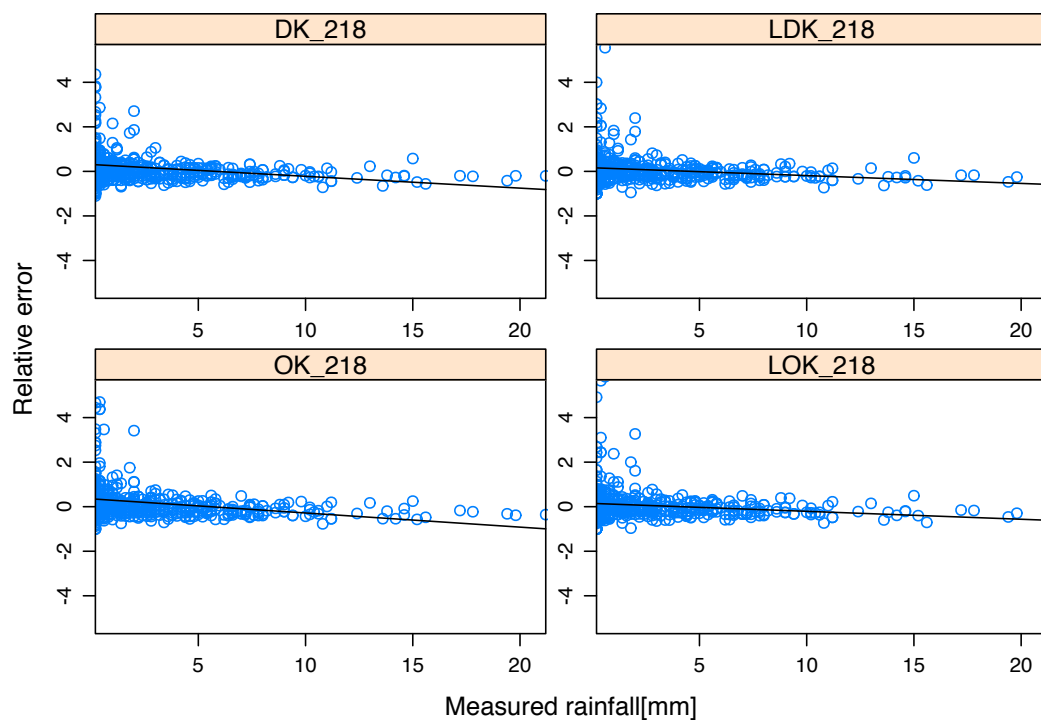
Figure 4.6: The scatterplot of measured rainfall and normalized (relative) errors of
different kriging interpolation methods for station ID 218. The kriging percentage error
analysed for the whole dataset is calculated to be 4.5%.

To briefly describe the nature of errors in relation to rainfall intensity at the mea-
surement stations, we used the forecasting errors that can be estimated from the leave-
one-out method. Due to the different effects of high rainfall magnitude and low rainfall

magnitude, the absolute residual analysis could not provide a clear bias of estimation. We used the relative error (interpolated minus measured rainfall values divided by measured rainfall values for each time step). Figure 4.6 shows that the relative residuals distributed across zero, with a relatively higher dispersion for small values. It is also estimated that, at a point location, the kriging estimation error (about 4.5% for non-zero rainfall values) is comparable to the rain gauge measurement errors reported in literature at hourly time-steps (Habib et al., 2001; Ciach, 2003). We also analysed the performances of the four kriging models plotted against elevation, as shown in figure 4.7. For all the kriging methods, the performances resulted lower for stations located at high elevations. All methods are competitive across different elevations, with slightly better behaviour from LDK and LOK in middle and higher elevation stations. Similar results are reported in Verworn and Haberlandt (2011); Tobin et al. (2011).
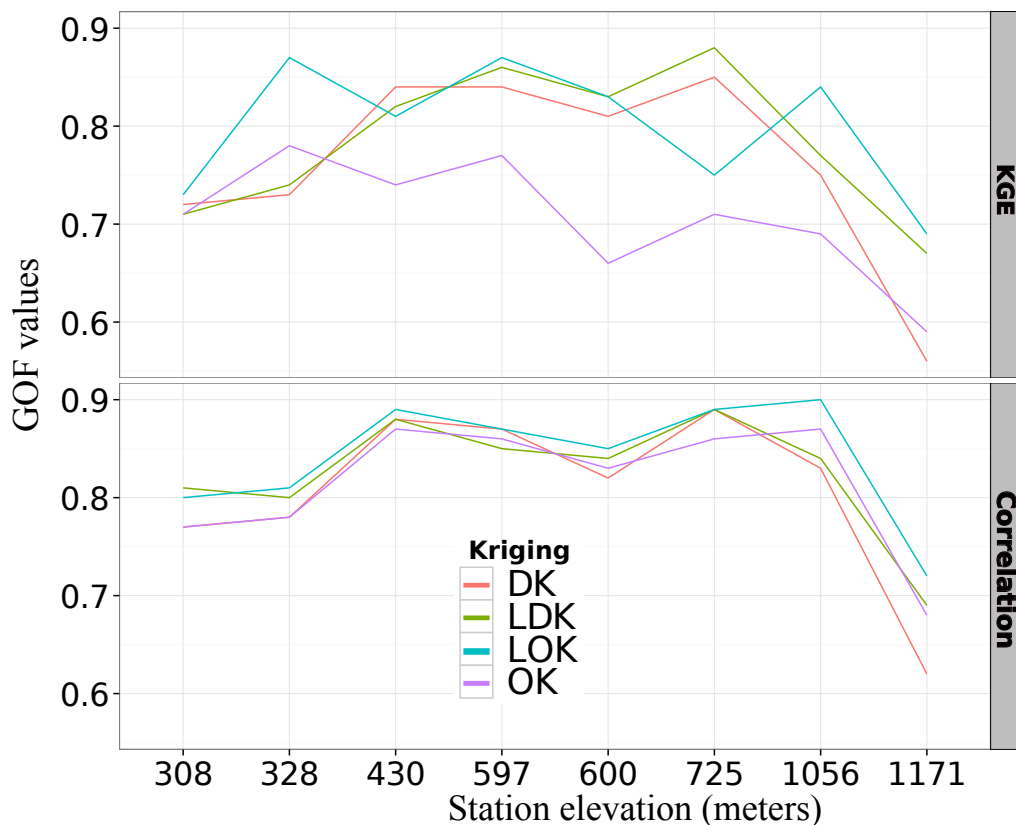
Figure 4.7: Plot of the four kriging model performances (as measured by KGE, on top, and correlation, on the bottom) and elevations of the measurement stations.

We used kriging to estimate errors spatially (Phillips and Marks, 1996). We analyzed multitemporal maps of kriging estimates and kriging errors for some events and obtained
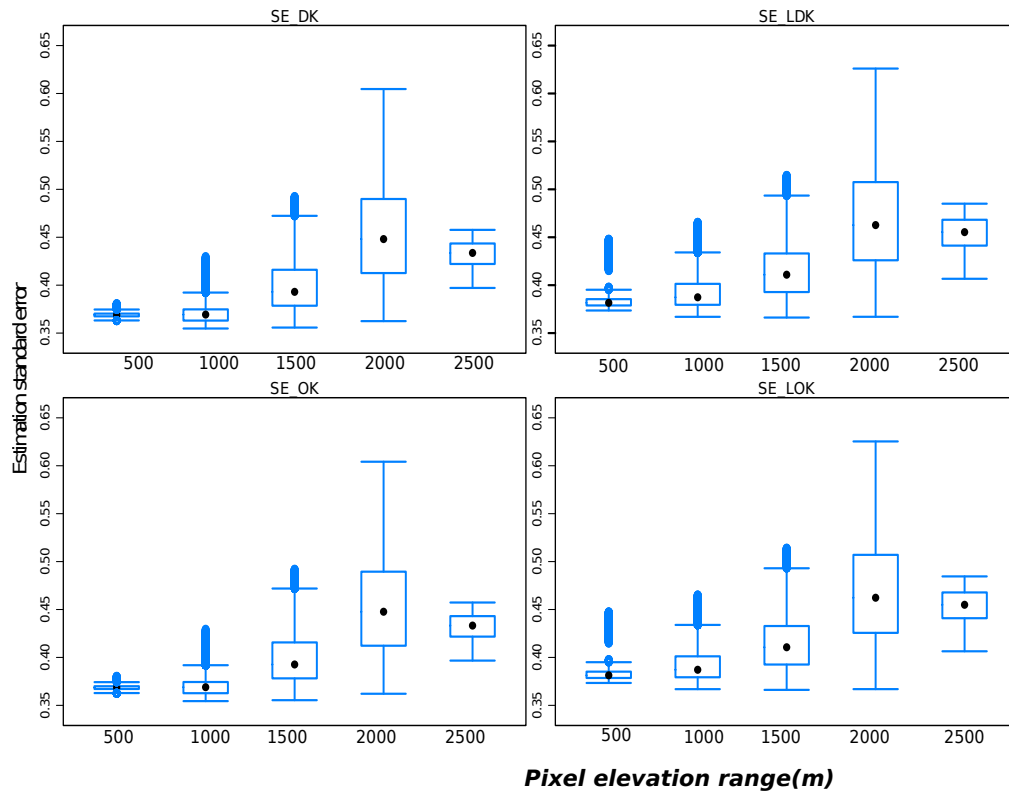
Figure 4.8: The spatial distribution of the standard error of rainfall estimate (in mm).
The plot shows the distribution of the kriging standard error across elevation. OK_SE is
the standard error for the OK estimate ($R^2 = 0.44$), LOK_SE is the standard error for
LOK ($R^2 = 0.37$), DK_SE is the standard error for DK ($R^2 = 0.44$), and LDK_SE is the
standard error for LDK ($R^2 = 0.37$). There is a clear difference between the local and
universal ordinary kriging in that the two local krigings reduce the standard error with
relation to elevation.

an inverse relationship between rainfall intensity and errors, with larger errors for lower
values of rainfall (in absolute term). As an example, the maps in figure 4.9 are shown. We
also found a slight correlation between elevation and kriging standard error, as shown
in figure 4.8 where the boxplot of the kriging standard error is reported for a time step
$(2003 - 11 - 26\ 11:00)$.

For use in conjunction with the runoff module, we had to aggregate the rainfall
estimate at the subbasin level, by assuming the centroid as representative of the en-
tire subbasin. This operation was repeated for each time step, and shown for a time
instant in figure 4.10. The aggregation still maintains a relevant spatial difference in
rainfall distribution. The variability in cumulative rainfall between the subbasins for
the represented event is more than 70 mm, and it is evident that rainfall is higher in the
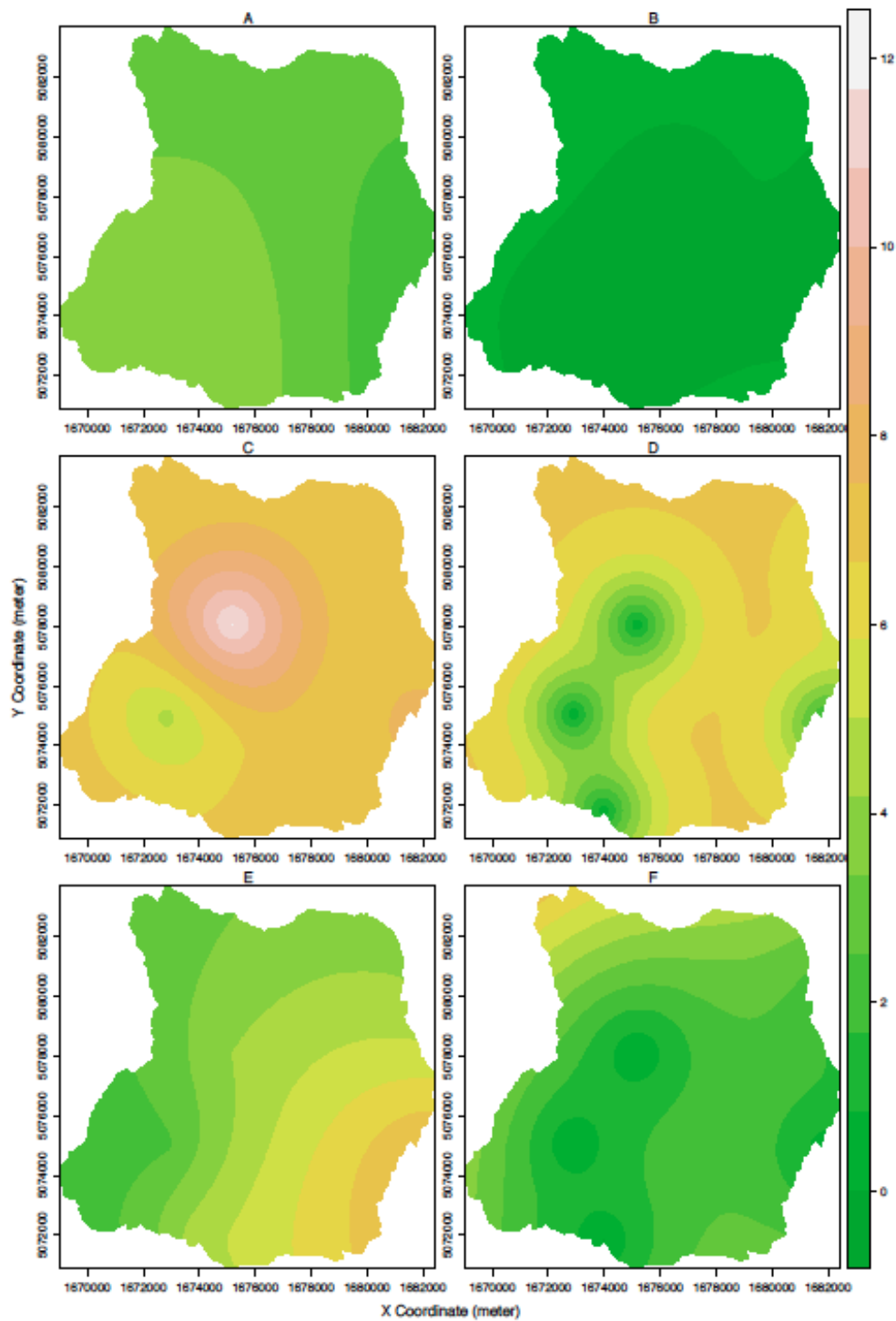
Figure 4.9: The spatial distribution of estimated rainfall (LOK kriging), on the left, and the kriging standard error, on the right. From top to bottom different time steps are represented, 2003-11-26 22:00, 2003-11-27 18:00 and 2003-11-28 04:00.
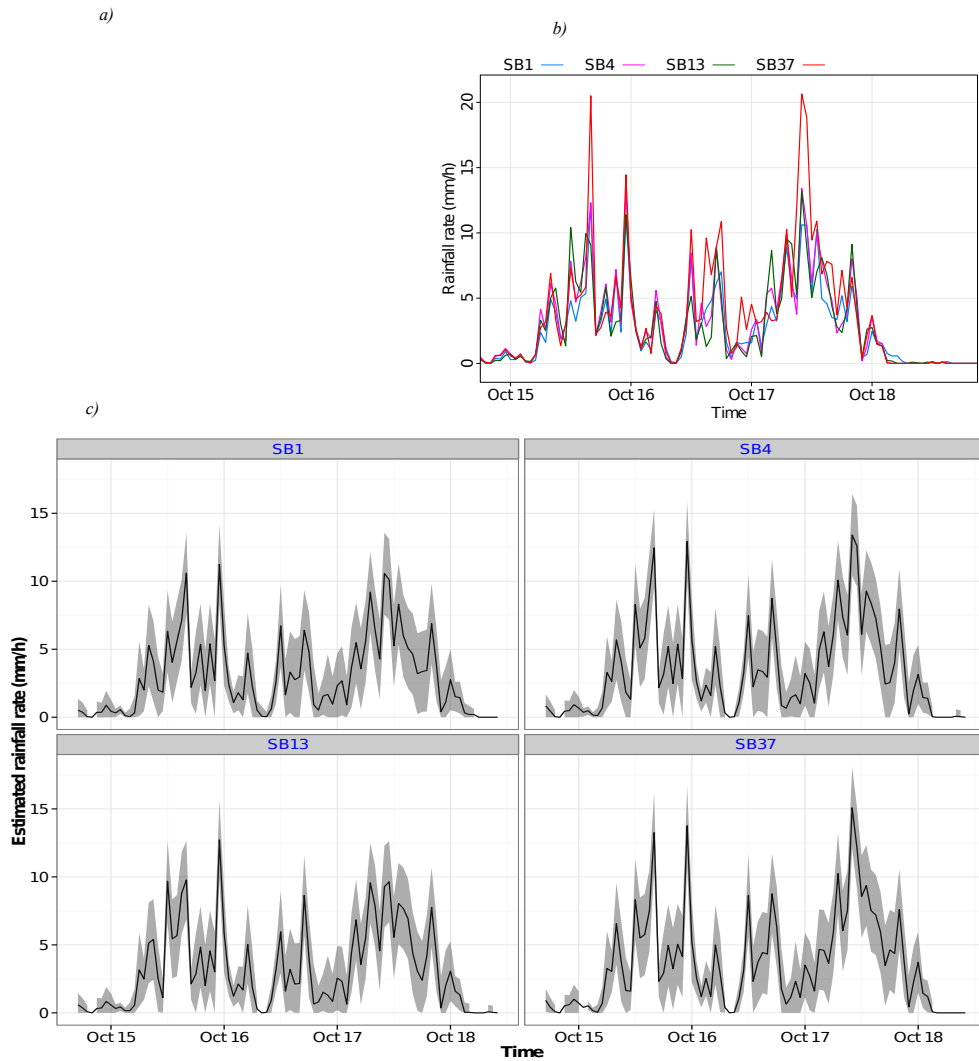
Figure 4.10: Spatial rainfall variability in an aggregated subbasin approach: (a) variability in the estimated total rainfall (the code number in the subbasin represents the subbasin number, while the color shows the total rainfall distribution), (b) comparison of four selected time series of subbasin rainfall estimates, and (c) further analysis on the kriging estimation error used to estimate the confidence interval of the estimates for some selected subbasins. The analysis is based on the Oct. 16, 1996 event.

south-western part of the basin (figure 4.10a). Figure 4.10b shows the rainfall variability for four selected subbasins (subbasin 1, 4, 13, 37) along a limited time-window. As a product of the Kriging procedure, the time-varying errors in rainfall can be estimated. Figure 4.10 shows the 95% confidence interval in grey.

4.4.2 Temperature estimation and error bounds
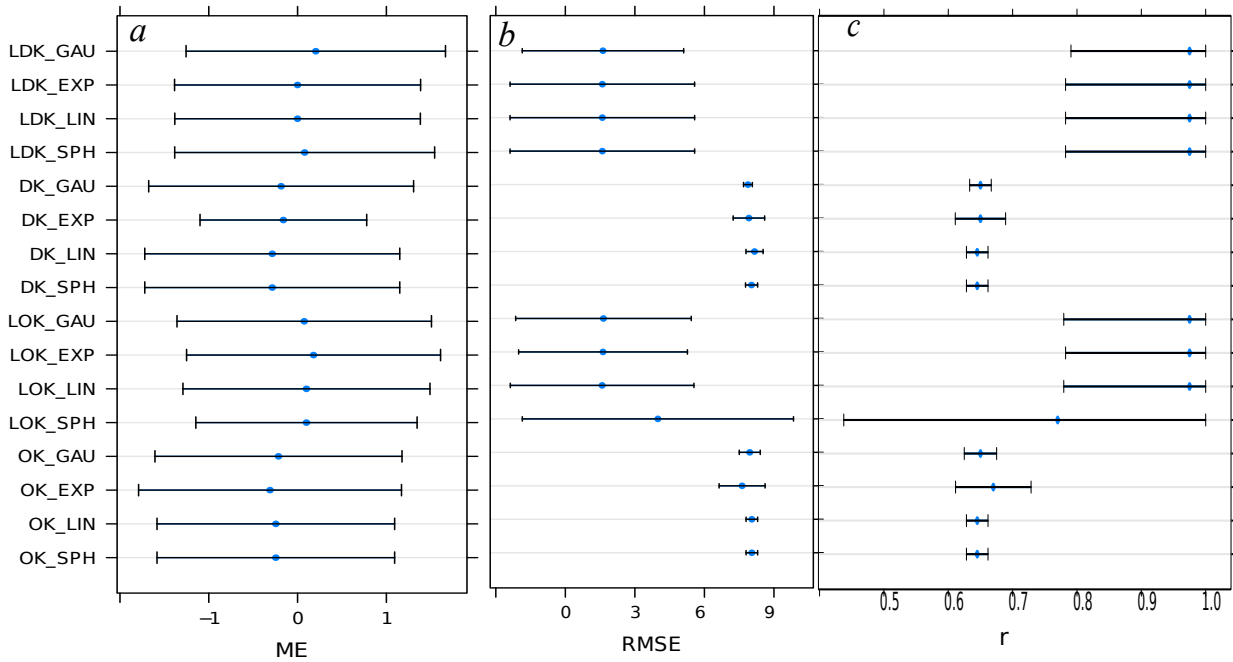
Figure 4.11: The mean performance value of temperature interpolations in terms of mean error (a), Root mean square error (b), and correlation coefficient (c) for all interpolation methods considered for this study. The dot in the middle is the mean value, whereas the length of the line shows the 95% confidence interval with respect to the mean.

Temperature forcing is an input for the next two components (Snow and ET) of the water balance. Hence, it is important to examine the spatial interpolation performances. Similarly to the rainfall interpolation comparison, the relative performances of the four kriging models (with four semivariogram model fitting each) are compared in terms of two error statistics (ME and RMSE) and the correlation coefficient (r). All three goodness-of-fit indices show that (figure 4.11) LOK and LDK are performing better than OK and DK. The ME is 0.0 ± 1.3 and 0.1 ± 1.4 for LDK and LOK and -0.23 ± 1.4 and -0.24 ± 1.3 for DK and OK respectively, indicating that the use of only nearby stations enhances temperature estimation performances. The cross-validation of temperature estimates shows that DK and OK have negative mean errors, while the local versions (LDK and

LOK) have almost no bias. The RMSE of LOK and LDK is lower (about 2.6 ± 3.25) than
DK and LDK (about 8.25 ± 0.5). Similarly, the four kriging interpolations comparison
using r shows that LOK and LDK are higher than DK and LDK. In general, figure 4.11
shows that the effects of semivariogram models for kriging temperature estimations
are minimal. Comparing with the rainfall estimation performances, the LDK and LOK
kriging temperature interpolation performances are relatively better($r = 0.97 \pm 0.03$, and
$ME = 0.05 \pm 1.35$).

For snow modelling purposes, we have several options for sampling HRU temper-
ature. One option is to further divide HRUs into different elevation bands. However,
considering the HRU size partition and the relatively smooth nature of temperature data,
the temperature at the centroids of each HRUs is shown to be a sufficiently realistic rep-
resentation of the physical phenomenon. This can be assessed by examining all the grid
temperatures inside each HRUs. To this scope, figure 4.12 shows the standard deviations
of temperature fields within each HRU, more precisely, the mean standard deviation of
temperature fields distribution for each HRUs against their elevation, averaged for 120
temperature maps, sampled for all the seasons across all the years. The boxplot shows
that the temperature distribution for most of the HRUs is mostly contained in half of a
degree centigrade. This validates the use of single location estimates (with high savings
of computational time) as representative values.

A sample of time-series temperature estimation for selected subbasins (1,4,13, and 37)
is shown (figure 4.13) as an analysis of internal subbasin variabilities. It shows estimated
time-series temperatures for selected HRUs with error bounds, where the errors are
the sum of the estimate errors, as derived from kriging and from the approximations
made with the sampling procedure. The result shows that the sampling error within
HRU is much smaller than the kriging interpolation error. There is pattern indicating
that HRUs at high elevations (e.g. HRU 1) have higher error bands than HRUs at low
elevations (e.g. HRU 4).

4.4.3   Snowfall estimates

The rainfall and snowfall separation equation (Eq.4.3) is calibrated using MODIS snow
data. Table 4.3 shows the optimal model parameters obtained.

A sample of MODIS maps and the spatial snowfall is shown in figure 4.15. For
instance, in the first column of map (11-11-2002) both the MODIS FSc and albedo tell
that, on this particular day, though there is precipitation, the surface is snow free; and
so does the model. However, on the next day (12-11-2002), the MODIS imagery data
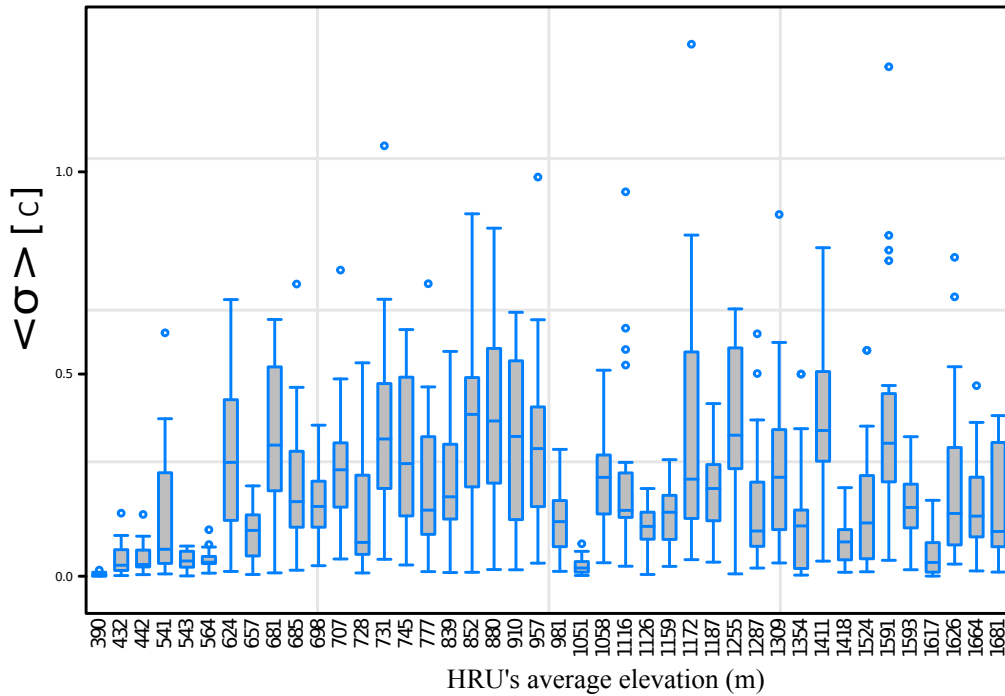
Figure 4.12: box-and-whisker plot of standard deviation of temperature field distribution within each HRU, plotted against their mean elevations. The median HRU temperature standard deviation is indicated by a horizontal line inside the boxes for which the range is determined by the 25th and 75th quantiles. The upper and lower whiskers represent the 95% confidence interval distribution of the Inter-quartile range. Each box of the plots is calculated from 120 temperature maps sampled from all the seasons across all the years. It clearly shows that temperature spatial variation as given by LDK is limited in each HRU to a less than half a degree.

shows that in some parts of the basin, the surface is covered with some level of snow. The model started separating the precipitation into snowfall and rainfall in this day, and the spatial distribution is consistent with the MODIS data. Note that where MODIS shows no snow, the model estimated very light snowfall that could be approximated to zero (figure 4.15, first column). It is also important to note that after the new snowfall that can be captured by MODIS, fresh snowfall on the snow surface can be depicted by the increase in FSc, which is an increase in the area of snow cover for each HRU, and albedo, which shows fresh snowfall. Figure 4.15 (third column) shows snowfall in the middle of the snow season, on 01-02-2003, as depicted by the FSc and albedo. Clearly, the basin is covered in snow, and the model also estimated spatially consistent snowfall.

For many reasons, such as the difference in MODIS and model time steps and spatial units, the spatial consistency between MODIS and the snowfall model is not very high, as
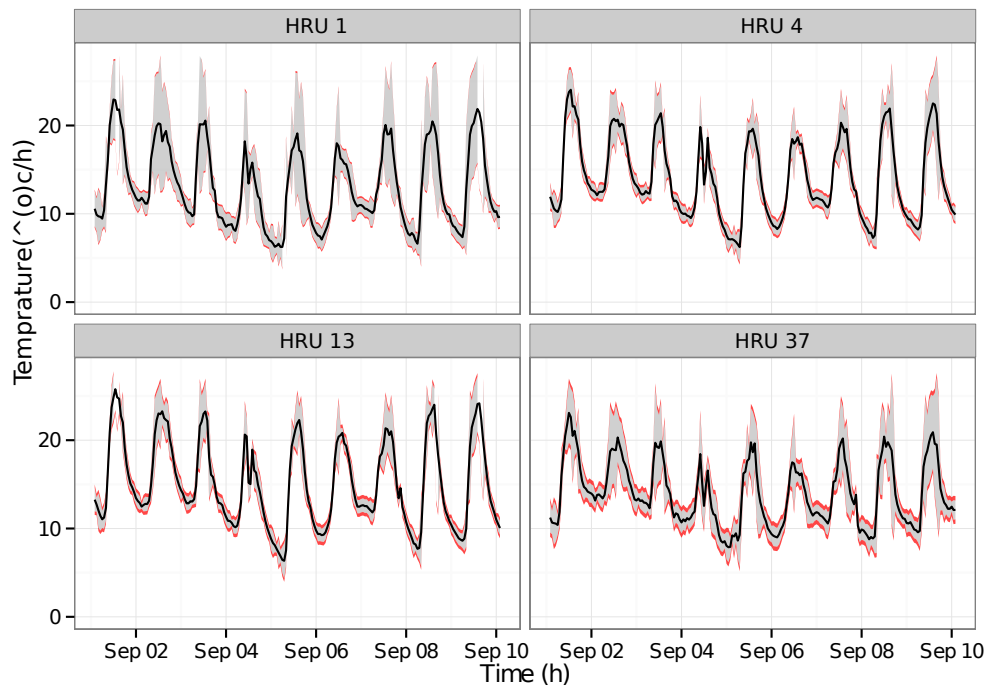
Figure 4.13: Estimated time-series temperatures and associated kriging estimates and
sampling errors for selected subbasins (1,4,13,37) for sept 1-10, 2002.The solid black line
shows the estimated temperature values, the gray area is the estimate plus or minus the
kriging standard errors, and the red area shows the sampling errors associated to each
HRU, as derived in figure 4.12.

described below. At basin scale, however, the approach is helpful to maintain some level
of spatial consistency. The estimated snowfall value mimics the spatial distribution of
the FSc and the snow albedo data. It was not possible to obtain similar spatial variability
using discharge data.

Table 4.3: Snowfall separation model optimized parameters using MODIS data

Parameters	$\alpha_r[-]$	$\alpha_s[-]$	$T_m[^oC]$
Values	1.08	1.05	1.94

As described in the previous section, there are slight decreases in temperature at
higher elevation HRUs, leading to more snowfall and higher spatial variability, even
in such a small basin. However, the relationship of the MODIS snow product with
topography is neither linear nor strong. Topographical complexities (such as slope,
aspect, wind speed, shading, and vegetation) might be suggested as responsible factors

for this non-linearity.

The time series of precipitation separation into rainfall and snowfall for the Feb. 21-22, 2004, event for the four selected HRUs (1,4,13,37) is shown in figure 4.15. It is interesting to observe that the variability in the partition into snowfall/rainfall from hour to hour during the same event. The spatial variability in snowfall (or the snowfall/rainfall ratio) between the different HRUs is also appreciable.

The overall performances of the snowfall separation model during the calibration and evaluation period is presented in table 4.4. The accuracy index between the snowfall estimate and the MODIS snow binary data during the calibration and validation period is 60% and 45% respectively. From a statistical point of view, the performances can be considered reasonably acceptable. These accuracy values can also be seen from the perspective of 85% of global accuracy of the MODIS snow product itself (Parajka et al., 2012). Hence the 60% of binary mapping accuracy is considered acceptable for the long term water balance analysis in this study. This could also be due to differences in the temporal and spatial scale between the model and MODIS data.

The rank correlation result of modelled snowfall with MODIS snow albedo and FSc, maintaining the 60% binary accuracy, is 0.41 and 0.52 respectively. This correlation value is considered to be of medium performance (Kottegoda and Rosso, 1997) . The performance of the rank correlation decreases during the validation period, as shown in table 4.4. However, it can still be considered to be in the medium performance range.

Table 4.4: ρ^1_{rank} and ρ^2_{rank} are the rank correlation coefficients between the model snowfall and the MODIS Albedo and FSc respectively. The calibration period covers the 2002/2003, 2003/2004,and 2004/2005 snow seasons, and the validation period is for the 2005/2006 snow season.

Period	AI	ρ^1_{rank}	ρ^2_{rank}
Calibration	60%	0.41	0.52
Validation	45%	0.34	0.37

It is clear that uncertainty is introduced in the snowfall estimates from both the precipitation and temperature data. In this study, the best performing temperature and precipitation estimation at each HRU is used to predict the snowfall estimate. If a different estimation approach is usedrather than ours, the new precipitation and temperature data sets need to be used to calibrate the rainfall-snowfall separation algorithms to optimize the model result with the MODIS snow data. Generally, therefore, the uncertainty due to the errors in the inputs data for the snowfall estimation algorithms (precipitation
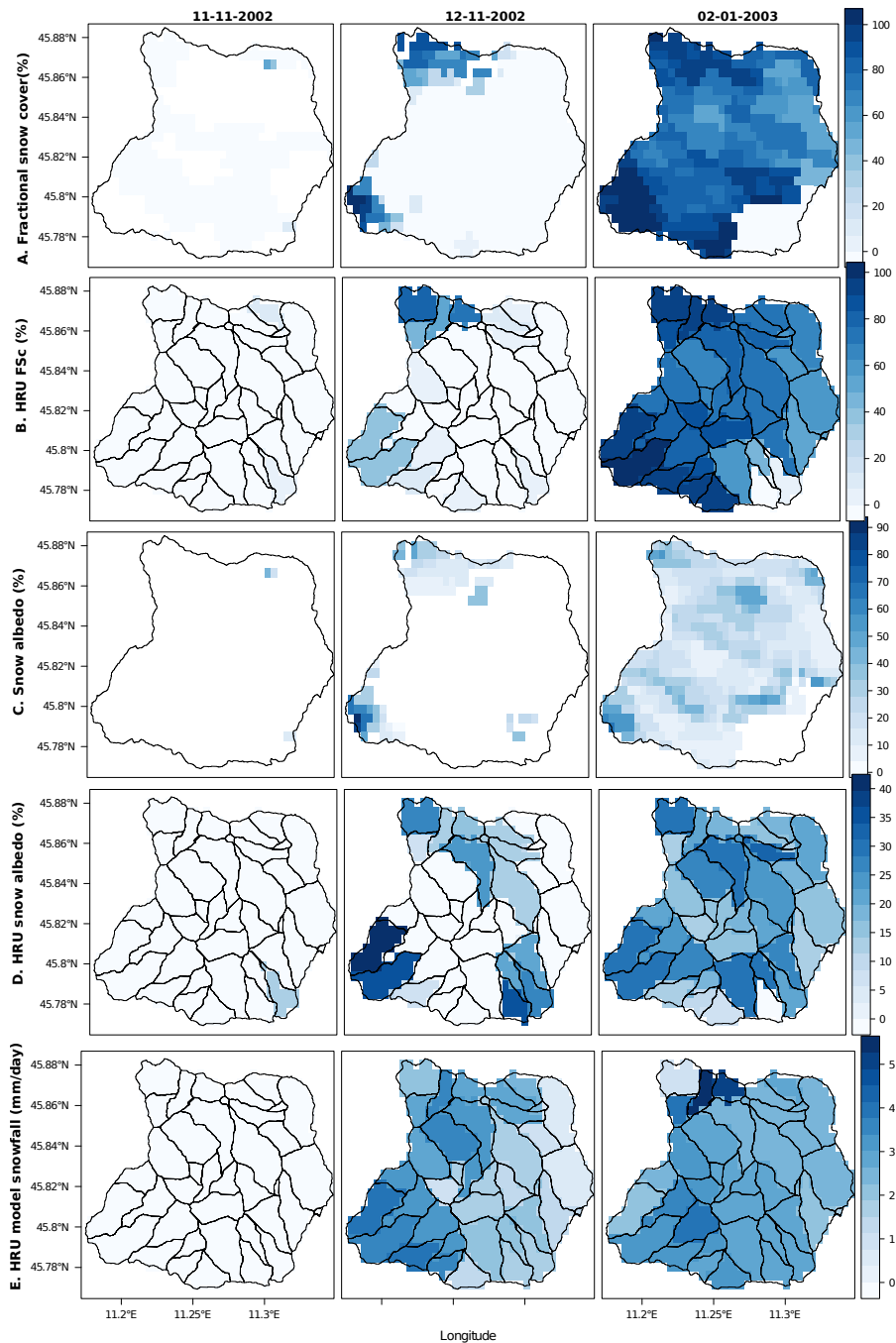
Figure 4.14: The Spatial distribution of MODIS fractional snow cover extracted from
both Terra and Aqua products (a), fractional snow cover aggregated into the HRUs (b),
MODIS snow cover albedo derived from both Terra and Aqua products (c), snow albedo
aggregated into HRUs (d), and HRU snowfall estimated using the separation algorithms
(e) for three days (11-11-2002, 12-11-2002, 02-01-2003).
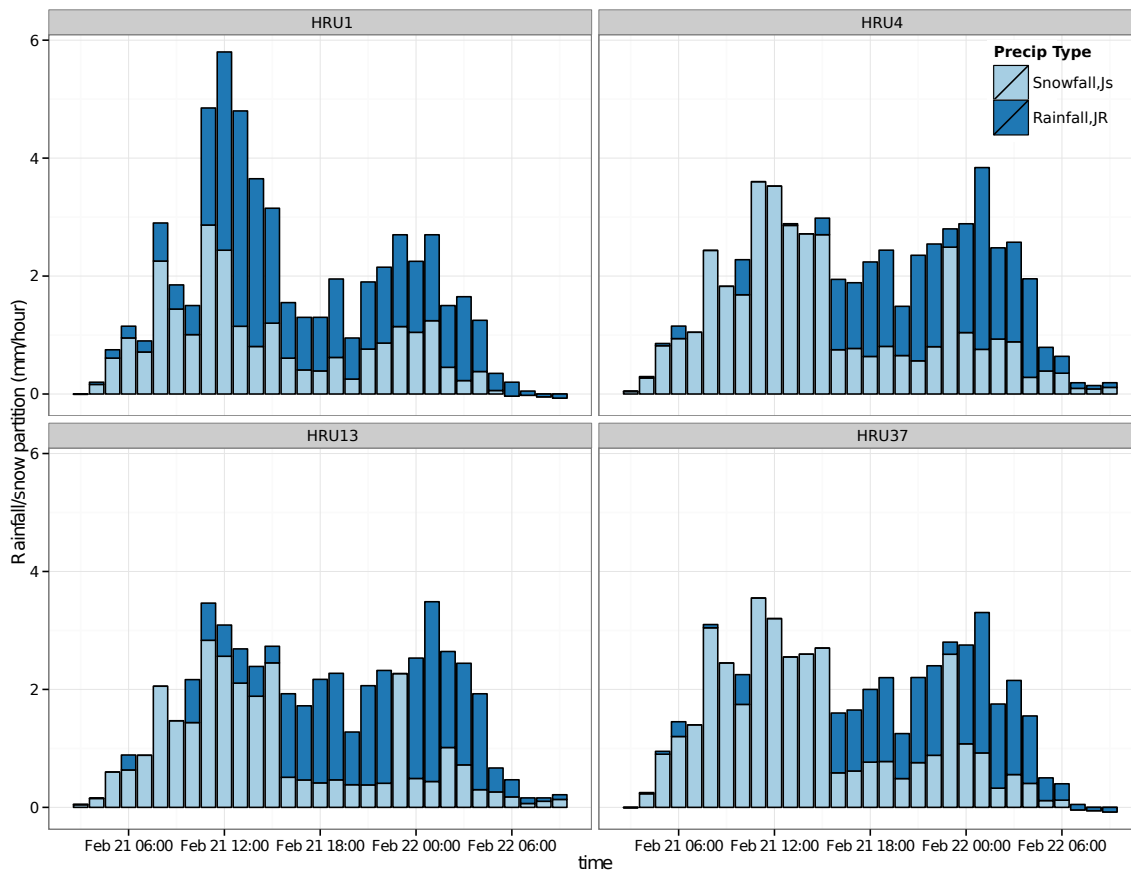
Figure 4.15: Comparison of time series snowfall separation estimates during the Feb. 21-22, 2004 event for four selected HRUs (HRU 1, 4, 13, 37). Modeling at HRU level, which is the aggregation of each point within the HRu that can be characterized by pure snowfall or pure rainfall or snow-water mix event, the water-snow mixing is more physically and statistically meaningful.

and temperature) is expected to be very small. Spatially, the precipitation and temperature kriging estimation errors for HRUs increases with elevation, as portrayed in figures 4.8 and 4.13. Comparatively, the HRUs at higher elevations have higher uncertainty of the snowfall separation model than the HRUs at lower elevations. More important factors that may be responsible for higher uncertainty in snowfall estimates in this approach could be high wind-induced undercatch precipitation during snowfall events and MODIS snow data error.

4.5 Summary and outlooks

In this study a series of procedures and methods are developed and deployed to estimate
the inputs necessary for a basin's water budget. These range from the topographic deline-
ation of control volumes at which the budget is estimated, to the spatialisation of input
forcings, to the separation of rainfall and snowfall. For each of the hydrological quantities
produced, an estimate of the errors made (assuming perfectly correct measurements)
has been performed. We have taken care that each operation is reproducible by sharing
the tools and some of the data we used.

Considering the Posina river basin, a small basin in Northeast Italy, this study
tested the performances of different kriging interpolation and semivariogram choices on
the estimations of rainfall and temperature. The study suggests that the effects of the
semivariogram model on small scale basins is minimal and that the main difference in
kriging performances is between the local and universal kriging versions, i.e, the LOK
and LDK perform better than the OK and DK. This result is true for both precipitation
and temperature data. However, the procedure we used allows for automatic selection of
the semivariogram at run-time, by performing a best-fit of incoming measures of rainfall
data.

Regarding temperatures, it has been assessed that, as long as HRUs remain of limited
extension, sampling the temperature at the centroid of the HRU does not imply large
errors. If larger HRUs are chosen, more temperature estimates can be easily used instead
.

Rainfall/snowfall separation has been obtained by means of a simple model taken
from literature, whose parameters are calibrated using MODIS snow albedo and snow
fractional cover data. This procedure, albeit relatively simple, is, to our knowledge,
completely new. Calibrated parameters that can be made to vary spatially, can be used
to produce rain-snow separation even when data are missing. Given the availability of
MODIS data at a global level, this procedure is also highly transportable to any region of
the world. Also in this case, calibration and validation are made easy by the modularity
of the NewAGE system.

Chapter 5 will illustrate how to use the spatial-field, time-varying, inputs presented
in this chapter for the estimation of water budget outputs, i.e. discharges and evapo-
transpiration and water storage. The assessment of input errors will be propagated to
estimate the uncertainties in water inputs.

ESTIMATING WATER BUDGET AND THEIR VARIABILITY AT THE BASIN SCALE WITH NEWAGE-JGRASS: OUTPUTS AND STORAGE COMPONENTS[*]

In this chapter, using the input component estimated in chapter 4, different components of NewAge-JGrass model system are calibrated for optimal estimation, and are used to resolve the basin water budget. At hourly time steps, 18 years of snow water equivalent, runoff, ET simulations has been conducted, and the model performances are acceptable. The simulation of hourly time scale and small spatial scale enable water budget closure at any given location and time. Aggregating at long temporal scale, for Posina river basin, the mean annual water budget is about 1269 ± 372 mm (76.4%) runoff, 503.5 ± 35.5 mm (30%) evapotranspiration, and -50 ± 129 mm (-4.2%) basin storage from the basin rainfall 1730 ± 344 mm. The highest variability is shown for precipitation, J, followed by discharge, Q. ET shows less interannual variability and less dependent on precipitation.

5.1 Introduction

The terrestrial water balance modelling at various scales using an appropriate control volume k requires to solve the water balance equation which is given by:

$$(5.1) \qquad \frac{\partial S_k(t)}{\partial t} = J_k(t) + \sum_{i}^{m(k)} Q_{ki}(t) - ET_k(t) - Q_k(t)$$

for an appropriate set of elementary control volumes, k, connected together. In Eq. (5.1) S [L^3] represents the total water storage of the basin, J [L^3 T^{-1}], AE_T [L^3 T^{-1}], Q [L^3 T^{-1}] are precipitation (including snowfall), evapotranspiration, runoff (surface and groundwater) respectively. The Q_{ki}s represent input fluxes to the k HRU coming from the set of $m(k)$ HRUs conencted to it, and are of the same nature of Q. The modelling framework set-up which enable to solve the equations at each control volume, and "input" term (J [L^3]) of Eq.(5.1) is analysed in chapter 4. Hence the main focus of this chapter is to estimate the "output" terms of the water budget equation i.e the ET [L^3 T^{-1}], Q [L^3 T^{-1}] and S [L^3], and estimate the long term space-time variability of the water budget in a small basin of Italian Prealps, where snowfall is a non negligible part of precipitations. of precipitations.

5.1.1   Literary review

Recent efforts on the estimations of water fluxes and storages are based on very diverse strategies and aimed to different purposes. Applications involves: the use of data (Hirschi et al., 2006; Becker et al., 2011; Rodell et al., 2004); the use of hydrometeorological data coupled to satellite measurements (Wang et al., 2014b; Woo, 2007; Wang et al., 2014a); stochastic approaches, as by Rodríguez-Iturbe and co-workers (Rodríguez-Iturbe et al., 2006; Rodríguez-Iturbe and Porporato, 2004; Botter et al., 2007; Caylor et al., 2006; D'Odorico and Porporato, 2006; Tamea et al., 2009; Laio et al., 2001; Settin et al., 2007). In some other cases process-based hydrological models such as GEOtop (Rigon et al., 2006; Endrizzi et al., 2013) and tRIBS(Tucker et al., 2001; Ivanov et al., 2004), PARFLOW(Kollet and Maxwell, 2006), CATHY(Camporese et al., 2010) are used. They have a detailed control on the physical processes (e.g. Noto et al., 2008; Liuzzo et al., 2009; Bertoldi et al., 2006; Kunstmann et al., 2013) to return the water budget with great accuracy over the elements of a grid. However, these detailed approaches, often confined to small areas, are data demanding and computationally intensive. Trials to assess the water budget within a modeling strategy of sound intermediate complexity, and reasonable computational demands are represented by models like LISFLOOD (Van Der Knijff et al., 2010), mHM (Samaniego et al., 2010), VIC (Liang et al., 1994), SWAT (Arnold et al., 1998).

5.1.2 Objectives
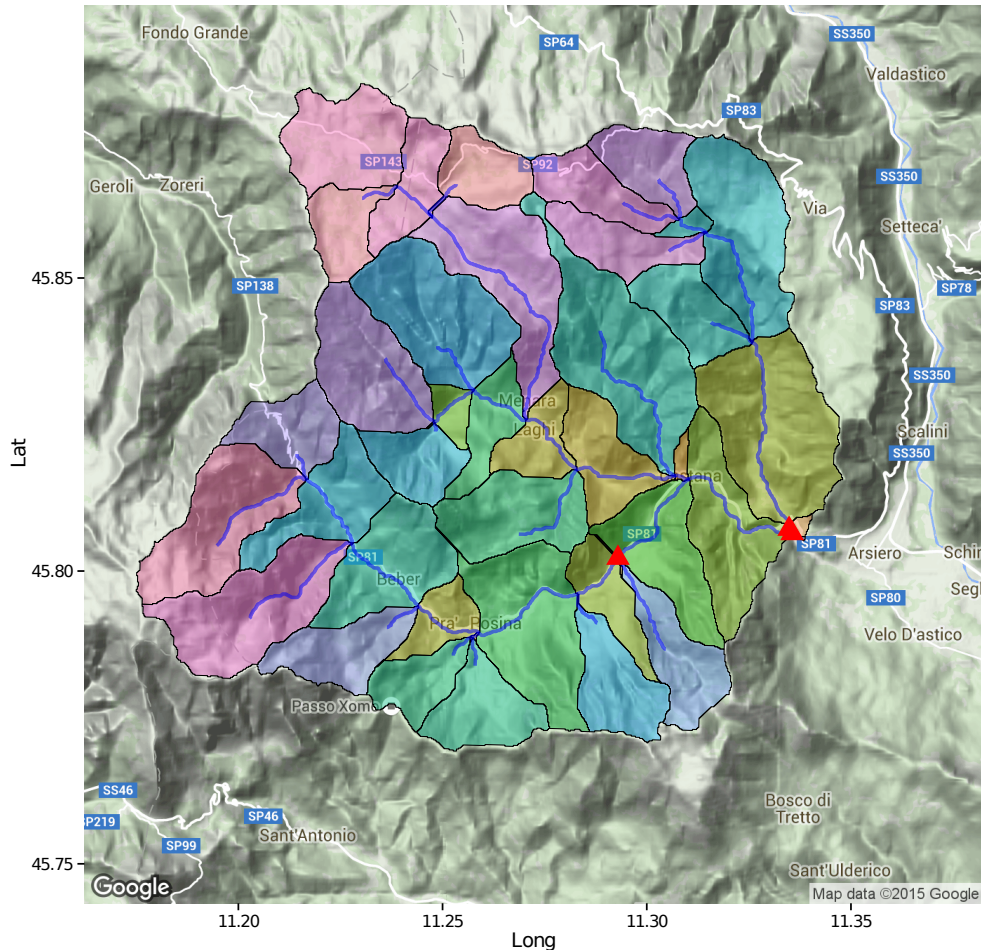
Figure 5.1: Posina basin and the HRU partition used for simulation. The triangle points are the discharge measurement stations. The location and elevation of the basin is described in 4

Learning from all of these various efforts, in this chapter we pursue the assessment the hydrological budget with the modelling system JGrass-NewAge (from now on, simply NewAge), which offers a set of model components built accordingly to the Object Modelling System version 3 (OMS) framework (David et al., 2013). OMS, modelling framework based on component-based software engineering, uses classes as fundamental model building blocks (components) and uses a standardized interfaces supporting component communication. In OMS3, the interaction of each component is based on the use of annotations. This enable model connectivity, coupling and maintaining easy and fast (David et al., 2013).

NewAge covers most of the processes involved in the water budget and its components were discussed with detail in: Formetta et al. (2011, 2013a); Formetta (2013); Formetta et al. (2013b, 2014c), and they are not fully re-discussed here. Components that can be used in various combinations inside of NewAge are shown in Table 5.1.

Table 5.1: NewAge-JGrass Hydrological modelling components. It ranges from hydrological pre-processing such as topography hydrological conditioning to automatic model parameter optimization components. The components in bold are the ones used in this study

Role	Component Name	Descriptions
Basin hillslope-link partitioning	**GIS spatial toolbox and Horton Machine**	A GIS spatial toolbox that uses DEM to extract basin, hillslopes, channel links for JGrass-NewAge set-up. The channel partition is according to pfafstetter enumeration system ((Formetta et al., 2014a), chapter 2)
Data interpolations	**Kriging**, Inverse Distance Weighting, and JAMI	Interpolates meteorological data from meteorological stations to points of interest according to variety of kriging algorithms (Goovaerts, 2000; Haberlandt, 2007; Goovaerts, 1999; Schiemann et al., 2011), Inverse Distance Weighting (Goovaerts, 1997) and JAMI(Formetta et al., 2014c)
Energy balance	**Shortwave radiation , Longwave radiation model**	Calculates shortwave and longwave radiation, respectively, from topographic and atmospheric data (Formetta et al., 2013b; Iqbal, 1983; Corripio and Purves, 2002; **?**).
Evapo - transpiration	Penman-Monteith, **Priestly-Taylor**, Fao-Evapotraspiration	Estimates evapotranspiration using Penman-Monteith (Monteith et al., 1965), Priestly-Taylor (Priestley and Taylor, 1972), and Fao-Evapotraspiration (Allen et al., 1998) options
Runoff	Duffy, **HYMOD**	Estimates runoff based on HYMOD (Moore, 1985) and Duffy (Duffy, 1996) algorithms
Optimization	**Particle Swarm Optimization**, DREAM, **LUCA**	Calibrates model parameters according to Particle Swarm Optimization (Kennedy et al., 1995), DREAM (Vrugt et al., 2009), LUCA (Hay et al., 2006) algorithms respectively.

The goals of this chapter are to determine the water budget of each Hydrologic Response unit (HRU) of a small catchment at high temporal resolution i.e hourly, that can be aggregated to different temporal scale, and define a methodology that can be used to analysed larger basins. A HRU represents a part of the basin that can be treated as a single unit, and a single control volume k for which eq. (5.1) is solved.

The working scheme followed are:

- For each model's component determine the parameters by calibration by using an automatic calibration algorithm, and comparing appropriate measured and simulated data;

- Validate the models using various goodness of fit methods (GoFs) to assess the model performances.

- Estimate the outputs of the budgets' terms i.e. discharge, actual evapotranspiration, and storage and thier errors

5.1.3 Chapter organization

The chapter is organized as follows: section 7.3 provides methodologies of modeling the "output" terms of the water balance equation, particularly rainfall-runoff modeling and discharge estimation (subsection 5.2.3) and evapotranspiration and water balance residual estimations (section 5.2.4). Brief description of the basin is at section 5.3. At section 5.4, the results of the hourly time series simulations for three components (snow water equivalent (sec 5.4.1), discharge (sec 5.4.2), and evapotranspiration and storage (sec 5.4.3), and results of basin scale water budget closure (sec 5.4.4)) is presented. Finally, the conclusions about the water flux of the basin follows.

5.2 Methodologies and models

Depends on the nature and availability of hydrometeorological data sets and question of interests, different combination of NewAge components can be used to solve basin water budget. In this study, kriging, snow melting, radiation budget (SWRB), Priestly-Taylor, HYMOD, and Particle swarm and LUCA are used. The components used in this study are marked in bold in table 5.1, and further described in their respective section below.

5.2.1 Calibration-validation procedures

For all the components we pursue an independent validation, if appropriate data are available. The procedure we use is standard. The data is separated into two sets, one for the calibration procedure and a second for the validation procedure (see section 5.3). Here, to achieve our objective, three calibration procedures are used. The first one is the calibration of snowfall based on MODIS imagery data as described in chapter 4. The second and the third calibration strategies are pursued for rainfall-runoff modelling. The first calibration on the rainfall-runoff is used to analyze the effects of different precipitation data sets (i.e generated from four kriging methods) on the runoff modelling. Then, based on the optimal data set identified from second calibration procedure, the third calibration aims to optimize the rainfall-runoff and the evapotranspiration models parameters jointly, as detailed in section 5.2.4, has been done to resolve the water budget. LUCA and particle swarm optimization tools, available in OMS among a few

choices, are used for the former and later calibration procedures respectively. The Let'Us
Calibrate (LUCA, (Hay and Umemoto, 2007)) is a multiple-objective, stepwise, based on
the Shuffled Complex Evolution global search algorithm procedures (Vrugt et al., 2003).
Whereas Particle swarm optimization is a population based stochastic optimization
technique inspired by social behavior of bird flocking or fish schooling (Kennedy et al.,
1995; Zhang et al., 2001; Formetta, 2013).

The objective function used as standard is the KGE (Kling et al., 2012) which was
considered more solid than Nash-Shutcliffe, but the goodness of fit was estimated by
two other indicators, the Pearson's correlation coefficient and the PBIAS, all of them
described in Appendix B. Other statistical indicators of performances are specified case
by case.

5.2.2 Snow melting

To simulate snow metamorphism processes, we used the degree-day modelling of snow
water equivalent (SWE) component as described in Formetta et al. (2014d). In this case,
the melting rate, $M[\text{mm t}^{-1}]$, is given by:

$$(5.2) \qquad M = \begin{cases} \alpha_{m1} * (T - T_m) & T > T_m \\ 0 & T \leqslant T_m \end{cases}$$

Where $\alpha_{m_1}[\text{mm t}^{-1}]$ is the melt factor, $T_m \ [^oC]$ is the snow-melting temperature,
and $T[^oC]$ is the air temperature. When the temperature is less than the melting
temperature, T_m, the melting is zero, instead freezing occurs. The rate of freezing $F[\text{mm}$
$\text{t}^{-1}]$ is given instead by:

$$(5.3) \qquad F = \begin{cases} \alpha_f * (T_m - T) & T < T_m \\ 0 & T \geqslant T_m \end{cases}$$

where $\alpha_f[\text{mm t}^{-1}]$ is the freezing factor.

The three unknown parameters in the above equations (T_s, m_1, and α_f) need to be
calibrated by comparing the simulated snow water equivalent with measured. How-
ever, we do not have any snow water equivalent measurement, hence, the unknown
parameters are calibrated using discharge data together with the parameters of the
ADIGE (described below) component. This follows a consolidated approach as applied for
instance in Li et al. (2012); Mou et al. (2008); He et al. (2014). However, in our approach

the snowfall parameters are already calibrated using MODIS snow imagery datasets (chapter 4).

Furthermore, MODIS snow albedo products (MOD10A1 and MYD10A1) are used (Shrestha et al., 2014; He et al., 2014; Blöschl et al., 1991; He et al., 2014; Parajka et al., 2012; Sirguey et al., 2009) as 'soft' information to compare with. The daily fractional snow cover (FSc) and snow albedo extracted, and aggregated to the HRU level, and are used to evaluate the space-time dynamics of the SWE estimations. The procedures of MOD10A1 and MYD10A1 imagery processes aims to produce useful data for SWE dynamics and snow metamorphism calibration are described in detail at appendix D. Since there is a directional relation between HRU's FSc (and albedo) and SWE, spearman rank correlation is used for evaluation. It is preferred because it provides a means to quantify the monotonic relationship between two variables with no frequency distribution assumption (nonparametric), and is given by (Kottegoda and Rosso, 1997):

$$(5.4) \qquad \rho_{rank} = 1 - \frac{6.\sum_{k=1}^{n} D_k^2}{n(n^2 - 1)}$$

where D is difference between the rank of the MODIS data (i.e. FSC or snow albedo) and SWE data at K^{th} pair, and n is the number of observations. The higher the value ρ_{rank}, the higher the correlation between SWE and the snow albedo. The use of the MODIS imagery data supplementary information is important to maintain the spatial distribution of the modeling solutions, which could never be assessed otherwise.

5.2.3 Runoff estimation

The NewAge component estimating runoff is called ADIGE. It is made by many Hymods (Moore, 1985), each one for each HRU in which the basin is subdivided. Besides, ADIGE can also model reservoirs and dams, and includes a routing model along the river network that connects the HRUs (Formetta et al., 2011). The inputs of ADIGE model are rainfall, evapotranspiration, and melting snow; and the output is discharge at each channel-link.

The Hymod core of the component is a conceptual rainfall-runoff model that separate a quick (shallow) flux from a slower (deeper) one. The first accounts for surface runoff by using three linear reservoirs, the latter accounts for subsurface storm flow with one single linear reservoir (Moore, 1985; Formetta et al., 2011; Formetta, 2013). Groundwater is described by a further storage. Essential to Hymod's calculation is also the estimation of the water "losses" by ET, which are modelled as detailed in the next section. The details of Hymod are reported in Appendix A, for readers convenience. The fundamental

parameters of the model can be interpreted as the mean travel time in each of the surface and subsurface compartments of the hydrological cycle.

The NewAge Hymod component is applied to any HRU, in which the basin is subdivided and the total watershed discharge is the sum of the contribution of the HRUs. This sum can include (or not include) the delay due to routing from the HRUs outlet to the basin outlet, but in this application we excluded it because at these scales (of around ten kilometers) travel time in channels is irrelevant (D'Odorico and Rigon, 2003). Eventually the Hymod component provides an estimate of the discharge at each link of the river network of the watershed, downstream to the HRUs.
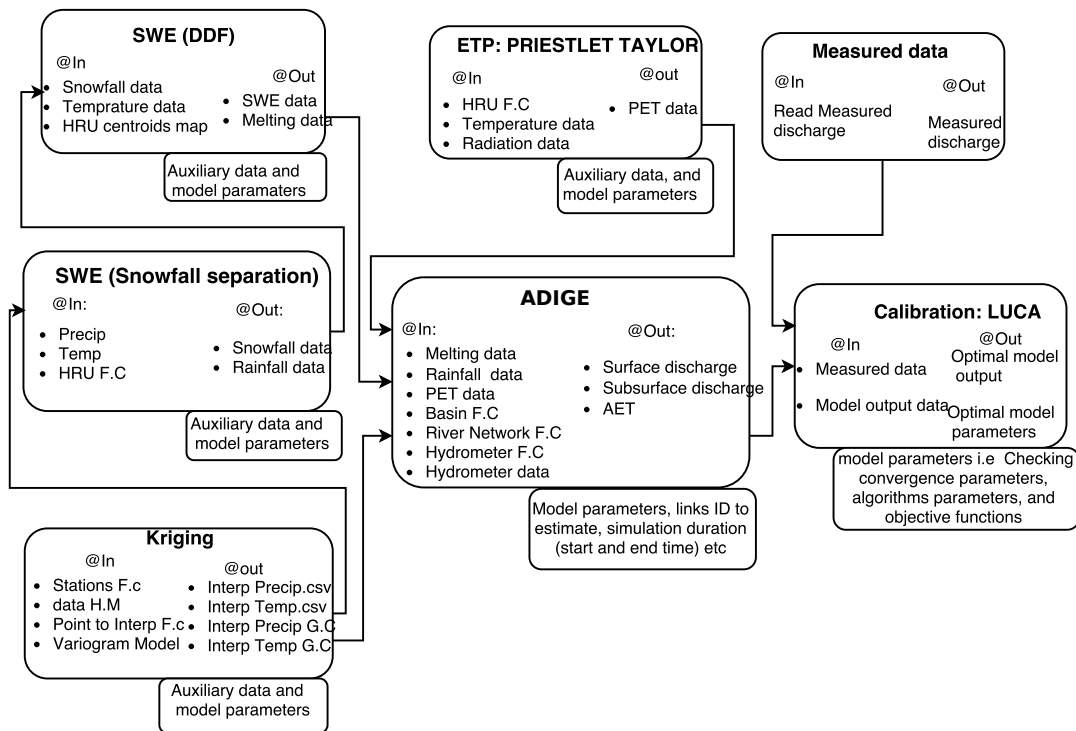
Figure 5.2: The HYmod component of NewAge system and its input providing components. It shows how different components are connected, here kriging, SWE, ETP, and calibration component connected with Adige to solve the runoff at high spatial and temporal resolution. The detail discussion about each component can be referred at its respective section.

The first part of the simulation analysis is to evaluate the effects of four precipitation data set generated using four krigings on the runoff calibration and modelling results. So HYMOD parameters are calibrated for all the four precipitation data sets for five years (1994-1999), using LUCA as optimization tool. The simulation from 2000-2012 is

used for validation for the data set comparison. Based on the validation strategies, the optimal data set is selected used to resolve the water budget of the basin.

5.2.4 Evapotranspiration (ET) estimation, and residual storage

ET measurements, in this case study, are completely missing and therefore, they need to be modeled. In situation illustrated in the previous pages, we can consider as a reasonable basis for the estimates, the following modification of the Priestley and Taylor (PT) Formula (Priestley and Taylor, 1972) for each HRU:

$$(5.5) \qquad AE_T(t) = \alpha \frac{S(t)}{C_{max}} \frac{\Delta}{\Delta + \gamma} (Rn - G)$$

where AE_T is the actual evapotranspiration [LT^{-1}], α is the so-called Priestley-Taylor coefficient, $S(t)$ is the water storage in the root zone, and C_{max} the maximum storage of water in the HRU. Rn[L^2T^{-1}] is surface net radiation; G [L^2L^{-1}] is the down-welling flux of thermal energy. The formula can be further simplified by assuming $G \propto R_n$, and including it in α (Clothier et al., 1982). Δ is the slope of the Clausius-Clapeyron relations which is given by a function of the air temperature (Murray, 1967):

$$(5.6) \qquad \Delta = \frac{4098 * e^{\frac{17.27T}{T+237.3}}}{T + 237.3^2}$$

where T[^oc] is temperature; and the γ is the psychometric constant [in K T^{-1}, where K means the temperature unit]. It is estimated by (Allen et al., 1998):

$$(5.7) \qquad \gamma = \frac{0.001013 * P}{0.622 * 2.501 - 0.002361 * T}$$

where P[kPa] is the atmospheric pressure. The choice of reducing AE_T with the relative water content, is similar to the one pursued in several studies, e.g. Porporato et al. (2002) Rodríguez-Iturbe and Porporato (2004). Cristea et al. (2012) reports that the value of α varies in previous studies from 0.6 to 2.4, depending on land cover and site conditions, making literature almost useless in determining the conditions specific to a basin.

In our modelling approach, we estimate α using the water budget as shown in appendix E obtaining, instead of the potential evapotranspiration, the actual evapotranspiration. The whole procedure, which involves an iterative procedure between the PT and runoff estimation, is detailed in E. Our procedure assumes that the water storage is null after a specified number of years, said Budyko's time, T_B, (after Budyko (1978)).

Here, two algorithms can be followed. The first neglects soil moisture variability and
generate α from the observed data using equation E.6. The second procedure uses
variable storages insides the HRUs (appendix E) and consists in optimising at the same
time the parameters of the Adige component, and requiring that the water storage is
null after T_B years.

In principle, for both the procedures, and for any specific Budyko's time, T_B, an α
is generated, thus producing a series of candidate αs whose variability is observed and
discussed. However, since the second procedure is highly demanding computationally,
only a single optimization procedure was actually performed for years 1995 to 1999, with
$T_B = 5$ years.

Radiation which enters in eq. (5.5) is estimated by using the two radiation compo-
nent included in JGrass-NewAGE system, NewAGE-SWRB component (Formetta et al.,
2013b). Temperature is interpolated by using kriging 4 from the meteorological stations
at single point of each HRU (centroids), since HRUs are of quite small extension (and its
variability internally to each HRU has been checked to be less than half Celsius degree).

In this approach, the uncertainty of ET estimation comes from other components'
errors of estimation. Assuming that measurement errors in J and Q component are
neglected (or predefined separately), the ET using the standard theory of errors (Rodell
et al., 2004), the standard deviation of ET estimates is:

$$(5.8) \qquad\qquad\qquad \sigma_{ET} = \sqrt{\sigma_J^2 + \sigma_Q^2 + \sigma_{\alpha'}^2}$$

where σ_{ET} is the standard deviation errors of ET, σ_J is rainfall estimation errors (in
this case the kriging error), σ_Q is the discharge estimation errors (model error) and σ_α is
the errors made on estimating α. The σ_α is estimated from the standard deviation of ET
caused by using different α following 17 years of stationary.

Varying the year of null storage, T_B, implies obviously different estimates of ET,
which remain however confined in certain range, that we interpret as the representative
of the epistemic uncertainty of the approach. Being assessed with this method, ET does
not automatically balance equation (5.1) for each year. The residual is, as a consequence,
interpreted as relative water storage. If the first years of simulation imply a negative
storage, this is assumed to be present at the initial time, which, in turn, imply that the
α coefficient must be recalculated to obtain null storage at the given year.

Therefore the whole procedure is repeated, until the initial storage, and estimated
ET are consistent. Once ET is estimated with the above procedure (and varying the zero
storage year for all year) the mean α coefficient is chosen as the most reliable, and used.

In the end, using our dataset and our modelling approaches, we close the water budget of the basin at any time scale (from hourly to yearly).

5.3 Description of the study area and input data

Here very brief description of the meteorological data sets and the study basin used in the study is presented, detail description can be found in Abera et'al (2016, submitted) and Norbiato et al. (2008). The study area is Posina river basin, located in the North Eastern part of prealpine mountainous parts of Veneto region in Italy. The area of the basin is about 116 km^2 (figure 5.1). The hourly time step data sets of precipitation, temperature and discharge that covers from 1995 to 2012 (18 years) are used for analysis. The time series estimation of input components (precipitation i.e both rainfall and snowfall, and temperature) data for each HRUs are estimated according to the procedures described in chapter 4.

For discharge, 18 years of hourly data are available at three hydrometer stations, at location indicated in figure 5.1. The first 5 years are used for calibration, and the rest for validation in the case of the rainfall-runoff component.

5.4 Results and discussions

The fundamental essence of presenting The results of the study is organized as follows. First brief results on SWE estimates of the basin are described. Next, the rainfall-runoff simulation results and their performances are evaluated. The third subsection contains results on spatio-temporal estimation of ET and storage. Lastly, following proper temporal and spatial characterization of all the water budget components, the results of water budget closure analysis are followed.

5.4.1 SWE estimations

The 18 years of hourly time series analysis of SWE for some selected HRUs is shown at figure 5.3 a. The 1995-2012 simulation shows that Snow forms mostly in the period of October to the following year March/April. The timing in the formation period varies across years. The annual variability of the snow accumulation also appreciable. The winter 1997/1998, 2000/2001, 2006/2007 shows small snow accumulation, and the years 2003/2004, 2005/2006, 2008/2009, 2010/2011 winters shows higher snow accumulations
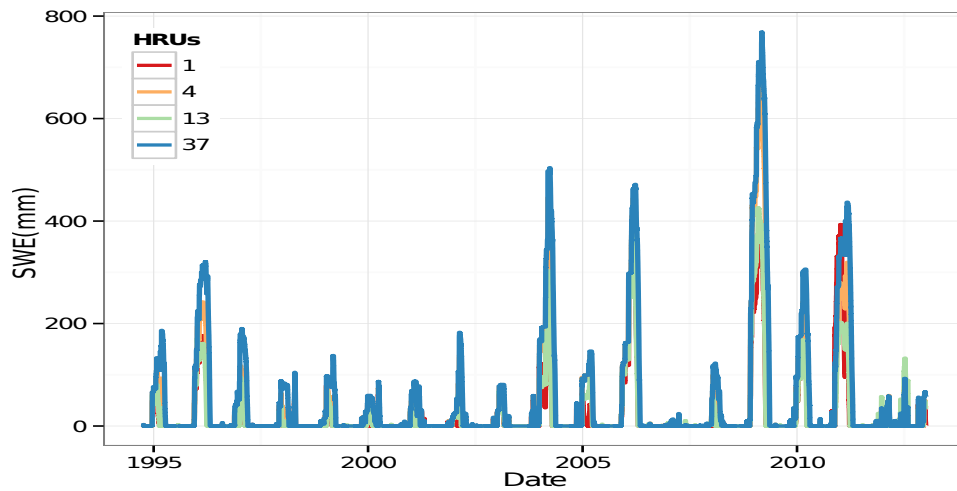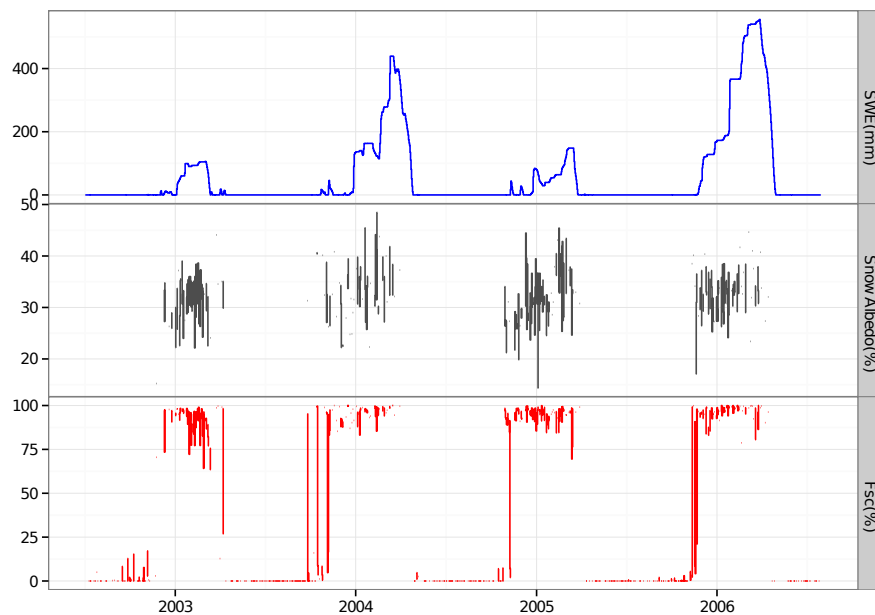
Figure 5.3: Time series SWE estimation of 18 years for four sample HRUs i.e 1, 4, 13,and
37 (a), and time series SWE estimation along with MODIS fractional snow cover (bottom)
and snow albedo (middle) for HRU 1 (b).

in the basin. Considering all the winter seasons of the 18 years, the year 2008/2009 is the highest and 2006/2007 the lowest accumulations. The SWE estimation comparison between the HRUs shows (figure 5.3a) that, as expected, the HRUs at high elevation (HRU 1 and 37) has always higher estimated value than HRUs at low elevation (HRUs 4 and 13).
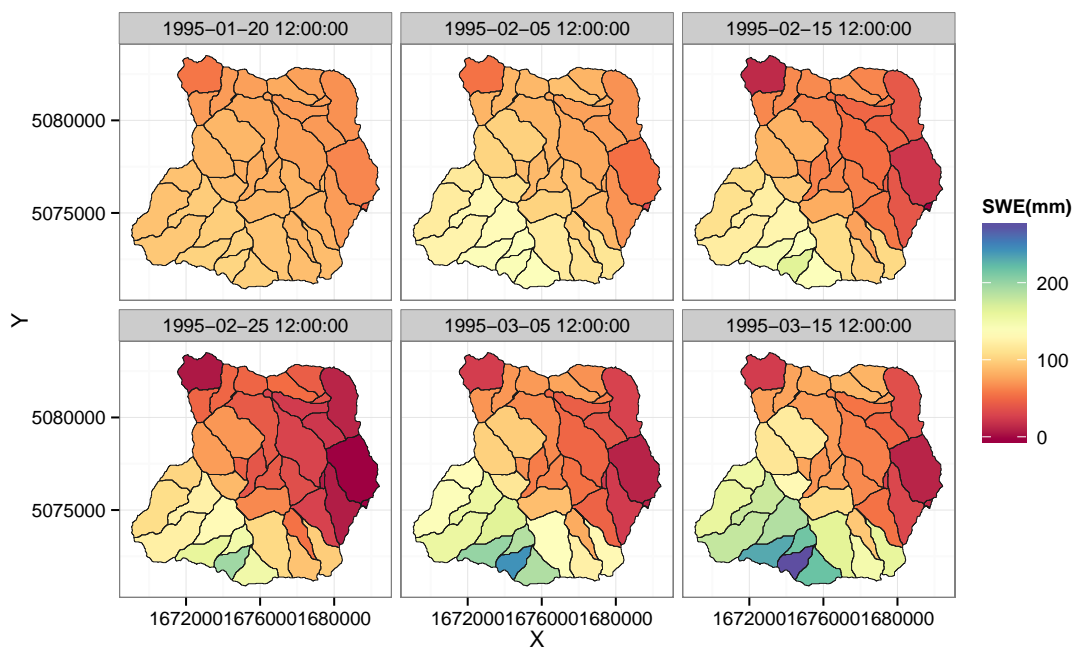
Figure 5.4: The spatial variability of SWE for some selected time steps.

The plot of SWE along with the MODIS FSc and snow albedo (figure 5.3 b) for a single HRU (HRU1) provide an insight that the SWE dynamics shows some level of consistency with MODIS imagery data. The correlation of SWE values with snow fractional area coverage and that of snow albedo is high (0.65) and low (0.15) receptively. A sample of simulated SWE spatial distribution is shown at figure 5.4. There is a notable spatial variability of SWE over the basin (i.e between the HRUs), and the difference reaches as high as 300 mm, and this could be due to the difference in topography and receiving solar radiation.

5.4.2 Stream flow modeling and impacts of rainfall interpolations

Four precipitation data sets generated using ordinary kriging (OK), Local ordinary kriging (LOK), Detrended kriging (DK) and Local detreded kriging (LDK) are used as input for the discharge modelling. The detail algorithms and their performances in comparison to the measured precipitation data is discussed in Abera et al. (2015, submitted). All four kriging interpolation data sets are used to calibrate the Rainfall-runoff model, even if LOK was actually found to perform better in rainfall reproduction (e.g. Abera et al., 2015). The calibrated parameters are reported in table 5.2. LUCA optimization produced the same model parameters values for the three data sets except the DK. (table 5.2).

However, the different kriging methods have different performances in reproducing runoff, reported in Table 5.3. Surprisingly, the result of LOK (relatively the best in reproducing measured precipitation, Abera et al., submitted) is actually the lowest in reproducing the observed discharge, with KGE=0.78 and KGE=0.40 during calibration and validation period respectively (table 5.3). The comparison of observed and simulated discharge at the outlet using PBIAS shows that simulation using DK has the lowest bias, while the LOK has the highest bias both during the calibration and validation periods. In general, the simulation results of LDK and DK are both acceptable according to the standard interpretation of the GOFs values (Moriasi et al., 2007) in both calibration and validation, while OK and LOK return very low GOFs during the validation period (table 5.3). In general, the the performances in validation period not high because the performances in the validation period decreases when the duration from the calibration period increases.

The higher performances of the DK methods could indicate, that this method, even if not visible in the calibration phase, could actually capture better the physics of the process. Contrary to our results, using SWAT model, Heijden and Haberlandt (2010) did not get any significant difference between different interpolation methods. Sample calibration and validation hydrographs from the four precipitation data set based on the four types of kriging interpolation methods are shown in figure 5.5, while the whole 18 years of hourly simulation are portrayed at the complimentary material of this chapter.

The overall ranking of Hymod model performance driven from the four types of krigings is evaluated by the KGE index (table 5.3). Based on the performance during the validation periods, DK interpolation method is found to be the most performing, and

Table 5.2: Optimized parameters obtained from hourly rainfall-runoff and snow modelling during the calibration periods (1995-1999). The first three parameters are for SWE component, and the next five parameters are of the rainfall-runoff component. DK* is set of optimized parameters based on DK precipitation, and optimized for both discharge and Budyko assumption for a five years, as detailed in appendix E.

Parameters	OK	LOK	DK	LDK	DK*
$\alpha_{m1}[mmC^{-1}h^{-1}]$	1.01E-4	1.08E-4	0.0856	1.98E-4	8.83E-02
$\alpha_f[mmC^{-1}h^{-1}]$	0.0367	0.0423	0.0029	0.0911	0.0204
$\alpha_1[-]$	0.949	0.985	0.2362	0.987	0.855
$C_{max}[L]$	978.778	997.438	758.688	999.682	838.449
$B_{exp}[-]$	1.506	1.604	3.348	1.692	0.565
$\alpha[-]$	0.255	0.229	0.247	0.231	0.0286
$Rs[T]$	0.001	0.001	0.0026	0.001	0.019
$Rq[T]$	0.211	0.204	0.206	0.184	0.312
α	-	-	-	-	1.895

Table 5.3: The model performance statistics of rainfall-runoff model based on the four types of kriging interpolation methods. Performance of the model during the calibration and validation. Percent bias (PBIAS) measures ranges form $-\infty$ to $+\infty$, with optimal value of 0.0. Positive values indicate model underestimation bias, and negative values indicate model overestimation bias. DK*, which is used for the water budget analysis, is based on DK precipitation, and optimized for both discharge and Budyko assumption for a five years.

	Calibration			Validation		
Methods	KGE	PBIAS	r	KGE	PBIAS	r
OK	0.80	1.80	0.80	0.40	66.8	0.50
LOK	0.78	5.2	0.79	0.35	40.1	0.49
DK	0.85	-0.8	0.85	0.56	14.30	0.68
LDK	0.83	1.30	0.83	0.56	15.50	0.66
DK*	0.71	14.6	0.81	0.63	-14.30	0.82
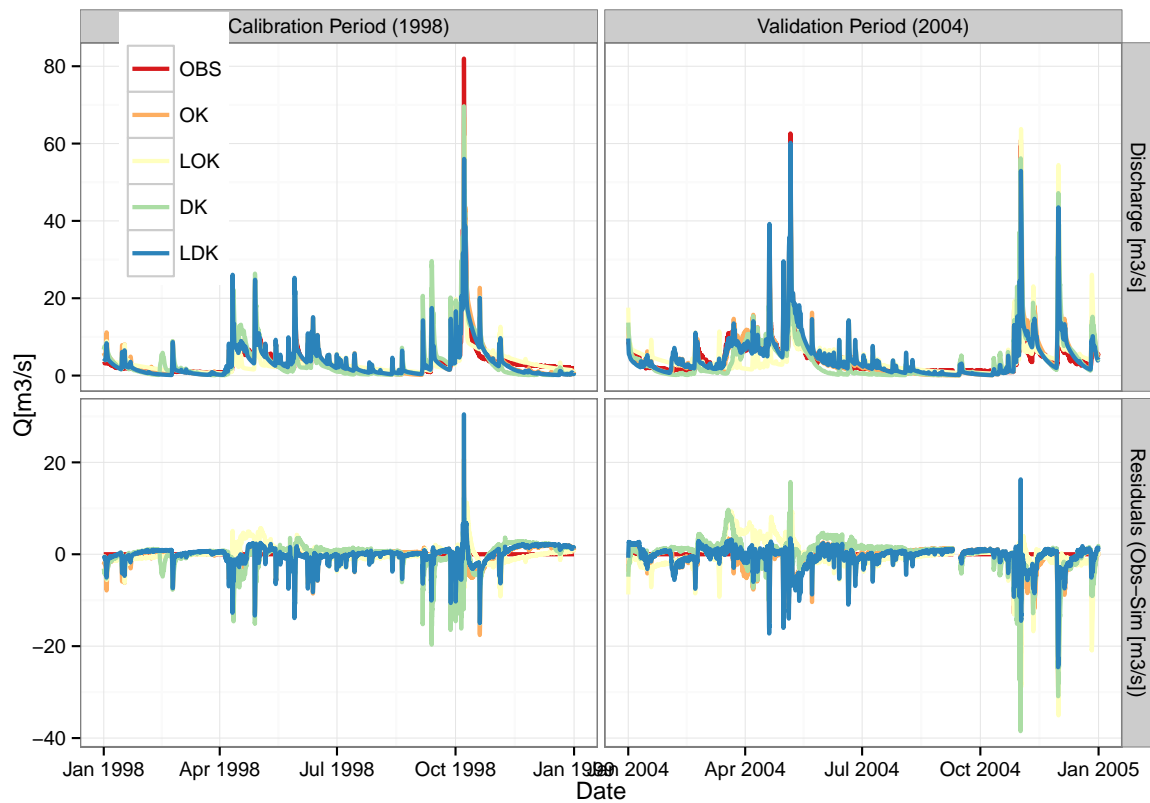
Figure 5.5: A comparison of four precipitation based simulations during calibration
period (1998) and validation period (2004) and the residuals (obs-sim) of the forecast

followed by LDK, OK and LOK respectively. Because of the overall better performances,
we decided to use DK (instead of LOK) for further discharge analysis. For implication
of impacts of different kriging generated precipitation data sets on long term runoff
estimation, figure 5.6 shows that, in general, all the precipitation data sets generate
higher long term annual runoff than the observed, and simulation using DK is relatively
better than the others.

Figure 5.6 shows long term annual mean runoff using different kriging data sets,
and in general, all the data sets generates higher mean annual runoff than the observed.
There is a slight difference between OK and LOK in one group and DK and LDK in other.
Generally, DK shows relatively the lowest long term annual mean runoff, and smallest
volume error from the observed (figure 5.6).

At this stage, the HYMOD and PT models are coupled to optimize for both the
discharge and for Budyko assumption of water budget, and the performance is reported
in table 5.3, last row. This simulation is used to simulate discharge at each links of the
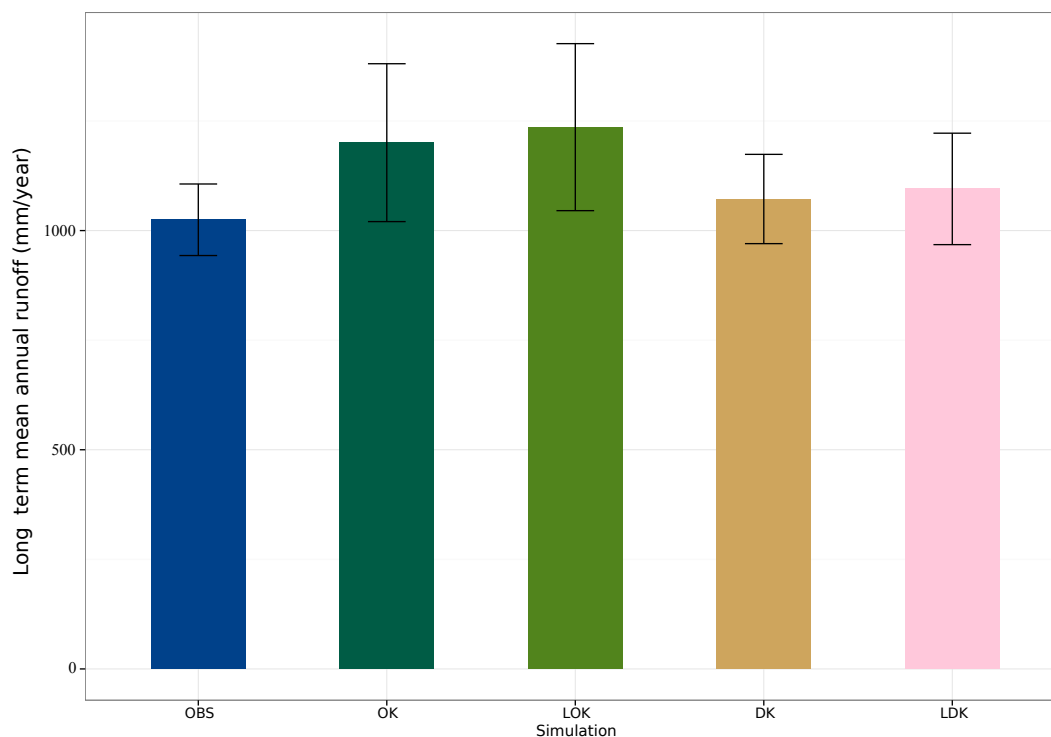
Figure 5.6: Comparison of long term mean annual runoff simulation with different kriging interpolation precipitation inputs with observed discharge at basin outlet.

basin, and if data available, the performance can be assessed. at any links. In this case, observed discharge at two interior points are used to evaluate the potential of the model for estimation of runoff at each links (figure 5.7).

The two internal links which are not used in the calibration processes, see figure 5.1 for their locations, are drain by 22.2 km^2 and 38.8 km^2 area. According to all the performance statistics, the calibrated model solution provides acceptable results at the two interior links In fact, a KGE=0.73 and a PBIAS=3.30% at Valoje (ID 201) and a KGE= 0.62 and a PBIAS=2.50% at Bazzoni (ID 203) are obtained. While there are some studies that shows degrade of model performances when applying basin outlet calibration parameters at the interior sites (Moussa et al., 2007; Feyen et al., 2008; Boscarello et al., 2013), the study of Lerat et al. (2012) using large number of basin demonstrated that a semi-distributed rainfall-runoff models using a single site (like basin outlet) calibration could give acceptable estimate ungauge internal points. Our case seems to confirm the latter and better case, but, obviously, we are not able to discern if this is due to the characteristics of our modeling solutions, or, perhaps, of the study site size, dimension and location, even if, the first two conditions certainly play a role.
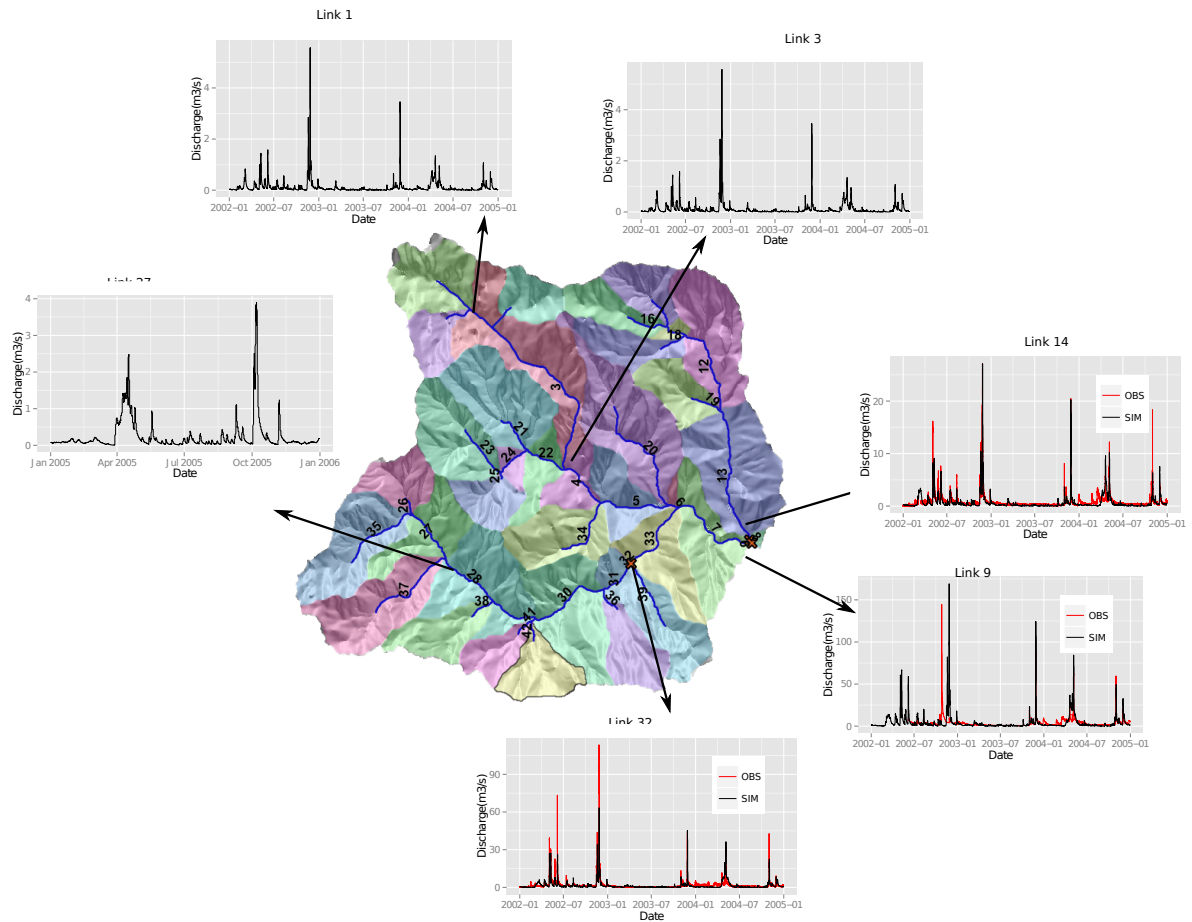
Figure 5.7: NewAge model forecasting validation at internal links. Discharge is estimated for all links, here, plotted for link 1,3, 9 (the outlet link), 14, 27, 32 as a sample. When data is available at any internal points, model performances can be evaluated (e.g. for link 14 and 32).

5.4.3   Evapotranspiration estimation and uncertainty

Once, hourly data of the solar radiation is estimated according to the NewAGE SWRB component (Formetta et al., 2013b) and temperature data interpolated as described in chapter 4, ET for each HRUs is estimated at hourly time steps, by optimizing the PT's $\alpha^{'}$ against water budget closure (stationarity). The procedure of calibration of parameter α returns the results shown in Figure 5.8.

Varying T_B from one year to eighteen years, as described in section 5.2.4, the value of PT's α changes from 0.38 to 0.8, with mean $\bar{\alpha} = 0.56$ (figure 5.8). This result represents an aftermath verification of the method chosen. The variability in α around the mean, still great, is much less than the one found in literature. Besides, α is relatively at the lower
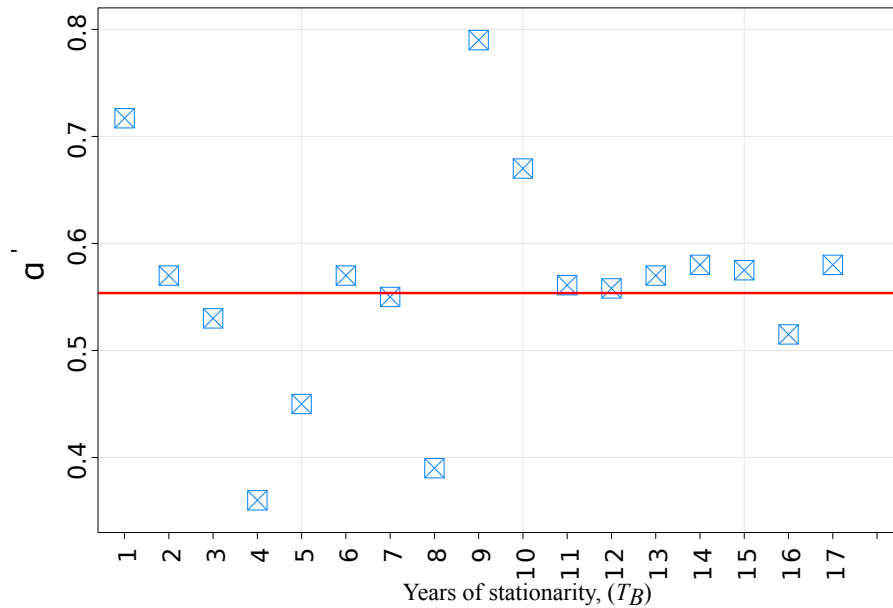
Figure 5.8: The scatterplot of ET's α' parameters plotted for different lengths of stationarity assumption years.

bound of values used in literature. In the first 10 years, increasing the number of years for water balance closure assumption, the α is highly variable, becoming subsequently relative stable around the mean (figure 5.8) Our result suggests that taking the $T_B \sim 10$ years could be a reasonable choice.

Following proper determination of α values of the PT equation, the ET of each HRUs are estimated with their uncertainty errors. Figure 5.9 is a sample of four HRUs (1,4,13,37) time-series of ET during august, 2005. The spatial variability for a sample of hourly simulated ET is shown in figure 5.10. The resulting annual ET ranges from maximum of 550 mm to a minimum of 424 mm, in 2001/2 and 2002/2003 respectively. The errors of estimation can vary as much as 20%. As it can be seen from figure 5.11, ET actually does not tend to vary much. This situation is common to many other places in humid areas (Lewis et al., 2000; Oishi et al., 2010; Möller and Stanhill, 2007).

Accordingly to the hypothesis of consistence we made, the relative water storage varies from a negative maximum of 410 mm to 87 mm positive maximum. Whilst the quantitative assessment of both ET and relative storage can be thought as imprecise, their overall internal variability cannot certainly be neglected, and must be considered a realistic product of this chapter, further discussed in the next section.
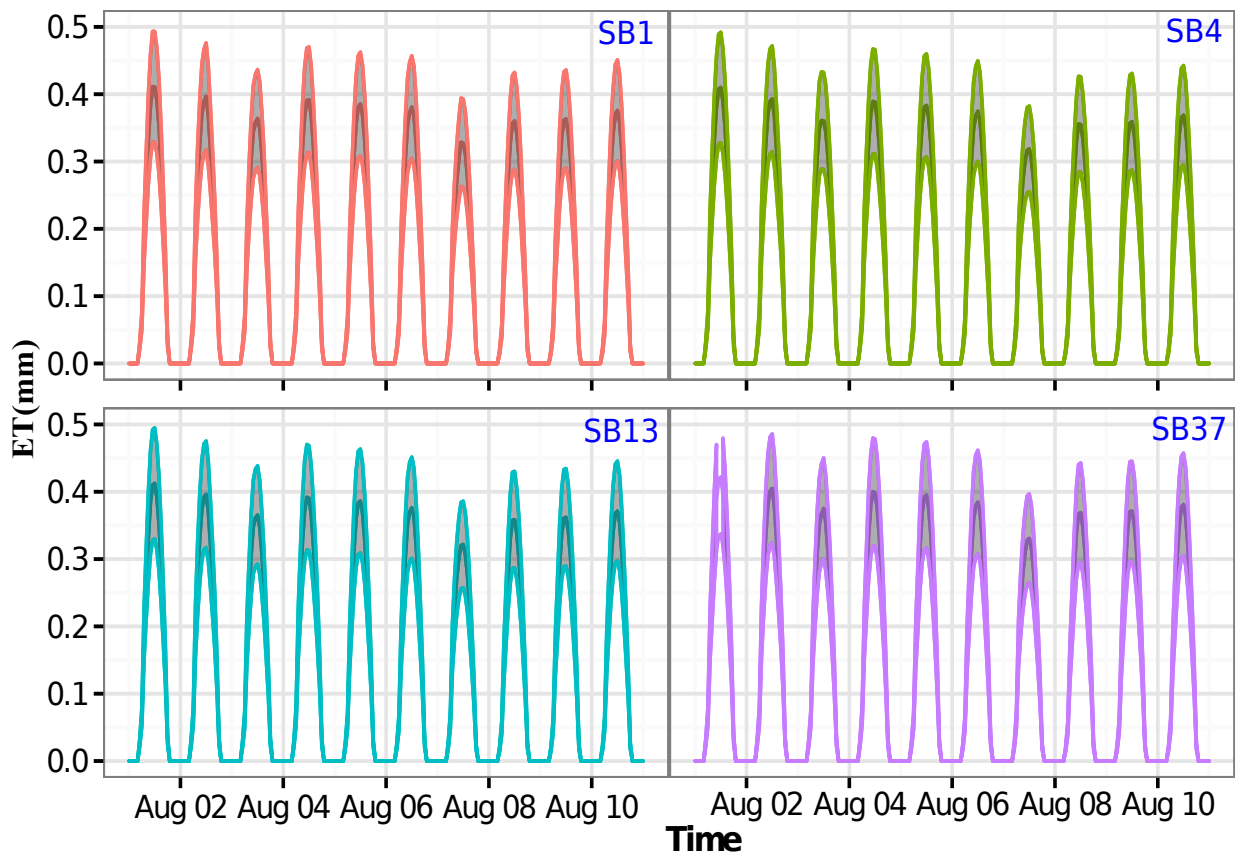
Figure 5.9: Estimated ET at hourly time steps and comparison between subbasins (1,4,13,37) for 10 days of hourly simulation August 2005.The gray band is the uncertainty band associated with the water balance approach ET estimations.

5.4.4 Closing the water budget at basin scale

Figure 5.11 shows the mean estimate of the water budget obtained with the method explained in the previous sections and in Appendix. The annual water balance is based on hydrological years, in our case from October to end of September of the following year. The components of the water balance of the basin is estimated for each years and the relative share of each components from the rainfall can be observed (figure 5.11). The hypothesis that budget is stationary after T_B years implies major interannual variability with both negatives and positive storages. This variability is very pronounced and, in the catchment under study, ET vary from around 19% to 35%, Q from 64% to 95% and S from -19% to 5% of the whole yearly budget. The main source of variability in the budget is clearly in the rainfall input.
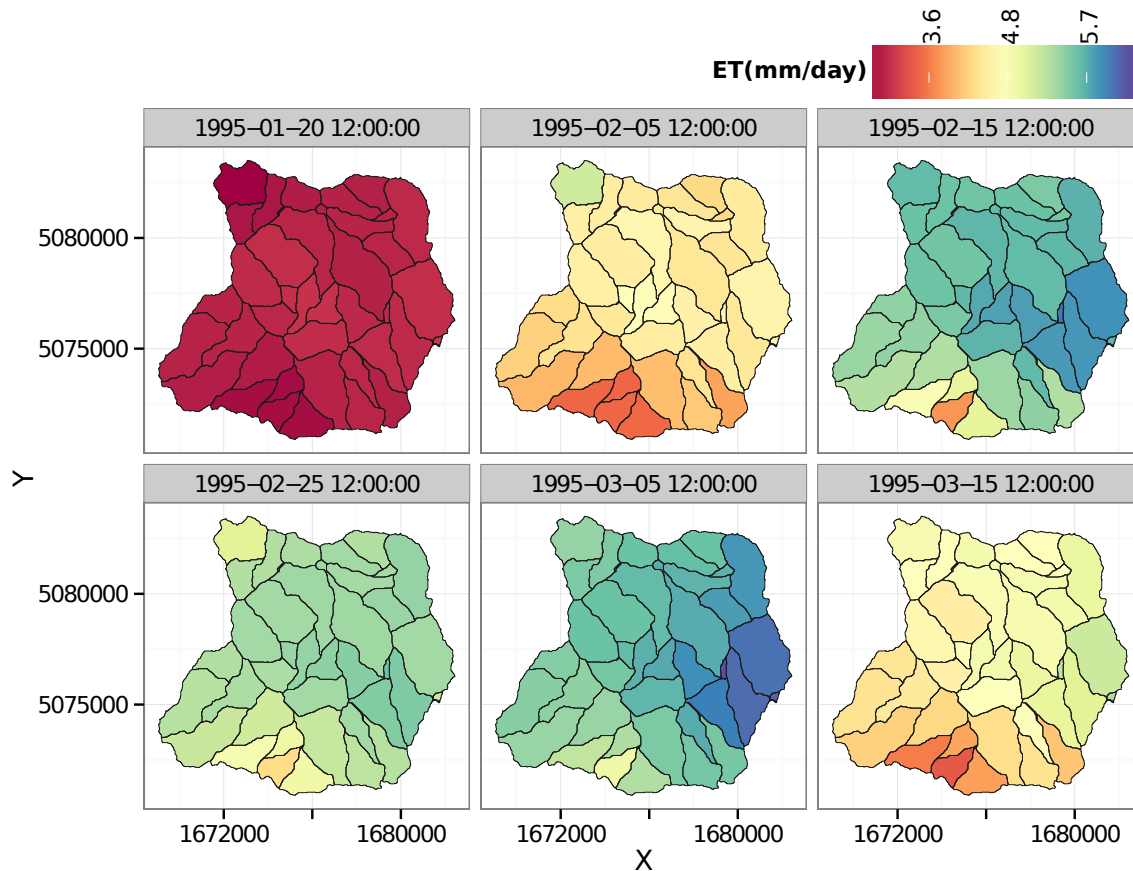
Figure 5.10: The spatial distribution of ET for some selected hourly time steps.

However, it has to be remarked that simulated ET is more smooth than in reality, since it has been estimated "in mean" by assuming a unique PT parameter along the seventeen years. In addition, the main driver of ET is radiation which is relatively consistent between years. Hence, the pronounced monthly and seasonal variability tends decrease a lot when aggregated to annual level. Similar studies has obtained that ET in forested basin has very low interannual variability. For instance, for oak woodland watershed in California, (Lewis et al., 2000) find out that the interanual variability of ET is low. For similar basin of our study, forested mountainous basin, Yoshiyukiishii and Nakamura (2004) analyzed 11 years of water balance from relatively well gauged basin, and show that the interannual variability is very small. The result of Oishi et al. (2010); Möller and Stanhill (2007) also indicate similar analysis.

Analyzing the relation between the simulated and measured output terms (ET, Q, and S) with the input term (i.e J) of the water budget at annual scale, in figure 5.11, it can be seen that higher precipitation years are accompanied by higher Q years, which
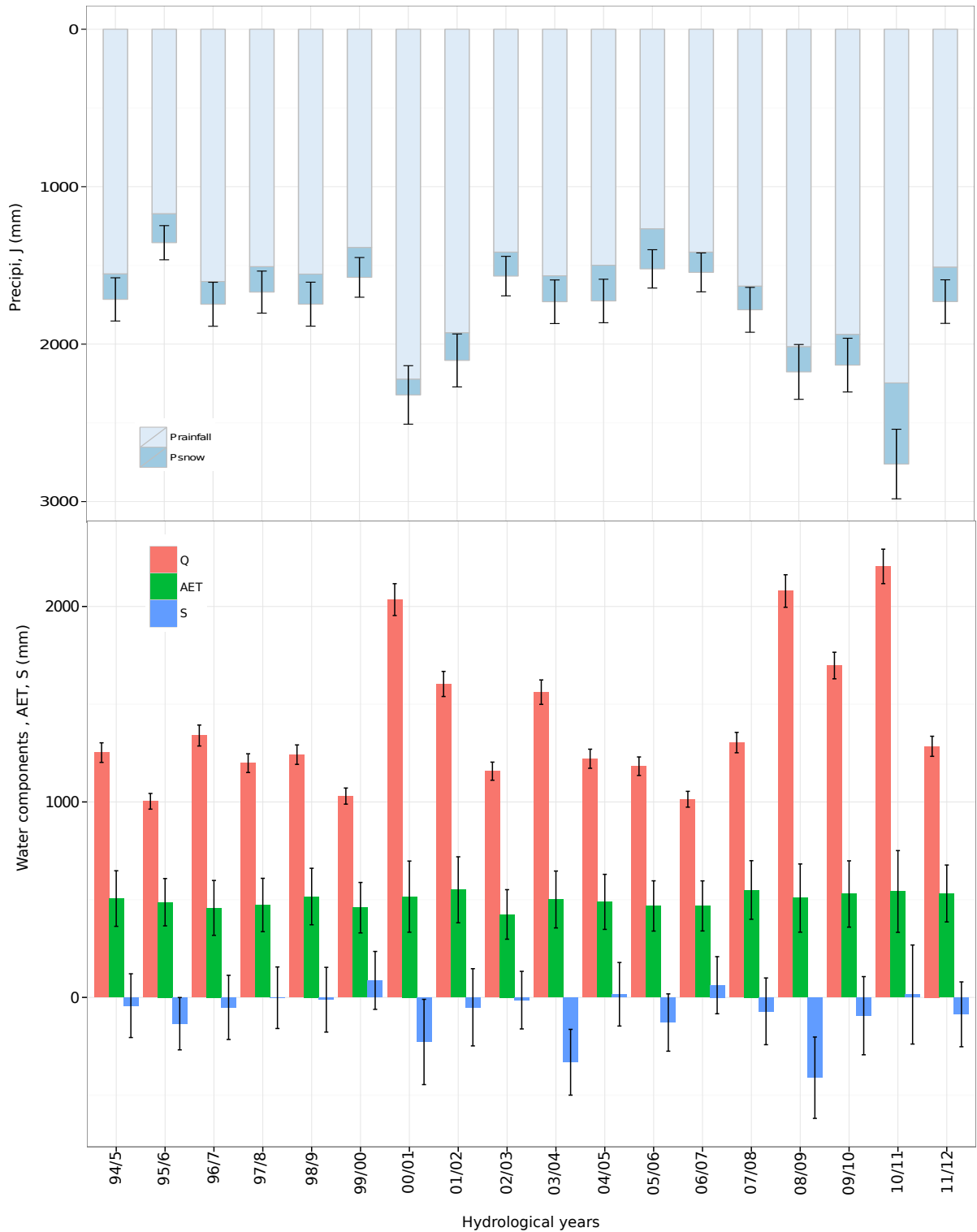
Figure 5.11: Water budget components of the basin and its annual variabilities from
1994/95 to 2011/2012. It shows the relative share (the size of the bars) of the three
components (Q, ET and S) of the total available water J.

indicates that increases in J tends to contribute directly to Q with minor effects on S and ET. The great part (88%, R^2=0.88) of Q variance is explained by the variance J. As aforementioned, the variability in ET is smaller than other components, and only 38% can be explained by J (i.e. R^2=0.38). Q and ET exchange their role during the years and there are clearly years where Q is larger than ET and vice-versa. Notwithstanding the uncertainties implied in the procedure, it is clear that the variability of the budget is impossibly to be denied. The error of estimation is shown by the error bar in figure 5.11, which is highest and lowest for S and Q respectively. This is expected because Q is the more reliable measured data set in the water budget equation at the basin scale (Wang et al., 2014b).

Since the budget was actually performed on hourly base and at small units (HRU), plot analogous to figure 5.11 can be produced for any hour of any day of the year of simulations and any HRUs of the basin, clearly, with increasing uncertainty with decreasing time step, due to the conditions in which the ET parameter, and storage were assessed.

As an example the monthly budget was estimated for year 2011/2012 in figure 5.12. For obtaining figure 5.12 were used the measured (but interpolated with DK) rainfalls, the simulated discharges, using the parameter calibrated between 1995-1999, and the PT calibrated for Budyko assumption in five years. Similarly, to show variability among the HRus, the water budget components for long term monthly mean are analyzed from the 18 years of simulations, and the mean monthly estimates of four months (January, April, July, and October, one from each season) is presented in figure 5.11. Figure 5.12 provides the monthly variability of the budget. The monthly variability is very pronounced. The highest variability is mainly by J and S. During summer all the components show high magnitude (high J, high Q). The variability in monthly S is governed by the J, though non-linearly. The variability in ET is evidently connected with the annual cycle of solar radiation, and highest in June and July and lowest from November-February, as expected. In this year, from late spring to august, evapotranspiration is sustained by the water storage more than from direct precipitation, indicating that, if not sustained by winter rainfalls catchment vegetation could go under considerable stresses, in these months. Figure 5.13 shows the long term monthly mean, of course it provides seasonal inference too as each month is sampled from each season, spatial distribution of water budget components over the basin. The result confirms the monthly analysis given for the year 2012 (figure 5.12).

The trend in Q follows the trend in precipitation, but actually not in a linear way.

This could have been deduced from the data alone, However, seeing it with the other
budget components enlighten the complexity of the interactions actually in place.
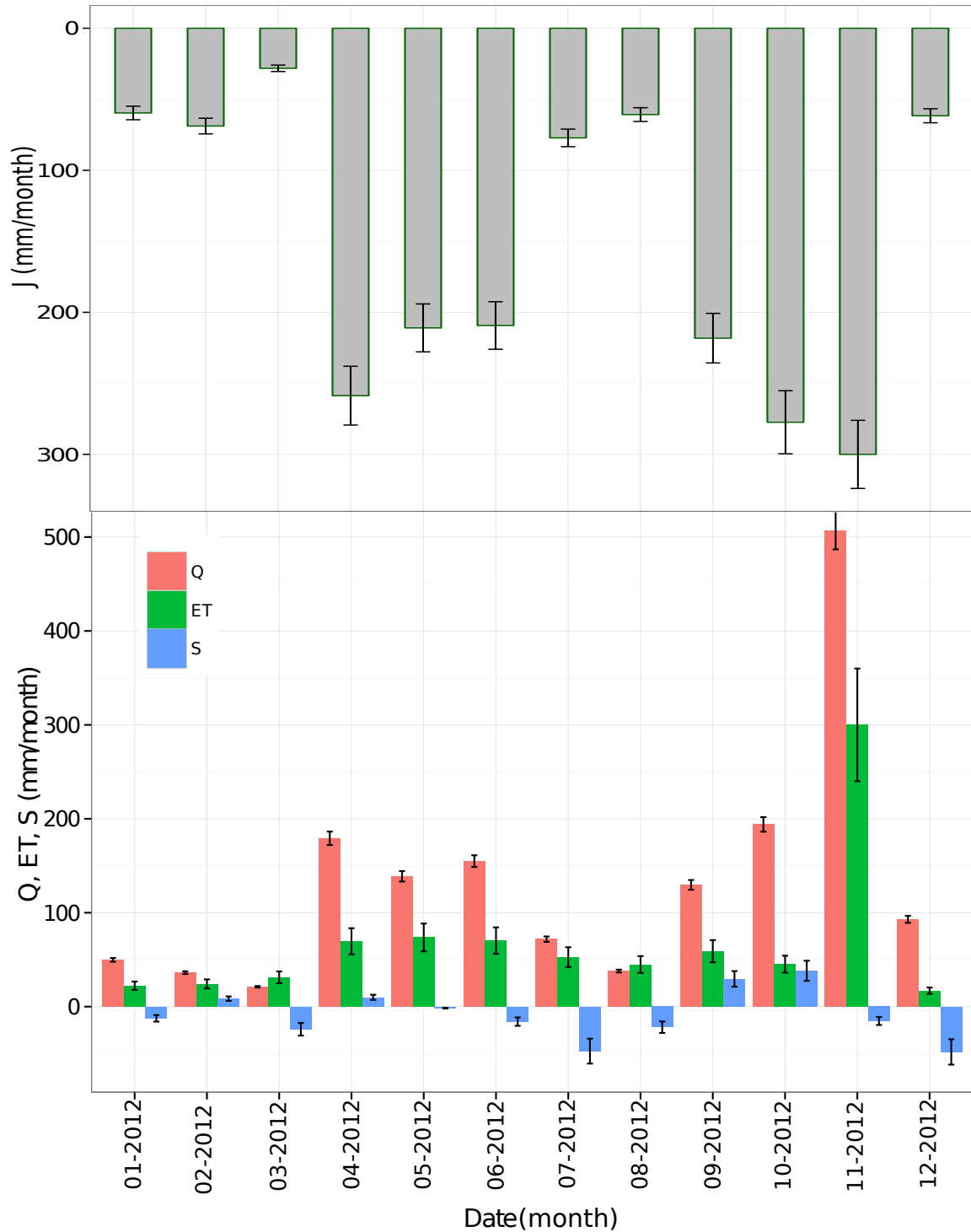
Figure 5.12: The same as figure 5.11, but monthly variability for the year 2012.
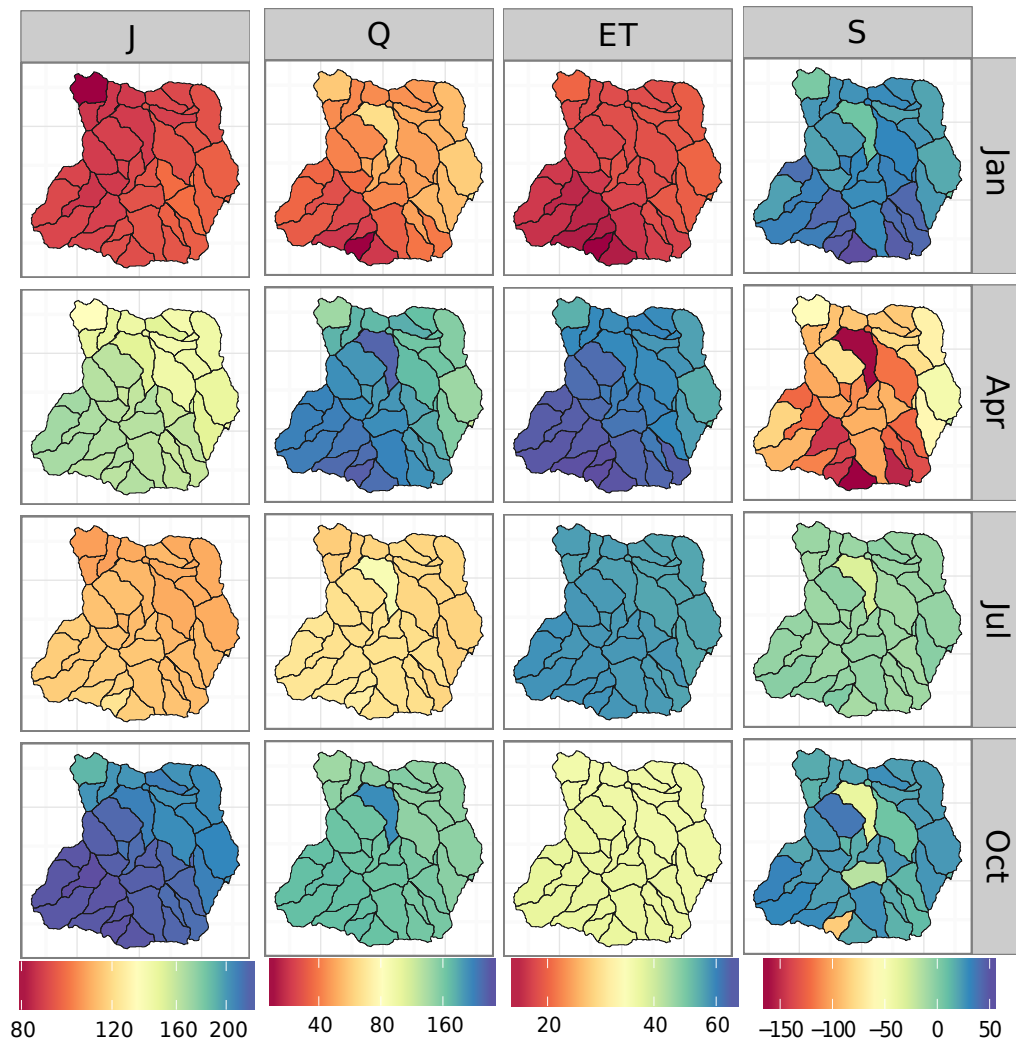
Figure 5.13: The spatial variability of the long term mean monthly water budget components (J, ET, Q, S). For reason of visibility, the color scale is for each component separately.

5.5 Conclusions

The water budget of the river Posina basin has been analyzed with the NewAge system
at hourly time-steps by using 18 years of meteorological data (rainfall and temperature)
and discharge. The analyses include estimations of the four components of water budget
(precipitation, discharge, relative storage, and evapotranspiration) under the hypothesis
of stationarity (i.e. null storage) in one of the years where measurements are available.
NewAge model components are used to capture the basin behaviour and forecast the wa-
ter cycle, in presence of known precipitation inputs, and to fill the gaps where distributed
data are necessary and only local measured are present. The procedure implemented,
with its imprecision, is general, and can be transposed to basins where rainfall and
discharge measurement are available.

In NewAge Hymod rainfall-runoff component, the inputs for runoff production such
as precipitation and temperature are produced for each hillslope. To asses the impact of
interpolation and its coarse graining at hillslope scale, as requested by the rainfall-runoff
model, we analyzed the discharge forecasting by using all four kriging methods. The DK
and LDK performances are better that the OK and LOK for discharge forecasting. The
GOF index of the simulated with observed discharge shows that the model performance
is acceptable. Using discharge measures inside the basin, it was possible to quantify the
reliability of internal discharges by assuming the validity of model parameters calibrated
at the overall outlet. The model performances actually maintain similar performances at
the interior sites.

Eventually, Priestley-Taylor method is used to estimate the evapotranspiration compo-
nents of the water budget, and to infer the relative storage of water under the hypothesis
of stationarity (null storage) at the 17th year. This hypothesis is sufficient to set a value
for the mean PT α' coefficient apt to obtain the mean actual ET. By moving the null stor-
age hypothesis along the first 17 years, we obtain variable values of the PT α' that we can
interpret as an estimate of the error in ET to be accumulated with uncertainty produced
in precipitation and discharge estimate. Changing the length of years of closure assump-
tion,starting from first year to 17th years assumption,it provide mean $\alpha' = 0.56 \pm 0.1$. To
consider both the atmospheric demand and local water storage supply at each hillslope
for ET estimation, the PT α' is optimized coupled with the HYMOD storage information
and PT radiation budget for five year null storage assumption (Budyko assumption).

The annual variability of the rainfall is as high as 1400 mm, with minimum annual J
of 1355 mm in 1995/1996 and maximum 2700 mm in 2010/2011. The low in errors of Q

annual estimation is due to its relatively good measurements and models to estimate at the basin scale. The inter annual variability in Q is high, with minimum annual Q of 1003 mm in 1995/96 and maximum 2072 mm in 2010/2011. Both the contribution and uncertainties of ET to the water budget is very high. While ET accounts 19-38% of J, its annual uncertainty is about 20% (148mm on average). Based on consistency of the water budget, it can be observed the high interannual variability of the fluxes, with certainly the variability of J dominating it. In all years Q is larger than ET, and vice versa. Either (relative) positive and negative water storages have been found. NewAge produces estimates for any hour of the year, and estimation of each component can be obtained actually for any hour, and for any subcatchment, even if with large uncertainty inherited, for instance, from the error in transposing Hymod model parameters, from the outlet to the interior point of the basin. With all the disclaimers of the case, the system once setup on a basin, can anyway produce data which can be of real interest in many practical cases of water management.

COMPARATIVE EVALUATION OF DIFFERENT SATELLITE RAINFALL ESTIMATION PRODUCTS AND BIAS CORRECTION IN THE UPPER BLUE NILE (UBN) BASIN *

In this chapter, a solution to the practical problem of water budget modelling input (precipitation) when dealing with large scale hydrology or basin with paucity of in situ observation, is investigated. In this study, five high resolution satellite products (3B42V7, CMORPH, TAMSAT, SM2R-CCI, and CFSR) are compared and analysed using the available in situ data in one of the most topographically and climatologically complex regions, the Upper Blue Nile basin. Considering three goodness-of-fit indexes, correlation, bias and root mean square error (RMSE) between the SREs and ground-based gauge rainfall, CMORPH, TAMSAT and SM2R-CCI outperform the other two. Furthermore, a confusion matrix is used to investigate the detection ability of satellite rainfall products for different rainfall intensities. TAMSAT has the highest (91%) detection skill for dry days, followed by CFSR (77%). On the contrary, SM2R-CCI has the highest accuracy index for medium rainfall ranges (10-20 mm). The empirical cumulative distribution ($ecdf$) mapping technique is used to correct the SREs intensities distribution. This method provides a means to improve the rainfall estimation of all SREs, and the highest improvement is obtained for CMORPH (bias reduction from -72% to -1%).

6.1 Introduction

Rainfall is the primary component of the water balance and is, therefore, the key input for hydrological modelling and water resources analysis. Before any analysis for water resource modelling and/or management can be carried out, it is essential to answer how much water is flowing to the basin (Shaw et al., 2010). Traditionally, rainfall estimation for hydrological modelling and water resource analysis is available from ground-based rain gauges. However, there are many regions in the world where ground-based gauge data are scarce, if available at all, and estimation of spatial rainfall field from ground-based gauge data is elusive. Recently, satellite rainfall estimates (SREs) provide viable alternative options (Ward et al., 2011; Tian et al., 2007; del Jesus et al., 2015; Gebremichael and Hossain, 2010). The key advantage of SREs is that they provide spatially and temporally continuous data that can be used to capture the variability of rainfall. However, the retrieval of rain rate from satellite data is not straightforward and, hence, over the past decades, numerous satellite rainfall estimation algorithms, applied to different satellite sensors, have been developed. For instance, we can mention the Tropical Rainfall Measuring Mission (TRMM) Multisatellite Precipitation Analysis (TMPA, (Huffman et al., 2007; Kummerow et al., 1998)), the Climate Prediction Center (CPC) morphing technique (CMORPH, Joyce et al. (2004)), the Precipitation Estimation from Remotely Sensed Information Using Artificial Neural Networks (PERSIANN, Sorooshian et al. (2000)) and recently products based on the novel SM2RAIN algorithm (Brocca et al., 2014). All these products vary in terms of resolution (spatial and temporal) and accuracy, hence, their performances and drawbacks for operational application in water resources modelling must be assessed.

The Blue Nile basin, particularly the Upper Blue Nile basin (hereinafter UBN), is one of the most physically and socially complex basins in Africa, but poorly covered by rain gauges. The Basin is the part of trans-boundary river basin, where different countries have different policies and legal regimes, sometimes with contrasting interest. This encompasses a challenge on the basin water resource development. Due to the lack of in situ data, most hydrological studies in the region are limited to small basins where there are relatively better hydrometeorological data (Rientjes et al., 2011; Uhlenbrook et al., 2010; Tekleab et al., 2011; Wale et al., 2009; Kebede et al., 2006; Bewket and Sterk, 2005; Steenhuis et al., 2009; Conway, 1997; Mishra et al., 2004; Mishra and Hata, 2006). These studies usually pay little attention to a proper spatio-temporal rainfall characterisation (Kim et al., 2008).
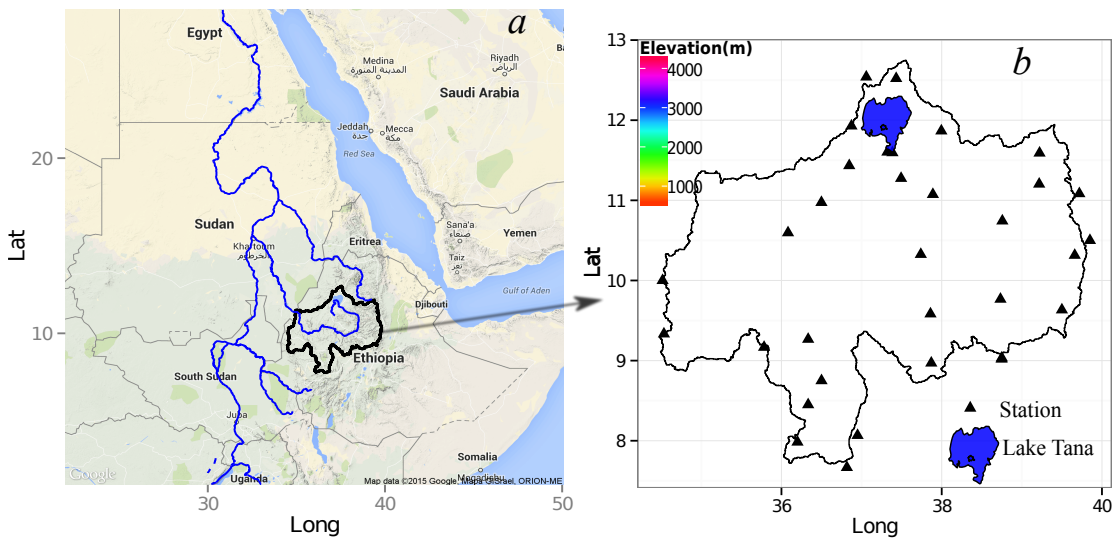
Figure 6.1: The geographic location of Upper Blue Nile basin in the Nile basin (a) and digitale elevation model of the basin (b). The points in figure b are the meteorological stations used for this study.

Several validation studies of SREs have been conducted in the Ethiopian UBN basin (Dinku et al., 2007, 2008; Haile et al., 2013; Gebremichael et al., 2014; Worqlul et al., 2014; Romilly and Gebremichael, 2011; Hirpa et al., 2010; Habib et al., 2012). For instance, two comparative studies by Dinku et al. (2007) and Dinku et al. (2008) on high temporal (less than and equal to 10 days) and spatial (less than or equal to 1^0) resolution products shows that CMORPH, TAMSAT (Grimes et al., 1999) and TRMM 3B42 (the gauge-corrected version of TMPA products, Huffman et al. (2007)) are three SREs with good accuracy and potentially useful for hydrological applications in the region. Dinku et al. (2008) reported that CMORPH works better in Ethiopia than other regions of Africa, while Haile et al. (2013), studying the accuracy of CMORPH over a subbasin of UBN basin for three months, found poor accuracy with respect to other regions. More recently, Gebremichael et al. (2014), by designing experimental rain gauges for two summer seasons in two experimental locations (one in the lowlands and one in the highlands) of the UBN basin, examined the accuracy of three high-resolution satellite rainfall products (CMORPH, TRMM 3B42RT - the real-time version of TMPA - and TRMM 3B42). Regarding the relationships between SREs goodness-of-fit values and topography (particularly elevation) of the experimental sites, SREs overestimate the mean rainfall rate in the lowlands and, vice versa, underestimate at the highland site.

On 3-hourly time scales, the SREs miss more rainfall at the highland sites than at the lowland sites. Worqlul et al. (2014) extended these studies by comparing TRMM-3B42 with two other products (Multi-Sensor Precipitation Estimate‚ÄìGeostationary (MPEG) and the Climate Forecast System Reanalysis (CFSR)) in the Lake Tana subbasin in 2010 and found that MPEG and CFSR are far better than TRMM-3B42. CFSR is one of the highest resolution (time and space), multiyear, global gridded reanalysis rainfall dataset, and is used as input to the rainfall-runoff modelling in Gumera basin (subbasin of the UBN) and provides similar performances to the ground-guage data model inputs (Fuka et al., 2014). This study compliments the above mentioned researches (Dinku et al., 2007, 2008; Haile et al., 2013; Gebremichael et al., 2014; Worqlul et al., 2014), which have been conducted either for some subbasin or only for short time series in some designated experimental sites.

The objectives of this chapter are twofold: 1. to comparatively evaluate five daily SREs, i.e. four commonly used products (TRMM 3B42, CMORPH, TAMSAT, and CFSR) and the new SM2R-CCI (see Data sets section) product; and 2. to assess the potential of improving the SREs by using a bias correction method. In the view of evaluating the SREs for hydrological modelling, the study aims to unify all the above results by analyzing relatively high resolution (daily) SREs against available daily gauged rainfall data for a 10 year period (2003-2012). It is known that some products such as CMORPH and IMERG are available at higher resolution (at sub daily time steps i.e. 30 min and 3 hour). However, in this study, we have focused at daily time steps due to two reasons. Firstly, at large basin scale as UBN, the hydrological simulation at daily time step can be considered high resolution. Secondly, there are no in-situ measured data to evaluate the SREs estimation skills at sub daily time steps.

The chapter is organized as follows: section 6.2 provides a basic introduction to the study basin, followed by data descriptions (section 6.3) of both SREs (subsection 6.3.1) and ground-based data (subsection 6.3.2). Section 6.4 elaborates the methods used for comparison and for bias correction of SRE. The comparison of SREs in relation to the ground-baed data and the bias correction results, and the conclusions of the study are presented in section 6.5 and 6.6 respectively.

6.2   Study area

The study basin is the Upper Blue Nile (UBN) basin. The UBN basin contributes to 60% Of the total contribution (85%) of the Ethiopian highlands to the Nile river flows

(Abu-Zeid and Biswas, 1996; Conway, 2000). The total area of UBN enclosed at the Ethio-Sudan border is about 175,315 km^2 (figure 7.1). The UBN originates at Lake Tana, and flows to Sudan, where it meets the White Nile River at Khartoum. The large scale hydrological behavior of the basin is described in a series of studies (Conway, 1997, 2000, 2005; Conway and Hulme, 1993). Its hydrological behavior is characterized by high spatio-temporal variability. Since UBN basin has the lion's share of the total Nile flow, it is the economic mainstay of downstream countries (Sudan and Egypt). Moreover, the Ethiopian highlands are highly populated and have high water demands for irrigation and domestic uses.

The topographic distribution of the basin is shown in figure 7.1 b. The topography of UBN is very complex, with elevation ranging from 500 m in the lowlands at the Sudan border to 4160 m in the upper parts of the basin. Due to the topographic variations, the climate of the basin varies from cool (in the highlands) to hot (in the lowlands), with large variations in a limited elevation range. The wet season, with low temperatures, is from June to September, while the hot season is from March to May. Three controlling mechanisms of the rainfall characteristics of the UBN, and Ethiopia in general (Seleshi and Zanke, 2004), are the Intertropical Convergence Zone (ITCZ) that mainly derive the wet monsoon rainfall in the wet season (June to September), the Saharan anticyclone that generates the dry and cool northeasterly winds in the dry season (from October-February), and the Arabian highlands that produce thermal lows in the mild season (February - May). The mean annual rainfall and potential evapotranspiration of the UBN basin are estimated to be in the ranges of 1200-1600 mm and 1000-1800 mm respectively (Conway, 1997, 2000), with high spatio-temporal variability. The annual temperature mean is 18.5^o with small seasonal variability.

6.3 Data sets

6.3.1 Satellite Rainfall Estimate (SRE) products

In this section, we describe five high resolution SRE products, TRMM 3B42, CMORPH, TAMSAT, CFSR, and SM2R-CCI, that will be used for rainfall estimates in the following sections. All the products are available at spatial resolution of 0.25^o (except TAMSAT which is 0.035^o) and temporal resolution of subdaily to daily. To obtain the rainfall estimation, some of these products have different procedures (i.e., SM2RAIN as described below), than the rainfall retrieval algorithm from passive microwave (PMW) / infrared

(IR) observations. Nevertheless, here, we are referring SRE for all the five satellite-based rainfall products. The detailed description of each algorithm/product can be referred to in the literature cited in table 6.1.

TRMM is the joint NASA and JAXA mission originally aimied at studying tropical rainfall (Kummerow et al., 2000; Rozante et al., 2010). TRMM 3B42 version 7 (hereinafter defined as 3B42V7) (Huffman and Bolvin, 2013; Huffman et al., 2007) is among the TMPA products with high spatial resolution of (0.25^o) and high temporal resolution (3-hour). The spatial coverage extends from 50 degrees south to 50 degrees north latitude. For this study, 3B42V7 is obtained from NASA‚Äôs TRMM Online Visualization and Analysis System (Liu et al., 2007, 2012) (`http://disc.sci.gsfc.nasa.gov/precipitation/tovas/`). The detailed information on processing and generation of the 3B42V7 can be found in the literature cited in table 6.1. We underline here that the 3B42V7 product is corrected with rain gauge observations (i.e., it is not based only on satellite data). Indeed, the 3-hourly rainfall fields are corrected on a monthly basis with the Global Precipitation Climatology Centre (GPCC) monthly rain gauge dataset by using inverse-error-variance weighting methods (Huffman and Bolvin, 2013; Huffman et al., 2007).

The CMORPH product (Joyce et al., 2004) is a rainfall estimation method that mainly relies on PMW observation. It uses precipitation estimates that have been derived from low orbit satellite PMW observations exclusively, and whose features are transported via spatial propagation information that is obtained from geostationary satellite IR data (Joyce et al., 2004). CMORPH is a near global product (60° north and south) and provides data at 3 hourly and daily resolution since 1998; and at temporal resolution of 30-min since December 2002. The 3-hourly precipitation at 0.25^o spatial resolution data are used for this study.

CFSR is one of the SREs assessed in this study. It is a reanalysis product that combines the weather forecasts generated by the National Weather Service's NCEP Global Forecast System, and satellite data (Saha et al. (2010)). The analysis is reinitialized every 6-hours, and it is obtained at hours 00:00, 06:00, 12:00, 18:00 UTC. The spatial resolution of CFSR is about 38 km, and it is available since 1979.

Tropical Applications of Meteorology Using Satellite and Ground-Based Observations (TAMSAT) (Grimes et al., 1999; Tarnavsky et al., 2014), is a rainfall product specialized for Africa. It has been providing 10-day rainfall estimates since 1983 and recently (since 2013) daily products are available. The TAMSAT rainfall estimation algorithm is calibrated using the historical rain gauges, TAMSAT African Rainfall Climatology And Time-series. The methodology and algorithms of the TAMSAT rainfall product derive

Table 6.1: Summary of the different satellite products used in this study. Because CMORPH is available since December 2002, the study is based on only 10 years of data. However, the statistical indexes analyzed for all the years with available data is almost the same and the difference is not statistically significant.

SREs	Spatial res.^{o}	Temporal res.	Available	Data used	References
3B42V7	0.25	3-hourly	1998-present	2003-2012	Zhao and Weng (2002); Huffman et al. (2007); Prakash et al. (2015); Kumar et al. (2014); Duan and Bastiaanssen (2013); Romilly and Gebremichael (2010)
CMORPH	0.25	3-hourly	1998-present	2003-2012	Ferraro (1997); Joyce et al. (2004); Haile et al. (2015); Romilly and Gebremichael (2010); Gao and Liu (2013)
TAMSAT	0.0375	daily	1983-present	2003-2012	Grimes et al. (1999); Maidment et al. (2014); Tarnavsky et al. (2014)
CFSR	0.3125	6-hourly	1979-present	2003-2012	Saha et al. (2010, 2006); Wang et al. (2011); Xue et al. (2011); Saha et al. (2014)
SM2R-CCI	0.25	daily	1990-present	2003-2012	Brocca et al. (2013, 2014); Ciabatta et al. (2015)

from Meteosat imagery and gauge data using contemporaneous cold cloud duration fields (Tarnavsky et al., 2014; Maidment et al., 2014). The product is available at a resolution of 0.0375^o at nadir (~4 km). Some studies (Laurent et al., 1998; Thorne et al., 2001; Chadwick et al., 2010; Maidment et al., 2013; Jobard et al., 2011) find that TAMSAT estimates (over ten days) are comparable to the other SREs, even better in some cases, when compared with gauge data. Dinku et al. (2007) showed that TAMSAT (over ten days) rainfall estimates perform as well as CMORPH and TRMM (version 6) in Ethiopia‚Äôs central highlands. However, the new TAMSAT daily rainfall estimates performances have not yet been assessed.

The SM2R−CCI rainfall product is based on the SM2RAIN method (Brocca et al., 2013) and is obtained from the CCI soil moisture product (Dorigo et al., 2015) for the period 1990-2013 at $0.25^{¬\infty}$ spatial resolution. The SM2RAIN algorithm is based on the inversion of the water balance equation by considering the soil as a natural rain gauge (Brocca et al. (2014)). The SM2RAIN-derived product provides an integrated estimate of rainfall (daily in this case). In this study, SM2RAIN is applied for the first time to the CCI soil moisture product, allowing to obtain a long-term (24-year) daily rainfall product, by using the same approach given in Ciabatta et al. (2015). Specifically, the SM2RAIN parameter values are calibrated by using the 3B42V7 product as benchmark in the period 1999-2005. In the evaluation period, there is 3 years (2003-2005) of overlap with the calibration period (1999-2005) between 3B42V7 and SM2R-CCI, that could

(slightly) affect the independency between the two products. However, the use of different length of data sets for SRE evaluation statistics (see section 6.4.1), which also have longer period of independent data, helps to understand if this dependency affects the results considerably. We note that this calibration is performed here for the UBN study area but, potentially, it can be easily applied on a global scale.

6.3.2   Rain gauge rainfall data sets

Rain gauges across the UBN basin are very scarce. In this study, 35 daily rain gauges are used. The in situ data is obtained from the national meteorological agency of Ethiopia. The spatial location and elevation of the stations used for this study are shown in figure 7.1b. The data are manually checked for quality and the final refined data are used in the following analysis. Looking at the distribution of the stations, the upper part of the basin has relatively higher station density than the lowland and the middle of the basin (figure 7.1b).

6.4   Methodology

The daily rainfall data estimates from 3B42V7, CMORPH, TAMSAT, CFSR, and SM2R-CCI at grid level are compared with daily rainfall data from raingauges. Since the density of the rain gauges is very low and the topography of the study area is complex, we decided not to interpolate the rainfall data over the spatial fields but to compare directly point rainfall at the stations, with the the grid rainfall as in (Porcù et al., 2014; Worqlul et al., 2014).

6.4.1   Performance metrics

To make the comparison we used the products at daily time steps. Therefore, all the SRE products at sub daily time steps are accumulated into daily totals. Since we are interested in assessing the entire performances of the SREs in the basin, the statistics are calculated for the whole data set (including zeroes). We used the Pearson linear correlation coefficient (r), the Root Mean Square Error (RMSE), and the BIAS goodness-of-fit (GOF) indexes, as defined in appendix B. An important question concerning SREs is their error sensitivity and variability to the length of data used for evaluation. In order to assess the effects of data series length on the performance statistics (GOF statistics), we used different sets of data series length for estimation of GOFs between SREs and

gauge observed data. We have evaluated the SREs error statistics progressively for 1, 4, 7 and 10 year period. The 1 year means the analysis is based on only the first year of the data set (2003), 4 years from 2003 to 2006, 7 years from 2003 to 2009 and 10 years the whole period. Accordingly, we calculate the GOF statistics for the four data sets with different length.

To further investigate the errors and prediction capacity of SREs, we decomposed the errors in classes as in (Salio et al., 2015; Cohen Liechti et al., 2012; Haile et al., 2013). They use two class of data, i.e., rain and no-rain distinction, and the products are evaluated using the accuracy index, given by:

$$Accuracy = \frac{N_a + N_d}{N_a + N_b + N_c + N_d}$$
(6.1)

Where the terms of the equation are described by the confusion matrix given in table 6.2.

Table 6.2: Confusion matrix based on the four possibilities of SRE detection of the guage observed rainfall. The four possibilities are true positive (a), false positive (b), false negative (c), and true negative(d).

	SREs:Yes	SREs:NO
Gauge: Yes	a	b
Gauge: NO	c	d

In this study, we further analyze the detection skill of the SREs by subdividing the SREs into several rainfall classes based on observed rainfall amounts. Specifically, the SREs are divided into 7 rainfall classes (all in mm/day): ≤ 0.1, 0.1-2; 2-5; 5-10; 10-20; 20-40; ≥ 40. The first class (class 0) characterizes dry days. In literature, separation of dry days is obtained by imposing a minimum detectable rainfall threshold. This threshold value is controversial, as it ranges from 0.1 to 1 mm/day (Jakob Themeßl et al., 2011; Moon et al., 1994; Lázaro et al., 2001; Schmidli and Frei, 2005; Kisaka et al., 2015). In this study, we use 0.1 mm as suggested by World Meteorological Organization (Jarraud, 2008).

The confusion (or matching) matrix of different SRE amounts versus rain gauge measured amounts is estimated for each rainfall class. As it can be seen in the results section, multi-class confusion matrix tells the proportion of SREs in different classes, shown on the y-axis, for a given observed rainfall classes, in the x-axis. In the ideal situation, where the SREs are perfectly consistent with the observed data, the matrix

would be an anti-diagonal matrix where all the entries are zero except on the diagonal going from the lower left corner to the upper right corner with ones.

6.4.2 Bias correction

The comparative evaluation study and selection of the best product may not always give an accurate enough product for hydrological modelling. Therefore, further bias correction of SREs could be important to obtain reasonable results (AghaKouchak et al., 2012). In the second section of the analysis, systematic bias correction of SREs is performed. The empirical cumulative distribution function ($ecdf$) mapping bias correction technique, initially proposed by (Panofsky et al., 1958), and recently applied for hydrological data correction by (Themeßl et al., 2012; Michelangeli et al., 2009; Iizumi et al., 2011; Maurer and Pierce, 2014; Hwang and Graham, 2013), is used. In this method, the $ecdf$ of the SREs is first matched to the $ecdf$ of the gauges observed rainfall estimates, generating a correction function depending on the data percentile. The correction function is derived for each percentile. In the case a new extreme value is available in the SREs used in the validation period/set, the correction function, based on the relationship between SREs at validation points and correction function generated during validation period, is linearly extrapolated. Then, the correction function is applied to the $ecdf$ of the SREs ($ecdf_i^{S,cal}$) and the $ecdf$ of the ground-gauge data at calibration points ($ecdf_i^{G,cal^{-1}}$) to transfer the original SREs ($S_{t,i}^{val}$) to the corrected SREs ($S_{t,i}^{Corr,val}$) at other validation points, as given by (Michelangeli et al., 2009; Themeßl et al., 2012)

$$(6.2) \qquad S_{t,i}^{Corr,val} = ecdf_i^{G,cal^{-1}}(ecdf_i^{S,cal}(S_{t,i}^{val}))$$

where $S_{t,i}^{Corr,val}$ is the new corrected SRE for a given stations ,i and t time steps. The $ecdf^{-1}$ is the inverse of the $ecdf$. S and G are SRE and gauge rainfall estimate, respectively. The subscript t,i are are the time steps and station number, respectively.

As shown in different studies (Cai et al., 2015; Hossain and Huffman, 2008; Ebert et al., 2007), biases and errors in SREs exhibit space and time variability. To reduce the effect of spatial variability in bias correction procedure, the 35 stations are systematic divided into two groups: 17 stations for calibration and 18 stations for validation as shown in (figure 6.2). The correction function (equation 6.2) is constructed based on all stations combined $ecdf$ matching between the observed rainfall and SREs at calibration stations. The function generated is used to develop new corrected SREs that can be evaluated at validation stations. While this approach may not provide the highest performance at a

particular station, it is useful to assess the basin scale performance of the bias correction procedure. Similarly, to reduce the effect of temporal SREs errors, the bias correction procedures is calculated for each season independently (Bennett et al., 2014). For the sake of simplicity, as the basin receives 75% of the rain in summer (Mellander et al., 2013), we apply the procedure only in the summer season (June, July, and August).
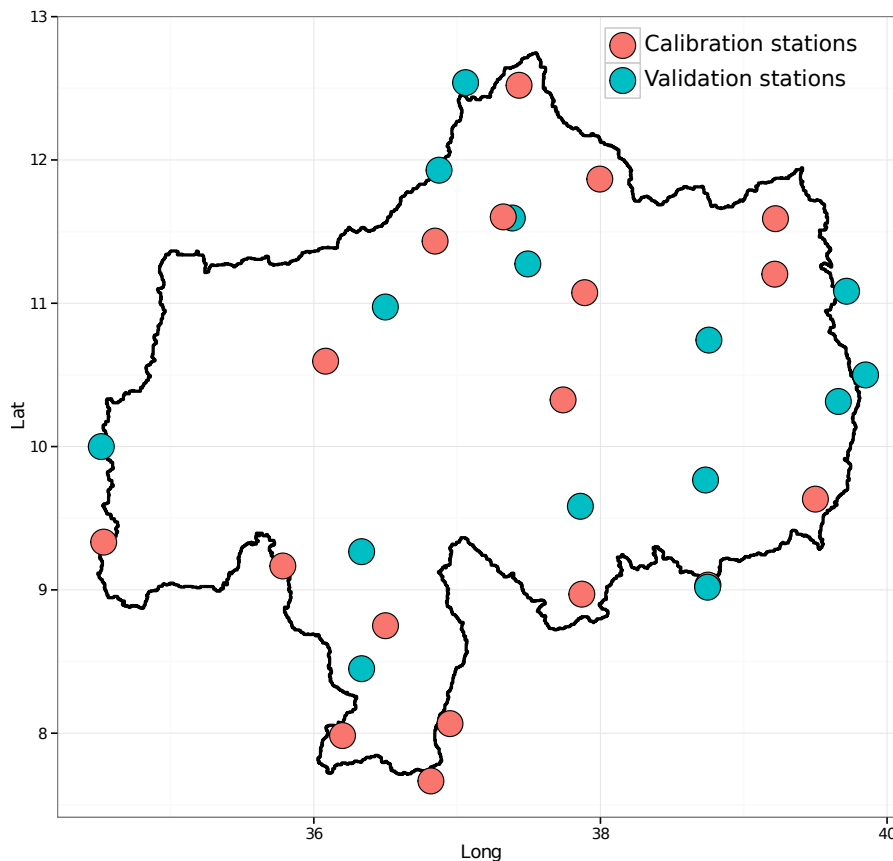
Figure 6.2: The spatial distribution of stations used to generate the correction function (calibration stations) and used to evaluate the performances of the $ecdf$ mapping method (validation points).

For validation of time series bias correction procedure, the data set (10 years of data for all stations) is split in to two; the first 5 years (2003-2007) to develop the transfer function, and the next 5 years (2008-2012) for subsequent evaluation of the bias correction procedures using the same approach of spatial cross validation. The procedures of transfer function generation and validation are applied for all stations combined.

6.5 Results and Discussions

The study results are presented in two subsections. The first part comparatively evaluates the five daily SREs against the gauge observed rainfall data. The second subsection focuses on the results of SREs bias correction using $ecdf$ matching method.

6.5.1 Comparative evaluation of SREs

The five SREs are analyzed based on GOF statistics (r, RMSE and BIAS) and on their detection capability (confusion matrix and accuracy index). In figure 6.3, we summarized the GOF statistics between the SREs and gauge observations by splitting the 10 years of data into subsets of 1, 4, 7 and 10 years.

Figure 6.3 illustrates that GOF statistics generally show stability with increasing length of data series used for the evaluation of SREs. For instance, for 3B42V7, the median value of r slightly decreases (from 0.5 to 0.47) with increasing the length of data period from 1 to 10 years. Similar patterns are observed for all the other SREs, except SM2R-CCI which shows an overall improvement when the whole period is considered. The latter result is expect due to the higher accuracy and temporal resolution of the CCI soil moisture product (Dorigo et al., 2015) on which the SM2R-CCI product is built on. The correlation coefficient comparison between the SREs shows that CMORPH, TAMSAT and SM2R-CCI perform better than the other two SREs. The same figure demonstrates that the correlation of CFSR is low and characterized by high variability as shown by the long boxplot. The median r value of 3B42V7 (0.47) is generallyhigher than the values reported by Worqlul et al. (2014), which however has a maximum value of 0.54 (monthly scale analysis).

The data analysis for 1, 4, 7, and 10 year data sets illustrates that also the effect of length of the data set on RMSE values is rather limited (figure 6.3, second row). For most SREs, RMSE median values for 1 year validation is smaller (likely due to the selection of 2003 that is a dry year), and it increases to 4 year, and then it keeps stable for 7 and 10 years. The comparison between the SREs for the 10 years evaluation results is consistent with the correlation results, i.e., the RMSE value of TAMSAT (6.85 mm/day), SM2R-CCI (6.88 mm/day), and CMORPH (7.3 mm/day) shows better performances in comparison to the other SREs.

The daily RMSE values of CFSR and 3B42V7 by Worqlul et al. (2014) at a specific subbasin (Lake Tana watershed) is 6.2 and 4.0 mm/day, respectively. These values are smaller than our results (CFSR=8.9 mm/day, 3B42V7 = 7.52 mm/day). The difference
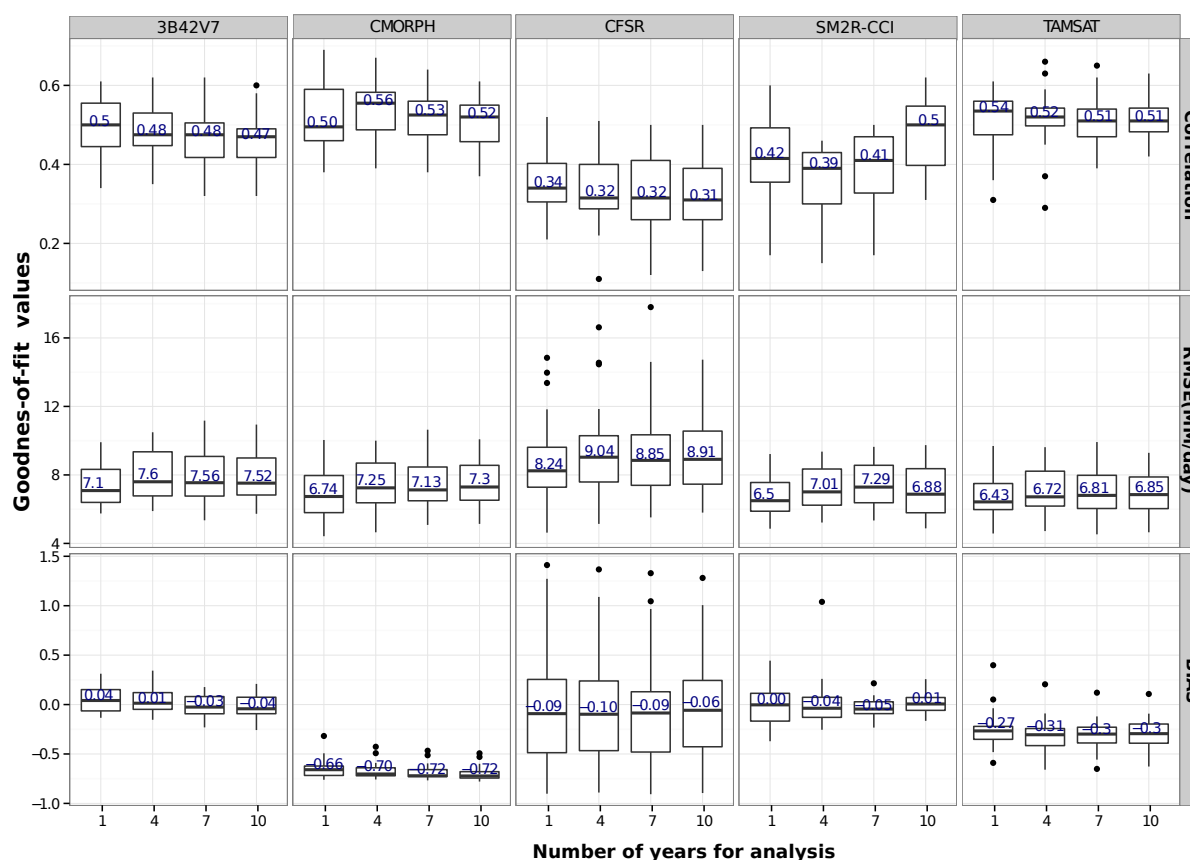
Figure 6.3: Comparison of SREs with the ground-based rainfall estimation using (above) correlation (-), (middle) Root mean square error (mm/day) and (below) BIAS (-). In the boxplot, the horizontal line in the middle shows the median, the bottom and top end of the box shows the 25th and 75th percentile, respectively, the whiskers (vertical line) shows the range of the data, of the GOF values. For CFSR and TAMSAT, some stations (with high annual gauge observed rainfall) shows outliers GOF values (dot in in the figure).

(as discussed below) could be due to the stations in the lowland area of the basin (the western part) which shows higher RMSE values than the eastern and north-eastern highlands where Lake Tana basin is located. Hence, it can be interpreted that RMSE of CFSR is smaller than the 3B42V7 in the highlands (to be specific Lake Tana basin), while the results in this study shows that at the whole UBN basin, 3B42V7 shows better performance (RMSE = 7.52 mm/day) than CFSR (RMSE=8.91 mm/day). The study of Young et al. (2014), in the Oromia region of Ethiopia, find similar results: TAMSAT and CMORPH have lower RMSE values in comparison to 3B42V7 at daily time steps. Based on the *r* and RMSE statistics, CMORPH outperforms 3B42V7, which is consistent with the results of Bitew et al. (2012) for the small subbasin of UBN basin, the Koga

watershed, but for a single year.

In general, the effect of data length on BIAS is very small, and it is valid for all the SREs (figure 6.3, third row). For instance, the BIAS for 3B42V7 decreases from 4% for 1 year evaluation to -4% in 10 years, the same level of BIAS but opposite sign. A similar slight decline in BIAS is shown for CMORPH (frm -66% to -72%) when the number of years in the analysis increases. The comparison of the five products using BIAS is not consistent with the products comparison using r and RMSE (figure 6.3, the third row). For instance, SM2R-CCI (0.001) has the lowest BIAS, followed by 3B42V7 (-0.042) and CFSR (-0.06). The low BIAS of SM2R-CCI has to be attributed to the use of 3B42V7 for the calibration of the parameter values of the SM2RAIN algorithm. Note that while CMORPH is better in estimating ground-gauge rainfall using the two previous statistics (i.e., r and RMSE), it is underestimating by 72%, thus being the most biased product of the five SREs. This could be because CMORPH is only based on satellite products, and not corrected using ground data as 3B42V7. TAMSAT, on average, is underestimating rainfall by 30%.
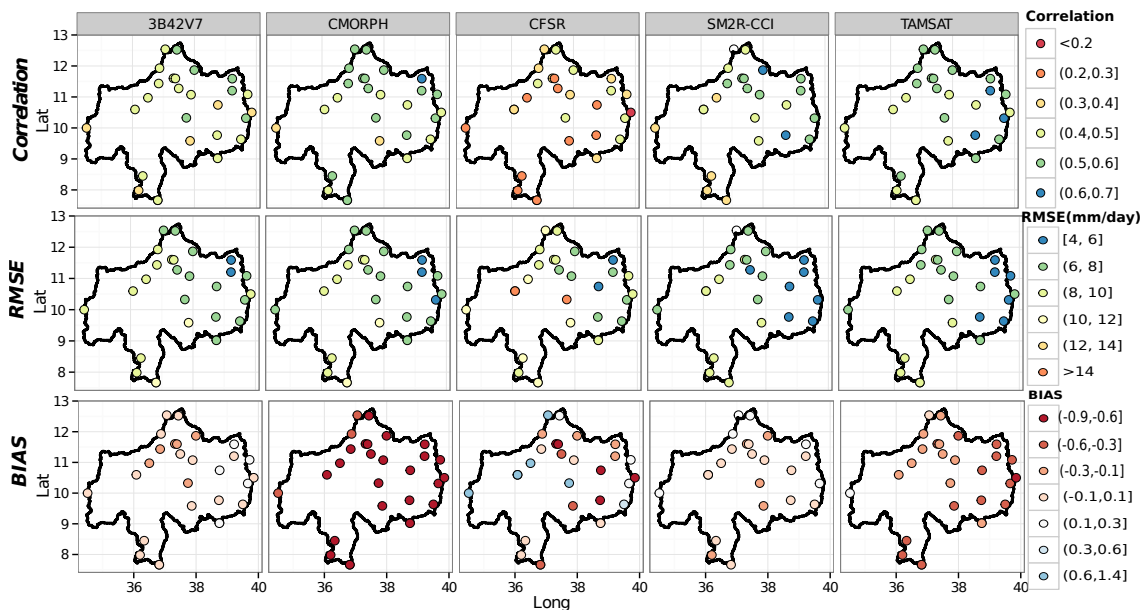
Figure 6.4: The spatial distribution of GOF values for different SREs: correlation coefficient (first row), RMSE (second row) and Bias (third row).

The spatial distribution of the the three GOF values (r, RMSE, BIAS) are presented in figure 6.4. Overall the distribution of the statistics can depict a spatial pattern, i.e., the correlations in the eastern and northeastern part of the basin are higher than western and southwestern part. Similar pattern can be inferred from the RMSE and BIAS

statistics that are smaller in the eastern part (the highlands), while they are higher in the western lowlands of the basin. The BIAS statistic shows a less pronounced pattern in comparison to r and RMSE. While CMORPH shows high underestimation at all stations, 3B42V7, CFSR, and SM2R-CCI shows the same described pattern. Generally, CFSR has less spatial pattern in the statistics, and has relatively high spatially mixed results (figure 6.4).As elevation increases from the west towards the east and northeast part of the basin, the pattern can be partly explained by elevation. The general pattern is that SRE performance increases with elevation (data not shown). Gebremichael et al. (2014) did a comparison study between the highland and lowland sites, when using RMSE and BIAS, they found the similar result. I.e., the highland sites show better performances than the lowland sites.

Following the results of GOF analysis, the comparison of SREs using the confusion matrix and the accuracy index is carried out. The confusion matrix in figure 6.5 summarizes the relative bias of SREs for a given observed rainfall class. To analyses the performances of each rainfall class, the SREs values were grouped based on the observed rainfall classes in the x-axis. For instance, the first column shows the distribution of SREs when the gauge recorded rainfall values ≤ 0.1: it describes the distribution of SRE records for this specific observed rainfall class.

3B42V7 (figure 6.5a) has the higher detection capacity for the first class (≤ 0.1 mm/day, 68%), with lower performances for the other rainfall classes (≤ 26%). Except for the first and second rainfall classes (≤ 0.1, 0.1-2mm), which have high detection capacity (73% and 52%, respectively), the higher rainfall classes (≥ 10mm) show very low detection by CMORPH (below 5%). It is important to note that apparently CMORPH does not detect observed rainfall ≥ 20 mm at all. In general, compared to 3B42V7, CMORPH has a systematic underestimation for all the rainfall ranges (figure 6.5b). The confusion matrix analysis results of CFSR (figure 6.5c) show that the pattern in the detection capacity is similar to CMORPH for the first class and to 3B42V7 for the other classes.

Two important results of the SM2R-CCI confusion matrix (figure 6.5d) are its relatively higher detection capacities for medium rainfall values (from 5mm to 20mm) and relatively lower detection for lower rainfall intensities (38%), likely due to noise in soil moisture observations (see e.g., Ciabatta et al. (2015)). It is only SM2R-CCI that has detection capacity of 25% and above for rainfall ranges between 5 to 20 mm. In general, SM2R-CCI, being based on soil moisture, tends to aggregate the rainfall volume thus being more accurate in the estimation of accumulated rainfall than 3B42V7 and CMORPH that relies on the estimation of instantaneour rainfall rates. This result is also
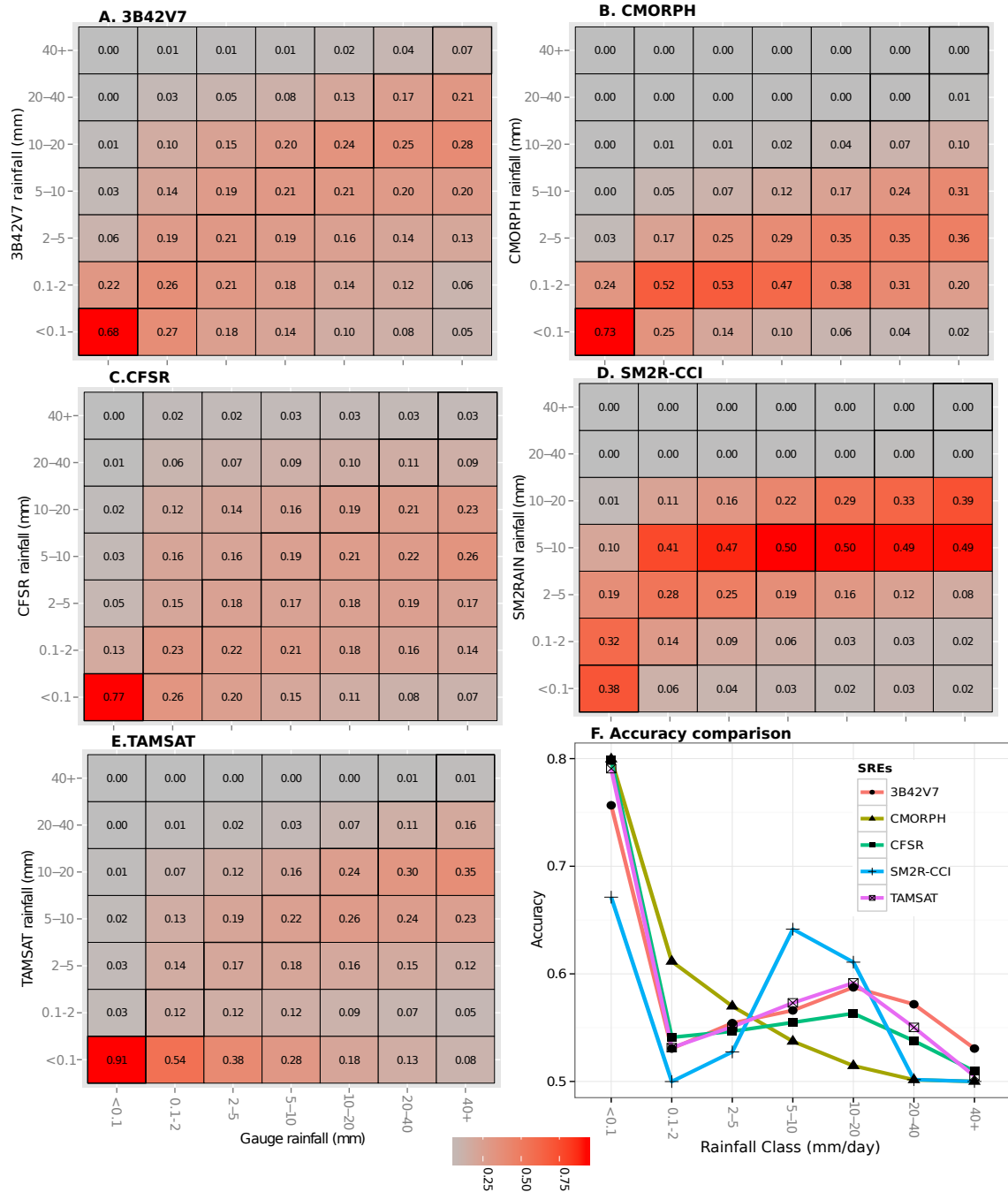
Figure 6.5: Confusion matrix that shows the proportion of observed rainfall classes in the x-axis reproduced by the different SREs (3B42V7 (a), CMORPH (b), CFSR (c), and SM2R-CCI (d), TAMSAT (e)) in the y-axis. Each value in the confusion matrix is the proportion of the gauge observed rainfall class (along column) that is estimated as a particular SREs class (along row). The comparison of SREs using accuracy index, for different rainfall classes, is shown in figure F. The statistics are based on the daily rain gauge data size of <0.1 mm (N = 71010), 0.1-2 mm (N = 11059), 2‚Äì5 mm (N = 8500), 5-10 mm (N = 8602), 10-20 mm (N = 8546), 20-40 mm (N=5141) and >40 mm (N = 1098).
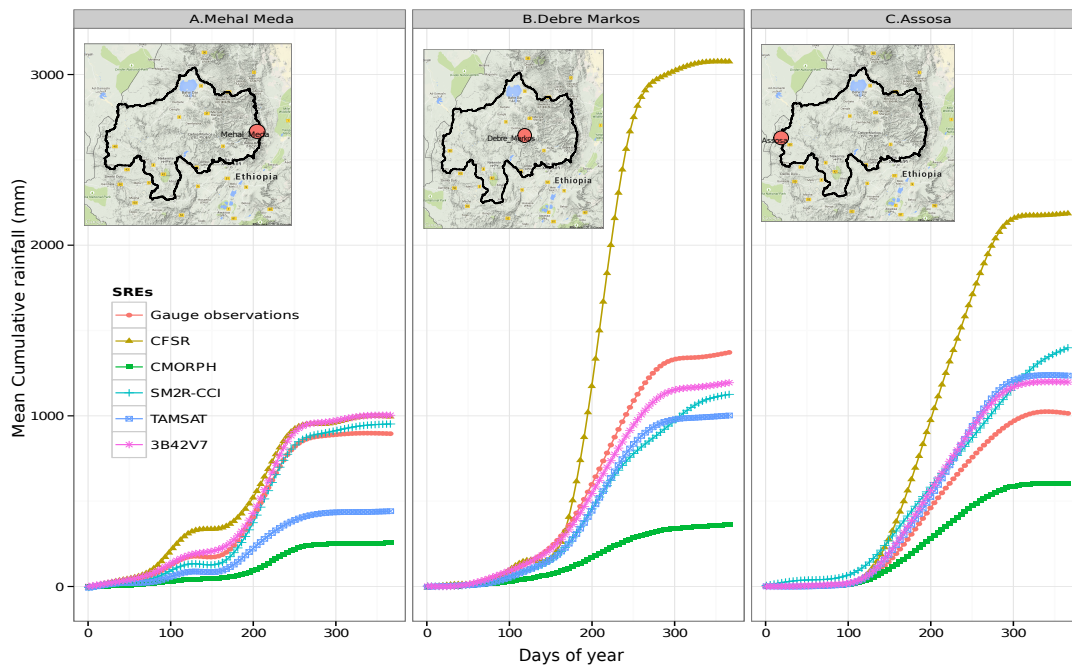
Figure 6.6: Annual mean cumulative rainfall estimations based on five SREs and gauges data.

important as it highlights the large potential that could be gained by the integration of these two kinds of SREs (e.g., SM2R-CCI and CMORPH or 3B42V7 or TAMSAT).

Among the five SREs, TAMSAT has the highest detection capacity for lowest rainfall intensities (91%). For all classes, TAMSAT has the highest missing rate and the highest recorded is for the 0.1-2 mm observed rainfall class (54%), while the systematic bias for all the classes is relatively low (figure 6.5e). The SREs detection capacity is further evaluated by the overall accuracy capacity, and the comparison is shown in figure 6.5f. The result confirms the confusion matrix analysis.

The time series rainfall summary analysis is useful for comparative evaluation, but does not provide insight into the aggregate effects of using different SREs on water resource modelling. Figure 6.6 shows the comparison of long term (2003-2012, 10 years), mean cumulative rainfall for different SREs and measured data. A sample of three stations systematically selected to represent different ranges of elevation and spatial location is used in the analysis. These are Mehal Meda, Debre Markos, and Assosa which are located at high (3084 meters), medium (2446 meters) and low (1600 meters) elevations, respectively. The spatial location of the three stations is shown in the maps plotted in figure 6.6. Four comments can be drawn:

1. Based on the three stations, the observed long term annual rainfall shows that the

effect of elevation is masked by the rainfall climatological regime difference (Mellander et al., 2013). Mehal Meda which is at the highest elevation has a lower mean annual rainfall than Debre Markos.

2. Although CFSR and CMORPH show consistent patterns across elevations, CMORPH always underestimates, whereas CFSR always overestimates rainfall. From this analysis, CMORPH and CFSR have a significant BIAS.

3. The errors on cumulative annual rainfall given TAMSAT, 3B42V7 and SM2R-CCI across elevation are rather contrasting. For instance, 3B42V7 and SM2R-CCI slightly overestimate in high and low elevation while underestimate in middle elevation. TAMSAT shows high underestimation in the highland station, and progressively overestimate in the lowland station.

4. The 10 year mean cumulative rainfall value of the five SREs differ tremendously. The total mean annual rainfall difference between the SREs is about 600 mm (in Mehal Meda), 2740 mm (in Debre Markos), and 1600 mm (in Assosa).

6.5.2   Bias correction using ecdf mapping

This subsection assesses and discusses the improvements obtained by using the bias correction function generated at the calibration stations (or calibration time series) and applied to the SREs at validation stations (or validation time series). This technique is evaluated i) by comparing the SRE ecdf and the gauge rainfall ecdf, and (ii) by computing statistics (e.g., BIAS, confusion matrix, and accuracy index) between ground data and the SREs before and after the correction.

Figure 6.7 shows the variance of SREs (before correction) $ecdf$ distribution from the gauge rainfall $ecdf$ distribution in the case of spatial cross-validation strategy. For all SREs except TAMSAT, it is shown that there is dry-day frequency underestimation. In comparison to the gauge observed rainfall, most SREs tend to overestimate very low (light) rainfall frequency („Äúdrizzling-effect‚Äù Wilcke et al. (2013)), as shown in $ecdf$ distribution at figure 6.7a. The observed drizzling traits for most SREs could be due to its large spatial scale representation in comparison to the point ground-gauge observation. To avoid this kind of effects, the selection of a proper threshold for dry/wet days plays an important role. In figure 6.7, the zoomed-out plot, gauge observed dry day frequency is used to determine the dry/wet threshold. However, in this approach, a problem arise when SRE dry-day frequency is much greater than the gauge observed rainfall (Themeßl
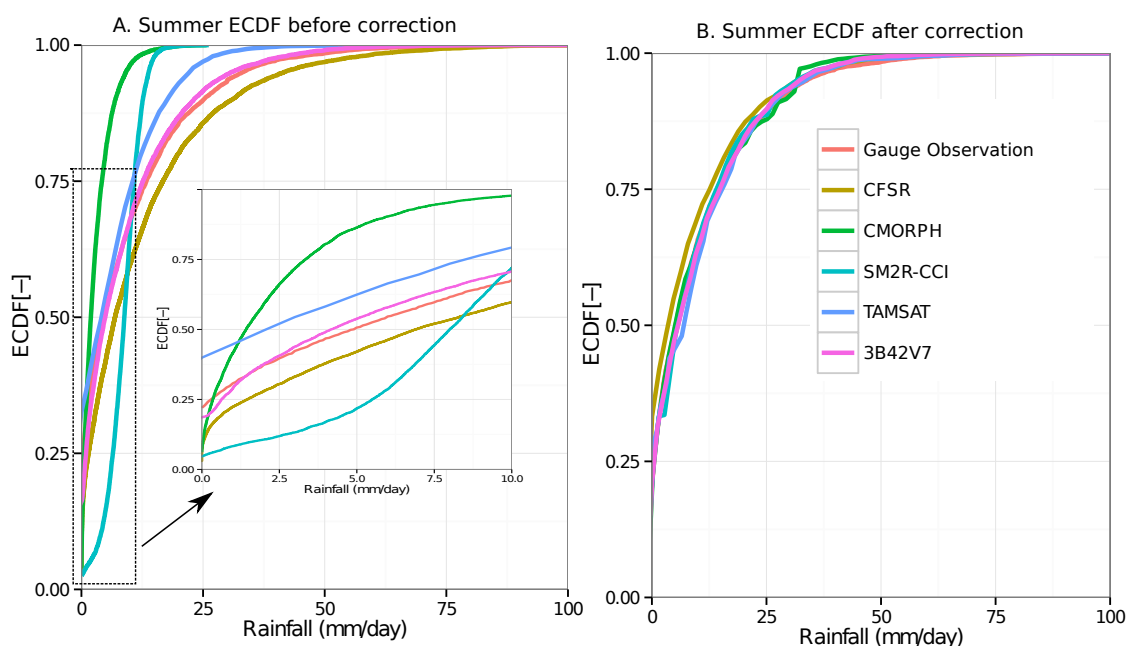
Figure 6.7: Cumulative distribution functions for different SREs and observed rainfall data before correction, used to construct the *ecdf* correction function (a), and SREs and observed data after the correction function applied for the validation data set (b). The zoomed-in plot in figure a is used to identify the dry and wet days for the SREs.

et al., 2012; Wilcke et al., 2013), and when dry-day frequency corresponds to high rainfall value for determining SRE threshold. The dry-day frequency matching approach , as shown in figure 6.7a, is used to define the threshold for CFSR (at 1 mm), 3B42V7 (at 0.5 mm) and CMORPH (at 0.3 mm) in the JJA period. However, for TAMSAT the dry-day frequency is already to high, and threshold is kept to the original 0.1 mm. Contrary to TAMSAT, SM2R-CCI dry-day and low intensity rainfall is much smaller than the gauge observation. For SM2R-CCI the dry-day frequency matching pointed to high threshold (4.5 mm). Since this will cut an important rainfall information, and as the use of this threshold (4.5 mm) reduce the bias correction performances, we also used the original 0.1 mm threshold for SM2R-CCI. Once the threshold information for the SREs is estimated, below these thresholds, the rainfall values are set to be zero, and above the threshold the *ecdf* of SREs are mapped to the *ecdf* of the observed data to construct the correction function. This correction function is thus used to correct new SREs.

The overall evaluation of SREs improvement from the bias correction application in both independent station (cross-validation) and time series GOF index (mainly bias), confusion matrix, and detection capacity (accuracy) are shown in table 6.3 and figure 6.8. The table 6.3 shows application of the *ecdf* bias correction in a spatial cross-validation

and future time series validation improves SREs. The result illustrate that for spatial cross-validation application, except CFSR, most SREs rainfall bias strongly improved. For instance, the highest bias observed was -70% for CMORPH, and the summer season bias correction method improves it to only -4% (table 6.3), followed by SM2R-CCI from -12% to 1%. The improvement in the detection capacity, however, is very small. This could be due to the use of a single correction function for the summer season as a whole. The construction of monthly correction functions could further improve the results. The results for time series split are very similar. The exceptional in the time series evaluation is 3B42V7 which does not show any improvement in bias.

The overall detection capacity improvement from the correction procedures is also presented in figure 6.8A and B. Generally, it improves the detection capacities and bias of the SRE products. For instance, for spatial cross-validation, large proportions of CFSR and SM2R-CCI estimates, 15 to 30% and 40 to 60% respectively, are concentrated in the 5-10mm rainfall range. The correction function improves this trend and BIAS for all classes is distributed to all classes of SREs estimations. The derivation of dry/wet rainfall threshold using the $ecdf$ matching also improves the detection capacity for the zero (dry) rainfall class, except for TAMSAT, which already has the highest detection capacity for dry days (figure 6.8). This is important because it gives an objective decision on reducing the small rainfall values by the SREs i.e drizzling effects of the products. In the case of TAMSAT, the correction function did not improve the detection capacity of the first class (class 0) because the products have no "drizzling effect" and instead overestimate dry days in comparison to the observed rainfall data. In this case, since it has the highest detection capacity for zero class (figure 6.5), the raw SREs are accepted for the first one or two classes and the $ecdf$ matching will be applied to high values. The correction in 3B42V7 improves the dry days estimation, however, it increases the missing rate to higher rainfall values. The result of future time series validation shows exactly the same pattern of improvement (figure 6.5B). The independent station and future time series validation results suggest that simple $ecdf$ bias correction procedure can be used to obtain better quality SREs at non-gauge sites and in future realization of UBN basin.

6.6   Conclusions

This chapter comparatively evaluates five satellite rainfall datasets over the Upper Blue Nile basin at daily time steps for 10 years, and uses $ecdf$ bias correction technique
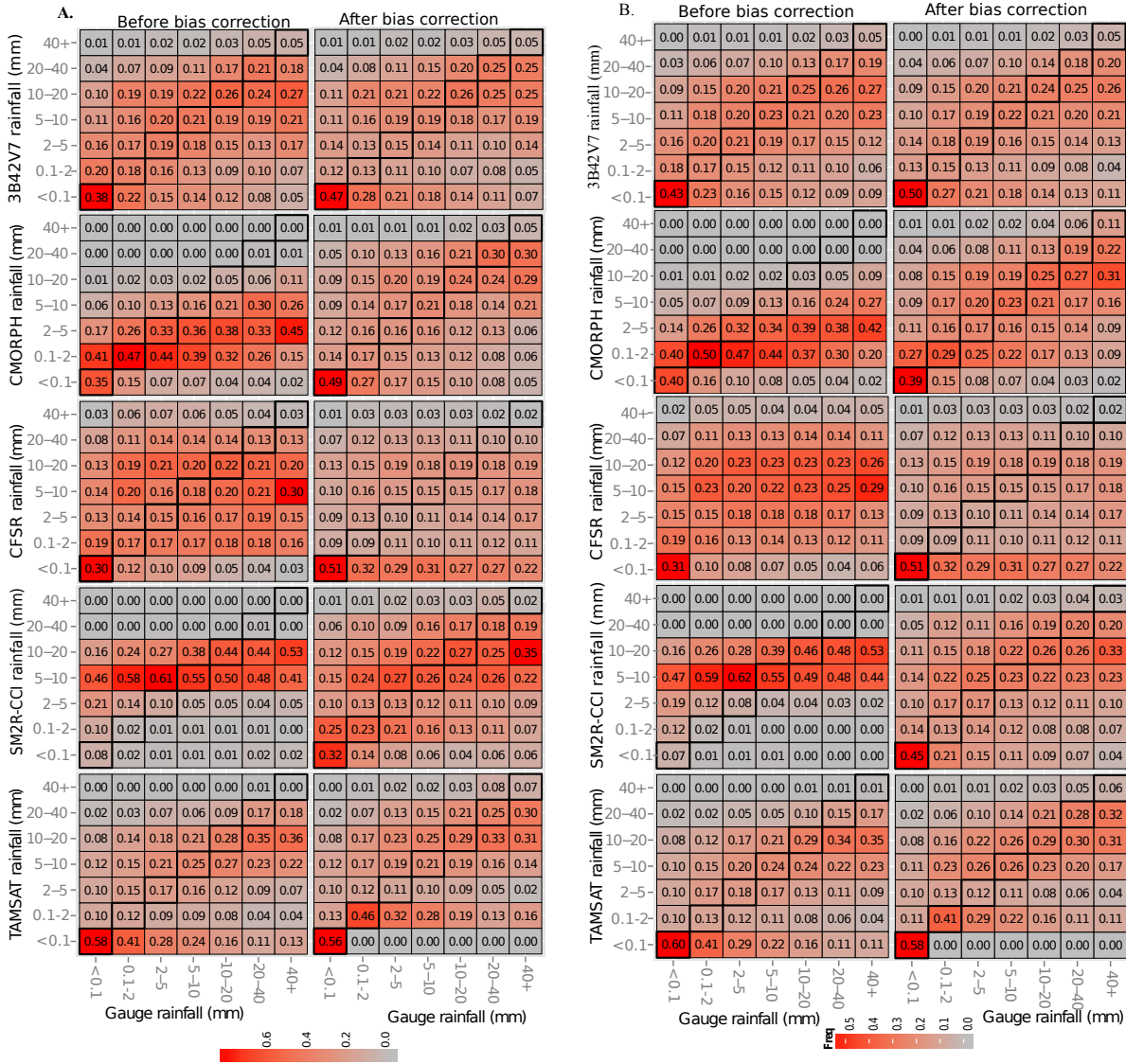
Figure 6.8: The effects of bias correction on the confusion matrix of different SREs (CFSR, CMORPH, SM2R-CCI, TAMSAT, and 3B42V7 from above to below) during the summer season(June, July, August) applied in independent stations (A) and in future time series (B). The first column shows the detection capacities of SREs before the bias correction and the second column is after bias correction.

Table 6.3: The comparison of different SREs using summary statistics (Bias) and detection capacity (accuracy index) against the gauge observed data at validation stations and time series during summer season (JJA) for about 10 years. The effect of bias correction on the other statistics (correlation coefficient and RMSE) is very small, and results are not reported

| | spatial cross validation | | | | time series validation | | | |
| | Before correction | | After correction | | Before correction | | After correction | |
SREs	BIAS (%)	Accuracy	BIAS	Accuracy	BIAS (%)	Accuracy	BIAS	Accuracy
CFSR	13.60	0.51	-16.00	0.52	16.40	0.52	15.20	0.51
CMORPH	-70	0.53	-4.0	0.56	-72.20	0.53	-1.10	0.55
SM2R-CCI	-12.70	0.52	-1.40	0.54	-7.70	0.51	-2.60	0.54
TAMSAT	-26.20	0.55	11.30	0.58	-23.80	0.55	11.30	0.57
3B42V7	-9.00	0.54	-1.60	0.55	-12.20	0.54	-12.80	0.55

to improve SREs. Different goodness-of-fit statistics (r, RMSE, BIAS) and confusion matrix are utilized to compare SREs and evaluate the bias correction strategy. The major findings are summarized as follows:

- The correlation coefficient based on 10 years of daily data at the whole basin scale shows similar value for TAMSAT (median=0.51), SM2R-CCI (0.5), and CMORPH (0.52), slightly better than 3B42V7 (0.47) and CFSR (0.3) performances.

- CFSR has the highest RMSE (8.9 mm/day) followed by 3B42V7 (7.5 mm/day) and CMORPH (7.3mm/day); TAMSAT (6.8 mm/day) and SM2R-CCI (6.8 mm/day) show relatively lower RMSE values.

- CMORPH has the highest BIAS (-72%), with most of the stations tends to have similar BIAS.

- The spatial distribution of GOF shows that the eastern part of the basin (highlands) has higher performances (lower RMSE and BIAS, and higher correlation) than the western part of the basin (lowlands).

- Generally, the detection skill decreases with increasing rainfall classes. TAMSAT has the highest detection skill for dry days while SM2R-CCI has better detection capacity for medium rainfall intensities (10-20 mm/day).

- The mean annual cumulative rainfall analysis shows, at some stations, that the difference amongst the various SREs is as high as about 2700 mm. Such a huge difference in rainfall is the real concern in using SREs for water balance modelling, and it shows that the choice of SRE product is a topic of real interest.

- The two validation strategy of $ecdf$ bias correction, grouped cross validation and time series split validation, show that there is room for improvement with relatively small efforts. The highest and lowest bias improvement following the $ecdf$ correction procedures is shown for CMORPH and CFSR, respectively.

In summary, different SREs exhibit different skills. The quantification of different SREs performances and characterization of errors is an important initial step for distributed hydrological model set-up in the basin. As it is not possible to depict the whole picture of SREs impact on the basin hydrological budget, the implementation of SREs and bias correction procedure in hydrological modeling framework in UBN basin is an important issue we would like to address in the next step.

WATER BUDGET MODELLING OF UPPER BLUE NILE BASIN USING JGRASS-NEWAGE MODEL SYSTEM AND SATELLITE DATA *

Learning from previous chapters' modelling and analysis experience, this chapter shifts to practical problems of data scarcity and modelling framework that requires to resolve water budget in the case of large scale hydrology. For this, one of the most complex basin in topographical, hydrological and social system, Upper Blue Nile (UBN) is used. To solve the issue of hydrometerological data shortage, different satellite products are employed. Precipitation product SM2R-CCI is used for forcing the water budget model, MODIS ET and GRACE storage are used as independent data comparison of JGrass-NewAge ET and storage component simulations. The rainfall-runoff simulation at each river links shows that JGrass-NewAge reproduce the discharge well. Finally, the calibrated model is used to estimate the space-time water budget of Upper Blue Nile basin from 1994-2009 (16 years). The results can be used as reference for any water resource development activities in the region.

7.1 Introduction

Freshwater is scarce resources in many regions of the world: the problem continued to be aggravated due to growing populations and significant increases in demand for agricultural and industrial purposes. Nile river basin is one of such regions, with relatively arid climate, due to high temperature and solar radiation fostering rapid evapotranspiration. Most of the countries in the basin such as Egypt, Sudan, Kenya, Tanzania, receives insufficient fresh water (Pimentel et al., 2004). The exceptions are the small area in the equators and the Upper Blue Nile basin in Ethiopian highlands which receives up to 2000 mm per year (Johnston and McCartney, 2010). Particularly, Upper Blue Nile (hereafter UBN) basin is the main sources of water resource in the region. However, it is probably one of the most hydroclimatologically and socio-politically complex basin. The water resources in the basin faces many pressures and challenges: (1) As a main contributor (i.e 85%) to the main Nile basin, it supports lives of hundreds of millions of people in the downstream, and it is refereed as "water Tower" of northeast Africa; (2) locally, the basin is inhabited by 20 million of people whose main livelihood is subsistence agriculture (Population Census Commission 2008); (3) topographically, the basin is very complex: it starts from mountain as high as 4300 meter and drains to lowlands, of about 450 meter; (4) UBN is a part of trans-boundary river, hence its development and management requires diplomatic discussion from many national governments; (5) Many international and nongovernmental organizations, with different policies, legal regimes, and contrasting interests, are involved for the basin freshwater governance; (6) Ethiopian government started many water resource development projects such as irrigation and dams, among which Grand Ethiopia Renaissance dam (GERD), which, upon completion, will be one of the largest in Africa.

To tackle all these complexities and challenges and develop better water development strategies is only possible based on quantitative information (Hall et al., 2014) on the hydrological system. Understanding the hydrological process of the basin, therefore, is the base for both transboundary negotiations about the sharing of the basin water resources (FAO 2000) and for assessment of sustainability of subsistence farming systems in the region.

Due to the lack of hydrometeorological data and proper modelling framework, however, spatio-temporal hydrological information in the basin is very scarce. Hence, the recent modeling efforts conducted in the basin has limitations to address this problem. Studies in the region are limited to small basin particularly in Lake Tana basin where

there are relatively better hydrometeorological data (Rientjes et al., 2011; Uhlenbrook et al., 2010; Tekleab et al., 2011; Wale et al., 2009; Kebede et al., 2006; Bewket and Sterk, 2005; Steenhuis et al., 2009; Conway, 1997; Mishra et al., 2004; Mishra and Hata, 2006; Teferi et al., 2010), or at the whole basin scale, but in which case information on spatial variability is usually ignored (Kim et al., 2008; Kim and Kaluarachchi, 2009; Gebremicael et al., 2013; Tekleab et al., 2011). Others are limited to a specific hydrological processes e.g. rainfall variability (Block and Rajagopalan, 2007; Abtew et al., 2009), time series and statistical analysis of in situ discharge/rainfall data (Teferi et al., 2010; Taye and Willems, 2011) or modelling at very low temporal resolution (monthly) (Kim and Kaluarachchi, 2008; Tekleab et al., 2011). Consequently, spatially distributed information on all the components of water budget does not exist.

This chapter is therefore an effort to contribute to the above mentioned problems, and aims to resolve the water budget of UBN basin using a hydrological modelling framework and remote sensing data. It is also a methodological chapter, in what it delineate various methodologies to overcome the data scarcity, and inherits from chapter 3 and 4.

The chapter is organized as follows: first descriptions of study area and model setup are given(section 7.2) then the methodologies for each water budget components and the model set-up is detailed in section 7.3. The results and discussions of each component and the water budget is presented in section 7.5. Then, conclusions of the study is followed (section 7.6).

7.2 The study basin

Upper Blue Nile (UBN) river flows from Lake Tana at Bahid Dar and flows to southwest through a series of cataracts. After about 150 km distance, the river enters into deep a canyon, and at the same slowly change direction south. After another 120 km flow, the river finally changes its direction to the west and northwest to the El Diem (Ethiopia-Sudan border). Many tributary rivers draining from many part of highlands of Ethiopia join the river along the way. The total distance of the river within Ethiopia is about 1000km.

UBN basin contributes to 60% Of the total contribution (85%) of the Ethiopian highlands to the Nile river flows (Abu-Zeid and Biswas, 1996; Conway, 2000). The area of UBN enclosed at the Ethio-Sudan border is about 175,315 km^2 (figure 7.1), covers about 17% of the total area of the country. The large scale hydrological behavior of the basin is described in a series of studies (Conway, 1997, 2000, 2005; Conway and Hulme,

1993). Its hydrological behavior is characterized by high spatio-temporal variability.
Since UBN basin has the lion's share of the total Nile flow, it is the economic mainstay of
downstream countries (Sudan and Egypt). Moreover, the Ethiopian highlands are highly
populated and have high water demands for irrigation and domestic uses.
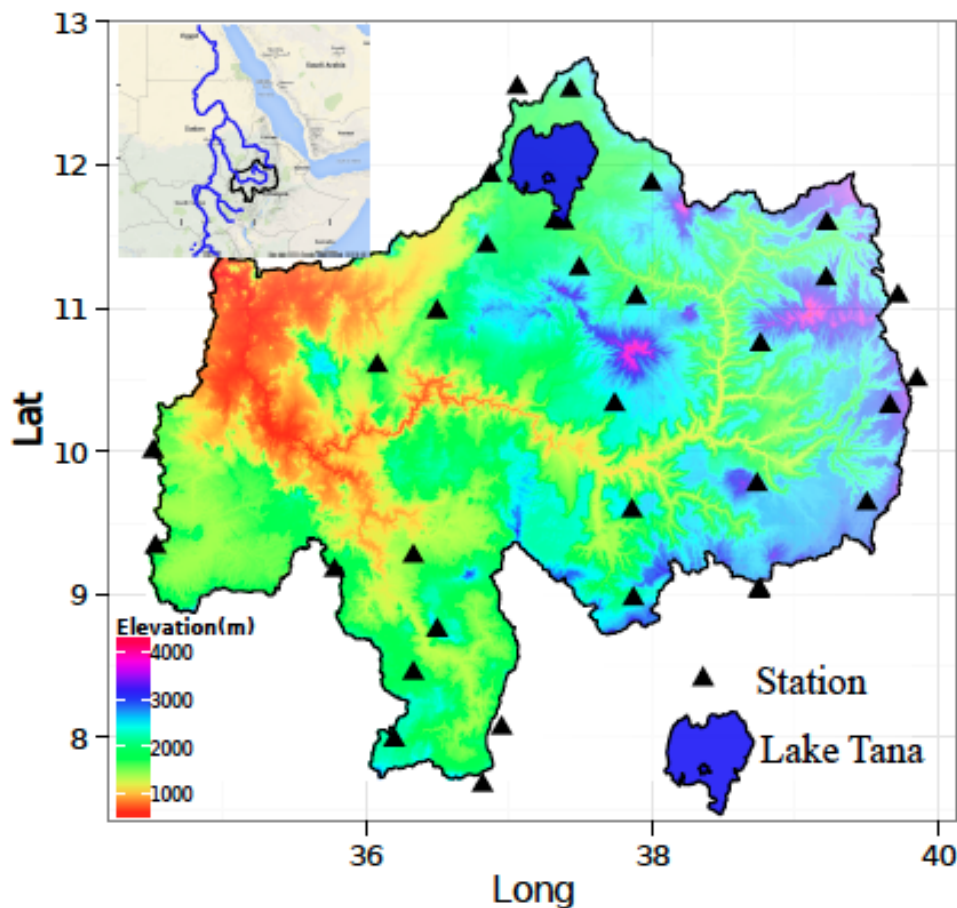
Figure 7.1: Upper Blue Nile basin and digital elevation map, along with the meteorological stations.

The topographic distribution of the basin is shown in figure 7.1. The topography of
UBN is very complex, with elevation ranging from 500 m in the lowlands at the Sudan
border to 4160 m in the upper parts of the basin. Due to the topographic variations, the
climate of the basin varies from cool (in the highlands) to hot (in the lowlands), with
large variations in a limited elevation range. The wet season, with low temperatures, is
from June to September, while the hot season is from March to May. Three controlling
mechanisms of the rainfall characteristics of the UBN, and Ethiopia in general (Seleshi
and Zanke, 2004), are the Intertropical Convergence Zone (ITCZ) that mainly derive the
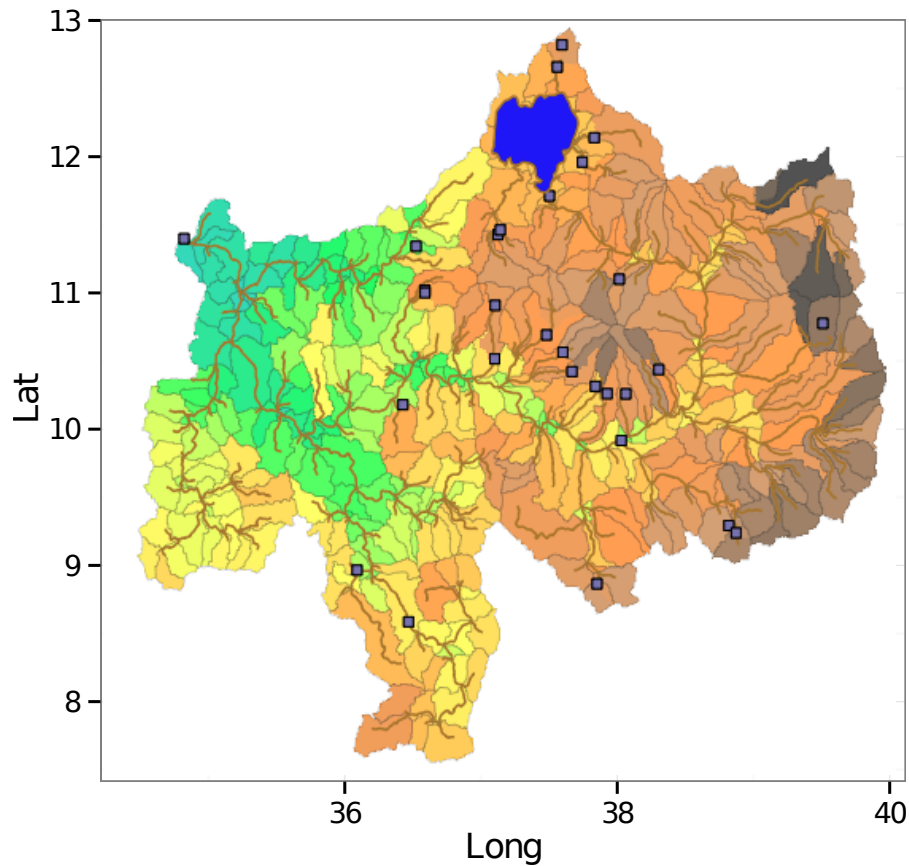
Figure 7.2: UBN basin and the subbasin partition used for simulation in this study. The square points are the discharge measurement stations.

wet monsoon rainfall in the wet season (June to September), the Saharan anticyclone that generates the dry and cool northeasterly winds in the dry season (from October-February), and the Arabian highlands that produce thermal lows in the mild season (February - May). The mean annual rainfall and potential evapotranspiration of the UBN basin are estimated to be in the ranges of 1200-1600 mm and 1000-1800 mm respectively (Conway, 1997, 2000), with high spatio-temporal variability. The annual temperature mean is 18.5^o with small seasonal variability.

7.3 Methodology

7.3.1 Water budget modelling

The water budget simulation is essential estimation of both storage and fluxes (rate of flow) of water for a given appropriate control volume and period of time. It is given by:

(7.1)
$$\frac{\partial S_k(t)}{\partial t} = J_k(t) + \sum_{i}^{m(k)} Q_{ki}(t) - ET_k(t) - Q_k(t)$$

where $J(t)$ is the rainfall data, and ET is actual evapotranspiration, $Q(t)$ is discharge, $Q_{ki}(t)$ is the discharge coming from the contributing streams. The index $k = 1, 2, 3...$ is the control volume where the water budget is solved. In our case, the control volume is a portion of the basin (a subbasin) derived from topographic partitioning as described in section 7.3.2.

In case of data scarcity, remote sensing (RS) observations contributes to fill the gaps, and therefore effective utilization of different RS products is clearly a new paradigm in hydrological modelling activities (Andrew et al., 2014; Sahoo et al., 2011; Gao et al., 2010). In large African basin, where in situ data are very poor, RS data could be even better than the in situ observation.

In this study, different RS data are used to close the water budgets, and are used both as input and for evaluation of the modelling solutions implemented.

7.3.2 JGrass-NewAGE system set-up

The JGrass-NewAGE hydrological model system is the one used to resolve the water budget of UBN basin. JGrass-NewAGE is actually a set of modelling components that can be connected at runtime (Formetta et al., 2014c) to form various modelling solutions. JGrass-NewAGE system (Formetta et al., 2011) and different individual components are described in a series of papers (Formetta, 2013; Formetta et al., 2014d, 2013b, 2011, 2014c,a; Abera et al., 2014), and is not re-discussed here. In this study, solar radiation budget (SWRB), Evapotranspiration component (Priestley and Taylor), Adige rainfall-runoff model, and all the components illustrated in 7.3 are used to estimate the various hydrological flows .

The necessary step for spatial hydrological modeling is partitioning of the topographic information into appropriate spatial scale. The GIS representation of the basin topography, as detailed in (Formetta et al., 2014a; Abera et al., 2014; Formetta et al., 2011), is based on the Pfafstetter enumeration (Formetta et al., 2014a; Abera et al., 2014). The basin is subdivided in Hydrologic Response Units (HRUs), where the model inputs (i.e. meteorological forcing data), the hydrological processes and outputs (i.e. evapotranspiration, discharge, net radiation) are averaged. The basic water budgets are estimated for each HRU, and, subsequently, a routing scheme is applied to move the discharge to the basin outlet through the channel network.

We divide the UBN basin into 402 subbasins and channel links as shown in figure 7.2. This spatial partitioning may not be the finest scale possible, however, considering the size of the basin, it can be considered an acceptable compromise to capture the water budget spatial variability.
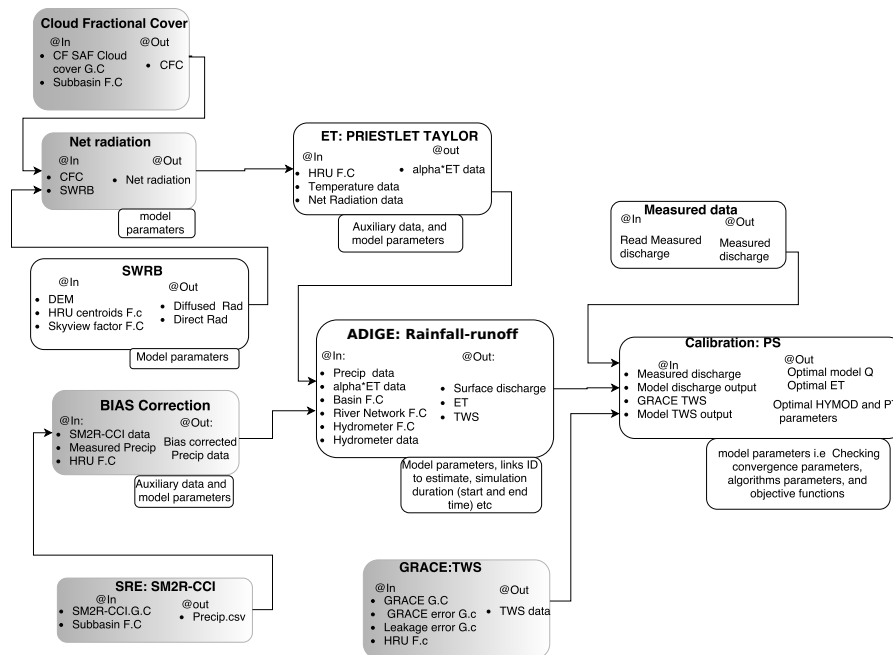
Figure 7.3: Workflow with a list of NewAge components (in white), and remote sensing data processing parts (gray shaded, not yet included in JGrass-NewAGE but performed with R tools) used to derive the water budget of UBN. It does not include the components used for the validation and verification processes.

7.3.2.1   Precipitation $J(t)$

Regards to the input term of Eq. 7.1 (J(t)), the spatio-temporal precipitation, it is quantified based on RS-based approaches (chapter 6). Different satellite rainfall estimates (SREs) available for varied accuracy and purposes. The use of SREs and lists products that can be used in hydrological applications can be found elsewhere in literature (Hong et al., 2006; Bellerby, 2007; Huffman et al., 2007; Kummerow et al., 1998; Joyce et al., 2004; Sorooshian et al., 2000; Brocca et al., 2014). Regardless of the recent advancement of rainfall retrieval algorithm, SREs are still subjected to significant uncertainty due to various factors including sensor problem, infrequent satellite overpasses, large spatio-temporal scale, and retrieval algorithm (Hong et al., 2006; AghaKouchak et al., 2009; Hossain et al., 2006).

Five, high spatial and temporal resolution, potentially good SREs for hydrological applications for the same basin is analyzed in chapter 6, shows that SM2R-CCI (Brocca et al., 2013, 2014) is one of the best products in the basin particularly in capturing the total rainfall volume. Hence, for this study, SM2R-CCI is used as input data for the modelling. The persistent nature of systematic errors i.e. bias (Habib et al., 2014) of SM2R-CCI is removed according to the ecdf matching techniques, as in chapter 6.

Once the SM2R-CCI are corrected for bias errors, it is used to examine the spatio-temporal precipitation variability of the basin and drive the JGrass-NewAGE modelling system to solve the discharge. Hence, the subbasin mean precipitation is estimated by averaging all the pixels inside each subbasin. Accordingly to the basin partition described in section 7.3.2, for 402 subbasin, 1994-2009 daily precipitation is generated.

7.3.2.2 Evapotranspiration ET

The ET component, as it is an important flux of a basin, is very crucial for agricultural and water resource management. However, the lack of in-situ data impedes the modelling effort and makes it probably the most difficult task in water budget estimation. In this study, ET is formulated according to NewAge evapotranspiration component using energy budget as input. This approach instead provide estimates at any temporal and spatial resolution required. The ET is mainly depends on net solar radiation, as it is the main quantity of radiant energy available at the surface to drive the surface biophysical processes and evapotranspiration (Kjaersgaard et al., 2009). Priestley and Taylor (hereafter referred as PT) Formula (Priestley and Taylor, 1972) is one of the simplified models to estimate ET, mainly based on net radiation, Rn, and simplified all the unknowns by α coefficient, as it shown in Eq. 7.2. PT formula is given by:

$$ET = \alpha \frac{\Delta}{\Delta + \gamma}(Rn) \qquad (7.2)$$

Here α the unknown factors to estimate the ET. Based on some empirical data, there are some specific values have been suggested in literature, α =1.26 is commonly used, however, a wide ranges of α is reported (Pejam et al., 2006) and are not enough to close water budget at a particular area. When aimed for water budget closure i.e actual evapo-transpiration at different temporal and spatial scale, Abera et al (submitted, chapter 5) modified PT introducing water storage constraint functions based on information that can be obtained from Adige rainfall-runoff component (i.e HYMOD). In this study, this approach has been followed. The reformulated ET equation is given by:

(7.3)
$$ET(t) = \alpha \frac{S(t)}{C_{max}} \frac{\Delta}{\Delta + \gamma} (Rn)$$

Where Δ and γ is slope of the Clausius-Clapeyron relations and psychometric constant, respectively, as given in 5. The α and the C_{max} (maximum water storage capacity of each HRUs) is calibrated together inside the rainfall-runoff model for a given Budyko assumption of null storage. In this study,Budyko's time,TB (Budyko, 1978), i.e. assumption of null water storage after a specified number of years, six years, has been taken. This approach is innovative because it combines the atmospheric demand and soil storage information to solve the α coefficient, hence the ET. The detail procedure on this is given in chapter 5.

In equation 7.3, While $S(t)/C_{max}$ determining the availability of water to be evaporated, the Rn is the main input modulating the atmospheric demand component of ET. NewAge shortwave radiation budget component SWRB, Formetta et al. (2013b) is used to estimate each subbasin shortwave radiation budget in clear sky condition. Irradiance at clear sky conditions is however unsuitable for all sky condition. Because surface Shortwave radiation is strongly affected by cloud cover and cloud type (Arking, 1991; Kjærsgaard et al., 2009), the cloud fractional cover (CFC) satellite data set (Karlsson et al., 2013) processed and provided by EUMETSAT Climate Monitoring Satellite Application Facility (CM SAF) project (Schulz et al., 2009) is used to cut the clear sky SWRB estimated using NewAge-SWRB to Rn all sky condition, as in the following formulation (Kim and Hogue, 2008):

(7.4)
$$Rn = (1 - CFC)SWRB$$

When SWRB is the net shortwave radiation estimated using the NewAge-SWRB component at each Subbasin, and Rn is the net radiation. For this, the daily CFC originated from polar orbiting satellites, version CDRV001, at the daily time resolution and $0.25^{'}$ spatial resolution from 1994 to 2009 (16 years) is processed (Karlsson et al., 2013) to obtain the mean daily CFC for each subbasin. In comparison to the effects of CFC, the surface albedo is very minimal particularly in highland area with vegetation cover and no snow cover like UBN basin.

Once the ET is estimated according to the methods described, it is useful to validate with independently obtained ET estimates or data. ET in situ observations are not available for this basin, as it is not for most regions. RS based estimates of ET have

been produced by different algorithms (Norman et al., 1995; Mu et al., 2007; Jarmain, 2009). We used the standard MODIS evapotranspiration product MOD16 (Mu et al., 2007). MOD16 is available at spatial resolution of 1-km and temporal resolution of 8-day, monthly and annual scales. Different from NewAge approach, MODIS ET product (MOD16) also considers vegetation index such as land cover type (Mu et al., 2007). Here, MOD16 ET specially provided for the Nile basin countries (Hofste, 2014) is used for assessment of the NewAge estimation. The only difference from the standard MOD16 is that it considers improved land cover and water bodies. The objective of the comparison is not for strict validation of either estimation, but to assess the level of consistency between the two independent estimation, and to provide feedback on the product. More detail on the comparison strategies is described section 7.4.

7.3.2.3 Discharge Q

For discharge estimation, ADIGE rainfall-runoff component is used. Adige component is based on the well know HYMOD model (Moore, 1985). The main inputs for ADIGE model are J(t) and ET(t), as estimated in the above sections. Detail description of HYMOD implementation in NewAge model system is given at Formetta et al. (2011) and chapter 5, and a concise summary is given at appendix C. The ADIGE rainfall-runoff has five calibration parameters, and the calibration is performed using the particle swarm (PS) optimization. PS is population based stochastic optimization technique inspired by social behavior of bird flocking or fish school (Kennedy et al., 1995). It is advantageous to obtain global optimal, and less susceptible to get trapped in local minima (Scheerlinck et al., 2009). The objective function used for the optimal value is Kling-Gupta efficiency (Kling et al., 2012). The formulation of the Kling-Gupta efficiency (KGE) and other GOF indexes used for evaluation of the model performances in this chapter are presented in appendix B.

7.3.2.4 Total water storage change ds/dt

The ds/dt in Eq. 7.1 is the water contained in the ground, soil, snow and ice, lakes and rivers, and biomass. It is total water storage (TWS) change, calculated as the residuals of the water budget fluxes for each control volume. In this chapter, the ds/dt estimation at daily time steps is based on the interplay of all the other components as presented in Eq. 7.1. There is no way to estimate areal TWS from in situ observations. The new Gravity Recovery and Climate Experiment (GRACE) data (Landerer and Swenson, 2012) has a potential to estimate this component, but at very low spatial and temporal resolutions.

GRACE is a mission based on two twin satellites that measures spatiotemporal variations of water storage that is derived from a continuous observation of the gravity field. At this scale, however, GRACE can still be used for constraining and validating data to the modelling solutions. Here, the performance of our modelling approach to close the water budget i.e. estimating storage following the characterization of all the terms, is assessed using the GRACE estimation at the basin scale. Since the other fluxes are modeled as function of basin water storage, for instance Q and ET, good estimation of water storage of a model has inference to its reasonable computation of other fluxes as well (Döll et al., 2014). GRACE data is an extraordinary resource to assess the over all performance of the simulation, at least at the basin scale.
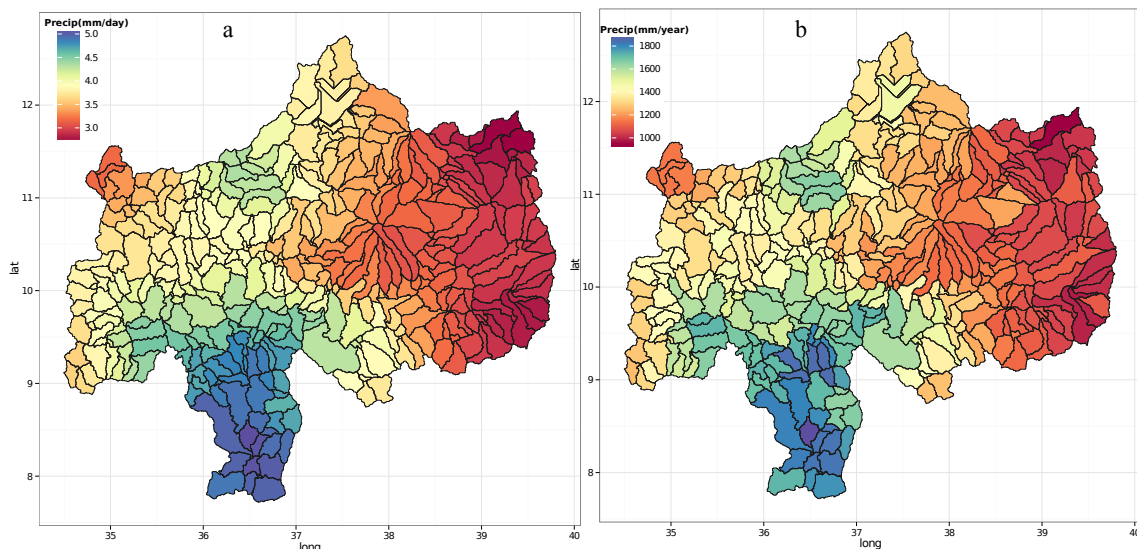
Figure 7.4: The spatial distribution of daily mean (a) and annual mean rainfall estimated from long term data (1994-2009).

7.4 Calibration and validation approach

The precipitation data is error corrected based on the in situ observation. The Adige rainfall-runoff component, i.e HYMOD model parameter, are calibrated to fit the observed discharge during the six years of calibration period (1994-1999) at daily time step. Based on the approach described ET estimation, the ADIGE component is also used to calibrate the PT α. The simulation for each hydrological component is verified using the available in-situ or remote sensing data as follows:
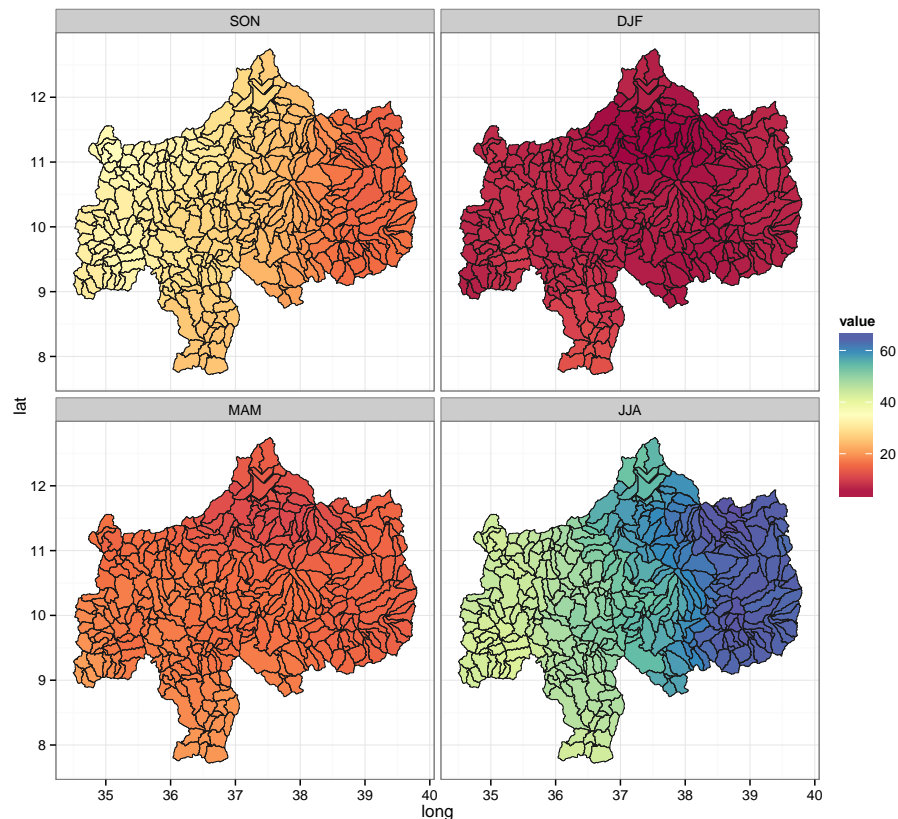
Figure 7.5: The spatial distribution of quarterly percentages of rainfall in Autumn (a),
Winter (b), Spring (c) and Summer (d) of the total annual precipitation.

- Discharge validation: Discharge simulation is calibrated for a separate time-series
  data at the outlet, where the model is calibrated. In addition, the simulation of
  NewAge at the internal links is validation where there is in situ data are available.
  The evaluation at the internal links provide an assessment of the model estimation
  capacity at a location where gauges are absent.

- ET validation: Once ET is estimated according to the procedures described, MOD16 (Mu
  et al., 2011) is used as independent data set for assessing the ET estimation. Since
  the MODIS is 8-daily data at 1km resolution, two steps are followed for easy com-
  parison. (1) the MOD16 ET is spatially aggregated at subbasin scale, and (2) the
  NewAge daily ET is temporally aggregated to 8-daily. Based on the same spatial
  and temporal resolution, the MODIS and the model ET is compared, and the GOF
  indexes are calculated based on 7 years data (2003-2009).

- ds/dt validation: The water storage change, ds/dt, estimated from the model-

ing solution is evaluated using GRACE data set. We used the GRACE product to estimate the total water storage change (TWSC) for the the whole basin. Monthly data is obtained from NASA Jet Propulsion Laboratory (JPL)ftp:// podaac-ftp.jpl.nasa.gov/allData/tellus/L3/land mass/RL05 in units of cm equivalent water thickness. The leakage errors and scaling factor (Landerer and Swenson, 2012) that is provided with the product is applied to improve the data before the comparison is made. The total error of GRACE estimation is a combination of GRACE measurement and leakage errors (Billah et al., 2015). Based on the two error data, the mean monthly error of GRACE TWSC in the basin is about 8.2 mm. To harmonize and enable comparison between the model and GRACE TWS data, it is necessary to do both time and spatial filtering. Following the GRACE TWSc temporal resolution, the model ds/dt is aggregated at monthly time steps. Since error of GRACE increases if used at small scale, the comparison is made only at the whole basin scale.

In summary, SM2R-CCI is evaluated against the available in-situ gauges, evapotranspiration is evaluation using the MOD16, discharge simulation using in situ discharge measurements, and the total storage estimation using the GRACE data. Once the performances of each component are evaluated, then, the spatio-temporal water budget of the basin is modeled and quantified.

7.5 Results and discussions

The results of the study are organized as follows: First, the results on the simulation performance and comparison with independent data, along with brief spatio-temporal characteristics of the fluxes and storage are presented. The simulated water budget components are described chronologically i.e. 1) Precipitation, 2) evapotranspiration, 3) discharge and 4) total water storage. Second, the components are used to resolve the water budget closure at each subbasin, hence, the contribution of each term is analyzed.

7.5.1 Precipitation J

The spatial and temporal variability of J(t) is analyzed in this section. The spatial distribution of long term mean daily and annual precipitation is presented in figure 7.4. SM2R-CCI shows that south and the southwest part of the basin receives high precipitation while the east and northeast part of the highland receives low precipitation. The

highest rainy subbasin are in the southern part of the basin in the Oromia regions. It
obtains mean annual rainfall about 1900 mm. The mean annual precipitation reported
for this region by Abtew et al. (2009) is about 2049 mm. The discrepancy could be
that Abtew et al. (2009) estimation is from point gauge data, while this study is based on
the areal data from SM2R-CCI. Generally, precipitation increases from the east (about
1000 mm/year) to south and southwest part (1800 mm/year). This distribution map is
consistent with the results of Mellander et al. (2013); Abtew et al. (2009).

To understand the spatial distribution of seasonal cycle, quarterly percentage of the
total annual precipitation calculated from 1994 to 2009 daily estimations is presented in
figure 7.5 . During the summer season, while the subbasin in the north and northeast
receives about 65% (figure 7.5 d), the subbasin in the south part do receives about
40% of the total precipitation. Generally, the seasonal variability of the basin is very
high. Studies found out that the interannual and seasonal variability of precipitation
in UBN basin is governed by Southern Oscillation Index (SOI), equatorial eastern
Pacific sea level pressure, sea-surface temperature (SST) over the tropical eastern Pacific
Ocean (Camberlin, 1997; Seleshi and Zanke, 2004).

7.5.1.1 Evapotranspiration *ET*

Based on the approach detailed in our methods, the ET is estimated for each subbasin at
daily time step. Figure 7.6 shows a sample of spatial and temporal estimation of MOD16
and NewAge ET for some systematically selected (selected from the four seasons) at
8-days time resolution. While the spatial pattern has some similarities, the magnitudes
of ET amount between the model and MOD16 estimation is different. In all the maps, ET
tends to be high in the lowlands of the basin (western part). MOD16 estimation, however,
considerable underestimates ET in comparison to NewAge. Time series comparison of
two ET from 2000-2009 for some selected subbasin (figure 7.7) shows that MOD16 highly
underestimates ET. Other studies also show similar results that MOD16 considerably
underestimate in comparison to some model estimations and eddy covariance flux towers
data (Yilmaz et al., 2014; Knipper et al., 2016; Schaffrath and Bernhofer, 2013; Ramoelo
et al., 2014).

NewAge revealed high level of temporal variability while MOD16 shows similar
temporal patterns between the years. The agreement between the two estimations vary
from subbasin to subbasin (figure 7.7). For instance, in figure 7.7b shows relatively better
consistency while figure 7.7d has lower agreement between the two. The spatial distri-
bution of the correlation and PBIAS between the model and MOD16 data is presented
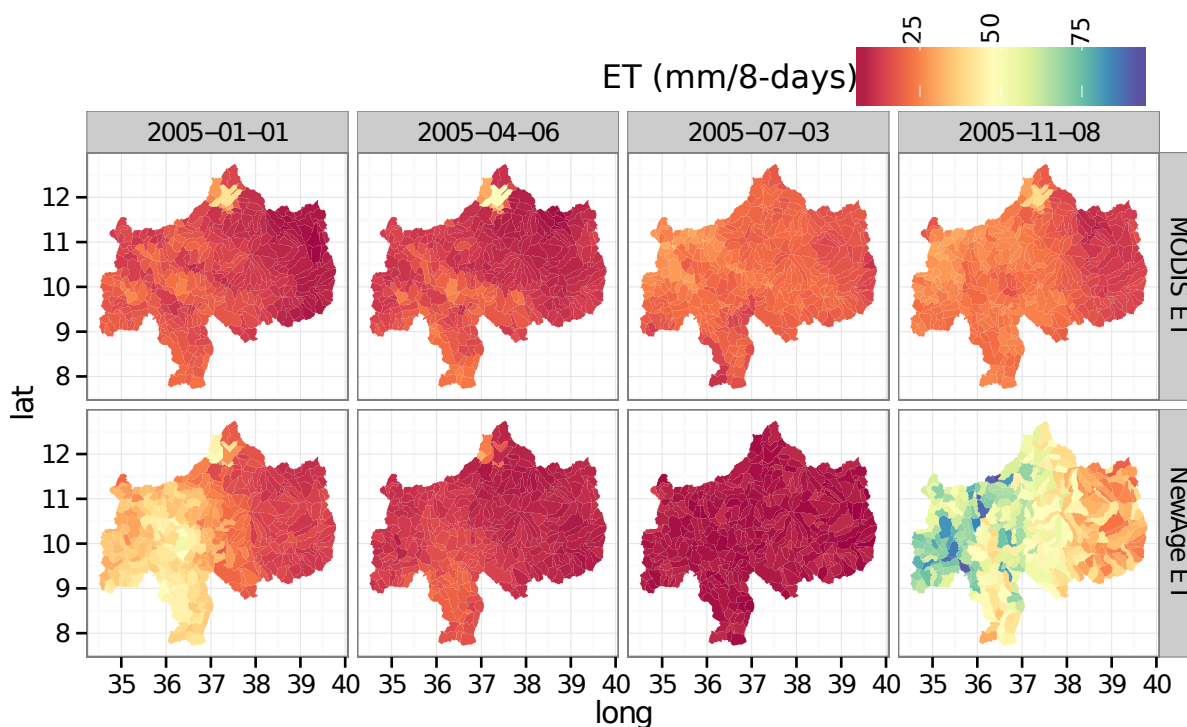
Figure 7.6: The Spatial and temporal variability of ET in 8-day intervals for both MOD16 and NewAge in the study area.

in figure 7.8a and b respectively. The NewAge estimation in the eastern part of the basin shows higher correlation with the MOD16 data, while the correlation tends to decrease systematically towards the west i.e. to the lowlands (figure 7.8a). Similarly, the PBIAS shows that the western part, border to the Sudan, has very high underestimation (figure 7.8b). The overall correlation and PBIAS between NewAge and MOD16 is 0.48 ± 0.15 and 14.5 ± 18.9 respectively. Based on the consistency we made, and our ability to characterize the other water budget solution with observation and GRACE, we can point out that the performance of MOD16 is low, and need to be improved in this region.

7.5.1.2 Discharge Q

The optimized Adige model parameters obtained at the Ethio-sudan border during the calibration period are presented at table 7.1. Automatic calibration of NewAge rainfall-runoff component conducted at Ethio-Sudan border during the calibration period provided very good GOF indexes values (KGE=0.93, PBIA = 2.2, r = 0.94). The model performance is verified during the validation period, and the performance is almost similar to the validation period. It is also evaluated at the internal river of the basin.
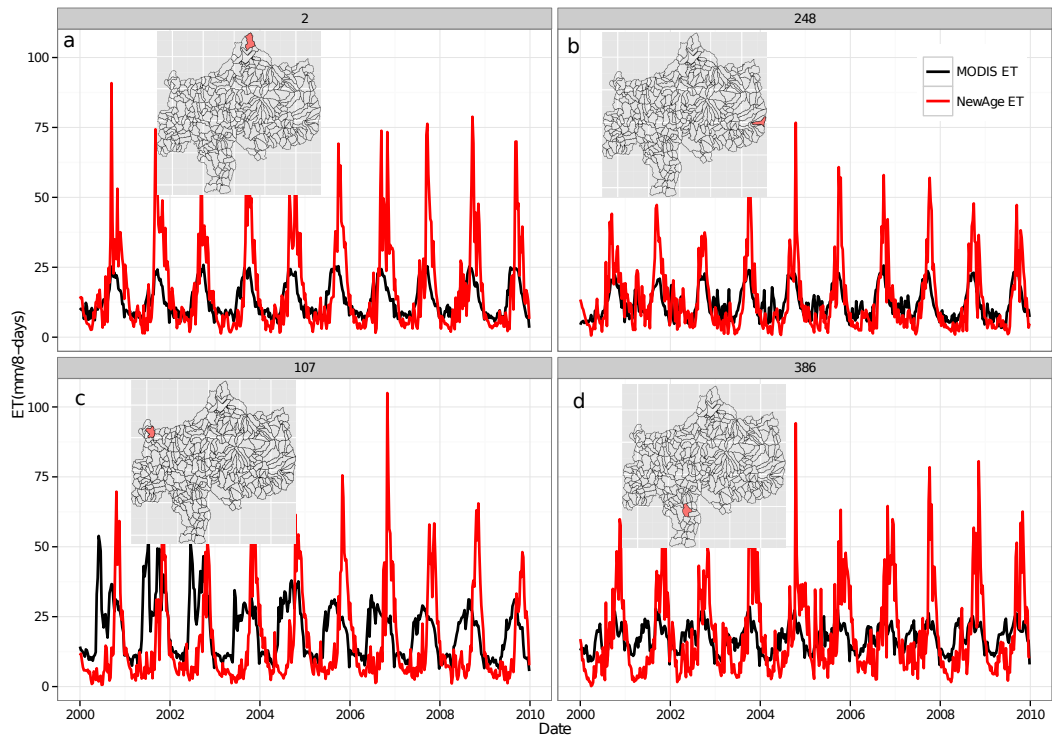
Figure 7.7: Time series ET estimation with NewAge and MOD16 at 8-days of time steps for four subbasin: subbasin ID2 (a), subbasin ID248 (b), subbasin ID107 (c) and subbasin ID386 (d). The location of the subbasin are indicated in the map inside the plots.
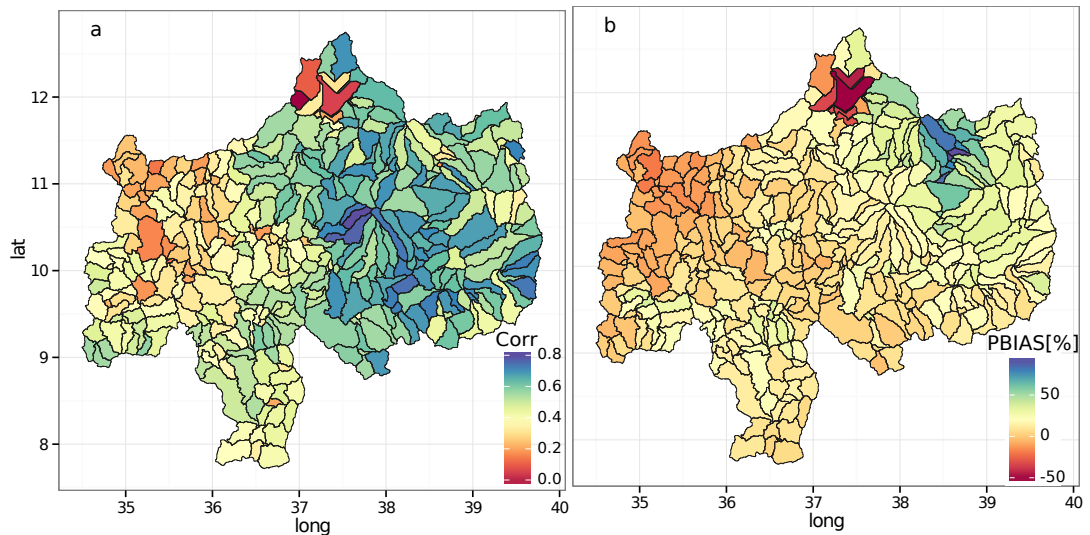
Figure 7.8: The spatial distribution of correlation Coefficient (a) and PBIAS between NewAge and MOD16 ET estimations at 8-days time steps.

Figure 7.9 shows simulated hydrograph for some channel links, when available, along with the observed discharge. At the outlet, even during the validation period, the model is able to capture the dynamics of the basin response very well (KGE=0.92, PBIAS = 2.4, r = 0.93). The results shows that the performances of NewAge simulation is better than the performances reported by Mengistu and Sorteberg (2012). Generally, the model predict well both the high flows and low flows, with slight underestimation of peak flows (figure 7.9 a) likely due to the underestimation of SM2R-CCI precipitation data for high rainfall intensities (Abera et al. Submitted, chapter 6).

Table 7.1: Optimized parameters obtained from daily ADIGE simulation during the calibration periods (1994-1999). The last parameter is of the ET component.

Parameters	value
$C_{max}[L]$	694.18
$B_{exp}[-]$	0.64
$\alpha[-]$	0.61
$Rs[T]$	0.086
$Rq[T]$	0.394
$\alpha[-]$	2.9

For further analysis and understanding on the forecasting capacity of NewAge for discharge, model fitness for some internal sites are described here. For Gelgel Beles river enclosed at the bridge near to Mandura, with area of 675 km^2, the hydrograph comparison between NewAge simulated and observed discharge is shown at figure 7.9 b. The performance of uncalibrated NewAge at Gelegel Beles has correlation coefficient and PBIAS value of 0.64 and 0.58% respectively. The KGE value is 0.48.

The forecasting skills of NewAge at the Ribb river enclosed at Addis Zemen (area 1592 km^2) is very high with KGE = 0.81, PBIAS = 12 and r = 0.82 (figure 7.9 c). Comparing with SWAT Model performances at this station during validation period (Tekleab et al., 2011; Setegn et al., 2008), despite SWAT was calibrated for this specific subbasin, the results of this study are much better.

In comparison to the SWAT, WASE-Tana, and Flex$_B$ models applied in Gilgel Abay River enclosed at Merawi (Wosenie et al., 2014), even with calibration for the particular basin, NewAge outperform. For instance, the simulation result (PBIAS=12, r=0.93) at Gilgel Abay based on the calibration at the basin outlet (see table 7.2), can be compared with the results of Wase-Tana (PBIAS=34, R^2=0.8), SWAT (PBIAS=5, R^2=0.63) and Flex$_B$ (PBIAS=77.6, R^2=0.75). It revealed that with out calibration the performances of NewAge is comparable with other models which is calibrated for this specific basin,

Table 7.2: The forecasting skill of NewAge Adige rainfall-runoff component at the internal
sites based on the optimized parameters calibrated at the outlet. The performance in the
outlet (El Diem) is the model performance at validation period.

River Name (Hydrometer stations)	Area (km^2)	KGE	PBIAS	r
Koga @ Merawi	244	0.58	24.00	0.73
Jedeb @ Amanuel	305	0.38	9.80	0.53
Neshi @ Shambu	322	0.58	32.00	0.57
Suha @ Bichena	359	0.40	53.20	0.82
Temcha @ Dembecha	406	0.70	3.30	0.71
Gilgel Beles @ Mandura	675	0.46	0.58	0.64
Lower Fettam @ Galibed	757	0.48	32.20	0.82
Gummera @ Bahir Dar	1394	0.10	-66.20	0.88
Ribb @ Addis Zemen	1592	0.81	12.00	0.86
Gelgel Abay @ Merawi	1664	0.81	12.00	0.93
Main Beles @ Bridge	3431	0.55	-17.70	0.74
Little Anger @ Gutin	3742	0.11	44.80	0.77
Great Anger @ Nekemt	4674	0.72	-14.10	0.77
Didessa @ Arjo	9981	0.55	19.60	0.81
Upper Blue Nile @ Bahir Dar	15321	0.26	5.10	0.60
Upper Blue Nile @ El Diem	174000	0.92	2.40	0.93

sometimes even better. From other study in this basin, Dile et al. (2013) found E_{NS}
value between 0.54 to 0.74 using SWAT calibration.

The Angar river subbasin is located in the southern region of the UBN basin. The
topography ranges from 860 to 3210 meter, and is dominated by forest land cover (Easton
et al., 2010). It is located in high rainfall zone of the basin. The performance of NewAge
for Angar river enclosed near Nekemt (area 4674 km^2) is KGE = 0.72, PBIAS = -14.10,
and r = 77 (table 7.2). The comparison of simulated and observed discharge and its
location is shown at figure 7.10h. Easton et al. (2010) obtained R^2=0.79, and NSE = 0.89
using SWAT model, also the parameters are calibrated for the subbasin.

The performances of NewAge simulation at the outlet of Lake Tana (area 15321 km^2)
is relatively low. This could be due to poor characterization of the Lake water fluxes. The
performance of NewAge simulation (KGE = 0.26, PBIAS = 5.10, and r = 0.60) can be
compared with SWAT simulation performance by Mengistu and Sorteberg (2012) (PBIAS
= 25, R^2=0.78) during validation period, but with calibrated parameters at this station.

Dedisa river basin is one of the main tributary of UBN basin, enclosed at hydromter
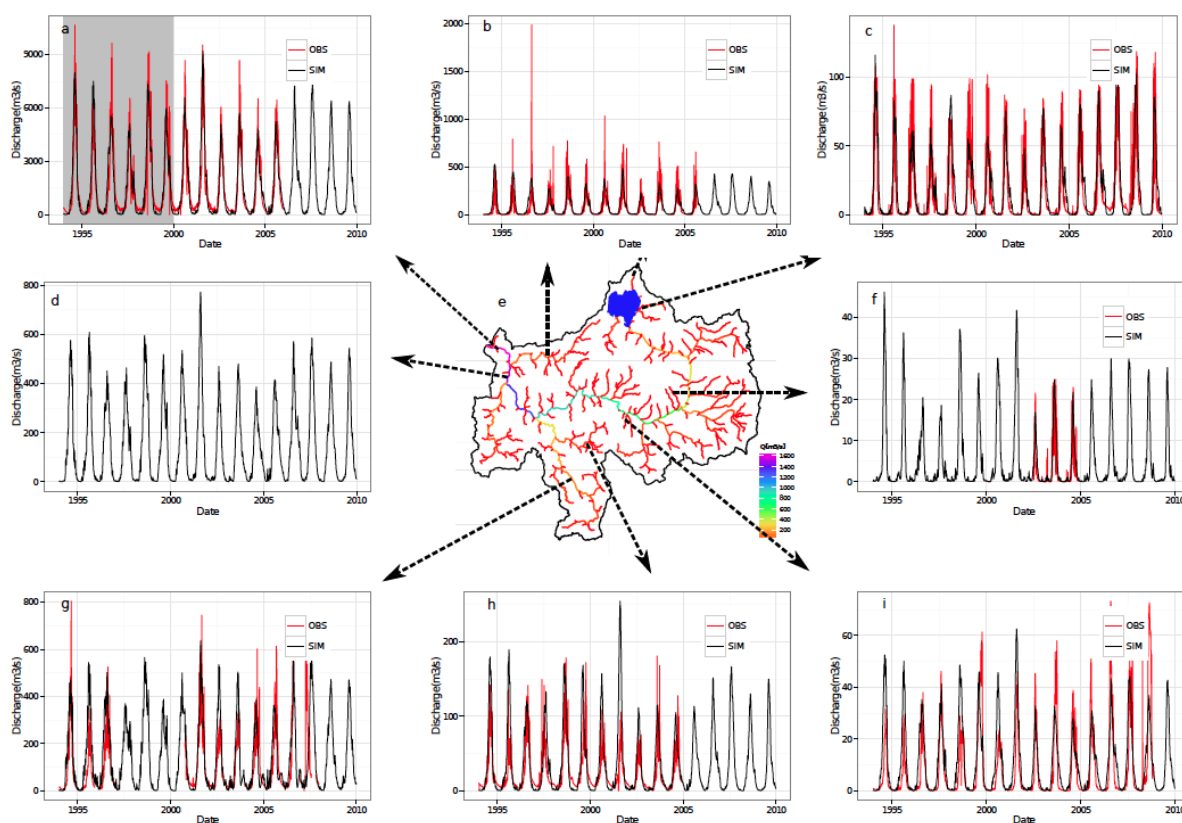
Figure 7.9: NewAge model forecasting validation at internal subbasins. The model calibrated and validated at El Diem (a) is used to estimate at each channel link, and verified at link where discharge measurements are available: main Beles bridge (b), Ribb river enclosed at Addis Zemen (c), just simulation of the main Blue Nile before joining Beles river (d), Jedeb near Amanuel (f), Dedisa river basin enclosed near Arjo (g), Angar river basin enclosed near Nekemt (h), and Nesh near Shambu (i). figure (e) shows the long term estimated daily discharge at all river links of the basin.

station near to Arjo, the total area is about 9981 km^2. The model performance for this station is KGE=0.55, PBIAS = 19.60, and r = 0.81. Hydrograph comparison between model and observed discharge is shown in figure 7.9g.

For most subbasin, because the model performances i.e. KGE is higher than 0.5 and PBIAS is within 20%, estimated discharges is deemed to be adequate for forecasting and estimating water resource at locations where gauges are unavailable. The model also able to reproduce discharge at across the range of scales. For instance, the performances at the Ethiopia-Sudan border (174 000 km^2), Dedisa near Arjo (9981 km^2), main Beles (3431 km^2), and Temcha near Dembecha are acceptable (figure 7.9 and table 7.2).

A sample of spatially distributed daily discharge at all the channel links is shown
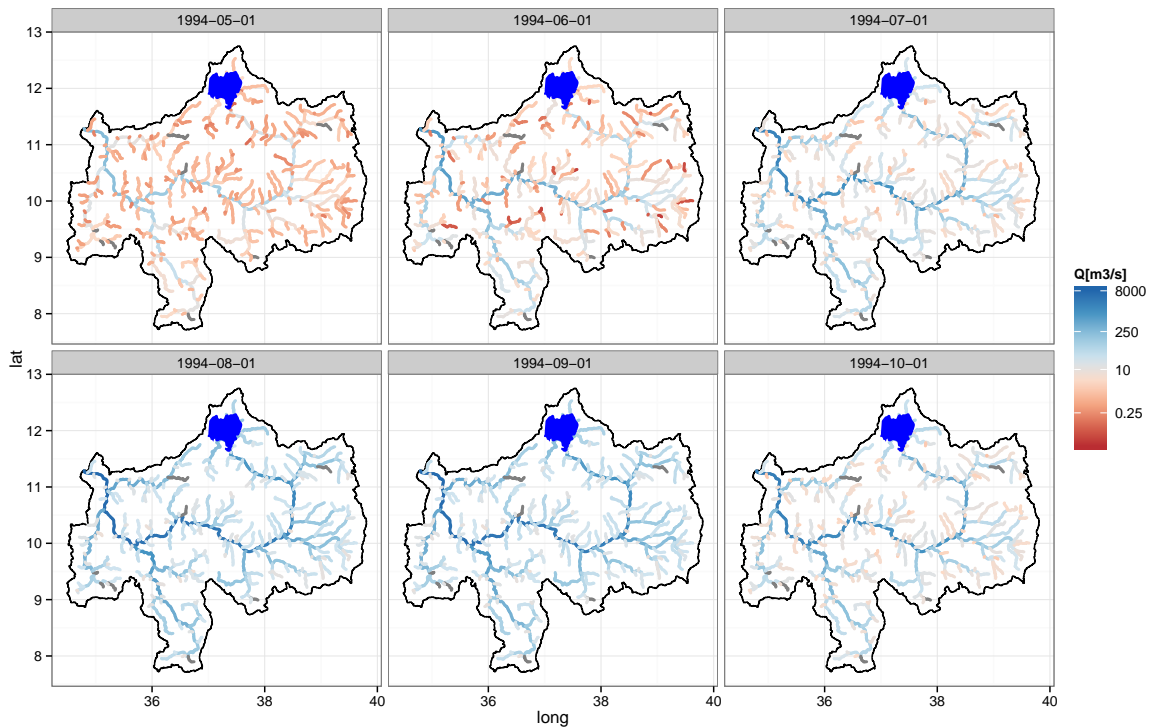
Figure 7.10: The spatial distribution of simulated discharge at each links of the basin at
daily time steps. Here, the spatial distribution of discharge is shown for the first day of
May, June, July, August, September, and October of 1994.

in figure 7.10. Here, the daily discharge for the first day of May, June, July, August,
September and October are presented to show the spatio-temporal dynamics of discharge.
The spatial distribution of the GOF values between the NewAge simulation and observed
discharge in all the available hydrometers is shows at table 7.2.

7.5.1.3 Total water storage change

The NewAge simulated ds/dt for 16 years for each subbasin as residuals of the flux terms.
We first compared the simulated ds/dt with GRACE based TWSC. Figure 7.11 shows
ds/dt time series for the whole basin estimated using NewAge and GRACE. The storage
change shows high seasonality over the basin, and with positive change in summer,
and negative change in winter. The change varies from -100 to +120 mm/month. The
model ds/dt aggregated at monthly time scale is in accordance with the GRACE TWSC,
both in temporal pattern and amplitude. Over the whole basin, correlation coefficient

0.84 is obtained. The good performances of the ds/dt also has an inference on the model capability to reproduce other components well,as it is the residual terms to balance the flux dynamics.

The spatial distribution of NewAge ds/dt and GRACE based TWSC for four months (January, April, July, and October) of 2005 is shown at figure 7.12. The comparison is based on the NewAge modelling at subbasin scale, and GRACE grid resolution of 1^0. Due to the possible high leakage error introduced at high spatial resolution (Swenson and Wahr, 2006), statistical comparison at subbasin level is not performed. However, focusing on maps of the sample months, some level of similar spatial and temporal pattern is revealed (figure 7.12).
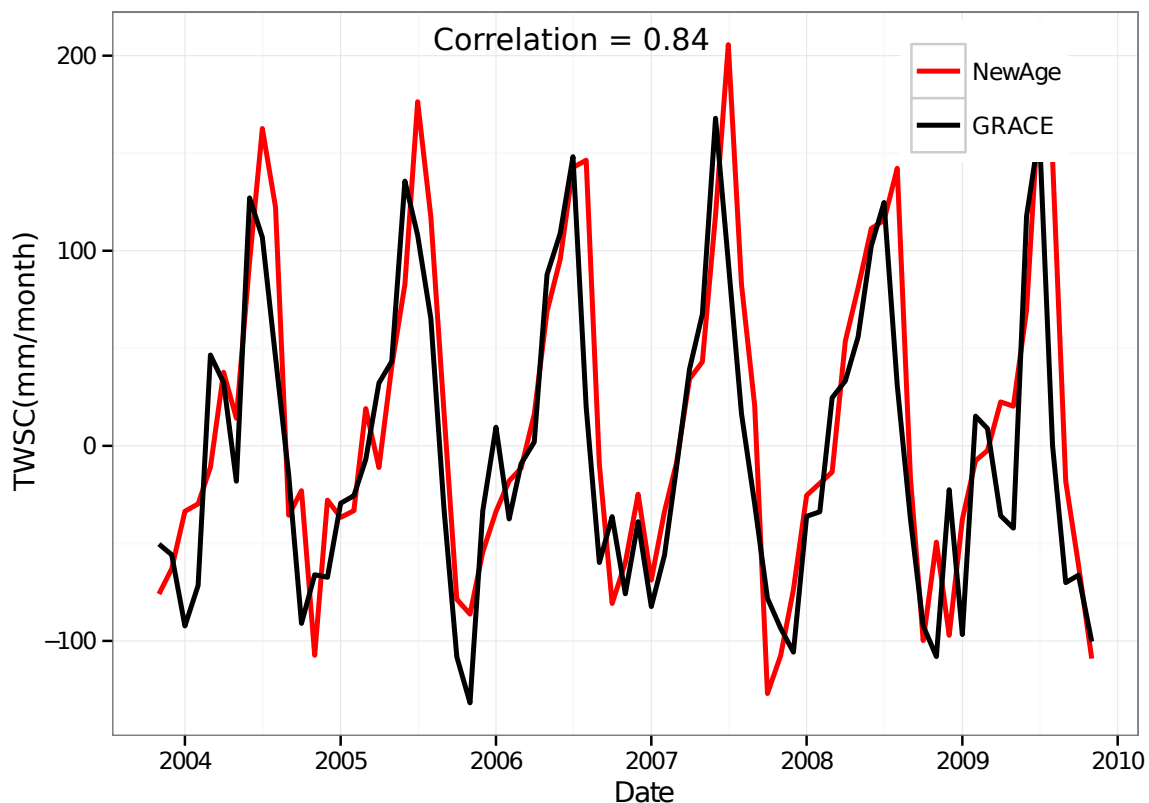
Figure 7.11: Comparison between basin scale NewAge ds/dt and GRACE TWSC from 2004-2009 at monthly time step.

7.5.2 Water budget closure

The water budget components (J, ET, Q, ds/dt) of 402 subbasin of UBN is simulated for duration of 1994-2009 at daily time series. Figure 7.13 is long term monthly mean water
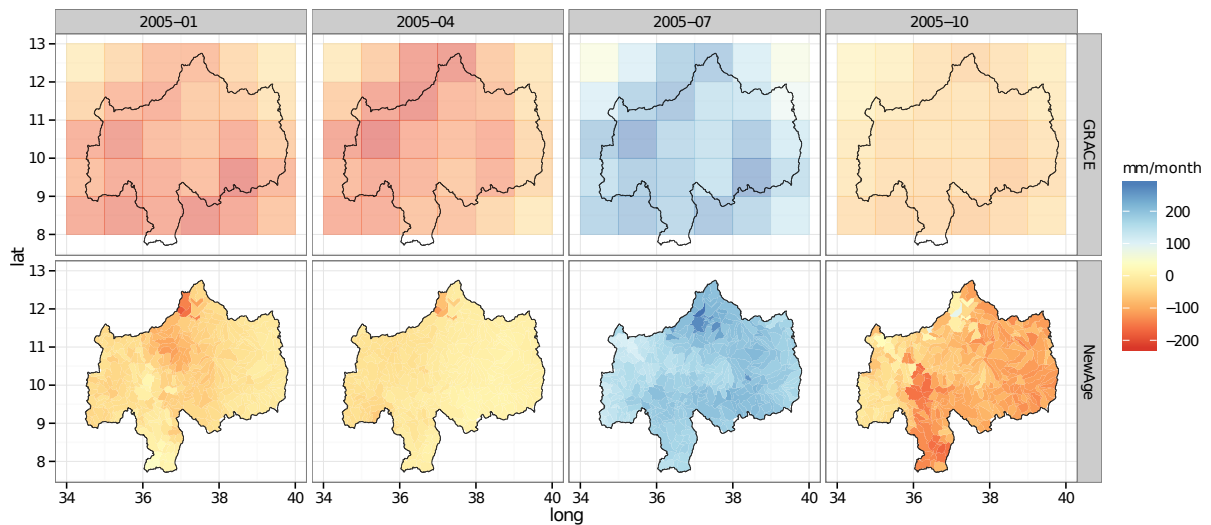
Figure 7.12: Comparison of Spatial distribution of NewAge ds/dt and GRACE TWSC for January, April, July, and October 2005. Note that the sptial resolution of NewAge ds/dt and GRACE is subbasin scale and 1^0 X 1^0 respectively

budget closure derived from 1994-2009. The four months (January, April, July, and October) are systematically selected to show the four seasons (winter, Spring, summer and Autumn). For all the components, the mean seasonal variability is very high. Generally, the seasonal patterns of Q and S follows the J, showing highest in summer (i.e July) and lowest in winter (i.e January). However, simulated ET shows distinct seasonal pattern from other components, and the highest is during spring (October), followed by winter (January). During summer, it is low most likely due to high cloud cover.

The variability between the subbasins also appreciable. Except summer season (July), all components tends to increase from east to southwest part of the basin. On the contrary, during summer, the eastern part of the basin receives its highest rainfall, store more water, and generate high runoff as well. In general, at this time scale, the dominant role vary with months. For instance, in January ET is the dominant while in June and July S is more dominant. After summer season, Q and ET are the dominate flux. This knowledge is very important for water resource management. Based on all subbasin and all year results, the variability in ET that can be explained by J is zero (R^2=0.01) at short time scale such as at a daily and monthly scale. Conversely, at yearly time scale, 78% of ET variance is explained by J.

The spatial variability of long term mean annual water budget closure is shows at figure 7.14. The spatial variability J and Q is higher than S and ET. The higher Q and ET in the southern and southwestern part of the basin could be due to higher J. Similarly Q
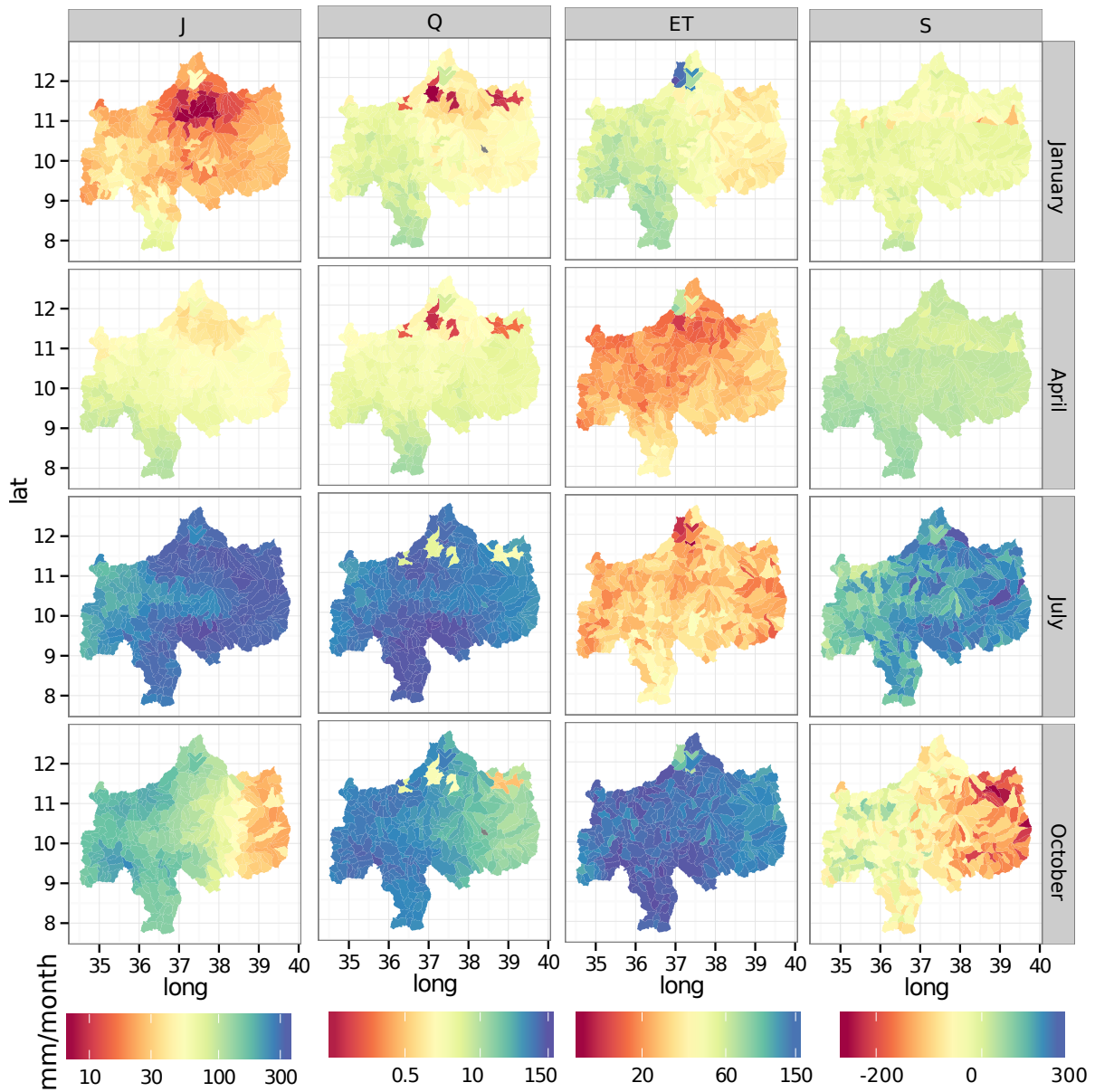
Figure 7.13: Long term mean monthly (January, April, July and October) water budget spatial distribution of UBN basin. For visibility reason, the legend is plotted separately and in logarithmic scale except storage component.
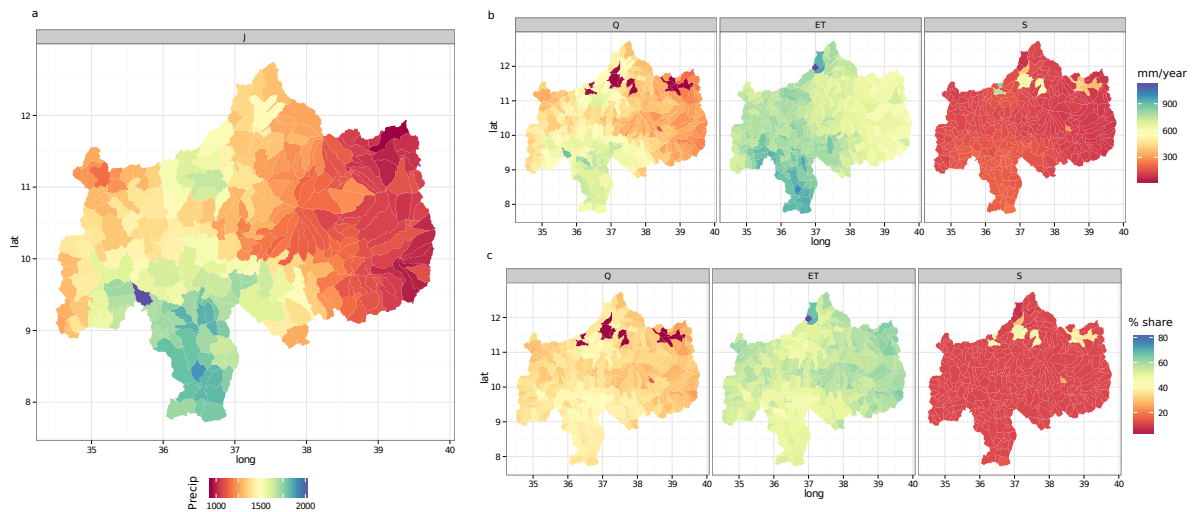
Figure 7.14: The spatial distributions of long term mean annual water budget closure:
precipitation in mm (a), the output term (Q, ET, S) in mm (b), and the percentage share
of the output term (Q, ET, S) of the total precipitation (c).

is lower in the eastern and northeaster part of the basin. Focusing on the percentage
share of the output term (Q, ET, S) of the J (figure 7.14 c), ET dominant the water budget
followed by Q. Note that the eastern subbasin with low ET have still high percentage
share of ET due to low amount of J receives.

The long term basin average water budget component shows that 1360 ± 230 mm of
J followed by 740 ± 87 mm of ET, 454 ± 160 mm of Q and -4 ± 63 mm of S. While the
spatial variability of the water budget is high, the annual variability is rather limited.
The higher annual variability is observed for J, followed by Q. years 2001 and 2006 are
wet years, characterized by high J and Q. Conversely, 2002 and 2009 are dry years with
1167.480 mm and 1215.123 mm per year of precipitation. Detail on the two dry years
(2002, 2009) can be refereed in Viste et al. (2013).

Figure 7.16 provides long term monthly mean estimates of water budget fluxes and
storage. The basin scale mean budget is highly variable. The highest variability is mainly
in J and S. During summer months, J, Q, and S shows high magnitude. ET is not highest
in June, July and August, but, in October and December. The accumulated S in the
summer season is feeding to the highest ET in autumn, and causes very high drops in S
(figure 7.16).
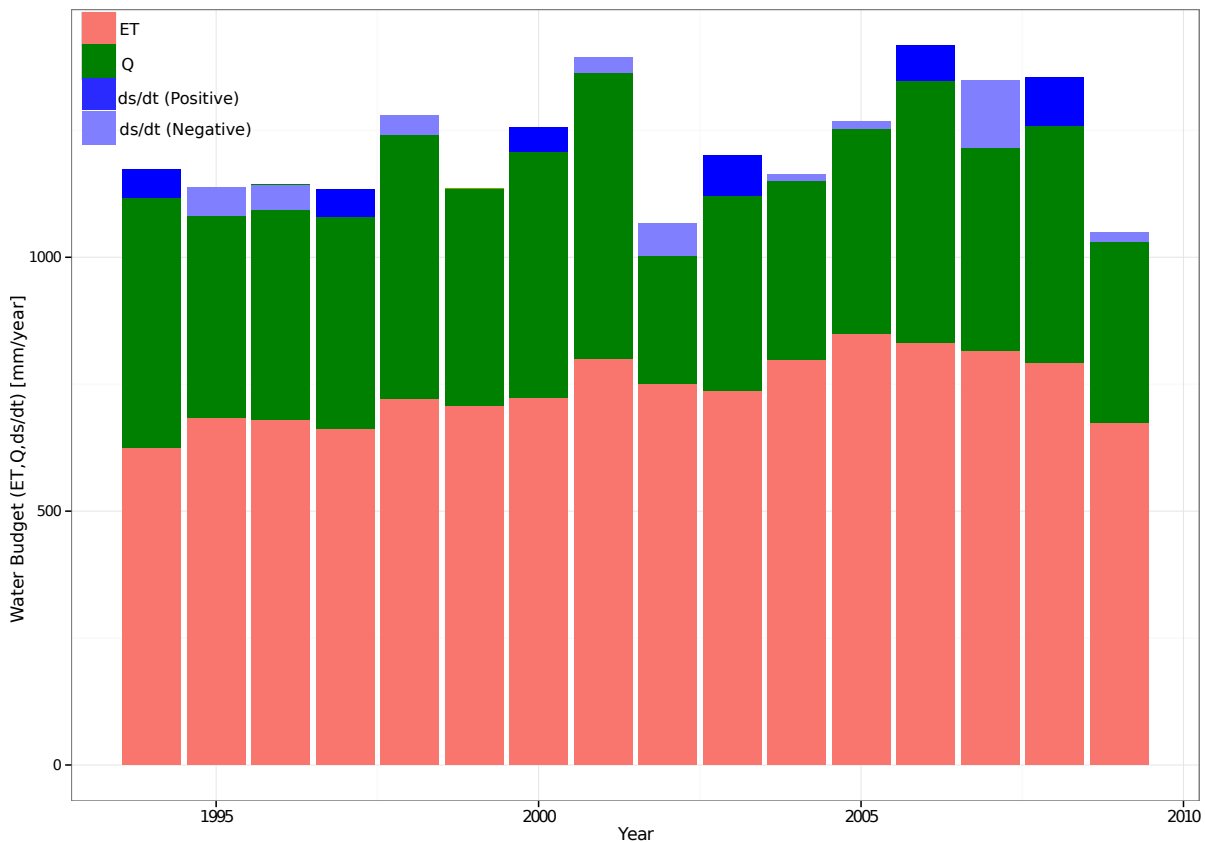
Figure 7.15: Water budget components of the basin and its annual variabilities from 1994 to 2009. It shows the relative share (the length of the bars) of the three components (Q, ET and ds/dt) of the total available water J. Note that the total length of the bar is J. The positive and negative storage of the years are shown by dark blue and light blue respectively).

7.6 Conclusions

The goal of this study is to estimate the water budget and its spatial and temporal variability using JGrass-NewAge hydrological model system and remote sensing data over upper Blue Nile basin from 1994-2009 (16 years). Different remote sensing data are used to force and verify the modeling results. The results can be summarized as in the following.

The basin scale annual precipitation over the basin is 1360 ± 230 mm, and spatially highly variable. The southern and southwestern part of the basin receives highest precipitation and tends to decrease towards the eastern part of the basin (figure 7.4).

The comparison of simulated ET with MOD16 shows that MOD16 underestimate ET considerable. Spatially, the Correlation between MOD16 and NewAge ET is higher in
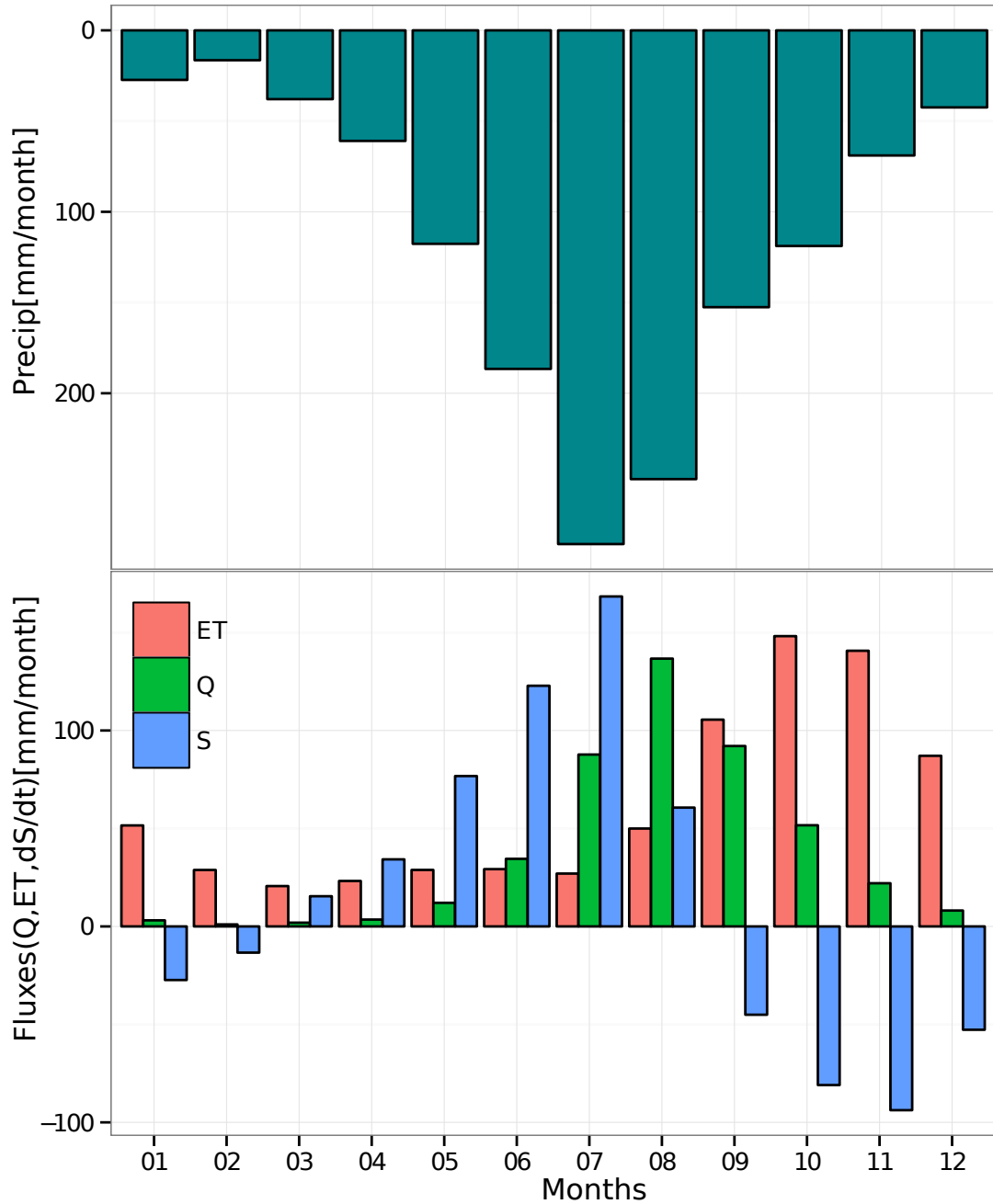
Figure 7.16: Basin scale long term monthly mean Water budget components based on
estimates from 1994 to 2009. It shows the relative share of the three components (Q, ET
and dS/dt) of the total available water J.

the east and northeast part of the basin. Generally, the interannual variability of ET is high, and tends to be higher (lower) in Autumn (summer). The average basin scale ET is about 740 ± 87 mm, and is the second dominant component of water budget in the basin.

NewAge Adige rainfall-runoff component is able to reproduce discharge very well at the outlet (KGE = 0.92), and the verification results at the internal sites revealed that the model can be used for forecasting at ungauged links. Here, discharge is estimated for each channel links in the basin. The long term annual runoff of UBN basin is about 454 ± 160 mm.

The NewAge storage estimations and its space-time variability is effectively verified by the basin scale GRACE TWSC data. The total water storage change estimated using GRACE and NewAge shows high correlation, and similar amplitude. Generally, the long term water budget simulation shows that, the basin is equilibrium around zero storage (-4 ± 63 mm).

Different remote sensing data (SM2R-CCI, SAF EUMETSAT CFC, MOD16, GRACE) are effectively employed to force the water balance modelling and verify model results, and the performance of the modelling solution is promising (figure 7.9 and 7.11, and table 7.2)

CONCLUDING SYNTHESIS

This study is conducted to characterize and simulate basin water budget at varying spatial and temporal scale. The study has also sought to identify different datasets useful for hydrological simulation in data scarce areas and in large scale basins. To obtain this, this study combined uDig GIS spatial toolbox to efficiently handle spatial data, and JGrass-NewAge model system to simulate different hydrological processes.

Spatially-distributed hydrological models, through their integration with GIS, explicitly represent basin physical properties and processes. However, different GIS tools used in hydrological models has been criticized for lack of sophisticated analytical and modelling capability. In addition, most of the GIS have limitation in processing time-series (or short time steps) data, are platform dependent, have closed source code that impedes customization of post and pre-processing of hydrogeomorphological data. The tools we use, the JGrass-Spatial toolbox is a specialized GIS for hydrogeomrophological application, with the aims to solve the aforementioned problems. It facilitates the work of the hydrologists (either developers/users), can efficiently integrate with spatial data, and allows researchers to modify the source codes at their demand (chapter 2).

The key advantage of spatially-distributed models is their ability to use spatial information of both basin geomorphology and forcing data. In the case of semi-distributed models, the spatial information is aggregated in some level. The spatial aggregation is not virtue by itself, but facilitates the modeling activities from different perspectives (Ajami et al., 2004; Khakbaz et al., 2012), and helps to obtain major hydrological fluxes at useful spatial and temporal time scales.

Focusing only on the spatial representation of geomorphological information, both the topographic and topological elements of basins are important variables required. It is obvious that the representation of geomorphology in hydrological models varies from model to model, and their impact on hydrological forecasting has been an active area of research. However, the results are inconclusive. The use of geomorphological information as formulated in the geomorphic unit hydrograph, first proposed by Rodríguez-Iturbe and Valdés (1979), and recently summarized by Rigon et al. (2015), is well established methods of analyzing the effect of basin geomorphology on basin response. By comparing the level of topographic information according to fully distributed (at finest scale grid data) and semi-distributed (some level of aggregated units such as Hydrologic Response Units, HRUs) models, some level of understanding can be obtained as shown in chapter 3. However, even though, some interesting results are found, further research is required to integrate the empirical findings into the practical modeling solutions.

Having hydrological information, at many locations inside the basin, contrary to the traditional estimation of integrated behavior of the hydrological system at outlet, is modern day societal demand. For that, a hydrological modelling framework which uses the spatial basin information and spatiotemporal forcing data is required (Fatichi et al., 2016).

Precipitation, with its spatial variability, is not only the main forcing, but it is the input component for any water budget computation. Hence, its proper representation is a key for reasonable water budget modelling. The effort to generating improved precipitation data brought two research directions. In the first approach, applicable when appropriate in situ data are available, sophisticated tools of statistics can be used to elaborate the spatial information. Kriging algorithms have been the standard tools for hydrological analyses, and efforts to improve these algorithms continues. The improvement in semivariogram model parameters calibration and the selection procedures of theoretical semivariogram is clearly very crucial and an important contribution as illustrated in chapter 4. Another important practical question is how to separate precipitation into snowfall and rainfall which was solved with the use of remote sensing. Particularly MODIS snow cover and snow albedo data has been very useful (chapter 4) in establishing a new methodology.

The second approach to generate spatial information of meteorological inputs is to use remote sensing data. Satellite rainfall estimates (SREs) are a practical option when the basin of interest lacks in situ data and is a large basin. However, different SREs have different skills and their accuracy greatly varies from area to area. The improvement

of this approach, pursued in chapter 6, includes the comparison of viable products with available in situ data and some kind of post processing such as bias correction.

The simulation results for water budget output terms, runoff and evapotranspiration, can follow different formulations, but need to be consistent with the level of coarse graining. In this thesis, coarse graining was implicitly obtained by using different spatial aggregation (i.e. Hydrologic Response Units, HRUs) of different sizes for basins of different dimensions, and switching form the hourly time scale to the daily time scale for the quantity forecasted. This has required a certain amount of pre-treatment of the input data, their averaging (or summation) that have been performed thanks to the ability of the JGrass-NewAGE system. Detailed conclusions of the single sections of this study are reported at the end of each chapter and are summarised for the readers' convenience here below.

The water budget of Posina river basin ($116km^2$) and Upper Blue Nile (UBN) basin (about $175315km^2$) are simulated with JGrass-NewAge model system. For Posina basin, the simulation is at hourly time-steps by using 18 years of meteorological data (rainfall and temperature) and discharge. The analysis of UBN basin is based on 16 years of daily steps and mainly based on the remote sensing data and few hydrometer measurements. The analyses include estimations of the four components of water budget (precipitation, discharge, relative storage, and evapotranspiration).

At Posina river basin, the spatial precipitation and temperature is characterized using Kriging. Four types of kriging are performed. Based on one-leave-out cross-validation, local ordinary kriging and local detrended kriging, those considering only the nearest stations, relatively outperform ordinary kriging and detrended kriging. The effect of semivariogram model selection at this spatial small scale is minimal. The kriging interpolation helps to estimates the spatial variability in a few km scales, and helps to obtain appreciable spatial variability for water budget input. The use of automatic selection of the semivariogram, instead of fitting a single semivariogram to the whole analysis period, improved kriging estimation.

For precipitation estimation in UBN basin, five satellite rainfall datasets are evaluated at daily time steps for 10 years (2003-2012). The mean annual cumulative precipitation analysis shows, at some stations, that the difference amongst the various satellite rainfall estimates is as high as about 2700 mm. The correlation coefficient based on 10 years of daily data at the whole basin scale shows almost similar value for TAMSAT (median=0.51), SM2R-CCI (0.5), and CMORPH (0.52), slightly better than 3B42V7 (0.47) and CFSR (0.3) performances. CMORPH has the highest BIAS (-72%), with most of the

stations tends to have similar bias. The ecdf-matching bias correction procedure provided highest performance for CMORPH. Based on the comparison analysis, SM2R-CCI is selected to be used as input to the water budget modeling.

The NewAge HYMOD rainfall-runoff component is used to estimate the spatial runoff. For both basins, discharge simulation is calibrated at the outlet of the basins and used to estimate at each channel link. Based on the goodness-of-fitness statistics, the rainfall-runoff component provides acceptable performances. The discharge measures inside the basin helps to quantify the reliability of internal discharges by assuming the validity of model parameters calibrated at the overall outlet. For Posina, the model performances at the interior sites are similar the outlet performances. Similarly, in UBN basin, NewAge rainfall-runoff component is able to reproduce discharge very well at the outlet, and the verification results at the internal sites revealed that the model can be used for forecasting at ungauged links.

Priestley-Taylor (PT) method is used to estimate the evapotranspiration component of the water budget, and to infer the relative storage of water under the hypothesis of stationarity (null storage). This approach is sufficient to set a value for the mean α coefficient apt to obtain the mean evapotranspiration if the precipitation and discharge data are measured well. For Posina basin, by moving the null storage hypothesis along the first 17 years, variable values of the PT α obtained and it can be interpret as an estimate of the error in evapotranspiration to be accumulated with uncertainty produced in precipitation and discharge estimate. To consider both the atmospheric demand and local water storage supply at each hillslope for ET estimation, the PT α is optimized coupled with the HYMOD storage information and PT radiation budget for five year null storage assumption (Budyko assumption). For UBN basin, the second approach is applied to estimate space-time dynamics of evapotranspiration. The results of NewAge simulated evapotranspiration are compared with MODIS evapotranspiration (MOD16), and shows that MOD16 underestimate ET considerably. Spatially, the correlation between MOD16 and NewAge ET is higher in the east and northeast part of the basin.

For both basins, the spatial and temporal dynamics of storage is estimation based on water budget equation for each HRU. In the case of UBN basin, storage estimation is effectively verified by the basin scale GRACE total water storage change data. The total water storage change estimated using GRACE and NewAge shows high correlation, and similar amplitude.

For Posina basin, the annual variability of the precipitation is as high as 1400 mm, with minimum annual value of 1355 mm in 1995/1996 and maximum 2700 mm in

2010/2011. The inter annual variability in discharge is high, with minimum annual value of 1003 mm in 1995/96 and maximum 2072 mm in 2010/2011. Both the contribution and uncertainties of evapotranspiration to the water budget is very high. While evapotranspiration accounts 19-38% of the precipitation, its annual uncertainty is about 20% (148 mm on average). Based on consistency of the water budget, it can be observed the high interannual variability of the fluxes, with certainly the variability of precipitation dominating it. In all years, discharge is larger than evapotranspiration. Either (relative) positive and negative water storages have been found.

In the case of UBN basin, the spatial variability in the water balance terms, as expected is high. The basin scale annual precipitation over the basin is 1360 ± 230 mm, and spatially highly variable. The southern and southwestern part of the basin receives highest precipitation and tends to decrease towards the eastern part of the basin. The interannual variability of evapotranspiration is high, and tends to be higher (lower) in Autumn (summer). The average basin scale evapotranspiration is about 740 ± 87 mm, and is the second dominant component of water budget in the basin. The long term annual runoff of UBN basin is about 454 ± 160 mm. Generally, the long term water budget simulation shows that, the basin is in equilibrium around zero storage (-4 ± 63 mm).

A

ANALYTICAL FORMULATION OF THE FOUR SEMIVARIOGRAM MODELS

Using h to represent lag distance, r to represent range, and s to represent sill, the four most frequently used semivariogram models for rainfall interpolation in literature, which are the ones used in this paper, are:

- Spherical semivariogram model

(A.1)
$$\begin{cases} \gamma(h) = s \cdot [1.5 \cdot \frac{h}{r} - 0.5 \cdot (\frac{h}{r})^3] & h < r \\ \gamma(h) = s & h \geq r \end{cases}$$

- Exponential semivariogram model

(A.2)
$$\gamma(h) = s \cdot [1 - e^{-\frac{|h|}{r}}]$$

- Linear semivariogram model

(A.3)
$$\begin{cases} \gamma(h) = s \cdot \frac{h}{r} & h < r \\ \gamma(h) = s & h \geq r \end{cases}$$

- Gaussian semivariogram model

(A.4)
$$\gamma(h) = s \cdot (1 - e^{-\frac{h}{r}})$$

B

MODEL PERFORMANCE CRITERIA

The model evaluation statistics used in the research are different goodness-of-fit (GOF) indices. These includes for comparison of observed and simulated data, comparison of two models, and between the model simulation and remote sensing observation data. The followings formulations of GOF statistics are used in this study.

1. Nash-Sutcliffe efficiency (NSE) is a normalized statistic that determines the relative magnitude of the residual variance compared to the measured data variance (Nash and Sutcliffe, 1970). The choice of this index is to give high emphasis to the peak of the hydrograph.

(B.1)
$$NSE = 1 - \frac{\sum_{i=1}^{N}(S_i - O_i)^2}{\sum_{i=1}^{N}(O_i - \overline{O}_i)^2}$$

2. Coefficient of determination (R^2) is a measure of how well the simulated data fit to the model simulation, and how much of the variance of the simulated data is explained by the observed data.

(B.2)
$$R^2 = \left[\frac{\sum_{i=1}^{n}(O_i - \overline{O})(S_i - \overline{S})}{\sqrt{\sum_{i=1}^{n}(O_i - \overline{O})^2}\sqrt{\sum_{i=1}^{n}(S_i - \overline{S})^2}} \right]$$

3. Mean Error (ME) is calculated as

(B.3)
$$ME = \frac{1}{n}\sum_{i=1}^{n} S_i - O_i$$

where S_i is the predicted value and O_i is the observed value of the rainfall data at a given time step.

4. The Root Mean Square Error (RMSE) (Chu and Shirmohammadi, 2004; Singh et al., 2005). The lower the RMSE the better the model performance is. It is given by

(B.4)
$$RMSE = \sum_{i=1}^{n} \sqrt{\frac{1}{n}(S_i - O_i)^2}$$

The RMSE is a joint measure of bias in the mean and in the variance, as the square of individual differences between estimated and observed values puts the emphasis on the errors in outliers or higher differences (Ashraf et al., 1997; Nalder and Wein, 1998).

5. The Pearson linear correlation coefficient (r):

(B.5)
$$r = \frac{1}{N}\frac{\sum_{n=1}^{N}(S_i - \bar{S})(G_i - \bar{G})}{\sqrt{\sum_{n=1}^{N}(S_i - \bar{S})^2 \sum_{n=1}^{N}(G_i - \bar{G})^2}},$$

where S and G are the SREs and gauge rainfall estimation respectively, N is the number of observations, and the overbar is the mean operator.

6. PBIAS: is a measure of the average tendency of estimated values to be large or smaller than the corresponding measured values. The value near to zero indicates high estimation, whereas a positive value indicates overestimation and a negative value indicates model underestimation (Moriasi et al., 2007; Gupta et al., 1999).

(B.6)
$$BIAS = \frac{\sum_{i=1}^{n}(P_i - O_i)}{\sum_{i=1}^{n} O_i}$$

This value can be used to estimate the systematic under- or overestimation of the model.

7. Kling-Gupta efficiency (KGE) is developed by Gupta et al. (2009) to provide a diagnostically interesting decomposition of the Nash-Sutcliffe efficiency (and hence

MSE), which facilitates the analysis of the relative importance of the different components (correlation, bias and variability) in the context of hydrological modelling. Kling et al. (2012) proposed a revised version of this index. It is given by

$$(B.7) \qquad KGE = 1 - ED$$

$$(B.8) \qquad ED = \sqrt{(r-1)^2 + (vr-1)^2 + (\beta-1)^2}$$

where ED is the Euclidian distance from the ideal point, β is the ratio between the mean simulated and mean observed flows, r is the Pearson product-moment correlation coefficient, and v is the ratio between the observed (σ_o) and modelled (σ_s) standard deviations of the time series and takes account of the relative variability (Zambrano-Bigiarini and Bigiarini, 2013).

8. The $BIAS$:

$$(B.9) \qquad BIAS = \frac{\sum_{i=1}^{N}(S_i - G_i)}{\sum_{i=1}^{N} G_i},$$

It is dimensionless and optimal value is 0.

HYMOD MODEL IN NEWAGE-JGRASS SYSTEM

The NewAge system executes one Hymod model at each HRU, and routes water downslope. Detailed descriptions of Hymod model is provided in many researches (Moore, 1985; Van Delft et al., 2009; Boyle et al., 2001; Formetta et al., 2011). In Hymod, each HRU, is supposed to be a composition of storages of capability C [L] according to distribution (Moore, 1985):

$$F(C < c) = 1 - (1 - \frac{c}{C_{max}})^{B_{exp}} \tag{C.1}$$

where $F(C)$ represents the cumulative probability of a certain water storage capacity, C; C_{max} is the largest water storage capacity within each hillslope and B_{exp} is the degree of variability in the storage capacity.

As shown in the schematic diagram (figure C.1), the precipitation exceeding C_{max} is send directly to the volume available for surface runoff. If we call the precipitation volume in a time interval Δt, $P(t) := J(t)\Delta t$, then this "direct" runoff can be estimated according to:

$$R_H(t) = \max(0, P(t) + C(t) - C_{max}) \tag{C.2}$$

where $C(t)$ defines the fraction of storages already filled at time t. The latter equation is true for any precipitation and storage level, even when the maximum storage C_{max} is not exceeded. When precipitation does not exceeds C_{max} runoff volume can be produced by filling some of the smaller storages. To which extent this happens, can be derived
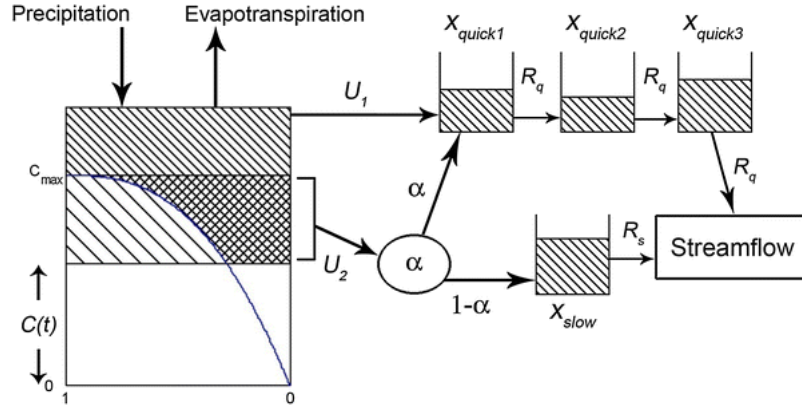
Figure C.1: Schematic diagram of hymod model (adapted from Van Delft et al. (2009))

by the knowledge of the storage distribution, eq. (C.1), the initial storage $C(t)$ and the precipitation $P(t)$. This residual runoff is, in fact, given by:

(C.3)
$$R(t) = \int_{C(t)}^{\min(C(t)+P(t),c_{max})} F(c) \, dc$$

An analytic expressions for the integral in eq. (C.3) is available, which makes the computation easier. Water in storage is made available to evapotranspiration. Water going into runoff the runoff volume, i.e. $R(t)$ and R_H, is further subdivided into a surface runoff volume and subsurface storm runoff. Surface runoff, in turn, is composed by the whole of $R_H(t)$ and part of $R(t)$, and $R(t)$ is split according to a partition coefficient Θ such that the part $\Theta R(t)$ goes into surface runoff volume and $(1-\Theta)$ into the subsurface storm runoff volume. In Hymod, Θ is a calibration coefficient.

Finally, surface runoff volumes are routed through three linear reservoirs, and, subsurface storm runoff volume is routed through a single linear reservoir. A summary of equations for the surface runoff is therefore:

(C.4)
$$\frac{dS_1(t)}{dt} = \Theta R(t) + R_H(t) - kS_1(t) \quad Q_1(t) = \frac{S_1(t)}{k}$$

where S_1 [L^3] is the storage in the first of the linear reservoirs, and k [T] is the mean residence time in each of the reservoirs. Then:

(C.5)
$$\frac{dS_i(t)}{dt} = Q_{i-1}(t) - kS_i(t) \quad Q_i(t) = \frac{S_i(t)}{k}$$

for the other two reservoirs, where S_i [L] with $i = 2, 3$ is the storage in the two remaining surface reservoirs. Subsurface storm runoff is then modeled by:

(C.6)
$$\frac{dS_{sub}}{dt} = (1-\Theta)R(t) - k_{sub}S_{sub}(t)$$

174

where S_{sub} [L^3] is the storage in the subsurface storm-flow system and k_{sub} [T] is its mean residence time. A budget equation can be written for the groudwater system as:

(C.7)
$$\frac{dS_g(t)}{dt} = (P(t) - R(t) - R_H(t)) - AET(t) - Q_g(t)$$

where $S_g(t)$ [L^3] is the groundwater storage, and $Q_g(t)$ the groundwater flow which becomes surface flow at the closure of the HRU.

Summarizing, Hymod subdivides each HRU into three reservoirs: a groundwater reservoir, from where evapotranspiration and groundwater flow is allowed, a subsurface storm-water reservoir, and a surface runoff reservoirs set. Partition of precipitation into the three reservoirs is obtained by a calibration coefficient, Θ, and the use of a probability distribution function of storages' capacity, $F(c)$.

ANCAPPENDIX

D
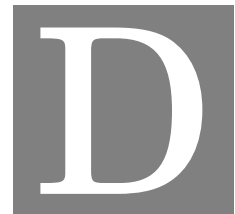
MODIS SNOW PRODUCT PROCESSING FOR SNOW FALLING MODEL CALIBRATION

The daily standard snow products of Terra and Aqua MODIS products, i.e. MOD10A1 and MYD10A1 (V005) (Hall et al., 2006), are used. Both products are downloaded from NASA, which is distributed through the National Snow and Ice Data Center in Boulder, Colorado Scharfen et al. (2000) at http://modis-snow-ice.gsfc.nasa.gov. Terra (MOD10A1) is collected since February 2000 while Aqua (MYD10A1) is since June 2002. The study basin is covered by the h18v04 MODIS tile. The technical steps on MODIS snow products processing is similar to that described by (Gascoin et al., 2015).

First the MOD10A1 fractional snow cover (FSc) of the study area is used. It provides the percentage coverage (0-100%) of a pixel with snow. If MOD10A1 does not provide FSc estimates due to any reason, it is replaced with the MYD10A1 for that particular time steps or pixel. This helps to produce much less "no values" and eliminates clouds, providing a much more useful pixel than using MOD10A1 or MYD10A1 alone, e.g. Parajka and Blöschl (2008).

The FSc itself has advantages over the snow/no-snow data, which is often used in routine applications. It provides the percentage of each pixel (or any intended aggregated scale) covered by the snow. This helps the decision on the discriminating threshold between snow/no-snow binary data, based on the scale, location and purpose of the application. Usually, to recover snow cover information, a threshold in FSc is used. In this study the threshold is set at 10%. Therefore, values of FSc below 10% are set to no snow cover and pixels with FSc larger than 10% are considered as snow covered.

Then the snow/no-snow based distributed information is used to optimize the rainfall-snowfall separation algorithm parameters. To maintain the model structure, and reduce parameter transfer error from pixel to HRU, the FSc is coarse grained to HRU level for daily time steps for 4 years (2002-2006). The first three years are used for optimization, and the last year, 2006, is used for validation.

E

ESTIMATION OF EVAPOTRANSPIRATION. PROCEDURE'S DETAILS

A gross estimation of evapotranspiration coefficient α (e.g. eq. (5.5) can be obtained directly from data available, under what we call Budyko Hypothesis.

This hypothesis implies that the water storage oscillates and after a number of days/years, let's call it Budyko's time, T_B, it is back at the same level it was at the initial time. This implies that the water budget is not very far from equilibrium, even in climate change times. In this case, considering each HRUs, or the whole basin as a unique control volume (as allowed by data), the water budget can be written as:

$$\text{(E.1)} \qquad S(t) - S(0) = \int_0^{T_B} (J(t) - Q_m(t) - \alpha ET(t))dt = 0$$

where $Q_m(t)$ is the measured discharge, and it has been defined

$$\text{(E.2)} \qquad ET(t) := \frac{\Delta}{\Delta + \gamma} R_n$$

where the dependence on water storage (which would bring in the process the necessary knowledge of the parameter C_{max}, the maximum allowable storage, a Hymod parameter that is object of calibration), has been, necessarily, neglected.

Therefore, from data only, the maximum we can obtain is:

$$\text{(E.3)} \qquad \tilde{\alpha}(T_B) = \frac{\int_0^{T_B} (J(t) - Q_m(t))dt}{\int_0^{T_B} ET(t))dt}$$

179

These values can then be used in Hymod either in calibration and forecasting phases. This averaged Priestley-Taylor coefficient is clearly a function of the Budyko's time, which we do not know, unless we can perform appropriate groundwater level measurements.

By using modelling, an estimation of an evapotranspiration dependent on storage can be obtained. It must use Hymod partition of the budget, and forecasted (instead of measured) discharges. This estimation process is not that smooth because the estimation of α is interwined with the process of calibration of Hymod's parameters.

Hymod, in fact, requires the knowledge on the Storage $S_g(t)$, which, in turn, depends on how much water is withdrawn by evapotranspiration (e.g. eq. C.7). In this case, the Budyko's hypothesis says that:

$$(E.4) \qquad S_g(T) - S_g(0) = \int_0^{T_B} (P(t) - R(t) - R_H(t)) - \alpha\, ET(t) dt = 0$$

where, now:

$$(E.5) \qquad ET(t) = \frac{S(t)}{C_{max}} \frac{\Delta}{\Delta + \gamma} R_n$$

and implies that we can estimate an average α as:

$$(E.6) \qquad \bar{\alpha}(T_B) = \frac{\int_0^{T_B} (J(t) - R(t) - R_H(t)) dt}{\int_0^{T_B} ET(t) dt}$$

Therefore,in a set of n years of data, let us assume to use $n-1$ years for setup the modelling and the last year for predictions (given precipitations). For each of the year in range [1,n-1], let us assume valid eq. (**??**). This implies that we obtain $n-1$ values of $\alpha(T_B)$ which can be used.

In the calibration phase, to update $C(t)$ in eq. (C.2) the knowledge of $alpha$ is necessary. Therefore, the calibration procedure must simultaneously estimate Evapotranspiration and the runoff parameters. An iterative procedure to obtain it, can be:

- Assign a first trial value for α, say $\hat{\alpha}^0$, as in eq. (**??**) ;

- Assign a tolerance, $\epsilon > 0$ for α estimates.

- Estimate through calibration Hymod's parameters, which are, obviously $alpha^0$ dependent;

- for an assigned T_B estimate $\hat{\alpha}^1$;

- Repeat the calibration procedure until $|\hat{\alpha}^n - \hat{\alpha}^{n-1}| < \epsilon$

This finally gives a value of α which is compatible with the estimation of ET dependent on variable storages.

It has to be remarked that, if, depending on available data $\hat{\alpha}$, can be a global or local (to HRUs) parameter, the storage fractions $S(t)/C_{max}$ are always estimated at the level of each HRU.

F

REPLICABLE RESEARCH

The model components used in this thesis and as much as possible material to reproduce findings will be posted at the AboutHydrology Blog `https://abouthydrology.blogspot.com` and `http://ecohydrogeomorpho-metry.blogspot.it`.

The source code of NewAGE is available on GitHub at `https://github.com/formeppeandhttps://github.com/geoframecomponents`.

Materials for reproducing chapter 2 can be find `http://abouthydrology.blogspot.it/2014/05/theudig-spatial-toolbox-paper.html`.

Complementary material that explains how the Figures in the paper were generated can be found at

`http://abouthydrology.blogspot.it/2014/05/theudig-spatial-toolbox-paper.html`.

The datasets used in chapter 6, mainly the five SREs, R codes, and supplementary material will be available for reproducing the results at `http://ecohydrogeomorpho-metry.blogspot.it/2015/09/satellite-rainfall-estimation-products.html`.

Abera, W., Antonello, A., Franceschi, S., Formetta, G., Rigon, R., 2014. The uDig Spatial Toolbox for hydro-geomorphic analysis, in: clarke & nield (eds.) geomorphological techniques (online edition) Edition. British Society for Geomorphology, London, UK.

Abtew, W., Melesse, A. M., Dessalegne, T., 2009. Spatial, inter and intra-annual variability of the upper blue nile basin rainfall. Hydrological processes 23 (21), 3075–3082.

Abu-Zeid, M. A., Biswas, A. K., 1996. River basin planning and management. Oxford University Press.

AghaKouchak, A., Mehran, A., Norouzi, H., Behrangi, A., 2012. Systematic and random error components in satellite precipitation data sets. Geophysical Research Letters 39 (9).

AghaKouchak, A., Nasrollahi, N., Habib, E., 2009. Accounting for uncertainties of the trmm satellite estimates. Remote Sensing 1 (3), 606–619.

Ajami, N. K., Gupta, H., Wagener, T., Sorooshian, S., 2004. Calibration of a semi-distributed hydrologic model for streamflow estimation along a river system. Journal of Hydrology 298 (1), 112–135.

Allen, R. G., Pereira, L. S., Raes, D., Smith, M., et al., 1998. Crop evapotranspiration-guidelines for computing crop water requirements-fao irrigation and drainage paper 56. FAO, Rome 300, 6541.

Andrew, M. E., Wulder, M. A., Nelson, T. A., 2014. Potential contributions of remote sensing to ecosystem service assessments. Progress in Physical Geography 38 (3), 328–353.

Arking, A., 1991. The radiative effects of clouds and their impact on climate. Bulletin of the American Meteorological Society 72 (6), 795–813.

Army, U., 1956. Snow hydrology. summary report of the snow investigations. north pacific division of corps of engineers. US-Army, Portland, Oregon.

Arnold, J. G., Srinivasan, R., Muttiah, R. S., Williams, J. R., 1998. Large area hydrologic modeling and assessment part i: Model development1.

Ascough, J., David, O., Krause, P., Heathman, G., Kralisch, S., Larose, M., Ahuja, L., Kipka, H., 2012. Development and application of a modular watershed-scale hydrologic model using the object modeling system: runoff response evaluation. Transactions of the ASABE 55 (1), 117–135.

Ashraf, M., Loftis, J. C., Hubbard, K., 1997. Application of geostatistics to evaluate partial weather station networks. Agricultural and forest meteorology 84 (3), 255–271.

Attorre, F., Alfo, M., De Sanctis, M., Francesconi, F., Bruno, F., 2007. Comparison of interpolation methods for mapping climatic and bioclimatic variables at regional scale. International Journal of Climatology 27 (13), 1825–1843.

Auer Jr, A. H., 1974. The rain versus snow threshold temperatures. Weatherwise 27 (2), 67–67.

Band, L. E., 1986. Topographic partition of watersheds with digital elevation models. Water resources research 22 (1), 15–24.

Band, L. E., 1993. Extraction of channel networks and topographic parameters from digital elevation data. Channel network hydrology, 13–42.

Barling, R. D., Moore, I. D., Grayson, R. B., 1994. A quasi-dynamic wetness index for characterizing the spatial distribution of zones of surface saturation and soil water content. Water Resources Research 30 (4), 1029–1044.

Basistha, A., Arya, D., Goel, N., 2008. Spatial distribution of rainfall in indian himalayas– a case study of uttarakhand region. Water Resources Management 22 (10), 1325–1346.

Becker, M., Meyssignac, B., Xavier, L., Cazenave, A., Alkama, R., Decharme, B., 2011. Past terrestrial water storage (1980–2008) in the amazon basin reconstructed from grace and in situ river gauging data. Hydrology & Earth System Sciences 15 (2).

Bellerby, T., 2007. Satellite rainfall uncertainty estimation using an artificial neural network. Journal of Hydrometeorology 8 (6), 1397–1412.

Bennett, J. C., Grose, M. R., Corney, S. P., White, C. J., Holz, G. K., Katzfey, J. J., Post, D. A., Bindoff, N. L., 2014. Performance of an empirical bias-correction of a high-resolution climate dataset. International Journal of Climatology 34 (7), 2189–2204.

Berne, A., Delrieu, G., Creutin, J.-D., Obled, C., 2004. Temporal and spatial resolution of rainfall measurements required for urban hydrology. Journal of Hydrology 299 (3), 166–179.

Berni, N., Viterbo, A., Pandolfo, C., Stelluti, M., Barbetta, S., Brocca, L., 2008. Effects of rainfall and soil/land use spatial distribution on hydrological response at different scales. Proceeding of iEMSs 4, 470–477.

Bertoldi, G., Rigon, R., Over, T. M., 2006. Impact of watershed geomorphic characteristics on the energy and water budgets. Journal of Hydrometeorology 7 (3), 389–403.

Beven, K., Kirkby, M. J., 1979. A physically based, variable contributing area model of basin hydrology/un modèle à base physique de zone d'appel variable de l'hydrologie du bassin versant. Hydrological Sciences Journal 24 (1), 43–69.

Bewket, W., Sterk, G., 2005. Dynamics in land cover and its effect on stream flow in the chemoga watershed, blue nile basin, ethiopia. Hydrological Processes 19 (2), 445–458.

Billah, M. M., Goodall, J. L., Narayan, U., Reager, J., Lakshmi, V., Famiglietti, J. S., 2015. A methodology for evaluating evapotranspiration estimates at the watershed-scale using grace. Journal of Hydrology 523, 574–586.

Bitew, M. M., Gebremichael, M., Ghebremichael, L. T., Bayissa, Y. A., 2012. Evaluation of high-resolution satellite rainfall products through streamflow simulation in a hydrological modeling of a small mountainous watershed in ethiopia. Journal of Hydrometeorology 13 (1), 338–350.

Blandford, T. R., Humes, K. S., Harshburger, B. J., Moore, B. C., Walden, V. P., Ye, H., 2008. Seasonal and synoptic variations in near-surface air temperature lapse rates in a mountainous basin. Journal of Applied Meteorology and Climatology 47 (1), 249–261.

Block, P., Rajagopalan, B., 2007. Interannual variability and ensemble forecast of upper blue nile basin kiremt season precipitation. Journal of Hydrometeorology 8 (3), 327–343.

Blöschl, G., Kirnbauer, R., Gutknecht, D., 1991. Distributed snowmelt simulations in an alpine catchment: 1. model evaluation on the basis of snow cover patterns. Water Resources Research 27 (12), 3171–3179.

Bogaart, P., Troch, P., 2006. Curvature distribution within hillslopes and catchments and its effect on the hydrological response. Hydrology and Earth System Sciences Discussions 3 (3), 1071–1104.

Borga, M., 2002. Accuracy of radar rainfall estimates for streamflow simulation. Journal of Hydrology 267 (1), 26–39.

Borga, M., Anagnostou, E. N., Frank, E., 2000. On the use of real-time radar rainfall estimates for flood prediction in mountainous basins. Journal of Geophysical Research: Atmospheres 105 (D2), 2269–2280.

Borga, M., Vizzaccaro, A., 1997. On the interpolation of hydrologic variables: formal equivalence of multiquadratic surface fitting and kriging. Journal of Hydrology 195 (1), 160–171.

Boscarello, L., Ravazzani, G., Mancini, M., 2013. Catchment multisite discharge measurements for hydrological model calibration. Procedia Environmental Sciences 19, 158–167.

Botter, G., Porporato, A., Daly, E., Rodriguez-Iturbe, I., Rinaldo, A., 2007. Probabilistic characterization of base flows in river basins: Roles of soil, vegetation, and geomorphology. Water resources research 43 (6).

Botter, G., Rinaldo, A., 2003. Scale effect on geomorphologic and kinematic dispersion. Water resources research 39 (10).

Boyle, D. P., Gupta, H. V., Sorooshian, S., Koren, V., Zhang, Z., Smith, M., 2001. Toward improved streamflow forecasts: Value of semidistributed modeling. Water Resources Research 37 (11), 2749–2759.

Bras, R., Tarboton, D., I, R.-I., 1988. The analysis of river basins and channel networks using digital terrain data. In: Cambridge mass. Cambridge mass., pp. Ralph M. Parsons Lab, M.I.T., Tech. Rep. no. 326.

Bras, R. L., 1985. Random functions and hydrology. Courier Dover Publications.

Brocca, L., Ciabatta, L., Massari, C., Moramarco, T., Hahn, S., Hasenauer, S., Kidd, R., Dorigo, W., Wagner, W., Levizzani, V., 2014. Soil as a natural rain gauge: estimating global rainfall from satellite soil moisture data. Journal of Geophysical Research: Atmospheres 119 (9), 5128–5141.

Brocca, L., Moramarco, T., Melone, F., Wagner, W., 2013. A new method for rainfall estimation through soil moisture observations. Geophysical Research Letters 40 (5), 853–858.

Budyko, M., 1978. 1., 1974: Climate and life. International Geophysics Series 18.

Burrough, P. A., McDonnell, R. A., 2011. Principles of geographical information Systems. Vol. 19988. Oxford University Press.

Buytaert, W., Celleri, R., Willems, P., Bièvre, B. D., Wyseure, G., 2006. Spatial and temporal rainfall variability in mountainous areas: A case study from the south ecuadorian andes. Journal of Hydrology 329 (3), 413–421.

Buytaert, W., Zulkafli, Z., Grainger, S., Acosta, L., Alemie, T. C., Bastiaensen, J., Bièvre, B., Bhusal, J., Clark, J., Dewulf, A., et al., 2014. Citizen science in hydrology and water resources: opportunities for knowledge generation, ecosystem service management, and sustainable development. Front Earth Sci 2, 1–21.

Cai, Y., Jin, C., Wang, A., Guan, D., Wu, J., Yuan, F., Xu, L., 2015. Spatio-temporal analysis of the accuracy of tropical multisatellite precipitation analysis 3b42 precipitation data in mid-high latitudes of china. PloS one 10 (4).

Caldwell, P., Chin, H.-N. S., Bader, D. C., Bala, G., 2009. Evaluation of a wrf dynamical downscaling simulation over california. Climatic Change 95 (3-4), 499–521.

Camberlin, P., 1997. Rainfall anomalies in the source region of the nile and their connection with the indian summer monsoon. Journal of Climate 10 (6), 1380–1392.

Camporese, M., Paniconi, C., Putti, M., Orlandini, S., 2010. Surface-subsurface flow modeling with path-based runoff routing, boundary condition-based coupling, and assimilation of multisource observation data. Water Resources Research 46 (2).

Carrera-Hernández, J., Gaskin, S., 2007. Spatio temporal analysis of daily precipitation and temperature in the basin of mexico. Journal of Hydrology 336 (3), 231–249.

Caylor, K. K., D'Odorico, P., Rodriguez-Iturbe, I., 2006. On the ecohydrology of structurally heterogeneous semiarid landscapes. Water Resources Research 42 (7).

Chadwick, R., Grimes, D., Saunders, R., Francis, P., Blackmore, T., 2010. The tamora algorithm: Satellite rainfall estimates over west africa using multi-spectral seviri data. Advances in Geosciences 25 (25), 3–9.

Chen, E., Mackay, D. S., 2004. Effects of distribution-based parameter aggregation on a spatially distributed agricultural nonpoint source pollution model. Journal of Hydrology 295 (1), 211–224.

Chu, T., Shirmohammadi, A., 2004. Evaluation of the swat model's hydrology component in the piedmont physiographic region of maryland. Transactions of the ASAE 47 (4), 1057–1073.

Ciabatta, L., Brocca, L., Massari, C., Moramarco, T., Puca, S., Rinollo, A., Gabellani, S., Wagner, W., 2015. Integration of satellite soil moisture and rainfall observations over the italian territory. Journal of Hydrometeorology (2015).

Ciach, G. J., 2003. Local random errors in tipping-bucket rain gauge measurements. Journal of Atmospheric and Oceanic Technology 20 (5), 752–759.

Clothier, B., Kerr, J., Talbot, J., Scotter, D., 1982. Measured and estimated evapotranspiration from well-watered crops. New Zealand journal of agricultural research 25 (3), 301–307.

Cohen Liechti, T., Matos, J., Boillat, J.-L., Schleiss, A., 2012. Comparison and evaluation of satellite derived precipitation products for hydrological modeling of the zambezi river basin. Hydrology and Earth System Sciences 16 (2), 489–500.

Conway, D., 1997. A water balance model of the upper blue nile in ethiopia. Hydrological sciences journal 42 (2), 265–286.

Conway, D., 2000. The climate and hydrology of the upper blue nile river. Geographical Journal, 49–62.

Conway, D., 2005. From headwater tributaries to international river: observing and adapting to climate variability and change in the nile basin. Global Environmental Change 15 (2), 99–114.

Conway, D., Hulme, M., 1993. Recent fluctuations in precipitation and runoff over the nile sub-basins and their impact on main nile discharge. Climatic change 25 (2), 127–151.

Corripio, J., Purves, R., 2002. Energy balance of high altitude glaciarised basins in the central andes: climatic and hydrological aspects. In: EGS General Assembly Conference Abstracts. Vol. 27. p. 4402.

Courault, D., Monestiez, P., 1999. Spatial interpolation of air temperature according to atmospheric circulation patterns in southeast france. International Journal of Climatology 19 (4), 365–378.

Crave, A., Gascuel-Odoux, C., 1997. The influence of topography on time and space distribution of soil surface water content. Hydrological processes 11 (2), 203–210.

Cressie, N. A., Cassie, N. A., 1993. Statistics for spatial data. Vol. 900. Wiley New York.

Creutin, J., Obled, C., 1982. Objective analyses and mapping techniques for rainfall fields: an objective comparison. Water Resources Research 18 (2), 413–431.

Cristea, N. C., Kampf, S. K., Burges, S. J., 2012. Revised coefficients for priestley-taylor and makkink-hansen equations for estimating daily reference evapotranspiration. Journal of Hydrologic Engineering 18 (10), 1289–1300.

Cudennec, C., 2007. On width function-based unit hydrographs deduced from separately random self-similar river networks and rainfall variability: Discussion of ?coding random self-similar river networks and calculating geometric distances: 1. general methodology? and ?2. application to runoff simulations? Hydrological Sciences Journal 52 (1), 230–237.

David, O., Ascough Ii, J., Lloyd, W., Green, T., Rojas, K., Leavesley, G., Ahuja, L., 2013. A software engineering perspective on environmental modeling framework design: The object modeling system. Environmental Modelling & Software 39, 201–213.

Davison, B., van der Kamp, G., 2008. Low-flows in deterministic modelling: a brief review. Canadian Water Resources Journal 33 (2), 181–194.

Dehotin, J., Braud, I., 2008. Which spatial discretization for distributed hydrological models? proposition of a methodology and illustration for medium to large-scale catchments. Hydrology and Earth System Sciences 12 (3), 769–796.
URL http://www.hydrol-earth-syst-sci.net/12/769/2008/

del Jesus, M., Rinaldo, A., Rodríguez-Iturbe, I., 2015. Point rainfall statistics for ecohydrological analyses derived from satellite integrated rainfall measurements. Water Resources Research 51 (4), 2974–2985.

Di Lazzaro, M., 2009. Regional analysis of storm hydrographs in the rescaled width function framework. Journal of hydrology 373 (3), 352–365.

Di Lazzaro, M., Zarlenga, A., Volpi, E., 2015. Hydrological effects of within-catchment heterogeneity of drainage density. Advances in Water Resources 76, 157–167.

Di Piazza, A., Conti, F. L., Noto, L., Viola, F., La Loggia, G., 2011. Comparative analysis of different techniques for spatial interpolation of rainfall data to create a serially complete monthly time series of precipitation for sicily, italy. International Journal of Applied Earth Observation and Geoinformation 13 (3), 396–408.

Dile, Y. T., Berndtsson, R., Setegn, S. G., 2013. Hydrological response to climate change for gilgel abay river, in the lake tana basin-upper blue nile basin of ethiopia. PloS one 8 (10), e79296.

Dinku, T., Ceccato, P., Grover-Kopec, E., Lemma, M., Connor, S., Ropelewski, C., 2007. Validation of satellite rainfall products over east africa's complex topography. International Journal of Remote Sensing 28 (7), 1503–1526.

Dinku, T., Chidzambwa, S., Ceccato, P., Connor, S., Ropelewski, C., 2008. Validation of high-resolution satellite rainfall products over complex terrain. International Journal of Remote Sensing 29 (14), 4097–4110.

Dobrowski, S. Z., Abatzoglou, J. T., Greenberg, J. A., Schladow, S., 2009. How much influence does landscape-scale physiography have on air temperature in a mountain environment? Agricultural and Forest Meteorology 149 (10), 1751–1758.

D'Odorico, P., Porporato, A., 2006. Dryland ecohydrology. Springer.

D'Odorico, P., Rigon, R., 2003. Hillslope and channel contributions to the hydrologic response. Water resources research 39 (5).

Dodson, R., Marks, D., 1997. Daily air temperature interpolated at high spatial resolution over a large mountainous region. Climate Research 8 (1), 1–20.

Döll, P., Fritsche, M., Eicker, A., Schmied, H. M., 2014. Seasonal water storage variations as impacted by water abstractions: comparing the output of a global hydrological model with grace and gps observations. Surveys in Geophysics 35 (6), 1311–1331.

Dorigo, W., Gruber, A., De Jeu, R., Wagner, W., Stacke, T., Loew, A., Albergel, C., Brocca, L., Chung, D., Parinussa, R., et al., 2015. Evaluation of the esa cci soil moisture product using ground-based observations. Remote Sensing of Environment 162, 380–395.

Duan, Z., Bastiaanssen, W., 2013. First results from version 7 trmm 3b43 precipitation product in combination with a new downscaling–calibration procedure. Remote Sensing of Environment 131, 1–13.

Dudhia, J., Gill, D., Henderson, T., Klemp, J., Skamarock, W., Wang, W., 2005. The weather research and forecast model: software architecture and performance. In: Proceedings of the Eleventh ECMWF Workshop on the Use of High Performance Computing in Meteorology. World Scientific, pp. 156–168.

Duffy, C. J., 1996. A two-state integral-balance model for soil moisture and groundwater dynamics in complex terrain. Water resources research 32 (8), 2421–2434.

Eagleson, P. S., 1994. The evolution of modern hydrology (from watershed to continent in 30 years). Advances in water resources 17 (1), 3–18.

Easton, Z., Fuka, D., White, E., Collick, A., Biruk Ashagre, B., McCartney, M., Awulachew, S., Ahmed, A., Steenhuis, T., 2010. A multi basin swat model analysis of runoff and sedimentation in the blue nile, ethiopia. Hydrology and earth system sciences 14 (10), 1827–1841.

Eberhart, R. C., Shi, Y., 2001. Particle swarm optimization: developments, applications and resources. In: Evolutionary Computation, 2001. Proceedings of the 2001 Congress on. Vol. 1. IEEE, pp. 81–86.

Ebert, E. E., Janowiak, J. E., Kidd, C., 2007. Comparison of near-real-time precipitation estimates from satellite observations and numerical models. Bulletin of the American Meteorological Society 88 (1), 47–64.

Endrizzi, S., Gruber, S., Dall'Amico, M., Rigon, R., 2013. Geotop 2.0: simulating the combined energy and water balance at and below the land surface accounting for soil freezing, snow cover and terrain effects. Geoscientific Model Development Discussions 6 (4), 6279–6341.

Endrizzi, S., Gruber, S., Dall'Amico, M., Rigon, R., 2014. Geotop 2.0: simulating the combined energy and water balance at and below the land surface accounting for soil freezing, snow cover and terrain effects. Geoscientific Model Development 7 (6), 2831–2857.

Evans, I., Dikau, R., Tokunaga, E., Ohmori, H., Hirano, M., 2003. Concepts and modelling in geomorphology. International Perspectives, Terrapub, Tokyo.

Fairfield, J., Leymarie, P., 1991. Drainage networks from grid digital elevation models. Water resources research 27 (5), 709–717.

Fatichi, S., Vivoni, E. R., Ogden, F. L., Ivanov, V. Y., Mirus, B., Gochis, D., Downer, C. W., Camporese, M., Davison, J. H., Ebel, B., et al., 2016. An overview of current applications, challenges, and future trends in distributed process-based models in hydrology. Journal of Hydrology.

Ferraro, R. R., 1997. Special sensor microwave imager derived global rainfall estimates for climatological applications. Journal of Geophysical Research: Atmospheres (1984–2012) 102 (D14), 16715–16735.

Feyen, L., Kalas, M., Vrugt, J. A., 2008. Semi-distributed parameter optimization and uncertainty assessment for large-scale streamflow simulation using global optimization/optimisation de paramètres semi-distribués et évaluation de l'incertitude pour la simulation de débits à grande échelle par l'utilisation d'une optimisation globale. Hydrological Sciences Journal 53 (2), 293–308.

Flanagan, D., Nearing, M., 1995. Usda-water erosion prediction project: Hillslope profile and watershed model documentation. NSERL Rep 10.

Formetta, G., 2013. Hydrological modelling with components: the oms3 newage-jgrass system. Ph.D. thesis, University of Trento.

Formetta, G., Antonello, A., Franceschi, S., David, O., R., R., 2014a. The basin delineation and the built of a digital watershed model within the jgrass-newage system. Bolet?n Geol?gico y Minero: Special Issue "Advanced GIS terrain analysis for geophysical applications.

Formetta, G., Antonello, A., Franceschi, S., David, O., Rigon, R., 2014b. Digital watershed representation within the newage-jgrass system. Boletín geológico y minero 125 (3), 369–379.

Formetta, G., Antonello, A., Franceschi, S., David, O., Rigon, R., 2014c. Hydrological modelling with components: A gis-based open-source framework. Environmental Modelling & Software 55, 190–200.

Formetta, G., Kampf, S., David, O., Rigon, R., 2013a. The cache la poudre river basin snow water equivalent modeling with newage-jgrass. Geoscientific Model Development Discussions 6 (3), 4447–4474.

Formetta, G., Kampf, S. K., David, O., Rigon, R., 2014d. Snow water equivalent modeling components in newage-jgrass. Geoscientific Model Development 7 (3), 725–736.

Formetta, G., Mantilla, R., Franceschi, S., Antonello, A., Rigon, R., 2011. The jgrass-newage system for forecasting and managing the hydrological budgets at the basin scale: models of flow generation and propagation/routing. Geoscientific Model Development 4 (4), 943–955.

Formetta, G., Rigon, R., Chávez, J., David, O., 2013b. Modeling shortwave solar radiation using the jgrass-newage system. Geoscientific Model Development 6 (4), 915–928.

Förster, K., Meon, G., Marke, T., Strasser, U., 2014. Effect of meteorological forcing and snow model complexity on hydrological simulations in the sieber catchment (harz mountains, germany). Hydrology and Earth System Sciences 18 (11), 4703–4720.

Fuka, D. R., Walter, M. T., MacAlister, C., Degaetano, A. T., Steenhuis, T. S., Easton, Z. M., 2014. Using the climate forecast system reanalysis as weather input data for watershed models. Hydrological Processes 28 (22), 5613–5623.

Gao, H., Tang, Q., Ferguson, C. R., Wood, E. F., Lettenmaier, D. P., 2010. Estimating the water budget of major us river basins via remote sensing. International Journal of Remote Sensing 31 (14), 3955–3978.

Gao, Y., Liu, M., 2013. Evaluation of high-resolution satellite precipitation products using rain gauge observations over the tibetan plateau. Hydrology and Earth System Sciences 17 (2), 837.

Garbrecht, J., Martz, L. W., 1997. The assignment of drainage direction over flat surfaces in raster digital elevation models. Journal of hydrology 193 (1-4), 204–213.

Garbrecht, J., Martz, L. W., 2000. Digital elevation model issues in water resources modeling. Hydrologic and hydraulic modeling support with geographic information systems, 1–28.

Garen, D. C., Johnson, G. L., Hanson, C. L., 1994. Mean areal precipitation for daily hydrologic modeling in mountainous regions1.

Garen, D. C., Marks, D., 2005. Spatially distributed energy balance snowmelt modelling in a mountainous river basin: estimation of meteorological inputs and verification of model results. Journal of Hydrology 315 (1), 126–153.

Gascoin, S., Hagolle, O., Huc, M., Jarlan, L., Dejoux, J.-F., Szczypta, C., Marti, R., Sánchez, R., 2015. A snow cover climatology for the pyrenees from modis snow products. Hydrology and Earth System Sciences 19 (5), 2337–2351.

Gebremicael, T., Mohamed, Y., Betrie, G., van der Zaag, P., Teferi, E., 2013. Trend analysis of runoff and sediment fluxes in the upper blue nile basin: A combined analysis of statistical tests, physically-based models and landuse maps. Journal of Hydrology 482, 57–68.

Gebremichael, M., Bitew, M. M., Hirpa, F. A., Tesfay, G. N., 2014. Accuracy of satellite rainfall estimates in the blue nile basin: Lowland plain versus highland mountain. Water Resources Research 50 (11), 8775–8790.

Gebremichael, M., Hossain, F., 2010. Satellite rainfall applications for surface hydrology. Springer.

Germann, U., Joss, J., 2001. Variograms of radar reflectivity to describe the spatial continuity of alpine precipitation. Journal of Applied Meteorology 40 (6), 1042–1059.

Ghosh, I., Hellweger, F. L., 2011. Effects of spatial resolution in urban hydrologic simulations. Journal of Hydrologic Engineering 17 (1), 129–137.

Githuia, F., Thayalakumaranb, T., 2011. The effect of discretization of hydrologic response units on the performance of swat model in simulating flow and evapotranspiration. In: MSSANZ 2011 Perth.

Gleick, P. H., 2003. Global freshwater resources: soft-path solutions for the 21st century. Science 302 (5650), 1524–1528.

Goovaerts, P., 1997. Geostatistics for natural resources evaluation. Oxford university press.

Goovaerts, P., 1999. Geostatistics in soil science: state-of-the-art and perspectives. Geoderma 89 (1), 1–45.

Goovaerts, P., 2000. Geostatistical approaches for incorporating elevation into the spatial interpolation of rainfall. Journal of hydrology 228 (1), 113–129.

Grimes, D., Pardo-Iguzquiza, E., Bonifacio, R., 1999. Optimal areal rainfall estimation using raingauges and satellite data. Journal of Hydrology 222 (1), 93–108.

Gupta, H. V., Kling, H., Yilmaz, K. K., Martinez, G. F., 2009. Decomposition of the mean squared error and nse performance criteria: Implications for improving hydrological modelling. Journal of Hydrology 377 (1), 80–91.

Gupta, H. V., Sorooshian, S., Yapo, P. O., 1999. Status of automatic calibration for hydrologic models: Comparison with multilevel expert calibration. Journal of Hydrologic Engineering 4 (2), 135–143.

Gupta, V. K., Mesa, O. J., 1988. Runoff generation and hydrologic response via channel network geomorphology?recent progress and open problems. Journal of Hydrology 102 (1), 3–28.

Gupta, V. K., Waymire, E., Wang, C., 1980. A representation of an instantaneous unit hydrograph from geomorphology. Water Resources Research 16 (5), 855–862.

Haberlandt, U., 2007. Geostatistical interpolation of hourly precipitation from rain gauges and radar for a large-scale extreme rainfall event. Journal of Hydrology 332 (1), 144–157.

Habib, E., ElSaadani, M., Haile, A. T., 2012. Climatology-focused evaluation of cmorph and tmpa satellite rainfall products over the nile basin. Journal of Applied Meteorology and Climatology 51 (12), 2105–2121.

Habib, E., Haile, A. T., Sazib, N., Zhang, Y., Rientjes, T., 2014. Effect of bias correction of satellite-rainfall estimates on runoff simulations at the source of the upper blue nile. Remote Sensing 6 (7), 6688–6708.

Habib, E., Krajewski, W. F., Kruger, A., 2001. Sampling errors of tipping-bucket rain gauge measurements. Journal of Hydrologic Engineering 6 (2), 159–166.

Haile, A. T., Habib, E., Rientjes, T., 2013. Evaluation of the climate prediction center (cpc) morphing technique (cmorph) rainfall product on hourly time scales over the source of the blue nile river. Hydrological Processes 27 (12), 1829–1839.

Haile, A. T., Yan, F., Habib, E., 2015. Accuracy of the cmorph satellite-rainfall product over lake tana basin in eastern africa. Atmospheric Research 163, 177–187.

Hall, D. K., Riggs, G. A., Salomonson, V. V., 2006. Modis snow and sea ice products. In: Earth science satellite remote sensing. Springer, pp. 154–181.

Hall, J., Grey, D., Garrick, D., Fung, F., Brown, C., Dadson, S., Sadoff, C., et al., 2014. Coping with the curse of freshwater variability. Science 346 (6208), 429–430.

Hannah, D. M., Demuth, S., van Lanen, H. A., Looser, U., Prudhomme, C., Rees, G., Stahl, K., Tallaksen, L. M., 2011. Large-scale river flow archives: importance, current status and future needs. Hydrological Processes 25 (7), 1191–1200.

Harder, P., Pomeroy, J., 2013. Estimating precipitation phase using a psychrometric energy balance method. Hydrological Processes 27 (13), 1901–1914.

Harder, P., Pomeroy, J. W., 2014. Hydrological model uncertainty due to precipitation-phase partitioning methods. Hydrological Processes 28 (14), 4311–4327.

Hay, L. E., Leavesley, G. H., Clark, M. P., Markstrom, S. L., Viger, R. J., Umemoto, M., 2006. Step wise, multiple objective calibration of a hydrologic model for a snowmelt dominated basin1.

Hay, L. E., Umemoto, M., 2007. Multiple-objective stepwise calibration using Luca. US Geological Survey.

He, Z., Parajka, J., Tian, F., Blöschl, G., 2014. Estimating degree-day factors from modis for snowmelt runoff modeling. Hydrology and Earth System Sciences 18 (12), 4773–4789.

Heijden, S., Haberlandt, U., 2010. Influence of spatial interpolation methods for climate variables on the simulation of discharge and nitrate fate with swat. Advances in Geosciences 27 (27), 91–98.

Hirpa, F. A., Gebremichael, M., Hopson, T., 2010. Evaluation of high-resolution satellite precipitation products over very complex terrain in ethiopia. Journal of Applied Meteorology and Climatology 49 (5), 1044–1051.

Hirschi, M., Viterbo, P., Seneviratne, S. I., 2006. Basin-scale water-balance estimates of terrestrial water storage variations from ecmwf operational forecast analysis. Geophysical research letters 33 (21).

Hjerdt, K., McDonnell, J., Seibert, J., Rodhe, A., 2004. A new topographic index to quantify downslope controls on local drainage. Water Resources Research 40 (5).

Hofste, R., 2014. Comparative analysis among near-operational evapotranspiration products for the nile basin based on earth observations. Ph.D. thesis, TU Delft, Delft University of Technology.

Højberg, A. L., Troldborg, L., Stisen, S., Christensen, B. B., Henriksen, H. J., 2013. Stakeholder driven update and improvement of a national water resources model. Environmental modelling & software 40, 202–213.

Hong, Y., Hsu, K.-l., Moradkhani, H., Sorooshian, S., 2006. Uncertainty quantification of satellite precipitation estimation and monte carlo assessment of the error propagation into hydrologic response. Water resources research 42 (8).

Horton, R. E., 1945. Erosional development of streams and their drainage basins; hydrophysical approach to quantitative morphology. Geological society of America bulletin 56 (3), 275–370.

Hossain, F., Anagnostou, E. N., Bagtzoglou, A. C., 2006. On latin hypercube sampling for efficient uncertainty estimation of satellite rainfall observations in flood prediction. Computers & geosciences 32 (6), 776–792.

Hossain, F., Huffman, G. J., 2008. Investigating error metrics for satellite rainfall data at hydrologically relevant scales. Journal of Hydrometeorology 9 (3), 563–575.

Hudson, G., Wackernagel, H., 1994. Mapping temperature using kriging with external drift: theory and an example from scotland. International journal of Climatology 14 (1), 77–91.

Huffman, G. J., Bolvin, D. T., 2013. Trmm and other data precipitation data set documentation. NASA, Greenbelt, USA, 1–40.

Huffman, G. J., Bolvin, D. T., Nelkin, E. J., Wolff, D. B., Adler, R. F., Gu, G., Hong, Y., Bowman, K. P., Stocker, E. F., 2007. The trmm multisatellite precipitation analysis (tmpa): Quasi-global, multiyear, combined-sensor precipitation estimates at fine scales. Journal of Hydrometeorology 8 (1), 38–55.

Hutchinson, M., 1995. Interpolating mean rainfall using thin plate smoothing splines. International journal of geographical information systems 9 (4), 385–403.

Hwang, S., Graham, W. D., 2013. Development and comparative evaluation of a stochastic analog method to downscale daily gcm precipitation. Hydrology and Earth System Sciences 17 (11), 4481–4502.

Hwang, Y., Clark, M., Rajagopalan, B., Leavesley, G., 2012. Spatial interpolation schemes of daily precipitation for hydrologic modeling. Stochastic Environmental Research and Risk Assessment 26 (2), 295–320.

Iizumi, T., Nishimori, M., Dairaku, K., Adachi, S. A., Yokozawa, M., 2011. Evaluation and intercomparison of downscaled daily precipitation indices over japan in present-day climate: Strengths and weaknesses of dynamical and bias correction-type statistical downscaling methods. Journal of Geophysical Research: Atmospheres (1984–2012) 116 (D1).

Iqbal, M., 1983. An introduction to solar radiation. Elsevier.

Isaaks, E. H., Srivastava, R. M., 1989. An introduction to applied geostatistics. Vol. 561. Oxford university press New York.

Isaaks, E. H., Srivastava, R. M., et al., 1989. Applied geostatistics. Vol. 2. Oxford University Press New York.

Ivanov, V. Y., Vivoni, E. R., Bras, R. L., Entekhabi, D., 2004. Catchment hydrologic response with a fully distributed triangulated irregular network model. Water Resources Research 40 (11).

Jabot, E., Zin, I., Lebel, T., Gautheron, A., Obled, C., 2012. Spatial interpolation of sub-daily air temperatures for snow and hydrologic applications in mesoscale alpine catchments. Hydrological Processes 26 (17), 2618–2630.

Jakob Themeßl, M., Gobiet, A., Leuprecht, A., 2011. Empirical-statistical downscaling and error correction of daily precipitation from regional climate models. International Journal of Climatology 31 (10), 1530–1544.

Jarmain, C., 2009. A Methodology for Near-real Time Spatial Estimation of Evaporation: Report to the Water Research Commission. Water Research Commission.

Jarraud, M., 2008. Guide to meteorological instruments and methods of observation (wmo-no. 8). World Meteorological Organisation: Geneva, Switzerland.

Jasiewicz, J., Metz, M., 2011. A new grass gis toolkit for hortonian analysis of drainage networks. Computers & Geosciences 37 (8), 1162–1173.

Jha, M., Gassman, P. W., Secchi, S., Gu, R., Arnold, J., 2004. Effect of watershed subdivision on swat flow, sediment, and nutrient predictions1.

Jobard, I., Chopin, F., Bergès, J. C., Roca, R., 2011. An intercomparison of 10-day satellite precipitation products during west african monsoon. International journal of remote sensing 32 (9), 2353–2376.

Johnston, R. M., McCartney, M., 2010. Inventory of water storage types in the Blue Nile and Volta river basins. Vol. 140. IWMI.

Joyce, R. J., Janowiak, J. E., Arkin, P. A., Xie, P., 2004. Cmorph: A method that produces global precipitation estimates from passive microwave and infrared data at high spatial and temporal resolution. Journal of Hydrometeorology 5 (3), 487–503.

Jury, W. A., Vaux, H., 2005. The role of science in solving the world's emerging water problems. Proceedings of the national academy of sciences of the united states of america 102 (44), 15715–15720.

K Ajami, N., Gupta, H., Wagener, T., Sorooshian, S., 2004. Calibration of a semi-distributed hydrologic model for streamflow estimation along a river system. Journal of Hydrology 298 (1), 112–135.

Karlsson, K.-G., Riihelä, A., Müller, R., Meirink, J., Sedlar, J., Stengel, M., Lockhoff, M., Trentmann, J., Kaspar, F., Hollmann, R., et al., 2013. Clara-a1: a cloud, albedo, and radiation dataset from 28 yr of global avhrr data. Atmospheric Chemistry and Physics 13 (10), 5351–5367.

Kavetski, D., Kuczera, G., Franks, S. W., 2006. Calibration of conceptual hydrological models revisited: 1. overcoming numerical artefacts. Journal of Hydrology 320 (1), 173–186.

Kebede, S., Travi, Y., Alemayehu, T., Marc, V., 2006. Water balance of lake tana and its sensitivity to fluctuations in rainfall, blue nile basin, ethiopia. Journal of hydrology 316 (1), 233–247.

Kennedy, J., Eberhart, R., et al., 1995. Particle swarm optimization. In: Proceedings of IEEE international conference on neural networks. Vol. 4. Perth, Australia, pp. 1942–1948.

Khakbaz, B., Imam, B., Hsu, K., Sorooshian, S., 2012. From lumped to distributed via semi-distributed: Calibration strategies for semi-distributed hydrologic models. Journal of Hydrology 418, 61–77.

Kidd, C., Levizzani, V., 2011. Status of satellite precipitation retrievals. Hydrology and Earth System Sciences 15 (4), 1109–1116.

Kienzle, S. W., 2008. A new temperature based method to separate rain and snow. Hydrological Processes 22 (26), 5067–5085.

Kim, J., Hogue, T. S., 2008. Evaluation of a modis-based potential evapotranspiration product at the point scale. Journal of Hydrometeorology 9 (3), 444–460.

Kim, U., Kaluarachchi, J. J., 2008. Application of parameter estimation and regionalization methodologies to ungauged basins of the upper blue nile river basin, ethiopia. Journal of Hydrology 362 (1), 39–56.

Kim, U., Kaluarachchi, J. J., 2009. Climate change impacts on water resources in the upper blue nile river basin, ethiopia1.

Kim, U., Kaluarachchi, J. J., Smakhtin, V. U., 2008. Generation of monthly precipitation under climate change for the upper blue nile river basin, ethiopia1.

Kirkby, M., 1976. Tests of the random network model, and its application to basin hydrology. Earth Surface Processes 1 (3), 197–212.

Kisaka, M. O., Mucheru-Muna, M., Ngetich, F., Mugwe, J., Mugendi, D., Mairura, F., 2015. Rainfall variability, drought characterization, and efficacy of rainfall data reconstruction: Case of eastern kenya. Advances in Meteorology 2015.

Kitanidis, P. K., Bras, R. L., 1980. Real-time forecasting with a conceptual hydrologic model: 2. applications and results. Water Resources Research 16 (6), 1034–1044.

Kjaersgaard, J., Allen, R., Garcia, M., Kramber, W., Trezza, R., 2009. Automated selection of anchor pixels for landsat based evapotranspiration estimation. American Society of Civil Engineers, Kansas City, Missouri.

Kjærsgaard, J. H., Cuenca, R. H., Martínez-Cob, A., Gavilán, P., Plauborg, F., Mollerup, M., Hansen, S., 2009. Comparison of the performance of net radiation calculation models. Theoretical and applied climatology 98 (1-2), 57–66.

Kling, H., Fuchs, M., Paulin, M., 2012. Runoff conditions in the upper danube basin under an ensemble of climate change scenarios. Journal of Hydrology 424, 264–277.

Knipper, K. R., Kinoshita, A. M., Hogue, T. S., 2016. Evaluation of a moderate resolution imaging spectroradiometer triangle-based algorithm for evapotranspiration estimates in subalpine regions. Journal of Applied Remote Sensing 10 (1), 016002–016002.

Kollet, S. J., Maxwell, R. M., 2006. Integrated surface–groundwater flow modeling: A free-surface overland flow boundary condition in a parallel groundwater flow model. Advances in Water Resources 29 (7), 945–958.

Kottegoda, N. T., Rosso, R., 1997. Probability, statistics, and reliability for civil and environmental engineers.

Kullback, S., Leibler, R. A., 1951. On information and sufficiency. The Annals of Mathematical Statistics, 79–86.

Kumar, P., Kishtawal, C., Pal, P., 2014. Impact of satellite rainfall assimilation on weather research and forecasting model predictions over the indian region. Journal of Geophysical Research: Atmospheres 119 (5), 2017–2031.

Kumar, S., Merwade, V., 2009. Impact of watershed subdivision and soil data resolution on swat model calibration and parameter uncertainty1.

Kummerow, C., Barnes, W., Kozu, T., Shiue, J., Simpson, J., 1998. The tropical rainfall measuring mission (trmm) sensor package. Journal of atmospheric and oceanic technology 15 (3), 809–817.

Kummerow, C., Simpson, J., Thiele, O., Barnes, W., Chang, A., Stocker, E., Adler, R., Hou, A., Kakar, R., Wentz, F., et al., 2000. The status of the tropical rainfall measuring mission (trmm) after two years in orbit. Journal of Applied Meteorology 39 (12), 1965–1982.

Kunstmann, H., Hingerl, L., Mauder, M., Wagner, S., Rigon, R., 2013. A combined water and energy flux observation and modelling study at the tereno-prealpine observatory. IAHS-AISH publication, 221–225.

Kuo, W.-L., Steenhuis, T. S., McCulloch, C. E., Mohler, C. L., Weinstein, D. A., DeGloria, S. D., Swaney, D. P., 1999. Effect of grid size on runoff and soil moisture for a variable-source-area hydrology model. Water Resources Research 35 (11), 3419–3428.

Lagacherie, P., Rabotin, M., Colin, F., Moussa, R., Voltz, M., 2010. Geo-mhydas: a landscape discretization tool for distributed hydrological modeling of cultivated areas. Computers & Geosciences 36 (8), 1021–1032.

Laio, F., Porporato, A., Ridolfi, L., Rodriguez-Iturbe, I., 2001. Plants in water-controlled ecosystems: Active role in hydrologic processes and response to water stress: Ii. probabilistic soil moisture dynamics. Advances in Water Resources 24 (7), 707–723.

Landerer, F., Swenson, S., 2012. Accuracy of scaled grace terrestrial water storage estimates. Water Resources Research 48 (4).

Lanni, C., Borga, M., Rigon, R., Tarolli, P., 2012. Modelling shallow landslide susceptibility by means of a subsurface flow path connectivity index and estimates of soil depth spatial distribution. Hydrology and Earth System Sciences 16 (11), 3959–3971.

Lashermes, B., Foufoula-Georgiou, E., 2007. Area and width functions of river networks: New results on multifractal properties. Water resources research 43 (9).

Laurent, H., Jobard, I., Toma, A., 1998. Validation of satellite and ground-based estimates of precipitation over the sahel. Atmospheric Research 47, 651–670.

Lázaro, R., Rodrigo, F., Gutiérrez, L., Domingo, F., Puigdefábregas, J., 2001. Analysis of a 30-year rainfall record (1967–1997) in semi–arid se spain for implications on vegetation. Journal of arid environments 48 (3), 373–395.

Leavesley, G. H., Lichty, R., Troutman, B., Saindon, L., 1983. Precipitation-runoff modeling system: User's manual. US Geological Survey.

Lehning, M., Bartelt, P., Brown, B., Russi, T., Stöckli, U., Zimmerli, M., 1999. Snowpack model calculations for avalanche warning based upon a new network of weather and snow stations. Cold Regions Science and Technology 30 (1), 145–157.

Lerat, J., Andreassian, V., Perrin, C., Vaze, J., Perraud, J.-M., Ribstein, P., Loumagne, C., 2012. Do internal flow measurements improve the calibration of rainfall-runoff models? Water Resources Research 48 (2).

Lewis, D., Singer, M., Dahlgren, R., Tate, K., 2000. Hydrology in a california oak woodland watershed: a 17-year study. Journal of Hydrology 240 (1), 106–117.

Li, H., Sivapalan, M., Tian, F., 2012. Comparative diagnostic analysis of runoff generation processes in oklahoma dmip2 basins: The blue river and the illinois river. Journal of Hydrology 418, 90–109.

Li, J., Heap, A. D., 2011. A review of comparative studies of spatial interpolation methods in environmental sciences: performance and impact factors. Ecological Informatics 6 (3), 228–241.

Liang, X., Lettenmaier, D. P., Wood, E. F., Burges, S. J., 1994. A simple hydrologically based model of land surface water and energy fluxes for general circulation models. JOURNAL OF GEOPHYSICAL RESEARCH-ALL SERIES- 99, 14–415.

Lin, J., 1991. Divergence measures based on the shannon entropy. Information Theory, IEEE Transactions on 37 (1), 145–151.

Lindsay, J. B., 2005. The terrain analysis system: A tool for hydro-geomorphic applications. Hydrological processes 19 (5), 1123–1130.

Liu, Z., Ostrenga, D., Teng, W., Kempler, S., 2012. Tropical rainfall measuring mission (trmm) precipitation data and services for research and applications. Bulletin of the American Meteorological Society 93 (9), 1317–1325.

Liu, Z., Rui, H., Teng, W. L., Chiu, L. S., Leptoukh, G., Vicente, G. A., 2007. Online visualization and analysis: A new avenue to use satellite data for weather, climate, and interdisciplinary research and applications. In: Measuring Precipitation From Space. Springer, pp. 549–558.

Liuzzo, L., Noto, L. V., Vivoni, E. R., La Loggia, G., 2009. Basin-scale water resources assessment in oklahoma under synthetic climate change scenarios using a fully distributed hydrologic model. Journal of hydrologic engineering 15 (2), 107–122.

Lloyd, C., 2005. Assessing the effect of integrating elevation data into the estimation of monthly precipitation in great britain. Journal of Hydrology 308 (1), 128–150.

Lobligeois, F., Andréassian, V., Perrin, C., Tabary, P., Loumagne, C., et al., 2014. When does higher spatial resolution rainfall information improve streamflow simulation? an evaluation using 3620 flood events. Hydrology and Earth System Sciences 18 (2).

Lookingbill, T. R., Urban, D. L., 2003. Spatial estimation of air temperature differences for landscape-scale studies in montane environments. Agricultural and Forest Meteorology 114 (3), 141–151.

Ly, S., Charles, C., Degre, A., 2011. Geostatistical interpolation of daily rainfall at catchment scale: the use of several variogram models in the ourthe and ambleve catchments, belgium. Hydrology & Earth System Sciences 15 (7).

Ly, S., Charles, C., Degré, A., 2013. Different methods for spatial interpolation of rainfall data for operational hydrology and hydrological modeling at watershed scale. a review.

Maidment, R. I., Grimes, D., Allan, R. P., Tarnavsky, E., Stringer, M., Hewison, T., Roebeling, R., Black, E., 2014. The 30 year tamsat african rainfall climatology and time series (tarcat) data set. Journal of Geophysical Research: Atmospheres 119 (18), 10–619.

Maidment, R. I., Grimes, D. I., Allan, R. P., Greatrex, H., Rojas, O., Leo, O., 2013. Evaluation of satellite-based and model re-analysis rainfall estimates for uganda. Meteorological Applications 20 (3), 308–317.

Marani, M., Eltahir, E., Rinaldo, A., 2001. Geomorphic controls on regional base flow. Water Resources Research 37 (10), 2619–2630.

Marani, M., Rinaldo, A., Rigon, R., Rodriguez-Iturbe, I., 1994. Geomorphological width functions and the random cascade. Geophysical Research Letters 21 (19), 2123–2126.

Matheron, G., 1981. Splines and kriging: their formal equivalence. Down-to-earth statistics: solutions looking for geological problems 8, 77–95.

Maurer, E. P., Pierce, D. W., 2014. Bias correction can modify climate model simulated precipitation changes without adverse effect on the ensemble mean. Hydrology and Earth System Sciences 18 (3), 915–925.

Mellander, P.-E., Gebrehiwot, S. G., Gardenas, A. I., Bewket, W., Bishop, K., 2013. Summer rains and dry seasons in the upper blue nile basin: the predictability of half a century of past and future spatiotemporal patterns. PloS one 8 (7), 1932–6203.

Mengistu, D., Sorteberg, A., 2012. Sensitivity of swat simulated streamflow to climatic changes within the eastern nile river basin. Hydrology and Earth System Sciences 16 (2), 391–407.

Mesa, O. J., Mifflin, E. R., 1986. On the relative role of hillslope and network geometry in hydrologic response. Springer.

Michelangeli, P.-A., Vrac, M., Loukos, H., 2009. Probabilistic downscaling approaches: Application to wind cumulative distribution functions. Geophysical Research Letters 36 (11).

Mishra, A., Hata, T., 2006. A grid-based runoff generation and flow routing model for the upper blue nile basin. Hydrological sciences journal 51 (2), 191–206.

Mishra, A., Hata, T., Abdelhadi, A., 2004. Models for recession flows in the upper blue nile river. Hydrological processes 18 (15), 2773–2786.

Mitášová, H., Mitáš, L., 1993. Interpolation by regularized spline with tension: I. theory and implementation. Mathematical geology 25 (6), 641–655.

Mitasova, H., Neteler, M., 2004. Grass as open source free software gis: accomplishments and perspectives. Transactions in GIS 8 (2), 145–154.

Möller, M., Stanhill, G., 2007. Hydrological impacts of changes in evapotranspiration and precipitation: two case studies in semi-arid and humid climates/impacts hydrologiques de changements dans l'évapotranspiration et les précipitations: deux cas d'études en climats semi-aride et humide. Hydrological Sciences Journal/Journal des Sciences Hydrologiques 52 (6), 1216–1231.

Monteith, J., et al., 1965. Evaporation and environment. In: Symp. Soc. Exp. Biol. Vol. 19. p. 4.

Montgomery, D. R., Dietrich, W. E., 1988. Where do channels begin? Nature 336 (6196), 232–234.

Montgomery, D. R., Dietrich, W. E., 1989. Source areas, drainage density, and channel initiation. Water Resources Research 25 (8), 1907–1918.

Montgomery, D. R., Dietrich, W. E., 1992. Channel initiation and the problem of landscape scale. Science 255 (5046), 826.

Montgomery, D. R., Dietrich, W. E., 1994. A physically based model for the topographic control on shallow landsliding. Water resources research 30 (4), 1153–1171.

Moon, S.-E., Ryoo, S.-B., Kwon, J.-G., 1994. A markov chain model for daily precipitation occurrence in south korea. International journal of climatology 14 (9), 1009–1016.

Moore, I., 1992. Tapes: Terrain analysis programs for the environmental sciences. Agricultural systems and information technology 4, 37–39.

Moore, I. D., Grayson, R., Ladson, A., 1991. Digital terrain modelling: a review of hydrological, geomorphological, and biological applications. Hydrological processes 5 (1), 3–30.

Moore, R., 1985. The probability-distributed principle and runoff production at point and basin scales. Hydrological Sciences Journal 30 (2), 273–297.

Moradkhani, H., Sorooshian, S., 2008. General review of rainfall-runoff modeling: model calibration, data assimilation, and uncertainty analysis. In: Hydrological modelling and the water cycle. Springer, pp. 1–24.

Moriasi, D., Arnold, J., Van Liew, M., Bingner, R., Harmel, R., Veith, T., 2007. Model evaluation guidelines for systematic quantification of accuracy in watershed simulations. Trans. ASABE 50 (3), 885–900.

Mou, L., Tian, F., Hu, H., Sivapalan, M., 2008. Extension of the representative elementary watershed approach for cold regions: constitutive relationships and an application. Hydrology and Earth System Sciences 12 (2), 565–585.

Moussa, R., 2008. What controls the width function shape, and can it be used for channel network comparison and regionalization? Water Resources Research 44 (8).

Moussa, R., Chahinian, N., Bocquillon, C., 2007. Distributed hydrological modelling of a mediterranean mountainous catchment–model construction and multi-site validation. Journal of Hydrology 337 (1), 35–51.

Mu, Q., Heinsch, F. A., Zhao, M., Running, S. W., 2007. Development of a global evapotranspiration algorithm based on modis and global meteorology data. Remote Sensing of Environment 111 (4), 519–536.

Mu, Q., Zhao, M., Running, S. W., 2011. Improvements to a modis global terrestrial evapotranspiration algorithm. Remote Sensing of Environment 115 (8), 1781–1800.

Muleta, M. K., Nicklow, J. W., Bekele, E. G., 2007. Sensitivity of a distributed watershed simulation model to spatial scale. Journal of Hydrologic Engineering 12 (2), 163–172.

Mulvany, T., 1850. On the use of self-registering rain and flood gauges. Making Observations of the Relations of Rain Fall and Flood Discharges in a Given Catchment.

Transactions and Minutes of the Proceedings of the Institute of Civil Engineers of Ireland, Dublin, Ireland, Session 1.

Murray, F. W., 1967. On the computation of saturation vapor pressure. Journal of Applied Meteorology 6 (1), 203–204.

Nalder, I. A., Wein, R. W., 1998. Spatial interpolation of climatic normals: test of a new method in the canadian boreal forest. Agricultural and forest meteorology 92 (4), 211–225.

Nash, J., Sutcliffe, J., 1970. River flow forecasting through conceptual models part i?a discussion of principles. Journal of hydrology 10 (3), 282–290.

Neitsch, S., Arnold, J., Kiniry, J., Srinivasan, R., Williams, J., 2002. Soil and water assessment tool user?s manual: Version 2000. gswrl report 02-02, brc report 02-06, publ. texas water resources institute. Tech. rep., TR-192, College Station, Texas.

Nicótina, L., Alessi Celegon, E., Rinaldo, A., Marani, M., 2008. On the impact of rainfall patterns on the hydrologic response. Water Resources Research 44 (12).

Norbiato, D., Borga, M., Degli Esposti, S., Gaume, E., Anquetin, S., 2008. Flash flood warning based on rainfall thresholds and soil moisture conditions: An assessment for gauged and ungauged basins. Journal of Hydrology 362 (3), 274–290.

Norman, J. M., Kustas, W. P., Humes, K. S., 1995. Source approach for estimating soil and vegetation energy fluxes in observations of directional radiometric surface temperature. Agricultural and Forest Meteorology 77 (3), 263–293.

Noto, L. V., Ivanov, V. Y., Bras, R. L., Vivoni, E. R., 2008. Effects of initialization on response of a fully-distributed hydrologic model. Journal of Hydrology 352 (1), 107–125.

O'Callaghan, J. F., Mark, D. M., 1984. The extraction of drainage networks from digital elevation data. Computer vision, graphics, and image processing 28 (3), 323–344.

Oishi, A. C., Oren, R., Novick, K. A., Palmroth, S., Katul, G. G., 2010. Interannual invariability of forest evapotranspiration and its consequence to water flow downstream. Ecosystems 13 (3), 421–436.

Orlandini, S., Moretti, G., Corticelli, M. A., Santangelo, P. E., Capra, A., Rivola, R., Albertson, J. D., 2012. Evaluation of flow direction methods against field observations of overland flow dispersion. Water Resources Research 48 (10).

Orlandini, S., Moretti, G., Franchini, M., Aldighieri, B., Testa, B., 2003. Path-based methods for the determination of nondispersive drainage directions in grid-based digital elevation models. Water resources research 39 (6).

Pahl-Wostl, C., 2007. Transitions towards adaptive management of water facing climate and global change. Water resources management 21 (1), 49–62.

Palacios-Velez, O., Cuevas-Renaud, B., 1986. Automated river-course, ridge and basin delineation from digital elevation data. Journal of Hydrology 86 (3), 299–314.

Panofsky, H. A., Brier, G. W., Best, W. H., 1958. Some application of statistics to meteorology.

Parajka, J., Blöschl, G., 2008. Spatio-temporal combination of modis images–potential for snow cover mapping. Water Resources Research 44 (3).

Parajka, J., Holko, L., Kostka, Z., Blöschl, G., 2012. Modis snow cover mapping accuracy in a small mountain catchment–comparison between open and forest sites. Hydrology and Earth System Sciences 16 (7), 2365–2377.

Parsons, A. J., 1988. Hillslope form. Routledge London.

Parsons, A. J., 2002. Hillslope form. Routledge.

Passalacqua, P., Belmont, P., Staley, D. M., Simley, J. D., Arrowsmith, J. R., Bode, C. A., Crosby, C., DeLong, S. B., Glenn, N. F., Kelly, S. A., et al., 2015. Analyzing high resolution topography for advancing the understanding of mass and energy transfer through landscapes: A review. Earth-Science Reviews 148, 174–193.

Passalacqua, P., Do Trung, T., Foufoula-Georgiou, E., Sapiro, G., Dietrich, W. E., 2010a. A geometric framework for channel network extraction from lidar: Nonlinear diffusion and geodesic paths. Journal of Geophysical Research: Earth Surface 115 (F1).

Passalacqua, P., Tarolli, P., Foufoula-Georgiou, E., 2010b. Testing space-scale methodologies for automatic geomorphic feature extraction from lidar in a complex mountainous landscape. Water resources research 46 (11).

Peckham, R. J., Gyozo, J., 2007. Digital terrain modelling. Springer.

Peckham, S., 2008. Geomorphometry in rivertools. Geomorphometry: concepts, software, applications. Elsevier, Amsterdam, 411–430.

Pejam, M., Arain, M., McCaughey, J., 2006. Energy and water vapour exchanges over a mixedwood boreal forest in ontario, canada. Hydrological Processes 20 (17), 3709–3724.

Penman, H. L., 1948. Natural evaporation from open water, bare soil and grass. In: Proceedings of the Royal Society of London A: Mathematical, Physical and Engineering Sciences. Vol. 193. The Royal Society, pp. 120–145.

Phillips, D. L., Dolph, J., Marks, D., 1992. A comparison of geostatistical procedures for spatial analysis of precipitation in mountainous terrain. Agricultural and Forest Meteorology 58 (1), 119–141.

Phillips, D. L., Marks, D. G., 1996. Spatial uncertainty analysis: propagation of interpolation errors in spatially distributed models. Ecological Modelling 91 (1), 213–229.

Pike, R. J., 2002. A bibliography of terrain modeling (geomorphometry), the quantitative representation of topography. USGS Open file report, 02–465.

Pimentel, D., Berger, B., Filiberto, D., Newton, M., Wolfe, B., Karabinakis, E., Clark, S., Poon, E., Abbett, E., Nandagopal, S., 2004. Water resources: agricultural and environmental issues. BioScience 54 (10), 909–918.

Porcù, F., Milani, L., Petracca, M., 2014. On the uncertainties in validating satellite instantaneous rainfall estimates with raingauge operational network. Atmospheric Research 144, 73–81.

Porporato, A., D?odorico, P., Laio, F., Ridolfi, L., Rodriguez-Iturbe, I., 2002. Ecohydrology of water-controlled ecosystems. Advances in Water Resources 25 (8), 1335–1348.

Prakash, S., Mitra, A. K., Pai, D., 2015. Comparing two high-resolution gauge-adjusted multisatellite rainfall products over india for the southwest monsoon period. Meteorological Applications.

Praskievicz, S., Chang, H., 2009. A review of hydrological modelling of basin-scale climate change and urban development impacts. Progress in Physical Geography 33 (5), 650–671.

Priestley, C., Taylor, R., 1972. On the assessment of surface heat flux and evaporation using large-scale parameters. Monthly weather review 100 (2), 81–92.

Prudhomme, C., Reed, D. W., 1999. Mapping extreme rainfall in a mountainous region using geostatistical techniques: a case study in scotland. International Journal of Climatology 19 (12), 1337–1356.

Ramoelo, A., Majozi, N., Mathieu, R., Jovanovic, N., Nickless, A., Dzikiti, S., 2014. Validation of global evapotranspiration product (mod16) using flux tower data in the african savanna, south africa. Remote Sensing 6 (8), 7406–7423.

Rientjes, T., Haile, A., Kebede, E., Mannaerts, C., Habib, E., Steenhuis, T., 2011. Changes in land cover, rainfall and stream flow in upper gilgel abbay catchment, blue nile basin–ethiopia. Hydrology and Earth System Sciences 15 (6), 1979–1989.

Rigon, R., Bancheri, M., Formetta, G., de Lavenne, A., 2015. The geomorphological unit hydrograph from a historical-critical perspective. Earth Surface Processes and Landforms.

Rigon, R., Bertoldi, G., Over, T. M., 2006. Geotop: A distributed hydrological model with coupled water and energy budgets. Journal of Hydrometeorology 7 (3), 371–388.

Rigon, R., D'Odorico, P., Bertoldi, G., 2011. The geomorphic structure of the runoff peak. Hydrology and Earth System Sciences Discussions 8 (1), 1031–1058.

Rigon, R., Rodriguez-Iturbe, I., Maritan, A., Giacometti, A., Tarboton, D. G., Rinaldo, A., 1996. On hack's law. Water Resources Research 32 (11), 3367–3374.

Rigon R, Ghesla E, T. C., A, C., 2006. The horton machine: a system for dem analysis. Tech. rep., University of Trento, Department of Civil and Environmental Engineering.

Rigon R, Ghesla E, T. C. C. A., 2006. The horton machine: a system for dem analysis. isbn 10:88-8443-147-6.
URL http://www.ing.unitn.it/dica/tools/download/Quaderni/Horton%20manual.pdf.

Rinaldo, A., Marani, A., Rigon, R., 1991. Geomorphological dispersion. Water Resources Research 27 (4), 513–525.

Rinaldo, A., Vogel, G. K., Rigon, R., Rodriguez-Iturbe, I., 1995. Can one gauge the shape of a basin? Water Resources Research 31 (4), 1119–1127.

Robeson, S. M., 1992. Spatial interpolation, network bias, and terrestrial air temperature variability.

Rodell, M., Famiglietti, J., Chen, J., Seneviratne, S., Viterbo, P., Holl, S., Wilson, C., 2004. Basin scale estimates of evapotranspiration using grace and other observations. Geophysical Research Letters 31 (20).

Rodríguez-Iturbe, I., González-Sanabria, M., Bras, R. L., 1982. A geomorphoclimatic theory of the instantaneous unit hydrograph. Water Resources Research 18 (4), 877–886.

Rodríguez-Iturbe, I., Isham, V., Cox, D., Manfreda, S., Porporato, A., 2006. Space-time modeling of soil moisture: Stochastic rainfall forcing with heterogeneous vegetation. Water resources research 42 (6).

Rodríguez-Iturbe, I., Mejía, J. M., 1974. The design of rainfall networks in time and space. Water Resources Research 10 (4), 713–728.

Rodríguez-Iturbe, I., Porporato, A., 2004. Ecohydrology of water-controlled ecosystems. Soil Moisture and Plant Dynamics.

Rodriguez-Iturbe, I., Rinaldo, A., 1997. Fractal river basins: Chance and self-organization. Tech. rep., Cambridge University Press.

Rodríguez-Iturbe, I., Valdés, J. B., 1979. The geomorphologic structure of hydrologic response. Water Resources Research 15 (6), 1409–1420.

Rohrer, M., 1989. Determination of the transition air temperature from snow to rain and intensity of precipitation. In: WMO IASH ETH International Workshop on Precipitation Measurement. pp. 475–582.

Romilly, T. G., Gebremichael, M., 2010. Evaluation of satellite rainfall estimates over ethiopian river basins. Hydrology and Earth System Sciences Discussions 7, 7669–7694.

Romilly, T. G., Gebremichael, M., 2011. Evaluation of satellite rainfall estimates over ethiopian river basins. Hydrology and Earth System Sciences 15 (5), 1505–1514. URL http://www.hydrol-earth-syst-sci.net/15/1505/2011/

Rozante, J. R., Moreira, D. S., de Goncalves, L. G. G., Vila, D. A., 2010. Combining trmm and surface observations of precipitation: technique and validation over south america. Weather and Forecasting 25 (3), 885–894.

213

Ruelland, D., Ardoin-Bardin, S., Billen, G., Servat, E., 2008. Sensitivity of a lumped and semi-distributed hydrological model to several methods of rainfall interpolation on a large basin in west africa. Journal of Hydrology 361 (1), 96–117.

Saha, S., Moorthi, S., Pan, H.-L., Wu, X., Wang, J., Nadiga, S., Tripp, P., Kistler, R., Woollen, J., Behringer, D., et al., 2010. The ncep climate forecast system reanalysis. Bulletin of the American Meteorological Society 91 (8), 1015–1057.

Saha, S., Moorthi, S., Wu, X., Wang, J., Nadiga, S., Tripp, P., Behringer, D., Hou, Y.-T., Chuang, H.-y., Iredell, M., et al., 2014. The ncep climate forecast system version 2. Journal of Climate 27 (6), 2185–2208.

Saha, S., Nadiga, S., Thiaw, C., Wang, J., Wang, W., Zhang, Q., Van den Dool, H., Pan, H.-L., Moorthi, S., Behringer, D., et al., 2006. The ncep climate forecast system. Journal of Climate 19 (15), 3483–3517.

Sahoo, A. K., Pan, M., Troy, T. J., Vinukollu, R. K., Sheffield, J., Wood, E. F., 2011. Reconciling the global terrestrial water budget using satellite remote sensing. Remote Sensing of Environment 115 (8), 1850–1865.

Salio, P., Hobouchian, M. P., Skabar, Y. G., Vila, D., 2015. Evaluation of high-resolution satellite precipitation estimates over southern south america using a dense rain gauge network. Atmospheric Research 163, 146–161.

Samaniego, L., Kumar, R., Attinger, S., 2010. Multiscale parameter regionalization of a grid-based hydrologic model at the mesoscale. Water Resources Research 46 (5).

Sánchez-Moreno, P., Zarzo, A., Dehesa, J. S., 2012. Jensen divergence based on fisher?s information. Journal of Physics A: Mathematical and Theoretical 45 (12), 125305.

Schaffrath, D., Bernhofer, C., 2013. Variability and distribution of spatial evapotranspiration in semi arid inner mongolian grasslands from 2002 to 2011. SpringerPlus 2 (1), 547.

Scharfen, G. R., Hall, D. K., Khalsa, S. J. S., Khalsa, S., Wolfe, J., Marquis, M., Rigg, G., McLean, B., 2000. Accessing the modis snow and ice products at the nsidc daac. In: Geoscience and Remote Sensing Symposium, 2000. Proceedings. IGARSS 2000. IEEE 2000 International. Vol. 5. IEEE, pp. 2059–2061.

Scheerlinck, K., Pauwels, V., Vernieuwe, H., De Baets, B., 2009. Calibration of a water and energy balance model: Recursive parameter estimation versus particle swarm optimization. Water resources research 45 (10).

Schiemann, R., Erdin, R., Willi, M., Frei, C., Berenguer, M., Sempere-Torres, D., 2011. Geostatistical radar-raingauge combination with nonparametric correlograms: methodological considerations and application in switzerland. Hydrology and Earth System Sciences 15 (5), 1515–1536.

Schmidli, J., Frei, C., 2005. Trends of heavy precipitation and wet and dry spells in switzerland during the 20th century. International Journal of Climatology 25 (6), 753–771.

Schulz, J., Albert, P., Behr, H.-D., Caprion, D., Deneke, H., Dewitte, S., Dürr, B., Fuchs, P., Gratzki, A., Hechler, P., et al., 2009. Operational climate monitoring from space: the eumetsat satellite application facility on climate monitoring (cm-saf). Atmospheric Chemistry & Physics 9 (5).

Schuurmans, J., Bierkens, M., Pebesma, E., Uijlenhoet, R., 2007. Automatic prediction of high-resolution daily rainfall fields for multiple extents: the potential of operational radar. Journal of Hydrometeorology 8 (6), 1204–1224.

Seguin, B., BAELZ, S., Monget, J.-M., Petit, V., 1982. Utilisation de la thermographie ir pour l'estimation de l'évaporation régionale i. mise au point méthodologique sur le site de la crau. Agronomie 2 (1), 7–16.

Seleshi, Y., Zanke, U., 2004. Recent changes in rainfall and rainy days in ethiopia. International journal of climatology 24 (8), 973–983.

Setegn, S. G., Srinivasan, R., Dargahi, B., 2008. Hydrological modelling in the lake tana basin, ethiopia using swat model. The Open Hydrology Journal 2 (1).

Settin, T., Botter, G., Rodriguez-Iturbe, I., Rinaldo, A., 2007. Numerical studies on soil moisture distributions in heterogeneous catchments. Water resources research 43 (5).

Shaw, E. M., Beven, K. J., Chappell, N. A., Lamb, R., 2010. Hydrology in practice. CRC Press.

Shrestha, M., Wang, L., Koike, T., Tsutsui, H., Xue, Y., Hirabayashi, Y., 2014. Correcting basin-scale snowfall in a mountainous basin using a distributed snowmelt model and remote-sensing data. Hydrology and Earth System Sciences 18 (2), 747–761.

Singh, J., Knapp, H. V., Arnold, J., Demissie, M., 2005. Hydrological modeling of the iroquois river watershed using hspf and swat1.

Sirguey, P., Mathieu, R., Arnaud, Y., 2009. Subpixel monitoring of the seasonal snow cover with modis at 250 m spatial resolution in the southern alps of new zealand: Methodology and accuracy assessment. Remote Sensing of Environment 113 (1), 160–181.

Skamarock, W., Klemp, J., Dudhia, J., Gill, D., Barker, D., Duda, M., Huang, X., Wang, W., Powers, J., 2008. A description of the advanced research wrf version 3, ncar, tech. note, mesoscale and microscale meteorology division. National Center for Atmospheric Research, Boulder, Colorado, USA.

Smith, R., Goodrich, D., Woolhiser, D., Unkrich, C., Singh, V., et al., 1995. Kineros-a kinematic runoff and erosion model. Computer models of watershed hydrology., 697–732.

Snell, J. D., Sivapalan, M., 1994. On geomorphological dispersion in natural catchments and the geomorphological unit hydrograph. Water Resources Research 30 (7), 2311–2323.

Sorooshian, S., Hsu, K.-L., Gao, X., Gupta, H. V., Imam, B., Braithwaite, D., 2000. Evaluation of persiann system satellite-based estimates of tropical rainfall. Bulletin of the American Meteorological Society 81 (9), 2035–2046.

Steenhuis, T. S., Collick, A. S., Easton, Z. M., Leggesse, E. S., Bayabil, H. K., White, E. D., Awulachew, S. B., Adgo, E., Ahmed, A. A., 2009. Predicting discharge and sediment for the abay (blue nile) with a simple model. Hydrological processes 23 (26), 3728–3737.

Steinacker, R., 1983. Diagnose und prognose der schneefallgrenze. Wetter und Leben 35 (81-90), 120.

Strahler, A. N., 1957. Quantitative analysis of watershed geomorphology. Eos, Transactions American Geophysical Union 38 (6), 913–920.

Sui, D., Maggio, R., 1999. Integrating gis with hydrological modeling: practices, problems, and prospects. Computers, environment and urban systems 23 (1), 33–51.

Swenson, S., Wahr, J., 2006. Post-processing removal of correlated errors in grace data. Geophysical Research Letters 33 (8).

Tabios, G. Q., Salas, J. D., 1985. A comparative analysis of techniques for spatial interpolation of precipitation1.

Tamea, S., Laio, F., Ridolfi, L., D'Odorico, P., Rodriguez-Iturbe, I., 2009. Ecohydrology of groundwater-dependent ecosystems: 2. stochastic soil moisture dynamics. Water resources research 45 (5).

Tarboton, D. G., 1989. The analysis of river basins and channel networks using digital terrain data. Ph.D. thesis, Massachusetts Institute of Technology.

Tarboton, D. G., 1997. A new method for the determination of flow directions and upslope areas in grid digital elevation models. Water resources research 33 (2), 309–319.

Tarboton, D. G., Ames, D. P., 2001. Advances in the mapping of flow networks from digital elevation data. In: World water and environmental resources congress. Am. Soc Civil Engrs USA, pp. 20–24.

Tarboton, D. G., Bras, R. L., Rodriguez-Iturbe, I., 1991. On the extraction of channel networks from digital elevation data. Hydrological processes 5 (1), 81–100.

Tarnavsky, E., Grimes, D., Maidment, R., Black, E., Allan, R. P., Stringer, M., Chadwick, R., Kayitakire, F., 2014. Extension of the tamsat satellite-based rainfall monitoring over africa and from 1983 to present. Journal of Applied Meteorology and Climatology 53 (12), 2805–2822.

Tarolli, P., Dalla Fontana, G., 2009. Hillslope-to-valley transition morphology: new opportunities from high resolution dtms. Geomorphology 113 (1), 47–56.

Tarolli, P., Sofia, G., Dalla Fontana, G., 2012. Geomorphic features extraction from high-resolution topography: landslide crowns and bank erosion. Natural Hazards 61 (1), 65–83.

Taye, M. T., Willems, P., 2011. Influence of climate variability on representative qdf predictions of the upper blue nile basin. Journal of hydrology 411 (3), 355–365.

Teferi, E., Uhlenbrook, S., Bewket, W., Wenninger, J., Simane, B., 2010. The use of remote sensing to quantify wetland loss in the choke mountain range, upper blue nile basin, ethiopia. Hydrology and Earth System Sciences, 14,(12).

217

Tekleab, S., Uhlenbrook, S., Mohamed, Y., Savenije, H., Temesgen, M., Wenninger, J., 2011. Water balance modeling of upper blue nile catchments using a top-down approach. Hydrology and Earth System Sciences, 15,(7).

Themeßl, M. J., Gobiet, A., Heinrich, G., 2012. Empirical-statistical downscaling and error correction of regional climate models and its impact on the climate change signal. Climatic Change 112 (2), 449–468.

Thiessen, A. H., 1911. Precipitation averages for large areas. Monthly weather review 39 (7), 1082–1089.

Thorne, V., Coakeley, P., Grimes, D., Dugdale, G., 2001. Comparison of tamsat and cpc rainfall estimates with raingauges, for southern africa. International Journal of Remote Sensing 22 (10), 1951–1974.

Tian, Y., Peters-Lidard, C. D., Choudhury, B. J., Garcia, M., 2007. Multitemporal analysis of trmm-based satellite precipitation products for land data assimilation applications. Journal of Hydrometeorology 8 (6), 1165–1183.

Tobin, C., Nicotina, L., Parlange, M. B., Berne, A., Rinaldo, A., 2011. Improved interpolation of meteorological forcings for hydrologic applications in a swiss alpine region. Journal of Hydrology 401 (1), 77–89.

Todini, E., 2007. Hydrological catchment modelling: past, present and future. Hydrology and Earth System Sciences 11 (1), 468–482.

Tripathi, M., Raghuwanshi, N., Rao, G., 2006. Effect of watershed subdivision on simulation of water balance components. Hydrological processes 20 (5), 1137–1156.

Troutman, B. M., Karlinger, M. R., 1984. On the expected width function for topologically random channel networks. Journal of applied probability, 836–849.

Tucker, G. E., Lancaster, S. T., Gasparini, N. M., Bras, R. L., Rybarczyk, S. M., 2001. An object-oriented framework for distributed hydrologic and geomorphic modeling using triangulated irregular networks. Computers & Geosciences 27 (8), 959–973.

Uhlenbrook, S., Mohamed, Y., Gragne, A., 2010. Analyzing catchment behavior through catchment modeling in the gilgel abay, upper blue nile river basin, ethiopia. Hydrology and Earth System Sciences 14 (10), 2153–2165.

Van Delft, G., El Serafy, G., Heemink, A., 2009. The ensemble particle filter (enpf) in rainfall-runoff models. Stochastic Environmental Research and Risk Assessment 23 (8), 1203–1211.

Van Der Knijff, J., Younis, J., De Roo, A., 2010. Lisflood: a gis-based distributed model for river basin scale water balance and flood simulation. International Journal of Geographical Information Science 24 (2), 189–212.

Veitzer, S. A., Gupta, V. K., 2001. Statistical self-similarity of width function maxima with implications to floods. Advances in water resources 24 (9), 955–965.

Velasco-Forero, C. A., Sempere-Torres, D., Cassiraga, E. F., Gómez-Hernández, J. J., 2009. A non-parametric automatic blending methodology to estimate rainfall fields from rain gauge and radar data. Advances in Water Resources 32 (7), 986–1002.

Verdin, K. L., Verdin, J. P., 1999. A topological system for delineation and codification of the earth's river basins. Journal of Hydrology 218 (1), 1–12.

Verworn, A., Haberlandt, U., 2011. Spatial interpolation of hourly rainfall–effect of additional information, variogram inference and storm properties. Hydrology and Earth System Sciences 15 (2), 569–584.

Viste, E., Korecha, D., Sorteberg, A., 2013. Recent drought and precipitation tendencies in ethiopia. Theoretical and Applied Climatology 112 (3-4), 535–551.

Vrugt, J. A., Bouten, W., Gupta, H. V., Sorooshian, S., 2002. Toward improved identifiability of hydrologic model parameters: The information content of experimental data. Water Resources Research 38 (12), 48–1.

Vrugt, J. A., Gupta, H. V., Bouten, W., Sorooshian, S., 2003. A shuffled complex evolution metropolis algorithm for optimization and uncertainty assessment of hydrologic model parameters. Water Resources Research 39 (8).

Vrugt, J. A., Ter Braak, C., Diks, C., Robinson, B. A., Hyman, J. M., Higdon, D., 2009. Accelerating markov chain monte carlo simulation by differential evolution with self-adaptive randomized subspace sampling. International Journal of Nonlinear Sciences and Numerical Simulation 10 (3), 273–290.

Wale, A., Rientjes, T., Gieske, A., Getachew, H., 2009. Ungauged catchment contributions to lake tana's water balance. Hydrological processes 23 (26), 3682–3693.

Wang, P.-j., Wang, R.-Y., 2002. A generalized width function of fractal river network for the calculation of hydrologic responses. Fractals 10 (02), 157–171.

Wang, S., Huang, J., Li, J., Rivera, A., McKenney, D. W., Sheffield, J., 2014a. Assessment of water budget for sixteen large drainage basins in canada. Journal of Hydrology 512, 1–15.

Wang, S., Huang, J., Yang, D., Pavlic, G., Li, J., 2014b. Long-term water budget imbalances and error sources for cold region drainage basins. Hydrological Processes.

Wang, W., Xie, P., Yoo, S.-H., Xue, Y., Kumar, A., Wu, X., 2011. An assessment of the surface climate in the ncep climate forecast system reanalysis. Climate dynamics 37 (7-8), 1601–1620.

Ward, E., Buytaert, W., Peaver, L., Wheater, H., 2011. Evaluation of precipitation products over complex mountainous terrain: A water resources perspective. Advances in Water Resources 34 (10), 1222–1231.

Wilcke, R. A. I., Mendlik, T., Gobiet, A., 2013. Multi-variable error correction of regional climate models. Climatic Change 120 (4), 871–887.

Wilson, J. P., Gallant, J. C., 2000. Terrain analysis: principles and applications. Wiley.

WMO, 1994. Guide to hydrological practices.

Woo, M.-K., 2007. Cold Region Atmospheric and Hydrologic Studies. The Mackenzie GEWEX Experience: Volume 2: Hydrologic Processes. Vol. 2. Springer.

Wood, E. F., Roundy, J. K., Troy, T. J., Beek, R., Bierkens, M., Blyth, E., Roo, A., Döll, P., Ek, M., Famiglietti, J., et al., 2012. Reply to comment by keith j. beven and hannah l. cloke. on hyperresolution global land surface modeling: Meeting a grand challenge for monitoring earth's terrestrial water. Water Resources Research 48 (1).

Wood, E. F., Roundy, J. K., Troy, T. J., Van Beek, L., Bierkens, M. F., Blyth, E., de Roo, A., Döll, P., Ek, M., Famiglietti, J., et al., 2011. Hyperresolution global land surface modeling: Meeting a grand challenge for monitoring earth's terrestrial water. Water Resources Research 47 (5).

Wood, J., 2009. The landserf manual. City University, London, 213.

Worqlul, A. W., Maathuis, B., Adem, A. A., Demissie, S. S., Langan, S., Steenhuis, T. S., 2014. Comparison of rainfall estimations by trmm 3b42, mpeg and cfsr with ground-observed data for the lake tana basin in ethiopia. Hydrology and Earth System Sciences 18 (12), 4871–4881.

Wosenie, M. D., Verhoest, N., Pauwels, V., Negatu, T. A., Poesen, J., Adgo, E., Deckers, J., Nyssen, J., 2014. Analyzing runoff processes through conceptual hydrological modeling in the upper blue nile basin, ethiopia. Hydrology and Earth System Sciences 18 (12), 5149–5167.

Xue, M., Droegemeier, K. K., Wong, V., 2000. The advanced regional prediction system (arps)–a multi-scale nonhydrostatic atmospheric simulation and prediction model. part i: Model dynamics and verification. Meteorology and atmospheric physics 75 (3-4), 161–193.

Xue, M., Droegemeier, K. K., Wong, V., Shapiro, A., Brewster, K., Carr, F., Weber, D., Liu, Y., Wang, D., 2001. The advanced regional prediction system (arps)–a multi-scale nonhydrostatic atmospheric simulation and prediction tool. part ii: Model physics and applications. Meteorology and atmospheric physics 76 (3-4), 143–165.

Xue, Y., Huang, B., Hu, Z.-Z., Kumar, A., Wen, C., Behringer, D., Nadiga, S., 2011. An assessment of oceanic variability in the ncep climate forecast system reanalysis. Climate dynamics 37 (11-12), 2511–2539.

Ye, H., Cohen, J., Rawlins, M., 2013. Discrimination of solid from liquid precipitation over northern eurasia using surface atmospheric conditions*. Journal of Hydrometeorology 14 (4), 1345–1355.

Yilmaz, M. T., Anderson, M. C., Zaitchik, B., Hain, C. R., Crow, W. T., Ozdogan, M., Chun, J. A., Evans, J., 2014. Comparison of prognostic and diagnostic surface flux modeling approaches over the nile river basin. Water Resources Research 50 (1), 386–408.

Yoshiyukiishii, Y. K., Nakamura, R., 2004. Water balance of a snowy watershed in hokkaido, japan. Northern Research Basins Water Balance (290), 13.

Young, M. P., Williams, C. J., Chiu, J. C., Maidment, R. I., Chen, S.-H., 2014. Investigation of discrepancies in satellite rainfall estimates over ethiopia. Journal of Hydrometeorology 15 (6), 2347–2369.

Zambrano-Bigiarini, M., Bigiarini, M. M. Z., 2013. Package ?hydrogof?

Zhang, H., Wang, Y., Wang, Y., Li, D., Wang, X., 2013. The effect of watershed scale on hec-hms calibrated parameters: a case study in the clear creek watershed in iowa, usa. Hydrology and Earth System Sciences Discussions 10 (1), 965–998.

Zhang, L., Dawes, W., Walker, G., 2001. Response of mean annual evapotranspiration to vegetation changes at catchment scale. Water resources research 37 (3), 701–708.

Zhao, L., Weng, F., 2002. Retrieval of ice cloud parameters using the advanced microwave sounding unit. Journal of Applied Meteorology 41 (4), 384–395.